

DISSERTATION

# **Helium Accreting White Dwarfs as Progenitors of Explosive Stellar Transients**

ZUR ERLANGUNG DES DOKTORGRADES (DR. RER. NAT.)  
DER  
MATHEMATISCH-NATURWISSENSCHAFTLICHEN FAKULTÄT  
DER  
RHEINISCHEN FRIEDRICH-WILHELMS-UNIVERSITÄT BONN

*vorgelegt von*  
*Patrick Neunteufel*  
*aus*  
*München*

June 8, 2017

Angefertigt mit Genehmigung der Mathematisch-Naturwissenschaftlichen Fakultät der Rheinischen  
Friedrich-Wilhelms-Universität Bonn

1. Gutachter: Prof. Dr. Norbert Langer
2. Gutachter: Prof. Dr. Frank Bertoldi

Tag der Promotion: 23.10.2017  
Erscheinungsjahr: 2017

“It has been said that astronomy is a humbling and character-building experience. There is perhaps no better demonstration of the folly of human conceits than this distant image of our tiny world. To me, it underscores our responsibility to deal more kindly with one another, and to preserve and cherish the pale blue dot, the only home we’ve ever known.”

*Carl Sagan, Pale Blue Dot: A Vision of the Human Future in Space*

Für meine Eltern

# Contents

<b>1. Introduction</b>	<b>1</b>
1.1. An introduction to stellar evolution . . . . .	2
1.1.1. Stars . . . . .	2
1.1.2. Characteristic timescales . . . . .	9
1.1.3. Stellar remnants . . . . .	10
1.2. Binary evolution . . . . .	17
1.2.1. Interacting binaries . . . . .	17
1.2.2. Mass transfer . . . . .	19
1.2.3. Common envelopes . . . . .	21
1.2.4. Effects on orbital parameters . . . . .	23
1.3. Angular momentum dissipation in rotating stars . . . . .	25
1.4. Explosive stellar transients . . . . .	27
1.4.1. Types of supernovae . . . . .	27
1.4.2. Accretion-induced transients . . . . .	28
1.5. This thesis . . . . .	30
 <b>2. Models for the evolution of close binaries with He-Star and WD components towards Type Ia supernova explosions</b>	 <b>33</b>
2.1. Introduction . . . . .	33
2.2. Numerical methods and physical assumptions . . . . .	35
2.2.1. Detonation conditions and mass-transfer efficiency . . . . .	35
2.2.2. Computational framework . . . . .	36
2.3. Simulation results . . . . .	39
2.3.1. Evolution of the donor star . . . . .	39
2.3.2. Initial parameters of the investigated binary systems . . . . .	41
2.3.3. Discussion of binary results . . . . .	41
2.4. Conclusions . . . . .	53
 <b>3. Helium ignition in rotating magnetized CO white dwarfs leading to fast and faint rather than classical Type Ia supernovae</b>	 <b>55</b>
3.1. Introduction . . . . .	55
3.2. Numerical methods and physical assumptions . . . . .	58
3.2.1. Numerical methods . . . . .	58
3.2.2. Initial models and input parameters . . . . .	61
3.2.3. Ignition conditions . . . . .	62
3.3. Results . . . . .	63
3.3.1. Rotational profile . . . . .	63
3.3.2. Chemical profile . . . . .	65

## Contents

3.3.3. Accretion behavior and ignition . . . . .	65
3.3.4. Impact of parameter variations . . . . .	71
3.3.5. Ignition densities and detonations . . . . .	79
3.4. Comparison with the non-magnetic rotating case . . . . .	82
3.5. Evolutionary fates . . . . .	83
3.6. Conclusions . . . . .	84
<b>4. Ignition in white dwarf models undergoing time-varying helium accretion.</b>	<b>91</b>
4.1. Introduction . . . . .	91
4.2. Methods and physical assumptions . . . . .	93
4.2.1. Numerical methods . . . . .	93
4.2.2. Input models . . . . .	95
4.3. Results . . . . .	97
4.3.1. Linear scenario systems . . . . .	97
4.3.2. Step scenario systems . . . . .	104
4.3.3. Rotation . . . . .	105
4.3.4. Realistic scenario systems . . . . .	106
4.4. Conclusions . . . . .	107
<b>5. Conclusions</b>	<b>111</b>
5.1. SNe Ia from He accreting WDs . . . . .	111
5.2. Ignition conditions . . . . .	111
5.3. Outlook . . . . .	112
<b>Appendix A. Model parameters for chapter 2</b>	<b>115</b>
<b>Appendix B. Additional data for chapter 3</b>	<b>129</b>
<b>Bibliography</b>	<b>143</b>

# 1. Introduction

Few things have embodied the concept of “eternity” in quite the same way in the course of human history as the sky in a cloudless night. Stars, and their wandering cousins, the planets, were seen as representatives of the gods, weavers of fate, beacons by which learned men and women could predict their own future. It comes as no surprise that unpredictable phenomena like eclipses, comets or supernovae were seen as grave portents, divine commentary on the state of the mortal world.

Ironically the attempt to create a science with the power to use the stars to predict the fate of human beings gave rise to a science with the power to allow human beings to predict the fate of stars. Stars, which earlier humanity had seen as immovable and eternal, revealed themselves to be physical processes, governed by the same laws that scientists could observe in their own world. Stars are not eternal but physical objects with a beginning, a finite period of existence and an end.

The evolution of stars is measured in millions or billions of years. This makes their empirical study challenging as many of the effects predicted by mathematical descriptions of their behavior proceed far too slowly for a human astronomer to observe in their lifetime. While short-term processes, like pulsations<sup>1</sup> are often short enough to be observable, longer lasting processes invariably require the study of statistically larger stellar populations with similar attributes.

Although stars have lost their mystical veneer, their study, whether as a means or an end, is doubtlessly the foundation of modern astrophysics. The reason for this importance is clearly visible in the night sky: Stars are the most prevalent source<sup>2</sup> of radiation in the cosmos. Bereft of this radiation, an Earth-based observer would be completely unable to observe any astrophysical process at all. Furthermore stars, as gravitationally interacting objects, trace the mass distribution of the universe on its largest scales. Contained within the grandest cosmological structures, filaments and walls millions of light years across (Colless et al. 2001), are galaxies, clustered in groups, some composed of trillions of individual stars. The radiation emitted by stars is fueled by the energy liberated from the binding forces of atomic nuclei. The elemental composition of the Universe subsequent to primordial nucleosynthesis was dominated by hydrogen and helium, with only traces of lithium and beryllium and their respective isotopes. Stars of all types and evolutionary stages are therefore by far the dominant source of heavier elements in the cosmos.

Stars heavily influence their own surroundings. The remaining quantities of the primordial gas from which they form may coalesce into dust clouds, companion stars, asteroids or planets. Their winds influence the nature of the interstellar medium, their gravitational fields alter the structure of their stellar neighborhood and, eventually, they enrich the Universe with heavy elements formed during their lifetimes or in the crucible of their fiery demise.

The expiration of more massive stars or certain binary systems results in supernovae, explosive transients luminous enough to allow for distance measurements of billions of light years (Perlmutter et al. 1999). The cataclysmic events are the dominant source of radioactive isotopes in the cosmos

---

<sup>1</sup>as in the famous  $\delta$ -cepheids (Stebbins 1908; Persson et al. 2004).

<sup>2</sup>excluding the universe itself in the form of the cosmic microwave background.

## 1. Introduction

and their products, black holes and neutron stars, exist in states which probe the limits of current physical understanding and are key candidate sources of the highest energy cosmic radiation.

### 1.1. An introduction to stellar evolution

This section contains a brief introduction to stars as a concept of stellar evolution, a short description of the processes involved in star formation and a description of stellar remnants. This section follows general outline of the description as presented in Carroll & Ostlie (2007) and Kippenhahn & Weigert (1990).

#### 1.1.1. Stars

Stars can be described as spheres of plasma kept in hydrostatic equilibrium by the radiative and gas pressure created by nuclear fusion reactions in their interior. Owing to the slow pace, compared to human standards, at which many processes in long-term stellar evolution proceed, observational studies are necessarily dependent on short-term measurements of larger populations of stars. The effort can, not entirely unreasonably, be compared to a biologist trying to deduce the life-cycle of a horse from a series of photographs of different horses taken at different times in their lives.

One way to visualize large samples of stars was developed in the form of the *Hertzsprung-Russell diagram* (HR diagram, see Russell 1914a,b) where luminosity or absolute magnitude is plotted in relation to color or effective surface temperature. Figure 1.1 shows an observational HR diagram of a sample of a number of stars chosen at random from the HIPPARCOS-catalogue (ESA 1997). There is an immediately obvious overdensity of stars at the center of the diagram. This feature is called the *main sequence*. If one accepts the idea that stars evolve and do not occupy the same spot in the HR diagram for the entirety of their existence, that not all stars in the diagram started their evolution at the same time and follow the same evolutionary path, then there must be a reason for them being mainly found on the main sequence. This is explained by the fact that stars spend most of their existence on some part of the main sequence. Even if, at some point during their evolution, they leave the main sequence, an observation at a random point in time will more likely find them on the main sequence than off it. As will be explained in the next section, a star on the main sequence is characterized by its maintenance of hydrostatic equilibrium while exhibiting stable hydrogen-burning.

The second overdensity, located at lower temperatures and higher luminosities (top right in the diagram), is less populated than the main sequence. Following the same argument as before, stars located in this area are either of a different type than those in the main sequence or, if they are essentially part of the same population, they spend less time in this portion of the HR diagram than on the main sequence. These stars are referred to as *giants*. The reason for this term lies in basic thermodynamical considerations: If stars can be approximated as spherical, radiating black bodies, then the Stefan-Boltzmann law

$$L = 4\pi R^2 \sigma T_{\text{eff}}^4 \quad (1.1)$$

holds, where  $T_{\text{eff}}$  is the effective surface temperature,  $\sigma$  is Boltzmann's constant,  $R$  is the radius of the star and  $L$  its luminosity. Accordingly, the more luminous a star is, while keeping its temperature constant, the greater its radius must be. This means that the further to the top right of the diagram a star is located, the greater its radius. In the same vein, stars located to the bottom left of the diagram



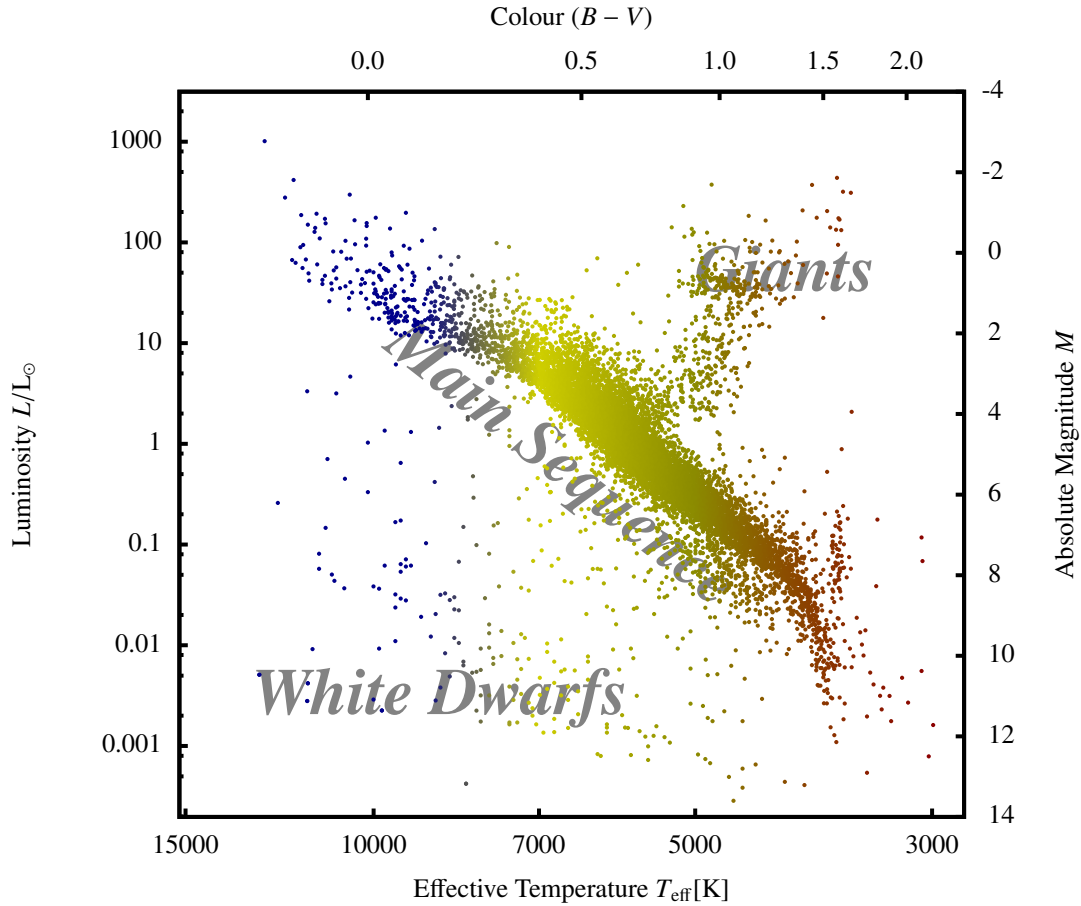


Figure 1.1.: Positions of 11 000 stars, chosen at random from the HIPPARCOS-catalogue (ESA 1997) and the Gliese-catalogue (WDs, Gliese & Jahreiß 1991), in the Hertzsprung-Russell diagram. The main sequence (as labeled) is the prominent cluster of data points in the center, running from lower effective temperatures and lower luminosities towards higher luminosities and effective temperatures. The feature branching off towards higher luminosities and lower temperatures (labeled "giants") is the red giant branch. White dwarfs tend to occupy the region (labeled as such) in the lower left of the diagram.

## 1. Introduction



Figure 1.2.: Star-forming Region IC 348 Around Protostar LRL 54361 - Spitzer

Image credit: NASA, ESA, J. Muzerolle (STScI), E. Furlan (NOAO and Caltech), K. Flaherty (University of Arizona/Steward Observatory), Z. Balog (Max Planck Institute for Astronomy), and R. Gutermuth (University of Massachusetts, Amherst)

will have comparatively smaller radii. These small but hot stars are referred to as *white dwarfs* (see e.g. Liebert 1980; Bergeron et al. 1992).

There are many peculiar ways a star can evolve throughout their lifetimes, each corresponding to a certain path in the HR diagram, dependent on its mass, initial chemical composition, rotation or the presence of binary companions.

### Star formation

Stars form in the collapse of extensive interstellar molecular clouds (see Fig. 1.2). During the first period of star formation in the Universe these clouds consisted of pristine helium and hydrogen and only traces of other light isotopes in the same ratio as formed during the primordial nucleosynthesis (see, e.g. Liddle 2003). The exact nature of this first stellar population (also called *population III-stars*) is still a matter of debate (Yoshida et al. 2004; Nakamura & Umemura 1999; Carr et al. 1984; Schaerer 2002), but they did provide the first significant quantities of elements heavier than helium ("metals") to the cosmos. Consequently, while still forming out of interstellar gas clouds, subsequent generations of stars featured an admixture of metals in their chemical composition from the beginning.

In a hydrostatically stable, gravitationally bound system in a state of equilibrium, the relation between the system's kinetic energy ( $T$ ) and its gravitational potential ( $U$ ) is described by the *virial theorem*:

$$2T + U = 0. \quad (1.2)$$

A system for which this relation holds will neither expand nor collapse. If, however, the kinetic energy dominates, the system will expand. If the potential energy dominates, it will collapse. On the

basis of the virial theorem it can be shown that a gravitationally bound cloud of constant density will collapse if it exceeds the *Jeans mass*

$$M_J \approx \left( \frac{5\sigma T}{G\mu m_H} \right)^{3/2} \left( \frac{3}{4\pi\rho_0} \right)^{1/2}, \quad (1.3)$$

where  $T$  is temperature,  $G$  is the gravitational constant,  $\mu$  the mean molecular weight,  $m_H$  the mass of the hydrogen atom and  $\rho_0$  the density of the cloud. Associated with the adiabatic collapse of a cloud exceeding the Jeans mass is the free-fall timescale<sup>3</sup>

$$t_{ff,J} = \left( \frac{3\pi}{32G\rho_0} \right)^{1/2}, \quad (1.4)$$

which describes the time it would take an arbitrary component of the cloud to reach the cloud's center of mass under the influence of the cloud's own gravitational attraction.

The Jeans masses of molecular clouds are usually higher than even the highest observed stellar mass by a few orders of magnitudes. This implies that during collapse, the cloud must fragment into smaller sub-entities which then proceed to form individual stars (see e.g. Clark et al. 2011). During adiabatic collapse and after fragmentation, the temperature of the individual cloud fragments increases and material at the center of mass approaches hydrostatic equilibrium, slowing the infalling material, which forms a core of several AU in diameter. The object is now referred to as a *protostar* (Larson 1969). The effective temperature of the evolving object eventually becomes high enough to dissociate and ionize the molecular hydrogen of the cloud matter, changing its opacity. The change in opacity, coupled with the still relatively low temperature of the protostar, leads to the development of convective currents throughout the interior while contraction continues. The extent of the convective envelope puts the fledgling star on the *Hayashi track*, which represents the “coolest” or “reddest” point a star can occupy in the HR diagram while still being close to hydrostatic equilibrium. On the cooler side of the Hayashi track convection would not be adequate to transport the protostar's luminosity and heat would have to be lost through the physical expulsion of stellar material until the luminosity decreased enough for convection to be effective again. It should be noted that, during the collapse of the primordial molecular cloud, the effective temperature is allowed to be lower since the object is not expected to be in hydrostatic equilibrium.

With continuing contraction, temperatures become high enough in more massive stars to facilitate the CNO-reaction, turning preexisting  $^{12}_6\text{C}$  into  $^{14}_7\text{N}$  and moving the star horizontally towards the blue end of the HR diagram until temperatures high enough for stable hydrogen-burning are reached. Once stable hydrogen burning is established, and it has reached hydrostatic equilibrium, the star has arrived on the main sequence. This point in the star's evolution is referred to as the *zero-age main sequence* (ZAMS). Low-mass stars generally do not reach high enough temperature during contraction towards ZAMS to facilitate the CNO-reaction, thereby skipping the horizontal development in the HR diagram before starting hydrogen-burning.

Some protostars are not massive enough to provide the conditions necessary for hydrogen-burning at all. These objects may still reach hydrostatic equilibrium and some nuclear burning may still occur, mainly in the form of lithium and deuterium processing, depending on mass, for which lower temperatures are sufficient. These objects are known as *brown dwarfs* (Burrows et al. 2001; Luhman

<sup>3</sup>Note the difference to the free-fall timescale of collapsing star in Sec. 1.1.2.

## 1. Introduction

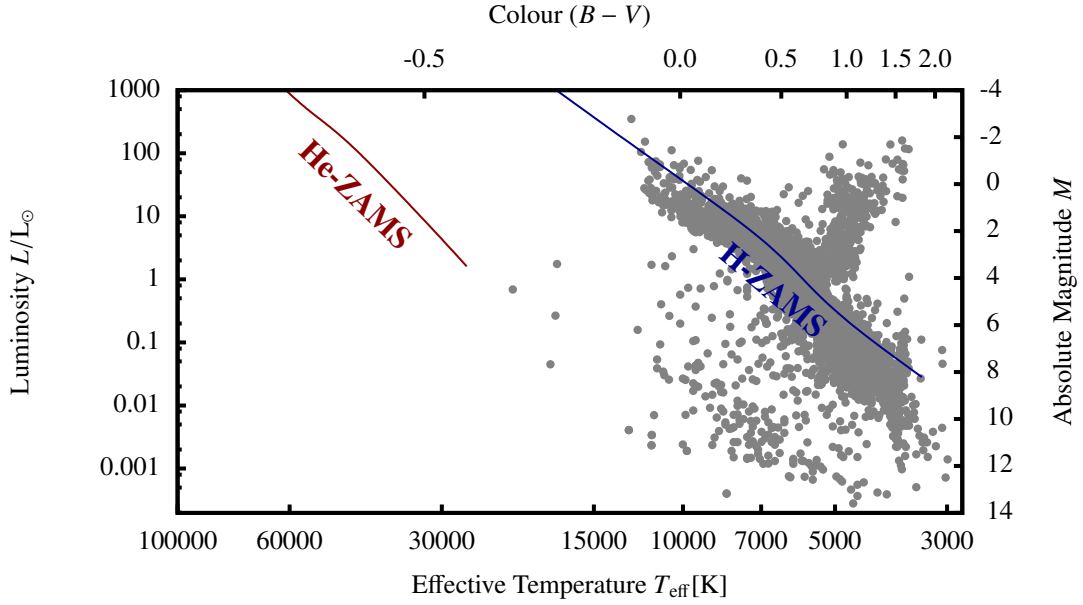


Figure 1.3.: Theoretical positions of the hydrogen and helium ZAMS in the HR-diagram, overlaid on the data presented in Fig. 1.1. Note that the presented ZAMS only include stars with  $M > 0.5M_{\odot}$ .

2012; Burrows & Liebert 1993). They usually exhibit masses of  $\leq 0.072 M_{\odot}$  and are comparatively cool and faint.

The contraction between the protostar phase and ZAMS is inversely correlated with the mass of the protostar and may be as short as tens of kyrs in very massive ( $\approx 60 M_{\odot}$ ) stars or as long as tens of Myr in low-mass ( $\leq 0.8 M_{\odot}$ ) objects. The masses of newly formed stars can be described with the so-called *initial mass function*. Star formation seems to be heavily biased towards lower masses with a majority of stars ( $\sim 90\%$ ) possessing masses of less than  $0.8 M_{\odot}$  (Salpeter 1955; Rana 1987; Bernasconi & Maeder 1996; Kroupa 2002).

In parallel to the main sequence, one may define the *helium main sequence* as the area in the HR diagram where stars composed mainly of helium might be found. These would be stars in hydrostatic equilibrium whose main source of energy is the nuclear burning of helium. Since the temperatures and densities required for helium burning are higher than those for hydrogen burning, one would expect these objects to be both smaller as well as hotter than stars of the main sequence. Fig. 1.3 shows the theoretical location in the HR diagram of both the ZAMS of hydrogen-burning stars and the helium ZAMS (He-ZAMS).

### Evolution during and after the main sequence phase

The life of a low-mass star (generally defined as  $M \leq 2.3 M_{\odot}$ , the Sun is a favorite example) is reasonably well understood and can provide an instructive example for the evolution of a star through the HR diagram: the star will start its life on the main sequence, converting (also referred to as “burning”) hydrogen into helium in its core via the three proton-proton chains (PP I - III, see Salpeter 1952). Due to the low temperatures encountered in the envelopes of these stars and correspondingly

high opacities, heat is generally transported convectively in the outermost layers and radiatively in the central regions. This phase lasts about  $10^{10}$  yr in stars with similar characteristics as the Sun. Once the star exhausts its central supply of hydrogen, the burning process moves outwards, leaving an inert helium core, which contracts. The contraction of the helium core leads to an increase in hydrogen burning in the surrounding shells, which in turn leads to an increase in luminosity and an expansion of the star's envelope while decreasing its effective temperature.

At this point the star has left the main sequence and entered the *subgiant branch* (SGB), which roughly corresponds to the fainter end of the cluster of stars labeled “giants” in Fig. 1.1. While on the SGB, the star continues to convert hydrogen into helium in a burning layer around the core, which increases in mass. The concurrent expansion of the envelope with decreasing opacity leads to the expansion of the convective envelope and with it the efficiency of the heat transport.

The star is now on the *red giant branch* with increasing luminosity but roughly constant surface temperature while the expanding convective zone starts to transport nuclear burning products from the deeper layers closer to the surface. The triple-alpha process, which fuses three  ${}^4_2\text{He}$ -nuclei into one  ${}^{12}_6\text{C}$  nucleus requires significantly higher temperatures and densities than hydrogen burning. At the tip of the RGB the mass of the helium core has increased sufficiently for this process to become possible. This leads to an expansion of the core.

In stars with  $M \leq 2.3 M_{\odot}$ , in which the helium core is electron-degenerate at this point, the onset of helium burning results in a *helium core flash*. During the helium core flash, the luminosity of the helium burning layers may be as high as  $L = 10^{11} L_{\odot}$  for a few seconds, the energy release being absorbed by the overlying layers and used for the reversal of the electron degeneracy.

In any case, with the start of helium burning the star contracts, continuing helium burning at its center, while increasing in effective temperature. Owing to the horizontal development in the HR diagram, this phase is known as the *horizontal branch* (HB). The HB is essentially the analogue of the main sequence during the central hydrogen burning portion of the star's evolution.

Once the star has exhausted its supply of helium in the core, helium burning moves into the envelope while the core, now composed of mainly carbon and oxygen, contracts. The envelope, counteracting the contraction of the inert core, expands and the star cools, entering the *asymptotic giant branch* (AGB). During the later phases of the AGB evolution, increasingly violent helium shell flashes induce a mass loss of up to  $10^{-4} M_{\odot}/\text{yr}$ , expelling a large portion of the remaining hydrogen and helium envelope, leaving only the inert and degenerate carbon-oxygen (CO) core. The initially very hot core subsequently cools, eventually occupying, depending on its temperature, the bottom portion of the HR diagram as a white dwarf.

This scenario describes only one of a number of possible characteristic evolutionary tracks of stars through the HR diagram. Fig. 1.4 outlines a few more scenarios for the outcomes of stellar evolution for stars of different initial masses. More massive stars will generally behave differently, starting their main-sequence evolution at higher temperatures and remaining on the main-sequence for a significantly shorter time.

The high luminosity of the hydrogen burning core characteristic to massive stars also leads to a feature not present in low-mass stars: a convective core (as opposed to the convective envelope of low-mass stars). The convective core is a result of the energy generation exceeding the ability of the stellar material to transport heat efficiently enough away from the burning regions radiatively. Convection leads to a practically chemically homogeneous core. Unlike low-mass stars, massive stars are able to provide temperatures high enough to synthesize heavier elements (up to and including iron) during the later stages of their evolution. Nucleosynthesis in stars is usually limited by the binding energy

## 1. Introduction

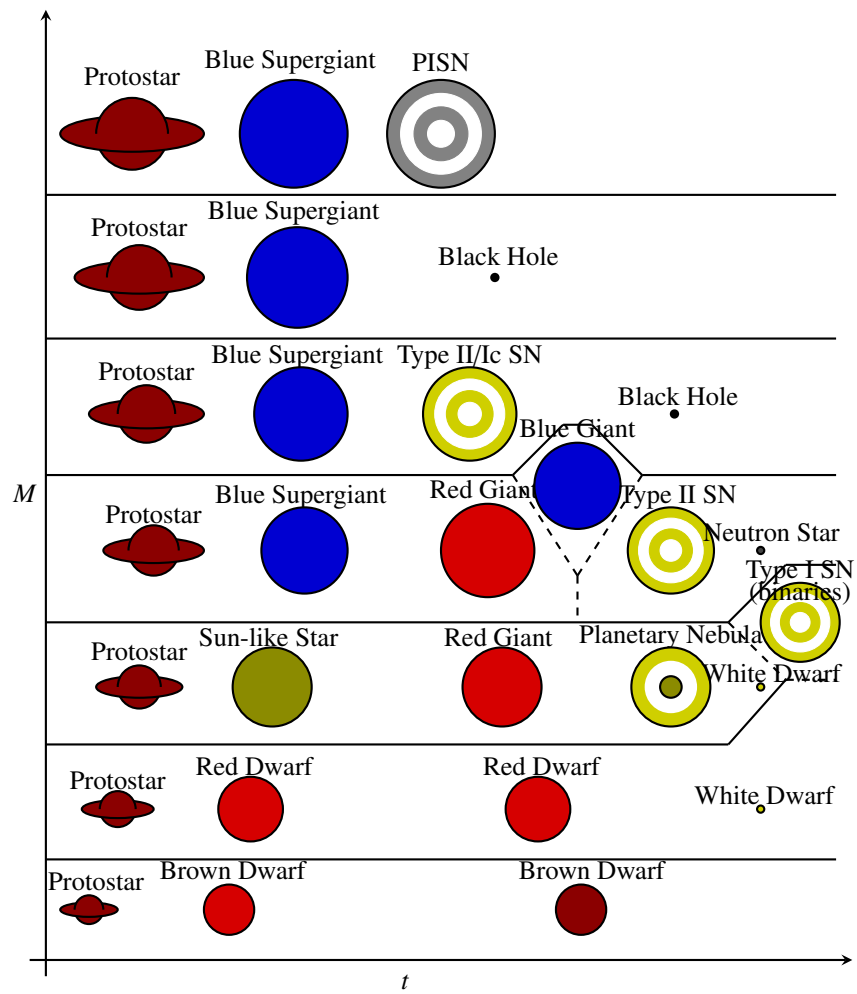


Figure 1.4.: Illustration of expected evolutionary fates of stars depending on their mass..

of nuclei per nucleon, the highest of which is possessed by iron. The most massive stars, unlike their lower-mass cousins, end their lives in core-collapse supernovae, during which elements heavier than iron may be synthesized, making them the most prevalent source of these most rare elements in the Universe.

### 1.1.2. Characteristic timescales

One way to estimate the length of time a star spends, e.g., on the main sequence is to correlate its luminosity with the amount of fuel it has left for nuclear energy generation. A star on the main sequence converts hydrogen into helium by (via a small number of intermediate steps) fusing four hydrogen nuclei into one helium nucleus. Atomic nuclei are bound by a negative potential created by the strong force between the hadronic components of the nucleus. The strong force is counteracted by the electroweak force trying to push the nucleus apart. Due to the shape of the potential of these two forces taken together (which may differ significantly depending on the number and ratio of different nucleons constituting as well as the physical shape of the nucleus), fusion of four hydrogen nuclei into one helium nucleus will liberate 26.731 MeV of energy - which also means that the resulting helium nucleus is less massive than the four hydrogen nuclei from which it was formed - by exactly 26.731 MeV/ $c^2$ . The total energy reservoir ( $E_{\text{nuc}}$ ) of the star during its hydrogen-burning phase is therefore 26.731 MeV per every four hydrogen nuclei it contains. If, during this phase, the luminosity of the star is  $L$  and can be approximately assumed to be constant, then the star's hydrogen reservoir will be exhausted after approximately the *nuclear timescale*

$$\tau_{\text{nuc}} = \frac{E_{\text{nuc}}}{L}. \quad (1.5)$$

has passed. For a Sun-like star this suggests a main-sequence lifetime of  $\approx 10^{10}$  yr.

Before nuclear burning was considered a possible energy source for stars it was theorized that the gravitational contraction of a gas cloud would free enough gravitational energy to account for the Sun's luminosity. This suggestion gave reason to define the *Kelvin-Helmholtz timescale*

$$\tau_{\text{KH}} = \frac{GM^2}{RL}, \quad (1.6)$$

where  $R$  is the radius of the star. For a Sun-like star the Kelvin-Helmholtz timescale is  $\approx 10^7$  yr. In the core of the Sun, this was found to be too short to account for the geologically derived age of the Earth and Moon, therefore the theory that stars mostly radiate gravitational energy had to be abandoned.

Another timescale, related to the Kelvin-Helmholtz timescale, is the *thermal-adjustment timescale* which describes the time a star takes to react to changes in its thermal profile. It can be estimated as

$$\tau_{\text{adj}} = \frac{c_v M^2}{\bar{\sigma}^*} \quad (1.7)$$

with  $c_v$  the specific heat and  $\bar{\sigma}^*$  the average of  $\sigma^* = (64\pi^6 a c T^3 r^4)/(3\kappa)$  with  $\kappa$  the opacity,  $c$  the speed of light in vacuum and  $a$  the radiation density constant. This, in turn can be approximated as

$$\tau_{\text{adj}} \approx \tau_{\text{KH}}. \quad (1.8)$$

## 1. Introduction

The time a star takes to react to perturbations of its hydrostatic equilibrium is described by the *hydrodynamical timescale*

$$\tau_{\text{hydr}} \approx \left( \frac{R^3}{GM} \right)^{1/2} \approx \frac{1}{2} (G\bar{\rho})^{1/2}, \quad (1.9)$$

where  $\bar{\rho}$  is the mean density.

If the internal pressure of the star were to suddenly disappear, the star would collapse. This would happen on the *dynamical timescale* (also referred to as free-fall timescale)

$$\tau_{\text{dyn}} \approx \left( \frac{R}{g} \right)^{1/2}, \quad (1.10)$$

where  $g$  is the surface gravity of the star.

If, on the other hand, the star's gravity were to suddenly disappear, the star would explode due to its internal pressure after a time

$$\tau_{\text{expl}} \approx R \left( \frac{\rho}{P} \right)^{1/2}, \quad (1.11)$$

where  $P$  is pressure.

If the star is in or near hydrostatic equilibrium, then

$$\tau_{\text{dyn}} \approx \tau_{\text{expl}} \approx \tau_{\text{hydr}}. \quad (1.12)$$

For a Sun-like star the hydrodynamical timescale is about 27 min, while for a white dwarf it is as short as 4.5 s.

### 1.1.3. Stellar remnants

When the ability to access their energy supply is exhausted, stars cease nuclear burning and become inert (though by no means inactive) objects. For many stars the transition from the nuclear-burning to the inert stage is heralded by some sort of cataclysmic event (see Sec.1.4) while for some the transition is less spectacular. Following Carroll & Ostlie (2007), this section gives a brief overview of the different stellar remnants encountered by observations.

#### White dwarfs

White dwarfs are essentially the cores of low-mass ( $\leq 8 M_{\odot}$ ) stars, exposed after the expulsion of the non-degenerate envelope during the post-AGB phase. Located, as mentioned above, in the lower and lower-left regions of the HR diagram, white dwarfs tend to be faint with a comparatively high temperature. Unable to use nuclear burning as an energy source their high temperature is a remnant of the heating experienced during the star's previous nuclear burning and further contraction. Fig.1.5 shows a field of WDs as observed by the Hubble telescope.

Since WDs are degenerate objects, unlike in non-degenerate stars, electron conduction plays a dominant role in conducting heat from the object's interior to the surface. Owing to the efficiency of this process, the temperature profiles in the WD's degenerate core are expected to be less steep than non-degenerate layers. As the star loses heat, potentially slowed by the presence of a non-degenerate envelope, which provides some insulation, the WD gradually crystallizes. Crystallization, owing to the associated coherent vibration of the regularly spaced nuclei of the stellar material, accelerates



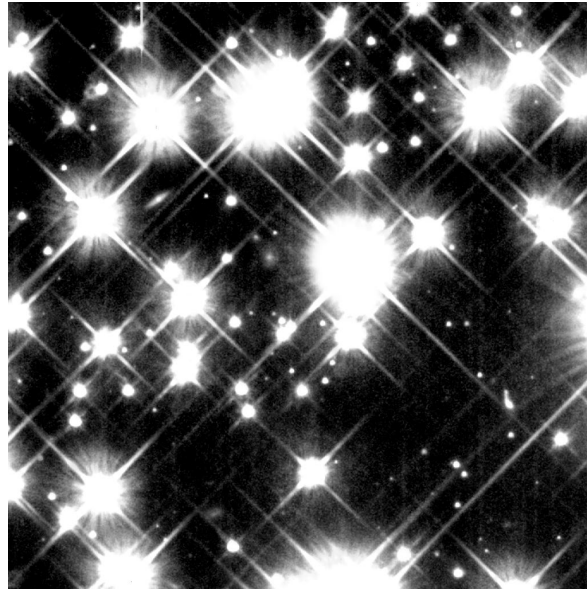


Figure 1.5.: Close Up of Ancient, White Dwarf Stars in the Milky Way Galaxy  
Image credit: NASA and H. Richer (University of British Columbia)

cooling. Eventually, all isolated WDs will cool until in thermal equilibrium with their environment<sup>4</sup>. Figure 1.6 shows theoretical cooling tracks and observations of WD populations in NGC 6791, where the changes of the rate of cooling are clearly visible.

Following Eq. 1.1 and the associated arguments about the size of stars, white dwarfs are small objects, but by no means point-masses. Hydrostatic equilibrium requires some force to cancel the self-gravity of an object such that further collapse is inhibited. In non-degenerate stars this counter-force is provided by the thermodynamic pressure related to the heat created by nuclear burning processes in their interiors. In planets (and any other low-density solid or liquid object), this counter-force is provided by the electromagnetic force between the atoms it is comprised of. White dwarfs, however, do not experience nuclear burning and they are far too massive for electromagnetic forces to provide enough of a counter-force, so the question becomes: Why do white dwarfs not simply continue collapsing into a singularity?

According to Pauli's exclusion principle, different fermions<sup>5</sup>, such as electrons, cannot occupy the same quantum state. This principle leads to the concept of a *Fermi-gas*, where every particle in a gas of entirely uniform density  $n$  (particles per unit volume), consisting entirely of fermions occupies the lowest energy state available to it<sup>6</sup>. Owing to Pauli's exclusion principle, only a finite number of fermions per unit volume may occupy the lowest energy state. If the gas contains more particles per unit volume than the finite number allowed in the lowest energy state, all supernumerary particles are forced to occupy a higher energy state. If that energy state is occupied as well, the additional particles are forced onto the next higher energy state (imagine a game of Tetris where, once one row has been filled, it becomes unavailable for additional blocks, but with energy states instead of displacement on

<sup>4</sup>eventually, their temperature will be the same as that of the cosmic microwave background.

<sup>5</sup>particles of spin 1/2.

<sup>6</sup>This is equivalent to demanding that the gas has a negligible temperature.

## 1. Introduction

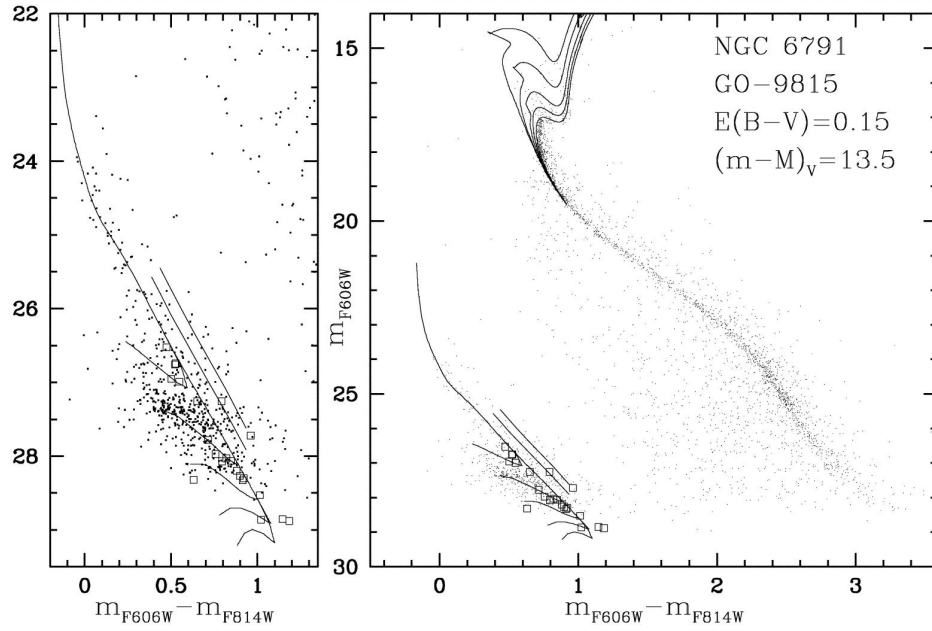


Figure 1.6.: Fit of theoretical isochrones and luminosity functions of CO WDs for ages 4, 6, and 8 Gyr to the observed color-magnitude diagram of NGC 6791 and to the WD star counts. Cooling sequences of He WDs with masses equal to, respectively, 0.327, 0.406, and 0.465  $M_{\odot}$  are also displayed. Figure and caption as presented by Bedin et al. (2008).

the y-axis), and so on, until all particles occupy are settled. Then, since every particle occupies the lowest energy state available to it, there is a state with higher energy than any occupied state, below which every energy state is fully occupied, but at lower energy than every other unoccupied state. A Fermi-gas in this condition is called *fully degenerate*. The energy contained in the gas associated with this state is known as the *Fermi-energy*

$$\epsilon_F = \frac{\hbar^2}{2m} (3\pi^2 n)^{2/3}, \quad (1.13)$$

where  $\hbar$  is the Planck's constant and  $m$  is the mass of the particles.

Fermi-gases with finite temperatures are generally not completely degenerate, with some particles occupying energy states higher than the Fermi-energy, leaving some of the lower energy states empty.

However, Pauli's exclusion principle is not only valid for energy states but also for the "location"<sup>7</sup> of the particle. If a degenerate Fermi-gas of nonzero volume is compressed, its constituent fermions are confined to smaller and smaller volumes. According to Heisenberg's uncertainty principle

$$\Delta x \Delta p_x \approx \hbar, \quad (1.14)$$

where  $\Delta x$  is the maximum uncertainty of the particle's location and  $\Delta p_x$  is the uncertainty of the particle's momentum. In order to satisfy Pauli's exclusion principle, each particle's waveform can't

<sup>7</sup>the word "location" is in parenthesis here because, as the argument belongs to the realm of quantum mechanics, the behavior of a fermion is most properly described as a probability waveform.

extend beyond the distance to the next particle, for otherwise two neighboring particles would not be occupying different quantum states. Further compression of the gas leads to further reduction of the maximum uncertainty in location, and to an increase in the momentum of the so constricted particle and, just as an increase in the statistical momentum of a classical ideal gas leads to an increase of the pressure inside the Fermi-gas. But unlike in the ideal gas where the particles constituting the gas are inhibited from occupying the same space by their electric charge, the fermions are, in addition, kept apart by the gas's *degeneracy pressure*. This leads to the realization that white dwarfs are kept in hydrostatic equilibrium by the degeneracy pressure exerted by their fermionic components, i.e. the electrons supplied by their atomic constituent isotopes.

For a non-relativistic Fermi-gas created by electrons supplied by a corresponding number of atoms with a certain average number of charges per nucleon, the degeneracy pressure can be expressed as

$$P_{\text{deg,nonrel}} = \frac{(3\pi^2)^{2/3}}{5} \frac{\hbar^2}{m_e} \left[ \left( \frac{Z}{A} \right) \frac{\rho}{m_H} \right]^{5/3}, \quad (1.15)$$

where  $Z$  is the number of protons and  $A$  is the total number of nucleons per atom. If the Fermi-gas is constricted sufficiently, the constituting fermions can become relativistic. For the relativistic limit, the electron degeneracy pressure becomes

$$P_{\text{deg,rel}} = \frac{(3\pi^2)^{1/3}}{4} \hbar c \left[ \left( \frac{Z}{A} \right) \frac{\rho}{m_H} \right]^{4/3}. \quad (1.16)$$

The more massive a white dwarf gets, the denser it becomes and, consequently the greater the momentum of the electron gas. The growth of the degeneracy pressure is disproportionately small with increasing mass, which means that more massive WDs will be smaller than less massive ones. This can be expressed in a mass-volume relation:

$$M_{\text{WD}} V_{\text{WD}} = \text{constant}. \quad (1.17)$$

There is, however, one more important implication: A white dwarf of high enough internal density will force its electrons to become relativistic, which in turn leads to the WD becoming dynamically unstable against gravitational collapse.

The mass where the change from hydrostatic stability to dynamical instability occurs is known as the *Chandrasekhar mass* after Subrahmanyan Chandrasekhar (Chandrasekhar 1931a,b). The Chandrasekhar-mass depends on the specific charge  $\frac{Z}{A}$  and can be estimated as

$$M_{\text{Ch}} \sim \frac{3\sqrt{2}\pi}{8} \left( \frac{\hbar c}{G} \right)^{3/2} \left[ \left( \frac{Z}{A} \right) \frac{1}{m_H} \right]^2. \quad (1.18)$$

For  $\frac{Z}{A} = 0.5$ , as expected in a pure CO WD, this gives

$$M_{\text{Ch}} \sim 1.44 M_{\odot}. \quad (1.19)$$

Note that the Chandrasekhar mass is a derived quantity. It follows that the Chandrasekhar mass can be modified by the effects of magnetic fields or rotation (see e.g. Hachisu et al. 2012).

Core collapse supernovae, as SNe Ia, are initiated in stars whose degenerate cores reach masses higher than the Chandrasekhar mass, becoming unstable against gravitational collapse (Sec. 1.4.1).

## 1. Introduction

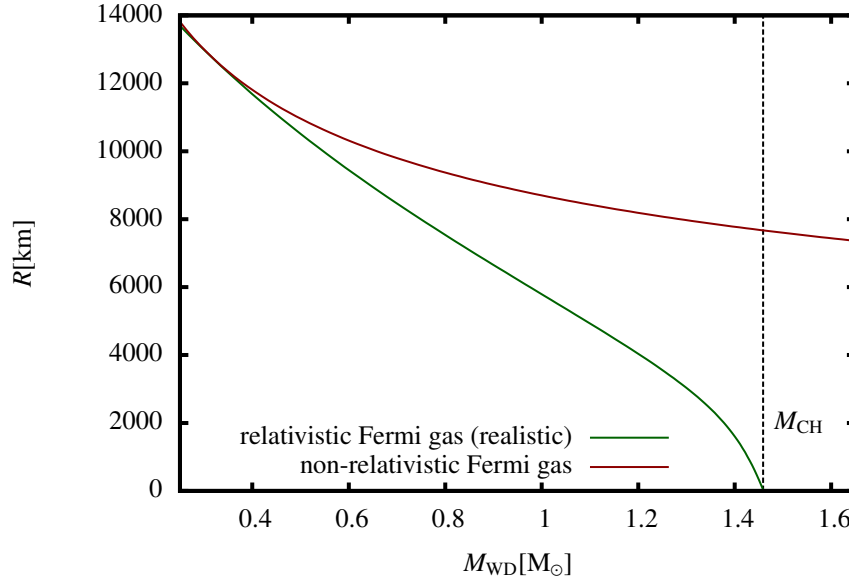


Figure 1.7.: Mass-radius relation of polytropic CO White dwarfs as calculated in the non-relativistic approximation of the Fermi-gas as well as the, realistic, relativistic one.  $M_{\text{CH}} = 1.44 M_{\odot}$  is the Chandrasekhar-mass. Figure after Kippenhahn & Weigert (1990).

Depending on the mass of the progenitor and its completed burning stages, WDs emerge from their progenitors with chemical compositions. Progenitors at the low-mass end of the WD-progenitor mass-spectrum tend to leave WDs primarily composed of helium, more massive progenitors shed their envelopes after the He-burning stage, leaving a WD primarily composed of carbon and oxygen and the high-mass end of the mass-spectrum will leave oxygen-neon-magnesium WDs. Figure 1.7 shows the (numerically computed) mass-radius relation for CO WDs.

## Neutron stars

The mass attainable by white dwarfs is limited by the Chandrasekhar mass, which represents the threshold at which the electron gas, which is non-relativistic at lower masses and thus able to inhibit gravitational collapse, becomes relativistic and the white dwarf unstable. But the insight that no object held up by the degeneracy pressure of its electrons can exceed the Chandrasekhar mass does not mean that the issue could not be forced somehow. So the question becomes: Would an object with a mass higher than the Chandrasekhar mass collapse into a singularity or can some force be found to supplement electron degeneracy pressure in the same way that electron degeneracy pressure supplemented electromagnetism? Is there a force strong enough to counteract gravity in objects more massive than the heaviest WD to allow for hydrostatic equilibrium and what kind of object would that be?

At this point it is necessary to remember that the electron gas in a WD does not exist in a vacuum, but is actually dissolved in a plasma containing atomic nuclei. Nuclei consist of hadrons, namely protons and neutrons. If the electron gas is compressed further (in the case of a WD exceeding the Chandrasekhar mass by gravity), the energy of the electrons increases. With increasing energy,

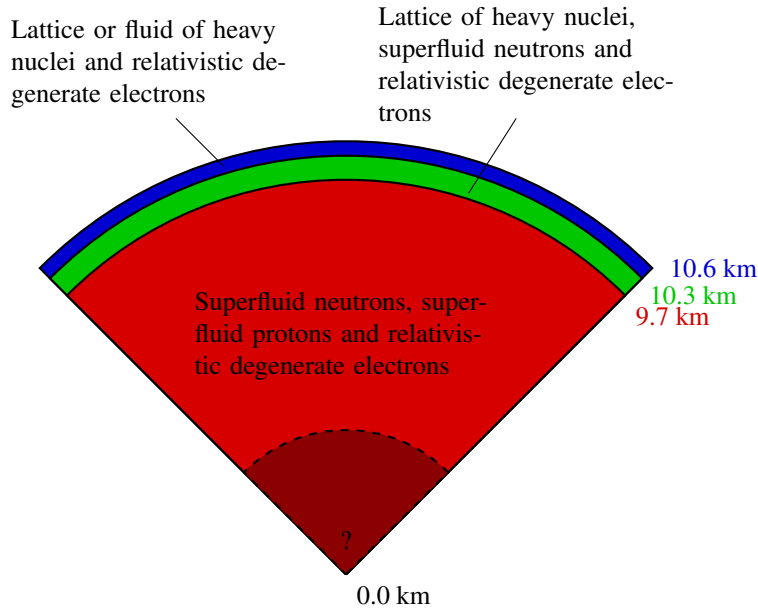


Figure 1.8.: Sketch of the interior structure of a neutron star. Adapted from Carroll & Ostlie (2007).

the interaction-cross section for electron capture increases and the electrons in the gas begin to fuse with protons in the nuclei, producing additional neutrons. The nuclei, having had their  $Z/A$  ratios altered, become unstable, releasing free neutrons which continue to be forced together by gravity. This process<sup>8</sup> continues until further contraction of the entire system is once again halted by degeneracy pressure, this time of the nucleons, which, like electrons, are fermions, but whose higher mass allows a significantly higher density.

The resulting object, called a *neutron star*, is held up against the pull of gravity by the degeneracy pressure of fermionic free nucleons, which make up the bulk of its structure (Gamow 1938; Oppenheimer & Volkoff 1939). Only in the outer layers traces of the progenitor's chemical composition are thought to remain. Fig. 1.8 shows the inferred internal structure of a neutron star. Neutron stars are extremely small objects with typical diameters of ten kilometers but masses on the order of that of the Sun. Since angular momentum is mostly preserved during collapse, many neutron stars rotate rapidly. Young, hot neutron stars, usually produced in core-collapse supernovae at the end of medium-mass stars, can be very luminous though mostly emitting radiation in the X-ray spectrum.

Just like white dwarfs, neutron stars obey a mass-volume relation ( $M_{\text{NS}}V_{\text{NS}} = \text{constant}$ ) and just like with white dwarfs, there is expected to be a maximum mass for neutron stars. The value of the maximum mass is a matter of some debate. Depending on the assumed equation of state of neutron star matter and investigative approach, maximum masses below  $1.4 M_{\odot}$  (Schulze et al. 2006) and up to  $2.9 M_{\odot}$  (Kalogera & Baym 1996; Zdunik & Haensel 2013) have been proposed. At the time of writing, the most massive observed neutron star is PSR J0348+0432, a neutron star in a binary with a white dwarf, with a mass of  $(1.97 \pm 0.04) M_{\odot}$  (Demorest et al. 2010).

Rapidly rotating, magnetized neutron stars have been identified as emitters of pulsed electromagnetic radiation (Gold 1968) (named "pulsars", according to their emission characteristics). The pul-

<sup>8</sup>also called *neutronization*.

## 1. Introduction

sation of these emissions is caused by the rotation of the neutron star as a directed beam of electromagnetic radiation, caused by synchrotron emissions of electrons moving in the star's magnetic field, illuminates a circular segment of the celestial sphere, as seen from the pulsar.

### Black holes

Just like white dwarfs, the upper limit for the mass of neutron stars depends on the maximum density a Fermi-gas can support, this time consisting of nucleons, held up against its self-gravity, but again there is no reason why a more dense object shouldn't be allowed to exist. However, this time the search for a counter-force strong enough to ensure some form of hydrostatic equilibrium turns up empty-handed. Objects exceeding the (assumed) mass maximum of neutron stars will continue collapsing and there is no currently known effect or process to stop them. At some point, according to the mathematics, all matter contained in the object would be contained in its exact center of mass. These objects are called *black holes*. The following description follows Carroll (2004) and Misner et al. (1973).

In the discussion of neutron stars, the tool-set of Newtonian gravity were (largely) sufficient to understand the nature these objects, but in the case of black holes this is no longer possible. Black holes exist at the extreme end of current physical understanding and many of their obvious (for the theoretical observer) characteristics are even more at odds with everyday experience than the - already exotic - effects encountered in the study of more mundane astrophysical phenomena. Since Albert Einstein's seminal works on the nature of gravity, the Newtonian formulation is known to be an approximation valid only for weak fields and low relative velocities. While this approximation already breaks down to some degree when the high masses involved in most astrophysical objects are concerned, a cursory understanding<sup>9</sup> of the nature of black holes is aided by discarding it.

In the picture provided by the theory of general relativity, gravity is described as the distortion of spacetime by the presence of a certain local mass distribution according to

$$R_{\mu\nu} - \frac{R}{2}g_{\mu\nu} = \frac{8\pi G}{c^4}T_{\mu\nu}, \quad (1.20)$$

where  $R_{\mu\nu}$  is the Ricci-tensor,  $R$  is the curvature scalar,  $g_{\mu\nu}$  is the metric tensor<sup>10</sup> and  $T_{\mu\nu}$  is the energy-momentum-tensor.

Liberal application of tensor algebra allows one to derive that, for a point outside of a spherically symmetric mass distribution, the metric tensor can be written as

$$g_{\mu\nu} = \begin{pmatrix} -\left(1 - \frac{2GM/c^2}{r}\right) & 0 & 0 & 0 \\ 0 & \left(1 - \frac{2GM/c^2}{r}\right)^{-1} & 0 & 0 \\ 0 & 0 & r^2 & 0 \\ 0 & 0 & 0 & r^2 \sin^2 \theta \end{pmatrix}, \quad (1.21)$$

where  $r$  and  $\theta$  are defined as usual in spherical coordinates. This metric is called the *Schwarzschild-metric* and is applicable not only to (appropriate) black holes but to any mass distribution. If used to calculate planetary orbits, this metric is able to predict the full observed<sup>11</sup> perihelion precession

<sup>9</sup>current physics is still unable to provide a complete description.

<sup>10</sup>which describes the shape of the space-time manifold;  $R_{\mu\nu}$  and  $R$  are derived from the metric tensor.

<sup>11</sup>most notably in Mercury.

unexplained by Newtonian gravity. In the case of black holes though, something interesting happens: The metric is singular in  $r = 2GM/c^2$ . This radius is known as the *Schwarzschild-radius*<sup>12</sup>. At this distance from the center of force, in the picture of general relativity, time-like paths become indistinguishable from space-like paths. This means, in a nutshell, that it becomes impossible for anything (including all particles, massive or otherwise, like photons) to move away from the center of force.

Black holes are the expected remnants of high-mass stars whose cores exceed the upper mass limit for neutron stars, although some black holes might actually be primordial (see e.g. Novikov et al. 1979). Unless accreting material from some outside source (such as a binary companion), they are detectable only through the deflection of light emitted by background sources and, theoretically, Hawking-radiation (Hawking 1974). Accreting black holes, or, more precisely, their accretion discs, are prolific sources of hard electromagnetic radiation. Furthermore, rapid accretion onto black holes, following a core collapse SN or merger event, is a candidate source for the elusive gamma ray bursts. Extremely heavy ( $\approx 10^6 M_\odot$ ) black holes have been identified as the engines of active galactic nuclei (Antonucci 1993).

Black holes have been known to exist for quite a while thanks to a number of indirect observations, most recently reinforced by the detection gravitational wave radiation emitted in the merger of two stellar mass black holes by the LIGO-collaboration in 2015 (Abbott et al. 2016).

Like with all of the stellar remnants discussed in this section, observation and theory of black holes are a vast field in their own right, description of which would exceed the scope of this introduction.

## 1.2. Binary evolution

Many stars do not form in isolation and instead are bound gravitationally to one or more companion stars. These systems are called, for obvious reasons, multiple star systems. Figure 1.9 shows two observations of wide binary stars.

### 1.2.1. Interacting binaries

In many binary star systems the individual components form at large enough distances that each of them essentially proceeds through its evolution as if in isolation. Other systems form with small enough of an initial orbital separation to allow for interaction. If one of the binary components exhibits a strong stellar wind, perhaps due to having a very high luminosity, the other component can accrete part of the mass lost by the other component. This process is called *wind accretion* (Anzer et al. 1987; Livio & Warner 1984; Theuns & Jorissen 1993; Theuns et al. 1996a; de Val-Borro et al. 2009). Depending on the amount and isotope composition of the material so received, this process can have a noticeable, even profound, influence on the observational properties of the accretor. This section will generally follow the description by Eggleton (2011).

Discounting wind accretion, interaction in binary systems is mostly governed by the interplay of the components' gravitational fields. The movement of masses in multi-body systems is one of the oldest and most intensely studied problems in classical dynamics, and one of the most frustrating. Many of the possible configurations of masses in systems containing more than two bodies are not

<sup>12</sup>it is often said that at the Schwarzschild radius a black hole's escape velocity equals the speed of light and while a derivation using this assumption will yield the correct result, this interpretation is incorrect from a physical standpoint.

## 1. Introduction



Figure 1.9.: Images of Polaris ( $\alpha$  Ursae Minoris), a multiple star system consisting of a yellow supergiant (Polaris Aa) in a close orbit with a smaller companion (Polaris Ab), in turn bound to a further companion in a wide orbit (Polaris B).

Left: Polaris A and Polaris B;

Right: Polaris Aa and Polaris Ab;

Image credit: NASA, ESA, N. Evans (Harvard-Smithsonian CfA), and H. Bond (STScI)

analytically approachable and have to be tackled numerically, which was an exceedingly arduous proposition before the advent of computers. Binary star systems, which can be approximated as systems containing two masses of comparable magnitude and an arbitrary number of bodies of negligible mass, represent a configuration known as the *reduced three-body problem*. The effective gravitational potential in such a system can be written

$$\Phi = -G \left( \frac{M_1}{|\mathbf{r} - \mathbf{r}_1^*|} + \frac{M_2}{|\mathbf{r} - \mathbf{r}_2^*|} \right) - \frac{1}{2} \omega^2 r^2, \quad (1.22)$$

where  $M_{1/2}$  are the masses of the stars,  $\mathbf{r}_{1/2}^*$  are the vectors from the system's center of mass to the centers of the stars,  $\mathbf{r}$  is the location of a body of negligible mass with respect to the system's center of mass and  $\omega$  is the system's angular velocity. Evaluating  $\Phi$  at every point in the binary system reveals a number of minima: the well-known Lagrangian-points, of which there are five. L1 is located in the libration point between the two stars, L2 outside of the orbit of the smaller of the two masses, L3 in opposition and L4 and L5 on the orbital path of the smaller mass but equidistant to both. While a test mass placed there is not necessarily stable<sup>13</sup>, in these points the cumulative forces exerted by the gravitational fields of both stars as well as inertia exactly vanish. In an application closer to home, these points have been used to explain the presence of an overdensity of asteroids on Jupiter's orbit<sup>14</sup>, and to position spaceborne experiments.

Further evaluation of eq. 1.22 reveals the existence of *equipotential surfaces*. These (closed) surfaces are constituted of every point in the system with the same effective potential. Cumulative inertial and gravitational forces will always act exactly perpendicular to these surfaces. If a star is large

<sup>13</sup>this is only true for L4 and L5.

<sup>14</sup>the well-known Trojan-asteroids.



enough to encompass such a surface, hydrostatic equilibrium ensures that its surface will assume the same external shape as the equipotential surface. While generally spherical in shape for small radii relative to the orbital separation of the two stars, the equipotential surfaces assume a “dumbbell”-shape for larger distances and then again a spherical shape for distances large relative to the orbital separation<sup>15</sup>. The equipotential surface encompassing the L1-point is of particular importance. A star exceeding this particular surface will lose mass to its companion through the L1-point. The volume enveloped by this surface and containing the star (as opposed to its companion) is called the star’s *Roche-lobe*. Consequently, every binary system has two Roche-lobes. The exact size of a binary system’s Roche-lobes cannot be calculated analytically, but numerical approximations have been available for some time, the most widely used having been proposed by Eggleton (1983) as

$$r_L = r_{\text{orbit}} \cdot \frac{0.49q^{2/3}}{0.6q^{2/3} + \ln(1 + q^{1/3})}, \quad (1.23)$$

where  $q = \frac{M_1}{M_2}$  is the system’s *mass-ratio* and  $r_{\text{orbit}}$  the system’s orbital separation.

Figure 1.10 shows possible configurations of binary systems. A system in which neither star fills its Roche-lobe (a) is commonly called a *detached* system. While there is no direct transfer of material from one star to the other in detached systems, depending on the orbital separation, the two components may still influence each other through wind accretion or tidal interaction. Many wide binaries will remain in this configuration for the entirety of their evolution. A system in which one star fills its Roche-lobe (b) is known as a *semidetached* binary. The Roche-lobe-filling star may be losing material to its companion in this configuration, which, depending on the nature of the companion, may produce a number of astrophysical phenomena associated with accretion, such as classical novae or supernovae, if the companion is a WD, or the system may be observed as an X-ray binary. It is further possible to have both stars filling their Roche-lobes (c). Depending on how this configuration came about (both stars being of similar mass and reaching similar stages in their evolution at the same time or unstable mass-transfer), there may be no significant transfer of material. Under certain conditions (as will be discussed in Sec. 1.2.3), the envelope of a mass-losing star may come to encompass both components of a binary star. This situation, as depicted in Fig. 1.10 (d), is called a *common envelope* (see e.g. Ivanova et al. 2013).

### 1.2.2. Mass transfer

The rate of mass-transfer intimately depends on the structure of the mass donor and the mass ratio. As such, Eggleton (2011) identifies three mass-transfer modes related to the structure of the donor star: Mass transfer on the nuclear timescale (see eq. 1.5), on the thermal timescale (see eq. 1.6) and on the hydrodynamic timescale (see eq. 1.9). Using the mentioned timescales as a basis, the expected mass-transfer rate can be estimated as

$$\dot{M} = \frac{M_{\text{donor}}}{\tau_{\text{nuc,KH,hydr}}}, \quad (1.24)$$

where  $M_{\text{donor}}$  is the mass of the donor star. The question which mass-transfer mode is realized in a particular system depends strongly on the the reaction of a star to mass loss. Stars possessing a stable radiative envelope tend to react to mass loss by contracting, whereas stars featuring a deep convective

<sup>15</sup>at large distances, the mass distribution of the binary system can be approximated as a point mass.

## 1. Introduction

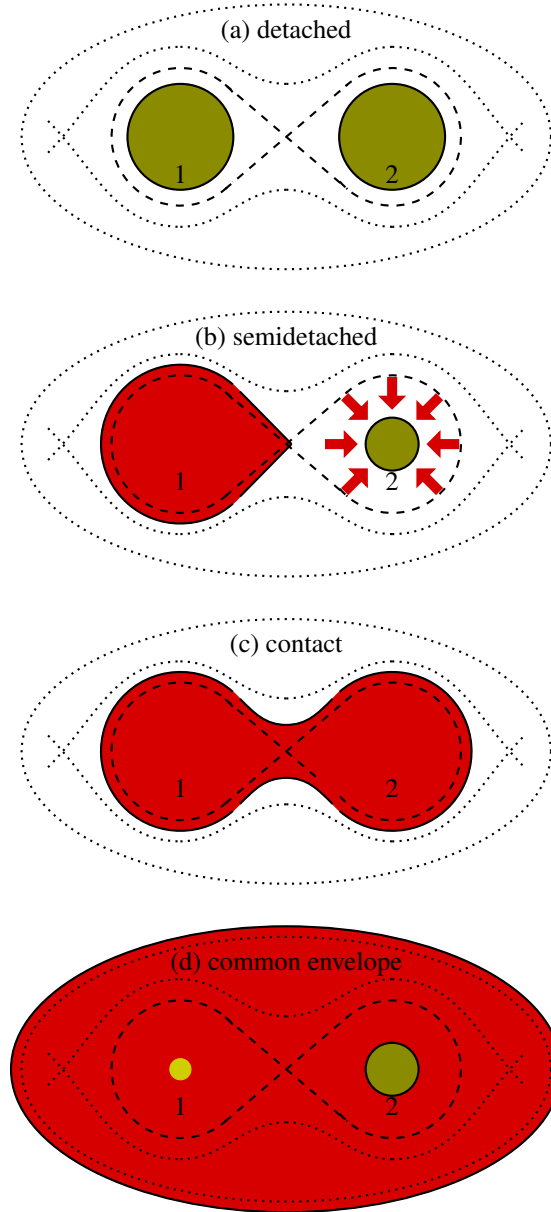


Figure 1.10.: Illustration of possible binary states for a system with equal mass components (not to scale) with the observer located in the orbital plane of the binary system. Dotted lines represent equipotential surfaces, dashed lines Roche lobe surfaces and solid lines boundaries between stellar matter and its surroundings. The white dot in (d) is the core of component 1. Adapted from Eggleton (2011).

envelope tend to expand. An appropriate measure of whether the extent of an existing convective envelope is sufficient to induce expansion as a response to mass loss is whether more than 50% of the star's radius lie inside it. Deep convective envelopes of this kind are usually encountered either in low-mass ( $\leq 0.75 M_{\odot}$ ) main sequence stars or red giants, both of which possess convective envelopes due to the high opacities associated with their low effective temperatures.

Owing to its dependence on radiative envelopes, stable nuclear timescale mass-transfer is usually encountered in all but the lowest-mass ( $\leq 0.75 M_{\odot}$ ) main sequence stars. It is also encountered, though, in low-mass helium main sequence stars, that, due to their steeper temperature gradients, tend to have a convective core.

A deep convective envelope will lead to thermal timescale mass-transfer, but the further development of the system depends on the rate of expansion. Mass loss leads to an decrease of a star's Roche-lobe radius. If the star responds to mass loss by shrinking, and the decrease in radius is faster than the shrinking of the Roche-lobe, the mass-transfer is stable, but shrinking of the Roche-lobe overtakes the shrinking of the star, mass-transfer proceeds unstably at hydrodynamic timescales.

Mass transfer is also classified according to the evolutionary stage of the donor star at the beginning of Roche-lobe-overflow (RLOF). Roche-lobe-overflow while the star is on the main sequence is called case A mass-transfer. Roche-lobe overflow during hydrogen shell burning is called case B mass-transfer. Roche-lobe overflow initiated after the beginning of helium core burning is called case C mass-transfer.

A corresponding system of mass-transfer classification can be defined for helium stars with case BA mass-transfer if RLOF is initiated while the star is on the helium main sequence and case BB mass-transfer if RLOF is initiated during the helium shell burning phase.

### 1.2.3. Common envelopes

A radiatively cooling cloud will contract on the Kelvin-Helmholtz timescale. This is not only true for protostars and the like, but also for material added to a star through mass-transfer in a binary system. This means that a star receiving material at a rate faster than dictated by its own Kelvin-Helmholtz timescale will not be able to add this material to the part of the star that is already in thermal equilibrium and the accumulated material will form an expanding shell surrounding the accreting star. Once the expanding shell of accreting material expands beyond the Roche-lobe of the accreting star, further material lost from the mass donor will enter the gravitational potential of both stars where their equipotential surfaces are no longer separate. Thus the donor star's envelope eventually encompasses both stars (see Fig. 1.11). This (unobserved, hypothetical) situation is called a common envelope (CE). Once the common envelope is established, hydrodynamic drag will induce differential rotation and as angular momentum is imparted on the envelope, the orbital separation of the core of the donor star and the secondary will shrink rapidly. This phase is called *spiral-in*. During the spiral-in phase the volumes of the Roche-lobes of both components of the binary decrease accordingly, which means that more material is lost from the Roche-lobe of the donor star to enter the domain of the entire system, leaving the core of the donor to contract.

Common envelope evolution is currently not well understood, but it thought that spiral-in can lead to one of two distinct outcomes:

- Spiral-in continues until (depending on the nature of the secondary) the two stars merge. If the secondary is a non-degenerate star or low-mass WD, the resulting object might be a chemically

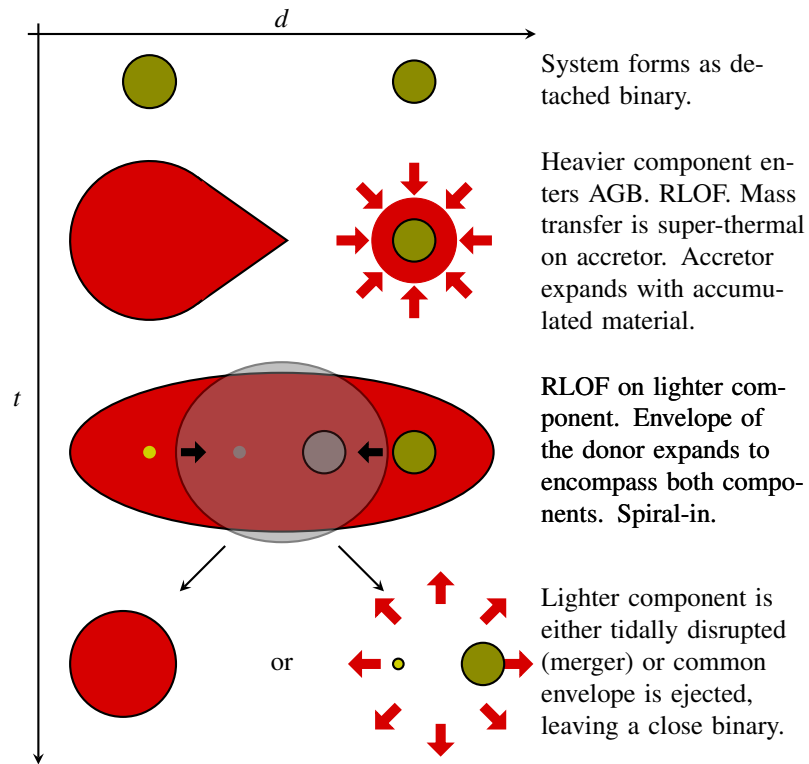


Figure 1.11.: Qualitative depiction of common-envelope evolution in an initially wide binary.  $t$  is a qualitative time coordinate,  $d$  a qualitative length. Illustration as described in Eggleton (2011).

peculiar, fast-rotating giant. If the secondary is a neutron star, the result might be a Thorne-Żytkow object (Thorne & Żytkow 1975, 1977).

- If the energy lost from the orbit during spiral-in exceeds the binding energy of the envelope, the envelope (and the angular momentum it carries) will be ejected from the system. Without the presence of an envelope to provide drag, spiral-in is stopped and the two components of the initial binary system survive as distinct entities. In this scenario, the donor star will lose most of its envelope, leaving only the core in its existing chemical composition. The orbital separation, compared to the initial state of the system, will be significantly reduced.

#### 1.2.4. Effects on orbital parameters

At this point it is useful to comment on a number of processes observable in binary systems that impact the orbital configuration of the components.

##### Angular momentum transfer

In a binary, each of the binary components carries a fraction of the system's total angular momentum. Since angular momentum (neglecting certain non-conservative processes, as will be discussed further on) is conserved, mass-transferred from one component to the other will change the angular momentum distribution of the system. Neglecting rotational effects in the individual components and assuming conservative mass-transfer, it can be shown that the change of the semi-major axis ( $a$ ) of a binary system is related to the mass-transfer rate through

$$\frac{1}{a} \frac{da}{dt} = 2\dot{M}_1 \frac{M_1 - M_2}{M_1 M_2}. \quad (1.25)$$

Accordingly, if the donor is the more massive component, the orbital separation decreases, if the donor is the less massive component, the orbital separation increases.

##### Tidal friction

As described in Sec. 1.2.1, a star will assume a shape conforming to its enveloping equipotential surfaces as defined by the configuration of the binary system. If the star's radius is comparable to the radius of its Roche-lobe, this shape will differ significantly from the hydrostatically defined sphere of single stars. If the star's rotational period differs from the orbital period of the system, the deviation from the spherical shape implies a continuing distortion of the star's envelope and induces a torque on the star. Since the system's angular momentum is conserved, the torque leads to a change of the orbital angular momentum. If the star's average angular velocity ( $\Omega$ ) is higher than the system's ( $\omega$ ), the torque will act to slow the star's rotation while increasing the orbital angular momentum, widening the orbit and vice versa. This effect is not only observable in stars but also much closer to home in the Earth-Moon system, where tidal forces decrease the Earth's rotation while increasing the orbital separation between the Earth and the Moon by about 4 cm each year.

One may define an associated timescale, the *tidal friction timescale*

$$\tau_{\text{TF}} = \frac{\tau_{\text{visc}}}{9} \left( \frac{a}{R} \right)^8 \frac{M_1^2}{M_2 M} (1 - Q)^2, \quad (1.26)$$

## 1. Introduction

where  $\tau_{\text{visc}} \approx \tau_{\text{G}} \approx (3MR^2/L)^{1/3}$  is the global timescale of viscous dissipation and  $Q$  is a constant describing the gravitationally distorted interior structure of the star.

For the case of generalized Keplerian orbits the excentricity  $e$  of a system changes approximately according to

$$\dot{e} = -\frac{9e}{\tau_{\text{TF}}} \left[ \frac{1 + \frac{15}{4}e^2 + \frac{15}{8}e^4 + \frac{5}{64}e^6}{(1-e^2)^{13/2}} - \frac{11\Omega}{18\omega} \frac{1 + \frac{3}{2}e^2 + \frac{1}{8}e^4}{(1-e^2)^5} \right]. \quad (1.27)$$

Hence, for small ratios of  $\Omega/\omega$  the system's excentricity is decreased by tidal friction, but for cases with  $\Omega/\omega \geq 18/11$  the excentricity increases. This increase of excentricity is called the *e-instability*. Another important instability related to tidal friction becomes apparent when investigating the time-derivative of  $\Omega/\omega$ , which, for  $e = 0$  reads

$$\frac{d \log(\Omega/\omega)}{dt} = \frac{1 - 3\lambda}{\lambda \tau_{\text{TF}}} \left( 1 - \frac{\Omega}{\omega} \right), \quad (1.28)$$

where  $\lambda = \frac{I\Omega}{\mu h}$  with  $I$  the moment of inertia of the star,  $\mu$  the reduced mass of the system and  $h$  the specific orbital angular momentum. If  $\lambda \geq 1/3$ , any ratio of  $\Omega/\omega$  other than unity will induce a runaway. This effect is called the *Darwin instability*. If  $e > 0$ , the condition for the Darwin instability becomes

$$\lambda > \frac{1 + 3e^2 + \frac{3}{8}}{(1-e^2)^5} \frac{(1-e^2)^6}{1 + \frac{15}{2}e^2 + \frac{45}{8}e^4 + \frac{5}{16}e^6}. \quad (1.29)$$

## Gravitational waves

Following Carroll (2004), another solution to the Einstein-equation (Eq. 1.20), besides the aforementioned Schwarzschild-solution, can be obtained by assuming a small perturbation in the unperturbed Minkowski-spacetime<sup>16</sup> in the form

$$g_{\mu\nu} = \eta_{\mu\nu} + h_{\mu\nu} \quad \text{with} \quad |h_{\mu\nu}| \ll 1. \quad (1.30)$$

solving eq. 1.20 with a non-zero energy-momentum tensor leads to

$$\bar{h}_{ij}(t, \mathbf{x}) = \frac{2G}{r} \frac{d^2 I_{ij}}{dt^2}(t_r), \quad (1.31)$$

where  $\bar{h}_{ij}(t, \mathbf{x})$  represents the space-components of  $h_{\mu\nu}$  trace-reversed,  $I_{ij}$  is the quadrupole moment tensor of an arbitrary mass distribution and  $t_r = t - r/c$ . Therefore, any system with a non-zero quadrupole moment will cause perturbations in the space-time manifold. These perturbations are called *gravitational waves*.

For a circularized binary system with orbital separation  $R$  and angular velocity  $\omega$  and components of equal mass  $M$ , the perturbation takes the form

$$h_{ij} = \frac{8GM}{rc^4} \omega^2 R^2 \begin{pmatrix} -\cos(2\omega t_r) & -\sin(2\omega t_r) & 0 & 0 \\ -\sin(2\omega t_r) & \cos(2\omega t_r) & 0 & 0 \\ 0 & 0 & 0 & 0 \\ 0 & 0 & 0 & 0 \end{pmatrix}. \quad (1.32)$$

<sup>16</sup>i.e. a “flat” spacetime.

### 1.3. Angular momentum dissipation in rotating stars

While gravitational waves differ from electromagnetic ones in that they constitute a periodic distortion of a tensor field instead of a vector field, they still carry energy. The power radiated through gravitational wave emission can be represented as

$$P_{\text{GW}} = -\frac{32}{5} \frac{G^4}{c^5} \frac{(m_1 m_2)^2 \cdot (m_1 + m_2)}{a^5}. \quad (1.33)$$

The energy lost from a binary star through gravitational radiation causes the system's angular momentum to decrease and the orbit to shrink. Owing to the  $\frac{1}{a^5}$ -dependence, the radiated power is negligible in wide systems, only becoming significant in very short-period binaries. In systems involving RLOF of a non-degenerate component, angular momentum loss through gravitational radiation can be instrumental in determining when the donor star fills its Roche-lobe. The timescale associated with the decrease in orbital separation can be written

$$\tau_{\text{GR}} = \frac{5}{32} \frac{c^5 R^4}{G^3 M_{\text{tot}} \mu}, \quad (1.34)$$

where  $M_{\text{tot}}$  is the total mass of the system and  $\mu$  the reduced mass.

Since interacting binaries continue to radiate gravitational waves and therefore undergo a continual decrease in orbital separation, mass-transfer is enhanced by gravitational radiation. The combined mass-loss rate can be approximated as

$$\dot{M} \approx \frac{M_1}{\tau_{\text{nuc/KH/dyn}}} + \frac{M_1}{\tau_{\text{GR}}}. \quad (1.35)$$

### 1.3. Angular momentum dissipation in rotating stars

Rotation may profoundly alter the structure and evolutionary path of a star. Since this thesis is, in part, concerned with the effects of angular momentum dissipation in explosive stellar transient progenitors, this section provides a brief overview of the most pertinent principles, broadly following Maeder (2009).

Non-degenerate stars are not solids. Unlike in a, e.g., rotating apple, there is nothing to stop stellar material located at different points along the star's radius rotating at different angular velocities<sup>17</sup>. This possibility for *differential rotation* begs the question: How do layers of differentially rotating stellar matter influence each other?

The customary way to address the transport of angular momentum in a spherically symmetric<sup>18</sup> stellar envelope is described by a diffusion equation (see also Endal & Sofia 1976, 1978):

$$\left( \frac{\partial \omega}{\partial t} \right)_{M_r} = \frac{1}{i} \left( \frac{\partial}{\partial M_r} \right)_t \left[ \left( 4\pi r^2 \rho \right)^2 \nu_{\text{turb}} \left( \frac{\partial \omega}{\partial M_r} \right)_t \right], \quad (1.36)$$

<sup>17</sup>This is an extremely simplified view. In practice, any given volume of stellar material has six degrees of freedom, potentially moving relative to any surrounding volume as dictated by the stellar evolution equations and its thermodynamic and electrodynamic state.

<sup>18</sup>This approach neglects the meridional variation of the effective gravitational potential associated with the rotation of a massive spheroid as well as the interaction of horizontally displaced elements, but a complete treatment would go beyond the scope of this introduction.

## 1. Introduction

Here  $\omega$  is the local angular velocity,  $t$  time,  $M_r$  the mass coordinate,  $i$  the local specific moment of inertia,  $r$  the radius,  $\rho$  the local density and  $\nu_{\text{turb}}$  the local shear viscosity as defined by the active diffusive processes.

Since this thesis is concerned with the evolution of accreting WDs the relevant rotational instabilities are those active in stably stratified zones with a monotonic, negative density gradient:

The *dynamical shear instability* (Zahn 1974) occurs if the difference of the kinetic energy of two volumes of material moving in two differentially rotating layers is larger than the work required to displace them against gravitational and buoyancy forces. This results in an exchange of kinetic energy and leaves both volumes with an averaged angular velocity on the dynamical timescale. Mathematically, the turbulent viscosity of the dynamical shear instability can be described

$$\nu_{\text{DSI}} = \frac{H_P^2}{\tau_{\text{dyn}}} \left( 1 - \frac{R_i}{R_{i,c}} \right)^2, \quad (1.37)$$

where  $H_P$  is the local pressure scale height,  $\tau_{\text{dyn}}$  is the local dynamical timescale (see Eq. 1.10),  $R_{i,c}$  is the critical Richardson number (canonically  $R_{i,c} = 1/4$ ) and the Richardson number  $R_i = N^2/\sigma^2$  with  $\sigma = \partial\omega/\partial \ln r$ .  $N$  is the Brunt-Väisälä frequency, which is a measure of the stability of the stellar medium against unstable convective displacement<sup>19</sup>. The condition for the instability to be active is  $R_i < R_{i,c}$ .

The Brunt-Väisälä frequency can be decomposed into a thermal ( $N_T$ ) and a chemical ( $N_\mu$ ) buoyancy frequency ( $N^2 = N_T^2 + N_\mu^2$ ). The activation of the dynamic shear instability requires the stratification of the stellar matter to be somewhat unstable (i.e. relatively small, but positive values of  $N$ ), but if the thermal buoyancy force (and, consequently, the thermal buoyancy frequency) is reduced through thermal diffusion, the *secular shear instability* (Zahn 1992) may come into force. The secular shear instability acts in essentially the same way as the dynamic shear instability, but requires the (comparatively) relaxed condition of

$$\frac{\nu_{\text{kin}} R_{e,c} N_T^2}{K \sigma^2} < R_{i,c}, \quad (1.38)$$

where  $\nu_{\text{kin}}$  is the kinetic viscosity,  $R_{e,c}$  is the critical Reynolds number (canonical value  $R_{e,c} = 2500$ ) and  $K$  is the thermal diffusivity. Since the secular shear instability is predicated on the efficiency of thermal diffusion, it acts on the thermal diffusion timescale. The associated turbulent viscosity can be written

$$\nu_{\text{SSI}} = \frac{K \sigma^2 R_{i,c}}{N^2}. \quad (1.39)$$

The *Goldreich-Schubert-Fricke instability* (Goldreich & Schubert 1968; Fricke 1969) arises from departures of the stellar medium from cylindrical rotation under baroclinic conditions. A volume element displaced either along the rotational axis or the radial direction (for which it must overcome both the thermal stability of the medium and gravity) experiences a larger centrifugal force than the surrounding material, inducing an instability. The condition (fulfillment of either is sufficient) for the Goldreich-Schubert-Fricke instability can be written

$$\frac{\nu}{K} N_{T,\text{ad}}^2 + N_\Omega^2 < 0 \quad \text{or} \quad \left| \bar{\omega} \frac{\partial \omega^2}{\partial z} \right| > \frac{\nu}{K} N_{T,\text{ad}}^2, \quad (1.40)$$

<sup>19</sup>The larger the value, the more stable. Negative values indicate instability and, hence, that the region is convective.



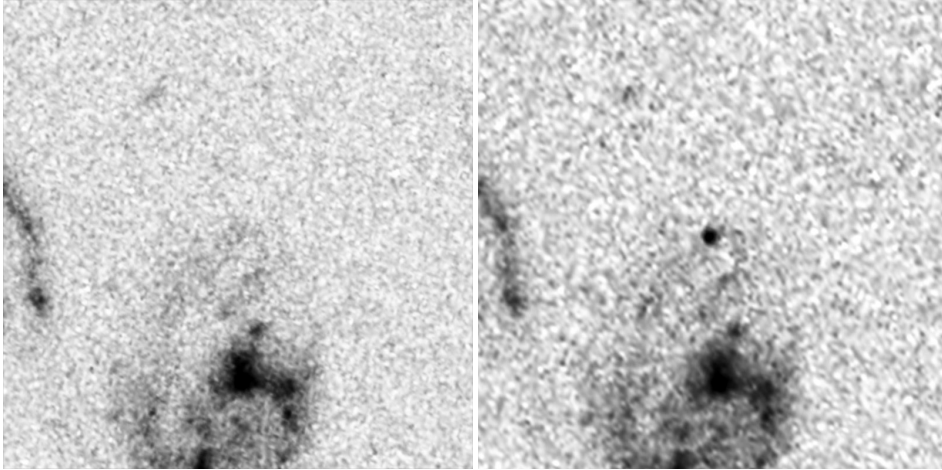


Figure 1.12.: Left: SN Tiberius before outburst

Right: SN Tiberius after outburst

Image credit: NASA, ESA, C. McCully (Rutgers University), A. Koekemoer (STScI), M. Postman (STScI), A. Riess (STScI/JHU), S. Perlmutter (UC Berkeley, LBNL), J. Nordin (NBNL, UC Berkeley), and D. Rubin (Florida State University)

where  $\bar{\omega}$  is the distance from the rotational axis,  $N_{T,ad}$  is the adiabatic thermal buoyancy frequency,  $\omega$  the angular velocity and  $N_{\Omega}$  the Rayleigh frequency.

Another important instability is the *Taylor-Spruit instability* (Tayler 1973; Spruit 2002). This instability occurs in the radiative parts of a differentially rotating stellar envelope and relies on the presence of a (possibly relatively weak) radially oriented magnetic seed field. As neighboring layers are displaced with respect to each other, the field is reoriented and strengthened, drawing energy from the rotational energy of the differential rotation. Since this instability draws energy from relative motion of stellar material, differential rotation tends to be decreased as the instability develops. This instability is one of the main points of study in chapter 3. The reader is referred to Sec. 3.2 for a more in-depth explanation.

## 1.4. Explosive stellar transients

Stars are, for the most part, stable objects, quietly converting the nuclei of the matter of which they are composed into more tightly bound ones, staying in hydrostatic equilibrium. However, under certain conditions a star turns into a decidedly unstable process, releasing staggering amounts of energy and, quite possibly destroying or changing itself in the process. The energy released ( $\sim 10^{46}$  J for a typical Type II supernova) can make the star outshine its host galaxy (see. Fig. 1.12). This section provides a short overview to the subject, broadly following Carroll & Ostlie (2007).

### 1.4.1. Types of supernovae

Supernovae are classified according to their observational features. A lack of hydrogen lines in a SN's early spectrum signifies a Type I SN, while SNe of Type II exhibit strong hydrogen lines. Type I SNe

## 1. Introduction

with strong Si II lines are classified Type Ia, while those without are either type Ib if their spectra exhibit strong helium lines or type Ic if they do not. There are numerous subtypes, but a complete description would exceed the scope of this introduction.

The absence of hydrogen lines in SN I, hydrogen being the most abundant element in the Universe as well as the most prominent raw material in star formation (and much easier to detect in a SN spectrum than helium, see Hachinger et al. 2012), makes these transients peculiar and hints that their progenitors must have shed their, initially present, hydrogen envelope. None of the progenitors of these types of SNe are known with certainty. SNe Ib and Ic have been associated with star forming regions in their host galaxies, although at least the Ca-rich subtype of type Ib SNe have been observed in old populations (Perets et al. 2011) and modeled as such (Yuan et al. 2013). A young environment, together with the lack of hydrogen lines, would hint at an origin in the core collapse of hydrogen-stripped massive stars with a short lifetime (Yoon et al. 2010; Woosley et al. 1993). On the other hand, at least some SNe Ib have been successfully modeled as a thermonuclear detonation of a WD (Waldman et al. 2011). Most importantly, SNe Ia in particular remain mysterious with either a merger of two WDs or accretion from a non-degenerate progenitor currently being most favored as possible production scenarios.

The picture is clearer when type II SNe are concerned. SNe II (and, as mentioned, some SNe I) are hypothesized to result from the collapse of massive ( $M \gtrsim 8.0M_{\odot}$ ) stars (Woosley & Janka 2005; Janka et al. 2007). As the cores, by this point largely composed of  $^{56}_{26}\text{Fe}$  and  $^{56}_{28}\text{Ni}$ , of these objects grow in mass during the star's various burning stages, the temperature and pressure increase. With an increase in temperature comes an increase of the energy of the photons dissolved in the plasma. At some point the energy of these photons becomes high enough for them to be able to overcome the binding energy of the highly bound  $^{56}_{26}\text{Fe}$  nuclei, disintegrating them into smaller nuclei and free nucleons:



$^{56}_{26}\text{Fe}$  is one of the most highly bound nuclei in existence<sup>20</sup>. This means that its breakup (*photodisintegration*) is endothermic, which in turn means that the process removes energy from the star, decreasing the radiative pressure of the core, resulting in further contraction. Once the pressure increases sufficiently, the free electrons in the now degenerate plasma are captured by the free protons (see Sec. 1.1.3) and the core collapses. Depending on the mass of the core it will either cease its collapse when the degeneracy pressure of its neutrons force it to stop, becoming a neutron star, or keep collapsing into a black hole. If the core collapses into a neutron star - an exceedingly solid object - it will rebound, sending a shock through the infalling non-degenerate material. The exact kinematics of the progress of the shock through the infalling material are still somewhat unclear, but it is hypothesized that neutrino emission (which carry about 99% of the SN's energy) plays a crucial role in keeping the shock going. The radiation emitted by the following outburst as well as the decay of the radioactive elements created in the shock and dissolved in the ejecta are then visible as a supernova.

### 1.4.2. Accretion-induced transients

Core collapse Supernovae are not the only way to create energy releases of the magnitude seen in SNe II. Other ways are found in the spectrum of accretion-induced transients. In principle, high energy

<sup>20</sup>the highest binding energy per nucleon is encountered in the rare Nickel-isotope  $^{62}_{28}\text{Ni}$ .

outbursts can be generated by accretion onto all sorts of objects (like black holes or neutron stars), but in the context of this thesis, accretion onto WDs is most relevant.

### Type Ia supernovae

As mentioned above, SNe Ia are characterized by the lack of hydrogen lines and strong Si II lines in their spectra. Further, (typical) SNe Ia outbursts exhibit a remarkable consistency in maximum luminosity (see e.g. Benetti et al. 2005), which makes them a favored tool for cosmological distance measurements. The nature of SNe Ia progenitors is still a matter of debate (and this thesis attempts, in part, to add to the discussion), but over the years, broadly, two categories of models have emerged: the *single degenerate scenario* and the *double degenerate scenario* (Maoz & Mannucci 2012; Hillebrandt & Niemeyer 2000).

The double degenerate scenario assumes that the immediate progenitor of a SN Ia is a binary system consisting of two WDs. As the orbital separation of the binary decreases due to the emission of GWR (see Sec 1.2.4), the less massive component (being the physically larger one, see Fig. 1.7) gradually fills its Roche-lobe (sec. 1.2.1) and is disrupted. The material accreted onto the more massive component then initiates a thermonuclear runaway (usually associated with the WD mass approaching the Chandrasekhar mass) which disrupts the star. The resulting outburst and the decay of the newly created radioactivities is then visible as a SN Ia. The process by which the thermonuclear runaway is initiated and proceeds through the WD is still somewhat unclear.

The single degenerate scenario assumes the immediate progenitor of a SN Ia to be a binary consisting of a WD and a non-degenerate companion. This system will initiate mass-transfer either by the orbit shrinking due to GWR or due to the non-degenerate companion expanding to fill its Roche-lobe. The lack of helium lines in the SN Ia spectrum have made investigations attractive following the idea of the donor being a hydrogen-deprived helium star (Fink et al. 2007; Sim et al. 2010; Kromer et al. 2010). However, hydrogen accretion, in accordance with observational evidence (Hamuy et al. 2003), is also being studied (Gilfanov & Bogdán 2010; Nomoto et al. 2007). In the case of hydrogen accretion (the accumulated material will still contain a significant admixture of primordial helium), competing hypotheses contend that either the helium carried with the hydrogen will accumulate on top of the CO core, becoming degenerate, until a helium shell flash initiates the runaway or that, as the WD approaches the Chandrasekhar mass, the CO core ignites at its center. Depending on the mass-accretion rate, a stably burning shell may develop on the WD's surface, converting the accumulated material into carbon and oxygen. All of these scenarios see the WD's mass approaching the Chandrasekhar mass in some way or another. How the runaway proceeds once ignited (either as a subsonic or a supersonic shock) is also quite uncertain.

In the case of helium accretion, proposed scenarios either mirror those for the hydrogen-accreting case or promote the *double detonation scenario* (Nomoto 1980, 1982a,b; Taam 1980a,b). The double detonation scenario involves the accumulation of helium in a layer on top of the core of a sub-Chandrasekhar-mass WD. This helium is then ignited (which requires either the density or the temperature of the helium to be raised sufficiently). The ignition turns into an unstable runaway and ignites the CO core either by propagating directly into it, which is likely if the ignition occurs some way above the core interface, or by compressing the core and inducing a detonation at the center, which is likely if the ignition occurs directly at the interface (Woosley & Kasen 2011).

A class of supernovae related to, but distinct from, SNe Ia are SNe of type Iax (Foley et al. 2013). These transients broadly resemble canonical SNe Ia but differ by exhibiting slower ejecta velocities,

## 1. Introduction

higher production of stable nickel and a larger scatter in maximum luminosities. Observationally, these transients have been linked to systems that (if assumed to be binaries) exhibit large mass-transfer rates and a high luminosity of the assumed donor star (McCully et al. 2014). The slower ejecta have led to speculation that a subsonic burning front (deflagration) as opposed to a supersonic one (detonation) may be involved in the explosion process.

### Cataclysmic variables

Not all mass-transfer induced ignitions on WDs lead to the destruction of the star and a supernova. In many cases a thermonuclear runaway will burn away the accumulated material but leave the WD's core intact. These objects are called *cataclysmic variables* and, while their outbursts do not reach the impressive luminosities of supernovae, their brightness can still increase by up to six magnitudes (Sion 1999; Sion & Godon 2012).

The most obvious consequence of the accretor not being destroyed in an outburst is that, after a period of quiescence, another outburst can follow. Novae are thus recurrent phenomena.

Classical novae result from the accretion of a small amount of material (typically hydrogen) on a WD. The material is mixed with the uppermost layers of the CO core. As the temperature and density increase, CNO-cycle hydrogen burning becomes possible and the accumulated material ignites explosively. As the burning shell exceeds its Eddington luminosity, most of the material is ejected. The retained material is added to the mass of the core, which, in turn, may increase and approach the Chandrasekhar mass, eventually ending in a SN Ia.

## 1.5. This thesis

This thesis investigates the viability of He-star + CO WD binaries as progenitor candidates for a variety of explosive transient phenomena, with an emphasis on supernovae, in particular SNe Ia, Iax and Ca-enhanced SNe Ic, and further emphasis on sub-Chandrasekhar mass explosions.

The evolutionary history of He-star + CO WD binaries is non-trivial (He-stars do not form out of primordial gas) and has some bearing on the correct choice of initial parameters for the investigated progenitor candidate. Figure 1.13 qualitatively depicts the formation of such a system: The binary forms as a pair of intermediate-mass hydrogen stars ( $\sim 4 M_{\odot}$ ). The mass of the stars must be unequal in order to ensure that both do not develop at the same evolutionary timescale.

The more massive of the binary components must reach the end of its helium burning stage before the other has finished its main-sequence lifetime. Once that is accomplished, the more massive component either sheds its hydrogen envelope in a planetary nebula, transfers its envelope to the secondary in a stable RLOF-phase, or the system enters a common envelope phase. Either way the more massive component loses its hydrogen envelope, leaving a CO WD, while the other component is still in its core hydrogen burning phase.

Once the other component has reached the end of its core hydrogen burning phase it expands and the system must enter a common envelope phase (at these low masses<sup>21</sup> there is no other way to remove the hydrogen envelope). The resulting system then contains a He-star and a CO WD in a short-period orbit. The state of this system includes some uncertainties, however, all predicated on

---

<sup>21</sup>Higher mass stars may be able to rid themselves of their hydrogen envelopes some other way, resulting in Wolf-Rayet star.

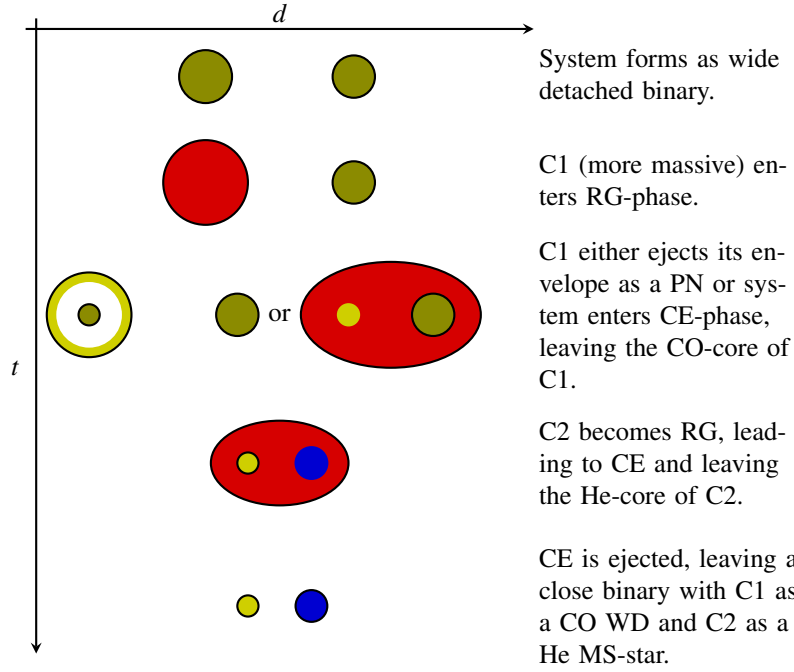


Figure 1.13.: Qualitative depiction of the creation of a close He-star + CO WD binary.  $t$  is a qualitative time coordinate,  $d$  a qualitative length. C1 and C2 are the two components (left and right, respectively), of the system.

the fact that the interaction between the two components during the common envelope phase are not precisely known.

For close to 40 years the idea that accretion of helium-rich material on a sub-Chandrasekhar mass CO WD at rates of  $\sim 10^{-8} M_{\odot}/\text{yr}$  could lead to an ignition in the accumulated helium layer, precipitating an explosive outburst has been studied with some interest (Taam 1980a,b; Nomoto 1980, 1982b,a). The lack of hydrogen in systems like this have made helium accretion an attractive proposition for the search for the, as of yet, elusive progenitor of SNe Ia. At the same time, clues that observed progenitors of SNe Iax (SN 2012Z in particular) possibly contain a helium star (McCully et al. 2014) make these systems interesting in that regard.

This thesis is organized as follows:

In chapter 2, He-star + CO WD systems are examined from a binary-evolution standpoint, using preexisting explosion calculations of sub-Chandrasekhar-mass WDs to link given initial binary parameters to possible observables. Particular emphasis is placed on the question of whether helium accretion can result in a transient that is spectrally similar to a canonical SN Ia. The model sequences are further studied with regard to other transients like strong He-flashes, weak He-flashes, mass loss. Possible outcomes are correlated.

In chapter 3, rotating, magnetized CO WDs are studied in isolation. Previous studies suggest that the effects of rotation and rotational instabilities may significantly affect the evolution of WDs undergoing accretion. This is expanded upon by including the effects of the Tayler-Spruit instability in the calculations. Uncertainties pertaining to the initial state of a WD in a He-star + CO WD system

## 1. Introduction

are taken into account as well as uncertainties related to the deposition of angular momentum on the WD through the accretion process. The implications for the chemical composition of the accreting models are looked into, as well as their rotational profile. Particular emphasis is placed on the ability of these system to produce a helium ignition and the possible further development of such an ignition. The results of the calculations are then discussed regarding the possibility these objects undergoing a double-detonation at sub-Chandrasekhar masses. The possible resulting transients are then correlated with the model results.

In naturally occurring systems, mass-transfer proceeds in accordance with the evolution of the binary's orbital separation as well as the donor star's evolution. This results in a time-variability of the mass-transfer rate. Chapter 4 attempts to quantify this effect by investigating a number of isolated WD models undergoing a range of different mass-transfer schemes. The reaction of the WD models to the chosen mass-transfer schemes is discussed. Results of models utilizing constant mass-transfer rates are compared with comparable time-variable ones<sup>22</sup>. The impact of the choice of the initial orbital separation and the development of the mass-accretion rate and its effect on the conditions of helium ignition on the WD is highlighted. The results are then put into context with possible related transients and are used to clarify the expected outcomes of constant accretion rate models.

The findings of the thesis are summarized in chapter 5.

---

<sup>22</sup>Constant mass-transfer is often used as a parameterized approximation for the realistic case in order to reduce the problem's complexity. This notion is challenged here.

## 2. Models for the evolution of close binaries with He-Star and WD components towards Type Ia supernova explosions

P. Neunteufel, S.-C. Yoon & N. Langer (A&A 2016, 589, A43)

### **Abstract:**

*Type Ia supernovae (SNe Ia) have been an important tool for astronomy for quite some time; however, the nature of their progenitors remains somewhat mysterious. Recent theoretical studies indicated the possibility of producing thermonuclear detonations of carbon-oxygen white dwarfs (CO WDs) at masses less than the Chandrasekhar mass through accretion of helium-rich matter, which would, depending on mass-accretion rate, mass, and initial temperature of the WD, spectrally resemble either a normal SN Ia or a peculiar one.*

*This study aims to further resolve the state of binary systems comprised of a sub-Chandrasekhar-mass CO WD and a helium star at the point where an accretion-induced detonation occurs and constrains the part of the initial parameter space where this kind of phenomenon is possible.*

*Preexisting data obtained through simulations of single, constantly accreting CO WDs is used as an indicator for the behavior of new binary models in which the WD is treated as a point mass and which include the non-degenerate partner as a fully resolved stellar model. We parameterize the ignition of the accumulated helium layer, changes in the WD temperature, and changes in the CO core mass depending on the mass-transfer rate.*

*The initial conditions allowing for detonation do not form a single contiguous area in the parameter space, whose shape is profoundly influenced by the behavior of the donor star. Mass loss due to Nova outbursts acts in favor of detonation. According to our criteria, about 10% of the detonations in this study can be expected to show spectra consistent with ordinary SNe Ia; the rest exhibit peculiar features.*

### 2.1. Introduction

Several decades ago, sub-Chandrasekhar mass thermonuclear detonation of carbon-oxygen white dwarfs (CO WD) initiated by an explosive ignition in an accreted layer of helium were deemed a promising model for a number of observed exploding stellar transients. These transients include Type Ia supernovae (SNe Ia) and other classes of transients resembling SNe Ia, like the spectrally peculiar “Iax” (see Foley et al. 2013) and, probably, subluminous “point Ia” (.Ia) Supernovae Bildsten et al. (2007). González-Gaitán et al. (2014) discuss the observational properties of peculiar SNe Ia, while observational evidence of the nature of the progenitors of SNe .Ia was presented by Kilic et al. (2014).

The possibility of a detonation in an accumulated helium envelope of a sub-Chandrasekhar mass CO WD was first investigated in the early 1980s Taam (1980a,b); Nomoto (1980, 1982a,b). It was soon realized that, depending on a number of factors, ignition in the accumulated He-shell either led

## 2. Close binary models for SNe Ia explosions

to the ignition and subsequent ejection of the He-shell only, leaving an intact CO core, or led to a secondary detonation of the CO core and thus the complete disruption of the WD. The mechanism leading to the complete destruction of the WD has become known as the “double detonation” scenario and has been investigated in a number of one- and multidimensional studies Livne (1990); Livne & Glasner (1990, 1991); Livne & Arnett (1995); Benz (1997); Livne (1997); Fink et al. (2007, 2010); Sim et al. (2010); Kromer et al. (2010); Woosley & Kasen (2011). This scenario is a subset of what has become known as “WD+He star channel”.

This channel forms part of a picture of He-accreting WDs, introduced as candidates for SN Ia or SN .Ia progenitors, which also includes double degenerate systems featuring a He WD instead of a He star. Arguments in favor of the WD+He WD channel have been investigated by Shen & Bildsten (2009).

During the course of the study of helium accreting WDs Bildsten et al. (2007); Fink et al. (2007), it was realized that helium detonations were possible even in comparatively low mass ( $< 0.0035M_{\odot}$ ) envelopes of accumulated material and that a detonation in the helium envelope of the WD (characterized by a supersonic shock in the medium) will robustly detonate the CO core Fink et al. (2010); Woosley & Kasen (2011). It was also realized that synthetic spectra produced for some of the models investigated in the studies mentioned above resembled those of observed “normal” SNe Ia Sim et al. (2010); Kromer et al. (2010); Woosley & Kasen (2011), while others more closely resembled those of SNe Iax.

These findings stimulated interest in whether double detonations could make a significant contribution to the rate of observed SNe Ia and that their subluminous and spectrally peculiar kin. More recently, a study by Wang et al. (2013) used detailed binary evolution models and subsequent binary population synthesis calculations to investigate the rate of SNe Iax that might result from double detonations. In that study, under the assumption that double detonation would always lead to a SN Iax or, at the very least, a spectrally peculiar SN, it was found that the rate of these phenomena can be adequately explained using the helium accretion double detonation model, assuming detonation at the point where a fixed amount of helium ( $0.1 M_{\odot}$ ) has accumulated on the WD (cited sources: Ivanova & Taam 2004; Ruiter et al. 2011).

Very recently, numerical studies using population synthesis simulations and the Cambridge stellar evolution code Liu et al. (2015a,b) have suggested the WD+He star channel as a promising candidate mechanism for the creation of SNe Iax, arguing, however, that a small fraction of SN Iax may be the result of helium deflagrations (see Sec. 3.2) on the WD component rather than detonation.

In reality, the amount of accumulated helium in a CO WD at detonation is expected to be a function of the initial mass and temperature of the CO WD and of the mass-accretion rate of helium-rich matter. This has been investigated by Ruiter et al. (2014), who compared occurrence rates of helium accretion-induced detonations of white dwarfs using a variation of assumptions regarding input physics, including a prescription of variable shell ignition masses adapted from Iben & Tutukov (1989). Whether the helium detonation leads to a peculiar SN event or to an ordinary-looking SN Ia would also depend on this. In our study we combine some of the data provided by preexisting research (mainly from Woosley & Kasen 2011) with new binary evolution calculations to investigate the impact of allowing for the mass of the helium accumulated on the WD to vary with parameters such as the system’s mass-transfer rate and the mass of the accreting WD on the distribution of detonating systems in the parameter space. From this data, we generate a distribution of the expected helium shell masses, allowing for an estimate of the ratio of high to low final helium shell masses, which have an impact on the spectra produced by double detonation Sim et al. (2010); Woosley &



Kasen (2011). We are also able to make a statement about the post-SN state of the donor star, which might be of use in the explanation of single high velocity stars (see Geier et al. 2015).

This article is organized as follows. In Sec. 2.2 we describe the input physics of our models and the computational framework. In Sec. 2.3, we first discuss the behavior of helium donor stars using single helium star models (Sec. 2.3.1), and describe physical and numerical restrictions and their impact on our choice of the considered parameter space. Then (Sec. 2.3.3) we present binary evolution models for which mass-transfer from the helium donor star is computed self-consistently with the orbital evolution of the binary system, while the CO WD is approximated as a point mass, and discuss the observational implications. We conclude our study in Sec. 2.4.

## 2.2. Numerical methods and physical assumptions

### 2.2.1. Detonation conditions and mass-transfer efficiency

The ability of single white dwarfs undergoing accretion of He-rich matter at a constant rate to produce a detonation in the accumulated He-shell has been studied in some detail by Woosley & Kasen (2011). A number of cases characterized by the WD mass and the mass-accretion rate were simulated and many of them produced helium detonations powerful enough to detonate the CO core either by way of an inward shock, if the detonation occurred above the surface of the CO core, or by simple compression, if the detonation occurred at the surface of the CO core. For CO white dwarfs between  $0.7 M_{\odot}$  and  $1.1 M_{\odot}$ , a helium ignition violent enough to lead to CO core detonation may occur at constant accretion rates  $\dot{M}$  between  $1 \cdot 10^{-8} M_{\odot}/\text{yr}$  and  $5 \cdot 10^{-8} M_{\odot}/\text{yr}$ . The critical mass of the helium shell depends on the initial temperature and mass of the white dwarf for a given mass-accretion rate. The initial temperatures of their models are defined according to the initial luminosity: hot with  $L = 1.0 L_{\odot}$  and cold with  $L = 0.01 L_{\odot}$ . Accretion rates and final helium shell masses for detonating models as found by Woosley & Kasen (2011) are shown in Fig. 2.1. It has also been shown that helium ignition, if occurring at accretion rates higher than those indicated in Fig. 2.1, would not lead to a subsequent detonation of the CO core. These systems instead underwent a “deflagration” event characterized by a subsonically propagating burning front, which led to the ejection of the shell in a nova-like process, leaving the CO core intact. Detonations, however, always led to a subsequent detonation of the CO core, provided the models’ zoning was sufficiently fine.

The response of the WD to accretion is described in terms of the the amount of mass retained on the WD versus the amount of mass accreted onto the white dwarf (with the remaining mass being ejected from the system). This relation is called “mass acculumation efficiency”, which can be expressed as

$$\eta = \dot{M}_{\text{acc}} / \dot{M} , \quad (2.1)$$

where  $\dot{M}_{\text{acc}}$  is the rate of material accumulated on the accretor and  $\dot{M}$  is the rate of material being transferred from the donor. Depending on the mass-transfer rate, in the case of  $\eta > 0$  the retained material either simply accumulates in the form of a helium layer of increasing thickness (low mass-transfer rates), hereafter referred to as “steady accumulation” or is partially or fully processed into carbon or oxygen (higher mass-transfer rates). At accretion rates higher than those allowing for steady accumulation, consecutive nova outbursts preclude the buildup of a helium layer of sufficient mass to trigger a CO core detonation. At even higher accretion rates, a stable nuclear burning shell may develop on the WD, leading to steady growth of the CO core. The value of  $\eta$  depends on the the mass of the white dwarf and the helium accretion rate.

## 2. Close binary models for SNe Ia explosions

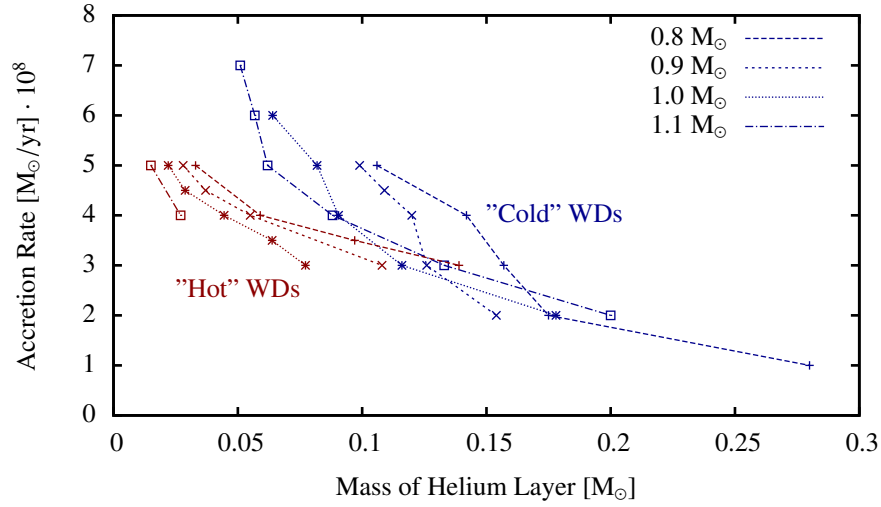


Figure 2.1.: Points of helium detonation as predicted by Woosley & Kasen (2011) in the relevant mass range. Points and lines plotted in blue are valid for cold dwarfs, red points and lines for hot dwarfs. Masses are given in units of  $M_{\odot}$ . We assume that a detonation on the white dwarf component occurs when a system crosses the interpolated lines.

The evolution of  $\eta$  for different white dwarf masses and accretion rates has been studied by Kato & Hachisu (2004), whose estimates we use whenever our systems show accretion rates high enough to make them a viable option. Numerically, the resulting values for  $\eta$  fall between 0.3 and 1 increasing with the mass-transfer rate. We use the following prescription for  $\eta$  over the whole range of occurring mass-transfer rates (see also Fig. 2.2),

$$\eta = \begin{cases} 1, & \text{if } 0 < [\dot{M}] < \dot{M}_{\text{WK,max}} , \\ 0, & \text{if } \dot{M}_{\text{WK,max}} < \dot{M} < \dot{M}_{\text{KH,min}} , \\ \eta_{\text{KH}}(M_{\text{WD}}, \dot{M}), & \text{if } \dot{M}_{\text{KH,min}} < \dot{M} , \\ 1, & \text{if } \dot{M}_{\text{KH,max}} < \dot{M}, \end{cases} \quad (2.2)$$

where  $\dot{M}_{\text{WK,max}}$  is the upper limit of the mass-transfer rates studied by Woosley & Kasen (2011) corresponding to the maximum sustainable mass-transfer rate for steady accumulation,  $\dot{M}_{\text{KH,min}}$  the lower limit of the range studied by Kato & Hachisu (2004) corresponding to the minimum sustainable rate for  $\eta \geq 0$ , and  $[\dot{M}]$  is the time averaged mass-transfer rate.

### 2.2.2. Computational framework

The time-dependent evolution of the donor star properties, mass-transfer rate, and binary orbital separation are calculated using the binary evolution code (BEC), a well-established simulation framework capable of performing detailed one-dimensional experiments of single or binary systems Langer et al. (2000); Yoon & Langer (2004b). This framework resulted from a development by Braun (1998) of a preexisting implicit hydrodynamic stellar evolution code Langer (1991, 1998). Here we study short-period binary systems with initial orbital periods ranging from 0.02 to 0.12 days, WD masses

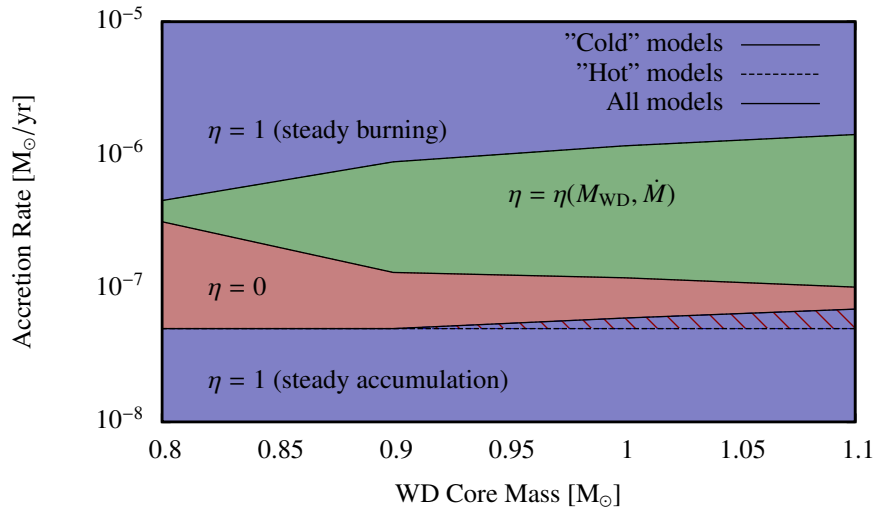


Figure 2.2.: Illustration of the parameters of the prescription used for the mass accumulation efficiency (see Eq. 2.2) at different mass-accretion rates. In the area denoted by red-blue stripes, the upper limit for  $\eta = 0$  differs for hot and cold models. The dash-dotted line applies to cold models and the dashed line to hot models.  $\eta$  is changed from 1 to 0 when the time-averaged accretion rate crosses the dash-dotted or dashed lines, while for all other lines the actual accretion rate is the deciding parameter. Note that the upper  $\eta = 1$ -regime denotes steady helium burning while the lower one denotes steady accumulation of helium on the CO core without nuclear burning.

## 2. Close binary models for SNe Ia explosions

between  $0.8$  and  $1.0 M_{\odot}$ , and helium star donor masses between  $0.5 M_{\odot}$  and  $1.0 M_{\odot}$ . The choice of the boundaries to the initial parameter space is explained in greater detail in Sec. 2.3.2. The WD component is approximated as a point-mass, while the He star component is a fully resolved, non-rotating, non-magnetic stellar model at solar metallicity.

The BEC code incorporates angular momentum loss due to gravitational wave radiation (GWR; see Landau & Livshitz 1975 for a mathematical description). Mass transfer is calculated by solving implicitly the equation

$$R_L - R + H_P \ln \left( \frac{\dot{M}}{\dot{M}_0} \right) = 0 \quad (2.3)$$

(see Ritter 1988; Kolb & Ritter 1990). Here,  $H_P$  is the photospheric pressure scale height,  $R$  the stellar radius as defined by the lower edge of the photosphere,  $R_L$  the Roche lobe radius for which we use the approximation by Eggleton (1983), and

$$\dot{M}_0 = \frac{1}{\sqrt{e}} \rho v_S Q, \quad (2.4)$$

where  $v_S$  is the speed of sound in a plasma as defined by  $v_S^2 = \mathfrak{R}T/\mu$  with  $\mathfrak{R}$  being the ideal gas constant,  $T$  the plasma temperature,  $\mu$  the mean molecular weight, and  $Q$  is the effective stream cross section calculated as prescribed by Meyer & Meyer-Hofmeister (1983).

At this point it should be noted that WDs in the mass range of  $M_{WD} = 0.8 - 1.0 M_{\odot}$  take about  $0.2$  Gyr to cool from  $L = 1.0 L_{\odot}$  to  $L = 0.01 L_{\odot}$  Renedo et al. (2010a). This means that the shortest period systems would not have sufficient time to cool to  $L = 0.01 L_{\odot}$ . Therefore, the temperature of the white dwarf at the end of the common envelope phase necessary to produce this kind of system will have a significant impact on the subsequent binary interaction. Detailed investigations of the thermal evolution of a white dwarf during a common envelope phase would be required to allow more precise predictions. However, such studies have not found their way into the literature as of this time.

Systems in which  $\dot{M}$  exceeds  $\dot{M}_{WK,max}$  but remains in the area of the parameter space where  $\eta < 1$  are in a phase of consecutive nova outbursts. If the mass of the CO core increases with stable helium burning, the corresponding detonation line is obtained by interpolating the existing detonation lines (Fig. 2.1). In the case of the WD mass exceeding  $1.1 M_{\odot}$ , which is the largest considered by Woosley & Kasen (2011), our simulation is aborted since the non-monotonic nature of the detonation points with respect to the CO core mass makes simple extrapolation towards higher masses a risky option. The great majority of systems containing donors more massive than  $1.0 M_{\odot}$  lead to CO cores heavier than  $1.1 M_{\odot}$  because the nuclear timescales of the heavy donors lead to high enough mass-transfer rates to induce stable burning of the accreted material. This increases the CO core mass considerably and precludes detonation via the double detonation mechanism. This is the reason why we limit the parameter space considered in this study to donor and WD masses smaller than  $1.0 M_{\odot}$ .

During the research described in this work, estimates of a wider range of parameters of the reactions to and outcomes of mass-accretion onto WDs has become available, and any future study of this kind would be well advised to utilize them Piersanti et al. (2014). We would also like to emphasize that the accretion efficiencies given by Kato & Hachisu (2004) are somewhat high and that the discrepancy with Piersanti et al. (2014) has been shown to have a non-negligible influence on the expected event rates and on the resulting final He-shell masses Ruiter et al. (2014). Crossover from the lower  $\eta = 1$ -regime into the  $\eta = 0$ -regime is treated as an indicator that the system undergoes a deflagration (i.e.,

a subsonic shell explosion), during which all of the accumulated helium is ejected, with the CO core left intact. If the WD model is in a “cold” state when this crossover occurs, it is switched to a “hot” state for the remainder of the simulation.

The resulting sudden loss of mass in a Nova event has a significant impact on the Roche lobe radii, which heavily influences the system’s mass-transfer rate, and therefore has to be taken into account. This is accomplished by subtracting the mass of the helium shell from the mass of the white dwarf whenever the time averaged mass-transfer rate exceeds the range given in Fig. 2.1. Since the binary evolution code assumes circular orbits for binary systems, the angular momentum loss associated with the loss of mass from the accretor is dealt with by changing the orbital separation to that of a circular orbit of the same angular momentum as the realistic, elliptical orbit after mass loss.

## 2.3. Simulation results

### 2.3.1. Evolution of the donor star

As described in Sec. 2.2, in this study we treat the white dwarf component of the system as a point mass. Its state is entirely defined by the mass of the white dwarf and the mass of the helium layer that has been deposited on it, and by the system’s current mass-transfer rate. This means that the evolution of the system is dominated by the evolution of the orbital separation, which is a product of the history of the binary interaction and of angular momentum loss due to GWR, and the evolution of the He-star. The evolution of the donor star is influenced by mass-transfer. In this section, we try to disentangle those behaviors that would be exhibited by the donor star in isolation from those that result from binary interaction.

The evolution of single helium stars has been studied extensively in the past (see, e.g., Eggleton 2011), but in the interest of consistency, we discuss below the evolution of the particular models used in this study. These models were created by following the evolution of a hydrogen main sequence star up to the onset of helium burning and then removing the remaining hydrogen envelope. The mass of the resulting model was then self-consistently changed to the desired value and, with nuclear energy generation switched off, computed until thermal equilibrium was achieved. Fig. 2.3 shows the theoretical paths through the Hertzsprung-Russell diagram (HR-diagram) taken by He stars in isolation. All of these stars possess convective cores having  $M_{\text{core}}/M_{\text{star}} = 0.2$  in our  $0.5 M_{\odot}$  models and  $M_{\text{core}}/M_{\text{star}} = 0.25$  in the  $1.0 M_{\odot}$  models at the helium zero age main sequence, which grow to between  $M_{\text{core}}/M_{\text{star}} = 0.3$  and  $M_{\text{core}}/M_{\text{star}} = 0.55$  at the end of core helium burning, respectively. Thermal pulses develop for  $0.5 M_{\odot} - 0.7 M_{\odot}$  after the core helium burning phase with radius changes of a factor of 2 to 3. Any mass-transfer occurring during these pulses will exhibit mass-transfer rates according to the thermal timescale ( $\dot{M} \sim 1 \cdot 10^{-6} M_{\odot}/\text{yr}$ ), which is above the regime required for detonation (see Fig. 2.1). After the end of the pulse phase, all of the low-mass stars will become CO WDs.

The more massive He stars ( $> 0.7 M_{\odot}$ ) exhibit no significant pulses, but after the end of core helium burning they expand to become giants. At this point the simulation is stopped with the understanding that mass-transfer rates during the giant phase of a donor would be far too high for double detonation to be possible. These systems would most likely enter a common envelope phase. In any case, these systems lie outside the parameter space accessible to this study (see Sec. 2.3.2).

## 2. Close binary models for SNe Ia explosions

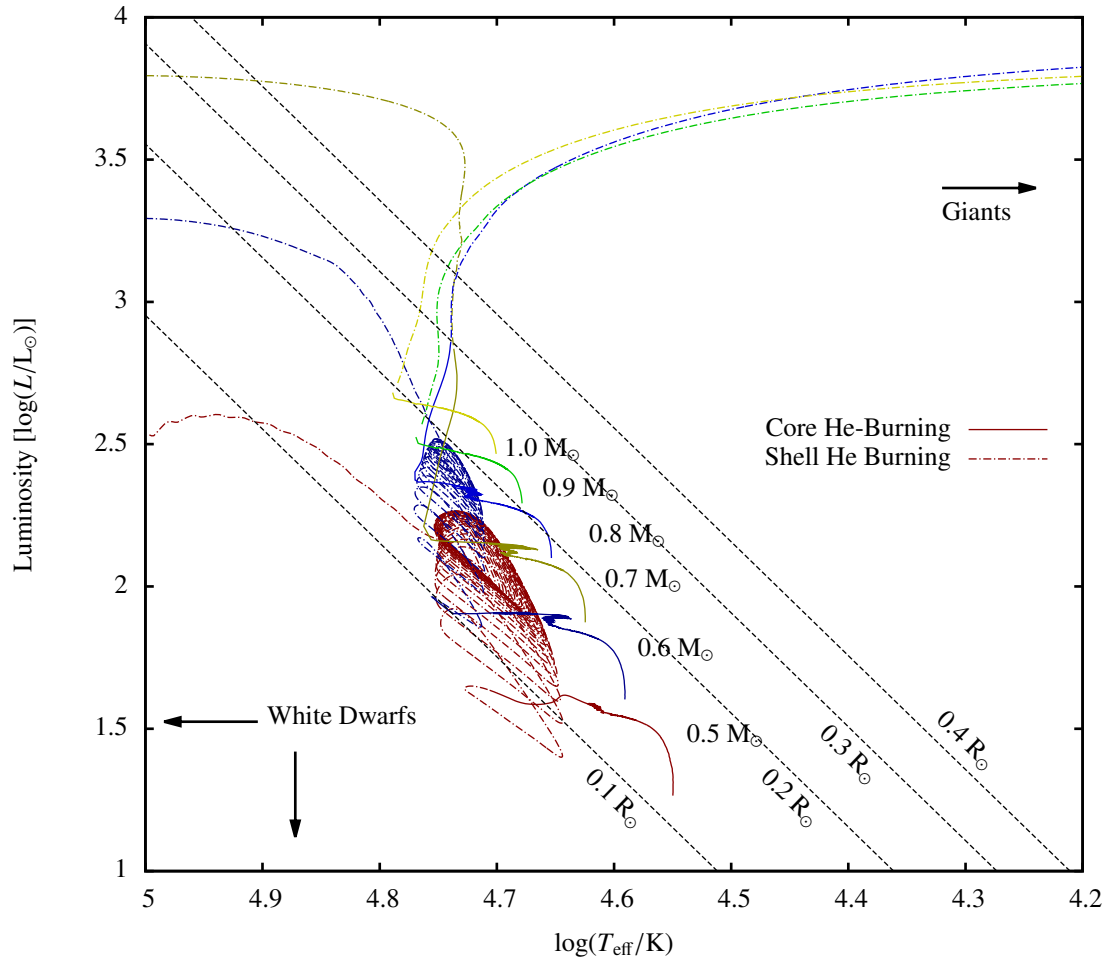


Figure 2.3.: Evolutionary tracks of single He stars with masses as used in this study in the HR-diagram. A large number of thermal pulses occur in the three lowest mass models after the end of core helium burning.

### 2.3.2. Initial parameters of the investigated binary systems

The parameter space under scrutiny in this study covers initial white dwarf masses  $M_{\text{WD}} = 0.8 M_{\odot} \dots 1.0 M_{\odot}$ ,  $M_{\text{He}} = 0.5 M_{\odot} \dots 1.0 M_{\odot}$ , and initial orbital periods  $P_{\text{init}} = 0.03 \dots 0.11$  days. Since we use the results of Woosley & Kasen (2011) for this study, we are generally restricted to the parameter space of white dwarf masses investigated by them ( $0.7 M_{\odot} \leq M_{\text{WD}} \leq 1.1 M_{\odot}$ ). Their data for  $M_{\text{WD}} = 0.7 M_{\odot}$  is too sparse for us to use. Their data for  $M_{\text{WD}} = 1.1 M_{\odot}$  is less sparse, but since the CO core masses of our white dwarfs may grow over the course of our calculations, we would be forced to extrapolate the existing data to CO core masses beyond  $1.1 M_{\odot}$ . This also limits the range of donor masses accessible to us. Since the nuclear timescale of helium stars of masses  $M_{\text{Donor}} > 1.0 M_{\odot}$  approaches  $10^6$  yr, mass-transfer will be in the steady burning regime ( $\eta = 1$ ) already on the helium main sequence (see also Yoon & Langer 2003). Calculations performed during the course of this study have shown that in these cases the CO core mass of the accretor invariably exceeds  $1.1 M_{\odot}$  at some point, regardless of the chosen initial WD mass or initial orbital period. We thus set the upper limit for the range of donor star masses at the cited value of  $M_{\text{Donor}} = 1.0 M_{\odot}$ .

The lower boundary of our donor star mass range is provided by the inherent behavior of low-mass helium stars. Helium stars with masses below  $0.3 M_{\odot}$  fail to ignite altogether, and contract to become He white dwarfs. Helium stars with masses of  $0.4 M_{\odot}$  experience nuclear burning in their core and expand, resulting in Roche-lobe overflow (RLOF) in binary systems, but owing to their long nuclear timescale ( $\sim 10^8$  yr), a rather large proportion (more than 50 % in all cases) of their initial mass needs to be lost to the companion in order to initiate a detonation. These models usually fail to converge after a significant amount of mass has been lost to the accretor. The donor, however, is expected to eventually become a CO WD. Readers are referred to Piersanti et al. (2015) and Brooks et al. (2015) for detailed evolutionary models of these systems.

The lower end of the initial period distribution is provided by the point for which the radius of a donor star at helium zero age main sequence equals that of its Roche-lobe. The upper end is the point where the lowest mass donor stars do not experience RLOF before becoming electron degenerate. Since higher mass donors become giants for periods larger than 0.12 d, low mass-transfer rates that lead to He detonation are not expected. This leads us to the conclusion that periods longer than 0.12 d are not relevant to the present study.

We expect our calculations to retain some predictive power when moving to smaller WD masses, provided their composition is similar. However, Iben & Tutukov (1985) showed that some possible outcomes of binary main sequence evolution contain hybrid HeCO white dwarfs as an intermediate between the mass ranges for archetypical He WDs and CO WDs. Whether the results in these cases are comparable would have to be verified independently.

### 2.3.3. Discussion of binary results

#### Mass accretion modes

The most obvious information to be gained from this study is which systems in the initial parameter space might result in a detonation. For the discussions that follow, the initial parameter space where detonation occurs is called the detonation zone. The graphs depicted in Fig. 2.6 indicate the positions of all systems in this study according to the initial mass of the WD and their positions in the initial parameter space. Furthermore, the color shading indicates the amount of helium accumulated until detonation. Our calculations have allowed us to distinguish four different kinds of systems:

## 2. Close binary models for SNe Ia explosions

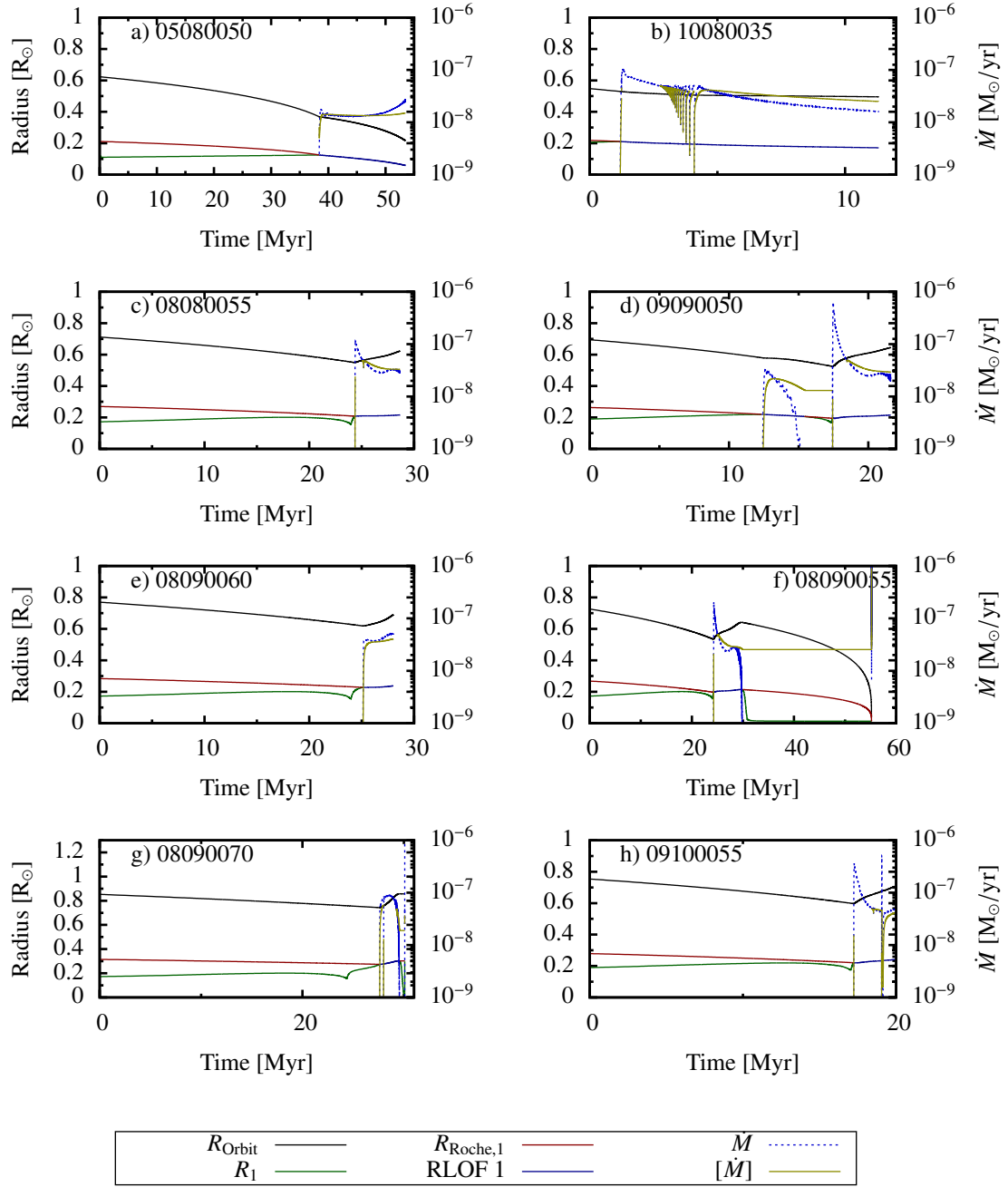


Figure 2.4.: Orbital parameters and mass-transfer rates over time after HeZAMS of various systems studied in this paper. Radii are mapped to the left hand y-axis of each diagram, mass-transfer rates to the right. The seven-digit numbers in each diagram denote the identity of the represented system as defined by its initial parameters. The first two digits are equal to the mass of the donor star divided by  $0.1 M_{\odot}$ , the second two digits are equal to the mass of the WD divided by  $0.1 M_{\odot}$ , and the last four digits are equal to the initial orbital period divided by  $0.001 \text{ d}$ .  $[\dot{M}]$  is the time-averaged mass-transfer rate,  $R_1$  the radius of the donor star,  $R_{\text{Roche},1}$  the radius of the donor star roche lobe. RLOF 1 denotes times when  $R_1 \geq R_{\text{Roche},1}$  and, consequently, the donor star experiences Roche lobe overflow.



*Steady accretors:* These systems experience a single episode of mass-transfer until detonation occurs or until the mass-transfer stops as the donor star becomes a WD. One implication of this mode of mass-transfer is that the donor star will still be on the helium main sequence at detonation, if detonation occurs. These systems tend to have relatively low mass-transfer rates ( $\dot{M} \approx 1 \cdot 10^{-8} M_{\odot}/\text{yr}$ ), and hence relatively high He masses at detonation ( $M_{\text{He}} > 0.15 M_{\odot}$ ). Steady accumulation ( $\eta = 1$ ) will lead to fairly predictable outcomes, as is discussed in Sec. 2.3.3. An example of this system type is 05080050. As shown in Fig. 2.4a, mass-transfer starts while the donor star is still on the helium main sequence. It proceeds at a relatively low rate, growing only as a result of angular momentum transport to the accretor until the detonation conditions are met, as shown in Fig. 2.5a, and then the WD detonates.

*Non-steady accretors:* These systems cross the boundary between  $\eta = 1$  and  $\eta = 0$  (see Fig. 2.2) multiple times during their evolution. Since  $\eta = 0$  means that the transferred He is ejected by helium deflagrations, significant amounts of matter can be removed from the system through multiple crossings. The donor mass and the mass-transfer rate decrease in the subsequent evolution. This can lead, in some high-mass-donor systems to otherwise unexpectedly massive helium shells at detonation. Usually, as explained in Sec. 2.3.1, massive donor stars would imply high mass-transfer rates, which then lead to low helium shell masses at detonation (see Sec. 2.2 and Fig. 2.1). Non-steady accretion can occur for any donor mass, but in low-mass donors, it will invariably remove such a large amount of helium from the donor that the helium remaining on the donor afterwards will be insufficient to cause a detonation on the WD. Non-steady accretion occurs exclusively in case BA-systems<sup>1</sup>. Non-steady accretors are therefore a special class among the systems of this study. One such system is 10080035. As shown in Fig. 2.4b, the critical mass-transfer rate for deflagrations is crossed multiple times while the donor star is still proceeding through helium main sequence evolution, each mass ejection widening the orbit and reducing the mass-transfer rate until the rate is low enough for steady accumulation of helium on the accretor. Fig. 2.5b shows that the detonation line is then crossed, and the WD detonates.

*Single deflagration:* These are systems that cross the boundary from  $\eta = 0$  to  $\eta = 1$  exactly once. Systems of this kind invariably cross into the regime of  $0 < \eta < 1$  initially. As in non-steady accretors, mass-transfer from the donor is very efficient, but instead the mass is partially or completely added to the mass of the accretor's CO core. Systems of this type usually exhibit very small helium shell masses at detonation, which are due to the accretor being heated by a deflagration early in its evolution and which makes them prime precursor candidates for ordinary-looking SNe Ia. One such system is 08080055, shown in Fig. 2.4c. Here, initially high mass-transfer rates are continually reduced by the increase of the donor's nuclear timescale following mass loss and angular momentum transfer to the accretor. Eventually the mass-transfer rate decreases sufficiently for steady accumulation of helium to become possible, and the WD detonates.

Single deflagration systems and non-steady accretors enter a phase of continual mass loss by crossing the  $[\dot{M}] > \dot{M}_{\text{WK,max}}$ -boundary as described in Sec. 2.2.

*Biphasic:* Biphasic systems, which occur exclusively in systems with mass ratios close to unity, are characterized by a limited phase of RLOF during the helium main sequence lifetime of the donor where the conditions for detonation are not met. The donor then contracts, ending mass-transfer

<sup>1</sup>In mass-transfer from hydrogen-rich stars, one differentiates between case A and case B mass-transfer. In case A systems, mass-transfer occurs before the end of central hydrogen burning and afterwards in case B systems. In the same vein, case BA systems begin their first mass-transfer phase before the end of central helium burning and case BB systems afterwards.

## 2. Close binary models for SNe Ia explosions

before initiating shell helium burning and expanding rapidly, which results in extremely high mass-transfer rates, eventually reducing the mass-transfer rates sufficiently for detonation to occur. An example of this kind of system is shown in Fig. 2.4d.

### Systems with $M_{\text{WD}} = 0.8 M_{\odot}$

Fig. 2.6a shows the final helium shell masses of CO WDs in systems with  $M_{\text{WD}} = 0.8 M_{\odot}$ . Below  $M_{\text{Donor}} = 0.7 M_{\odot}$ , steady accretion dominates (see Fig. 2.4a for example). The timescale for orbital angular momentum loss decreases as the orbit gets smaller, and the mass-transfer rate increases accordingly. This leads to a lower helium shell mass for a shorter orbital period for a given donor mass. As is seen in Fig. 2.4a, stars with masses of less than  $0.7 M_{\odot}$  expand slightly during their helium main sequence. Longer initial periods therefore mean that the donor fills its Roche lobe when both stellar and Roche-lobe radii are larger, thus only allowing relatively weaker enhancement of the mass-transfer rate due to emission of GWR, in turn leading to larger helium shell masses at detonation.

The decrease in the helium shell mass at the upper period boundary of the detonation parameter space is expected. Longer initial periods mean that RLOF will happen closer to the end of the donor star's main sequence lifetime. Towards the end of the donor's main sequence evolution, mass-transfer is mainly driven by the shorter nuclear timescale of the star, inducing higher mass-transfer rates. This results in smaller He-shell masses at detonation (see Fig. 2.1). The mechanism of this decrease is applicable to all systems in this class.

It is also evident that the mass of the helium shell necessary to detonate a CO WD of a given mass decreases with increasing donor star mass. This is consistent with expectations that the mass-transfer rate becomes higher as the nuclear timescale becomes shorter.

System 10080035 ( $M_{\text{Donor}} = 1.0 M_{\odot}$ ,  $M_{\text{WD}} = 0.8 M_{\odot}$ ,  $P = 0.035$  d) exhibits non-steady accretion (Figs. 2.4b and 2.5b). This system first experiences a high mass-transfer rate, driven by its relatively short timescales of nuclear burning and GWR. The mass ejected from the system is mostly lost via small-scale ejections. With the orbit widening under the influence of mass exchange, the radius of the Roche lobe exceeds the stellar radius and the mass-transfer stops. The donor continues to contract for a while thereafter, but expands again while the Roche lobe continues to contract owing to GWR. Once the star fills its Roche lobe again, depending on the star's current mass, the mass-transfer rate may again exceed  $\dot{M}_{\text{WK,max}}$ , inducing a deflagration and ejecting the helium accumulated on the WD up to that point. This in turn inflates the donor star's Roche lobe and prompts mass-transfer to cease, until the donor fills its Roche lobe once more. Repeated mass ejections lead to the loss of  $0.16 M_{\odot}$  in this system.

The two systems 08080055 and 08080060 are separated from the main body of the detonation zone (08080060 depicted in Fig. 2.4e). This seems to be caused by an interplay between the radius increase of the donor star and the loss of angular momentum via GWR. Systems with longer and shorter periods (namely 08080055 and 08080070, Figs. 2.4f and 2.4g, respectively) either exhibit too high a mass-transfer rate or fail to accumulate sufficient mass in order to initiate a detonation. This shows that He detonation may happen even in parts of the parameter space which is unconnected to the main detonation zone.

This particular grid contains two systems, denoted by filled circles, which became numerically unstable after approaching their detonation line to within 1% of the mass needed for detonation. Most likely these systems would eventually detonate, but we are unable to exactly calculate, within our methodology, the necessary amount of mass. In these cases, the color shading indicates the amount

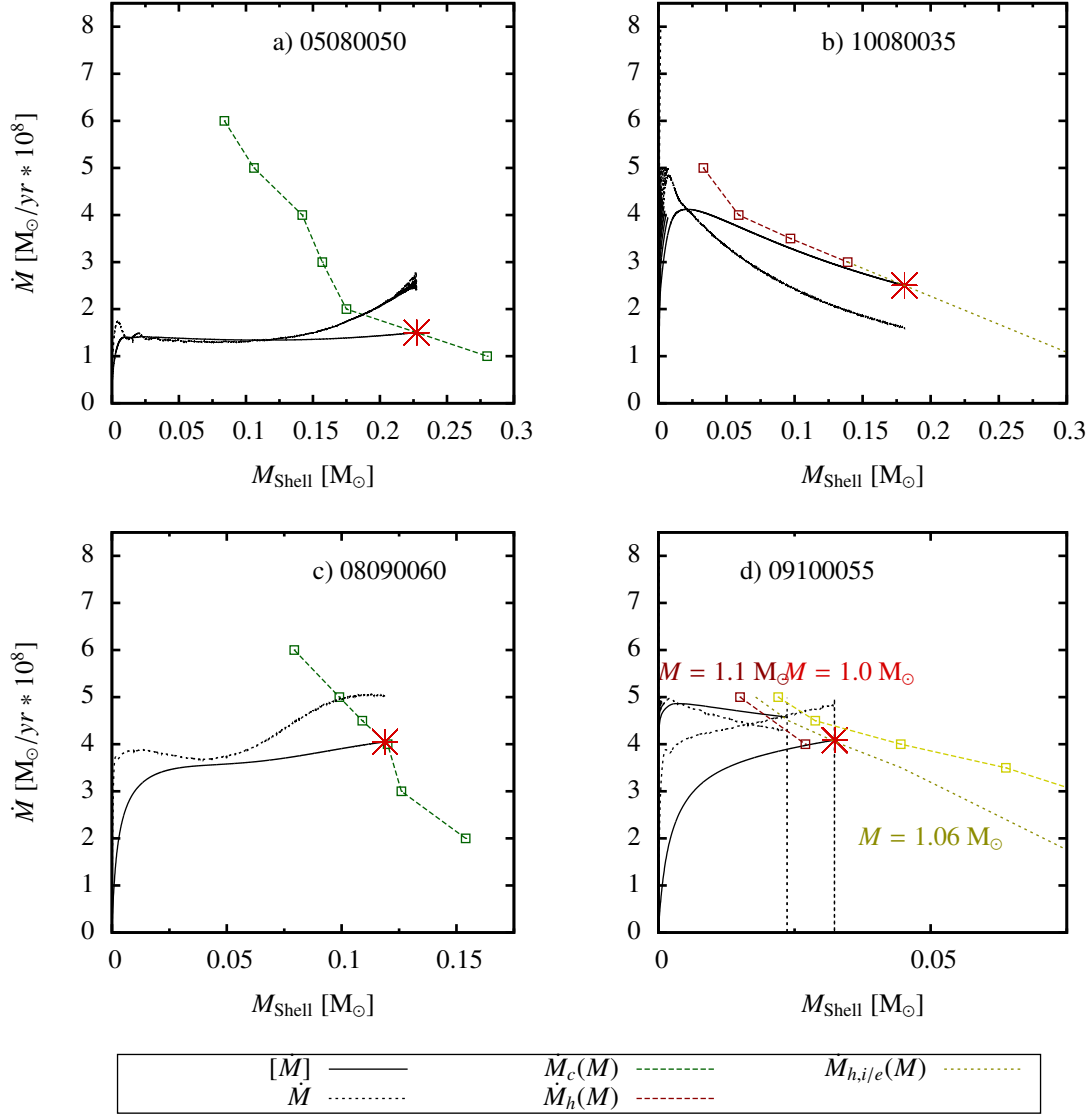


Figure 2.5.: Tracks of selected systems in the  $\dot{M} - M_{\text{Shell}}$  phase space.  $\dot{M}$  is, as before, the mass-transfer rate and  $[M]$  the time-averaged mass-transfer rate.  $\dot{M}_c(M_{\text{Shell}})$  is the detonation line for initially cold models and  $\dot{M}_h(M_{\text{Shell}})$  for initially hot models (see Sec. 2.2). The orange star represents the state of the system at the moment of detonation. The detonation lines shown in plots a) and c) are appropriate for each WD CO core mass at the time of detonation. In systems b) and d), the given detonation lines did not cover the necessary parameter space and had to be extrapolated to lower mass-transfer rates and interpolated with respect to the WD's CO core mass. The resulting inter- and extrapolations are given by  $\dot{M}_{h,i/e}(M_{\text{Shell}})$ . In systems b) and d), mass-transfer crosses into the nova regime, which allows for a change in mass of the CO core. The final WD's CO core mass of system b) is  $0.8 M_{\odot}$ , that of system d) is  $1.059 M_{\odot}$ . As in Fig. 2.4, the labels identify each system by means of their initial parameters.

## 2. Close binary models for SNe Ia explosions

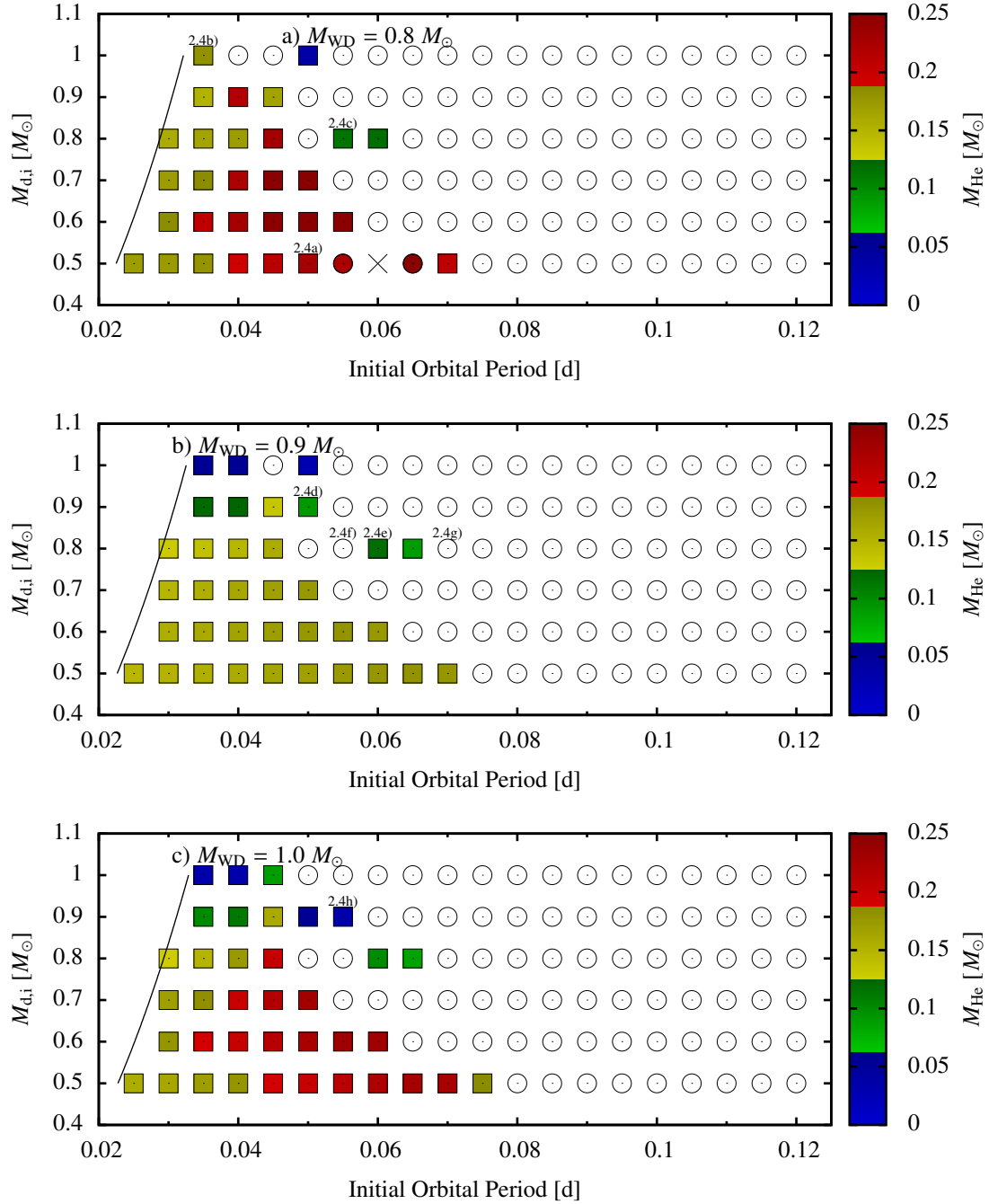


Figure 2.6.: Positions of individual systems in the initial parameter space.  $M_{d,i}$  is the initial mass of the mass losing helium star. Filled squares indicate systems that experience detonations at some point in their evolution, circles systems that do not. Crosses denote numerically unstable systems whose evolution could not be tracked to the point of detonation or to a time when the binary is unable to produce a detonation due to He-depletion in the donor. The color scale (applicable to detonating systems only) indicates the amount of helium present ( $M_{\text{He}}$ ) on the surface of the white dwarf at the time of detonation. Systems located on the black line fill their Roche lobes from the beginning of the simulation. The identity of each system shown in Fig. 2.4 is indicated.

of mass that was accumulated at the point where the model became unstable, with the understanding that the amount of helium present on the WD, were it to detonate, would be slightly larger than indicated.

### Systems with $M_{\text{WD}} = 0.9 M_{\odot}$

Fig. 2.6b shows the final helium shell masses of CO WDs in systems with  $M_{\text{WD}} = 0.9 M_{\odot}$ . As with systems containing WDs of masses of  $0.8 M_{\odot}$ , almost all detonating systems containing donor stars of  $M_{\text{Donor}} \leq 0.9 M_{\odot}$  undergo steady accretion; system 10090040 is of the non-steady type and Systems 09090050 (discussed below) and 10090050 are biphasic.

System 09090050 (see Fig. 2.4d) is an interesting case of biphasic mass-transfer. Case BA mass-transfer occurs initially, but the star contracts in response to high mass loss rates, then expands as a result of core helium depletion, initiating case BB mass-transfer. The initial mass-transfer rate in this second mass-transfer episode is high, but decreases owing to the increase in the orbital separation, induced by mass-transfer to the, then, more massive accretor, which then detonates.

System 10090050 is separated from the rest of the detonating systems. Both of these systems are biphasic, but in 10090045 – owing to the smaller orbital separation at the start of the BB phase – a deflagration is triggered. This leads to a premature ejection of the helium envelope of the white dwarf, inhibiting detonation.

### Systems with $M_{\text{WD}} = 1.0 M_{\odot}$

Fig. 2.6c depicts the final helium shell masses in the systems containing a  $1.0 M_{\odot}$  WD. All of these systems except 0910005, 0910006, 0810006, and 0810007 feature steady case BA accretion. System 0910005 undergoes two distinct phases of mass-transfer and the rest of the mentioned systems are of the single deflagration type. The unexpected (compare to Wang et al. 2013) extension of the detonation zone towards longer initial periods is due to the WD requiring less helium to be accumulated for detonation once it has been heated through accretion at high mass-transfer rates. Other features of this data set are similar to those containing lower mass WDs.

We note that the area of all these parameter spaces where detonation follows a single episode of case BA mass-transfer corresponds well to the contour found by Wang et al. (2013).

### Pre-detonation conditions

Fig. 2.7 shows the final mass of the accumulated helium shell of our models over the initial mass ratio (here defined as  $q = M_1/M_2$ ). Helium shell masses of less than about  $0.14 M_{\odot}$  are realized only at mass ratios higher than  $q = 0.8$ , i.e., there is a marked absence of systems with both small final helium shell mass and small mass ratios, roughly indicated by the hatched area, because lighter WDs require a larger buildup of helium (see Shen & Bildsten 2009; Iben & Tutukov 1991; Woosley & Kasen 2011) and the higher accretion rates from a higher mass donor star will cause stable burning on the WD, lowering the helium threshold for detonation. The apparent bias of longer initial periods towards larger final He-shell masses is mainly due to the fact that only lower mass donors will initiate a detonation at longer periods.

Fig. 2.8 shows the total mass lost by a system as a function of  $q$ . No system with  $q \leq 0.78$  undergoes any appreciable mass loss before detonation because mass donors will, after a short phase of expansion, contract to become a white dwarf.

## 2. Close binary models for SNe Ia explosions

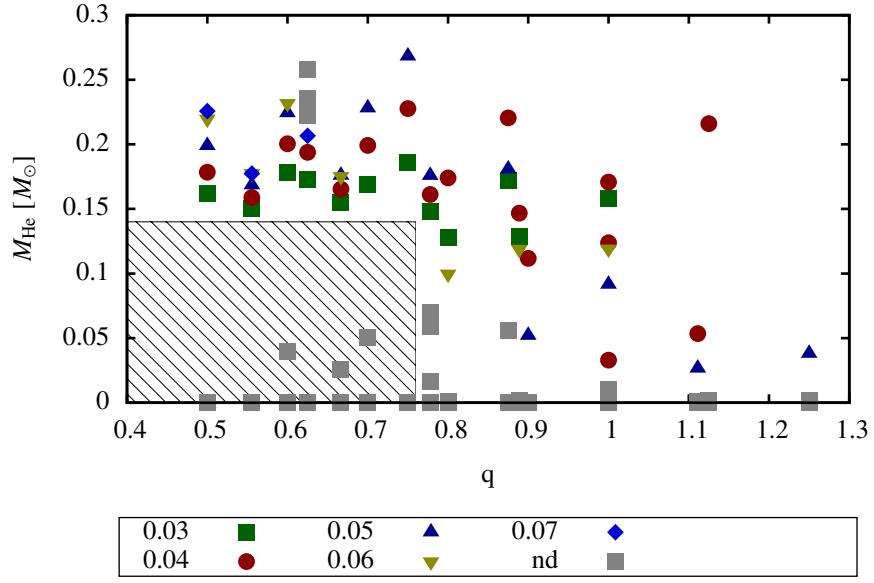


Figure 2.7.: Final He-shell masses of all simulated systems over  $M_1/M_2$ . Gray squares indicate systems that do not experience detonation during their evolution. Colored points indicate systems that do produce a detonation and their initial period. It is evident that detonation seems to be excluded for small values of  $M_1/M_2$  (hatched area). The exclusion is due to the decreasing gradient of the detonation line with decreasing  $\dot{M}$ , while lower mass WDs need to accumulate a larger mass of helium in general.

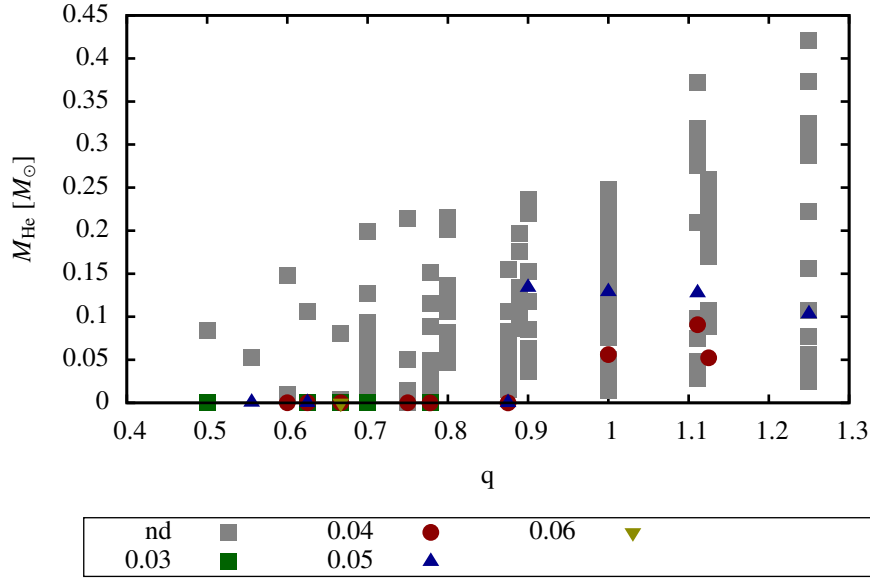


Figure 2.8.: Cumulative mass loss from systems over  $q$ , with systems that experience no mass loss not included. Gray squares indicate systems that experience mass loss but no detonation. Colored systems, with color indicating initial orbital period, do experience detonation. It is immediately evident that systems with low  $q$  only experience significant mass loss if detonation does not occur.

Systems with  $q \geq 0.78$ , however, do lose appreciable amounts of helium before detonation. This is due to higher mass donors transferring mass to the accretor, if RLOF happens during their helium main sequence, at higher mass-transfer rates corresponding to their relatively shorter nuclear timescale. Because the transfer rates are high enough to trigger a nova-cycle, the transferred mass is then lost from the system. With their initial mass reduced, and, consequently, their nuclear timescale increased, expected mass-transfer rates will be lower. This means that these initially more massive donors can still contribute sufficient amounts of helium at sufficiently low mass-transfer rates to lead to detonation.

At this point it should be mentioned that Mulligan & Wheeler (2015) have found evidence for a correlation between SNe Ia and observable circumstellar matter. However, since the mass ejections in our systems generally happen several Myr before detonation, the ejected matter will generally have dispersed sufficiently at the point of detonation to no longer be detectable, though we do not discount the possibility of circumstellar medium being generated by processes which cannot be resolved by our methodology.

### Final helium mass distribution and implications for ordinary SNe Ia

The cumulative probability for detonations involving less than a specified amount of helium based on the grids produced in this study is depicted in Fig. 2.9. It is immediately evident that in our parameter space there is a clear bias toward helium shell masses larger than  $0.15 M_{\odot}$ . This, again, is due to the fact that detonations induced through steady accretion in systems with small mass ratios

## 2. Close binary models for SNe Ia explosions

Table 2.1.: Parameters of hot WDs with accreted helium exhibiting normal type Ia spectra after detonation according to Woosley & Kasen (2011).  $M_{WD}$  is, as before, the mass of the WD’s CO core at the time of detonation and  $M_{He}$  is the mass of the accumulated helium layer.

$M_{WD}$	$M_{He}$
0.8	0.097
0.9	0.055
1.0	0.0445
1.1	0.027

Table 2.2.: Systems exhibiting low enough mass accumulation at detonation for which ordinary SN Ia spectra are expected.

SID	$M_{WD,f}$	$M_{He,f}$	Acc. Type
10090050	1.09484	0.0265	biphasic
09100055	1.09176	0.0324	biphasic
10100040	1.03293	0.0329	non-steady
10100035	1.0334	0.0334	non-steady
10080050	1.03758	0.0380	steady
10090035	0.9518	0.0518	non-steady
10090040	0.95350	0.0535	non-steady

are clearly favored. The median He-shell mass at detonation is found at  $0.171 M_{\odot}$  and the average mass at  $0.163 M_{\odot}$ .

Woosley & Kasen (2011) computed spectra for different WD masses and a range of final helium shell masses. The positions of our models in the stated parameter space is visualized in Fig. 2.10. In Tab. 2.1, we list the systems that satisfy the low He mass condition to produce ordinary SNe Ia. There is a significant bias towards mass ratios of  $q \geq 1$  and initial orbital periods smaller than 0.06 d for the formation of these systems. All of the steady case BA systems accumulate too much helium such that producing an ordinary Type Ia spectrum from an initially cold WD is not likely. Only accretion onto hot WDs, which can be produced by steady case BB mass-transfer or novae, would lead to final helium shell masses consistent with normal SNe Ia spectra. The fraction of these low helium shell systems of all detonating systems is only about 0.1. We conclude that short-period binary systems consisting of a He star and a CO WD in the considered mass range cannot be considered a major channel towards ordinary SNe Ia, but they might contribute significant to the rate of peculiar SNe Ia.

### Properties of donors at detonation

The donor star would be unbound from the binary system once the detonation disrupts the WD. Fig. 2.11 shows the positions of the donor stars in the HR diagram. The stars lie in close proximity to the helium main sequence. Fig. 2.11 also reveals a clear bias for brighter donors to have smaller final orbital velocities, which have been found to lie between  $\sim 300$  km/s and  $\sim 440$  km/s. A similar study was conducted by Wang & Han (2009), though using a different methodology. Owing to the differences in methodology and range of the initial parameters, the results of this study cannot easily



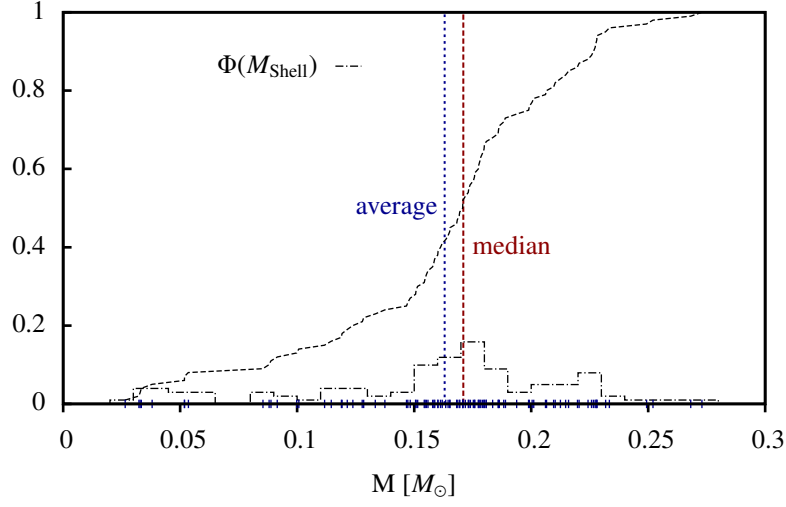


Figure 2.9.: Cumulative probability distribution of accumulated He-shell masses prior to detonation. The probability of a system having a given set of initial parameters at the HeZAMS is assumed to be equal for the entire initial parameter space. The blue ticks at the bottom of the graph show the helium shell mass of all individual data sets. The vertical lines indicate the median and average He-shell masses at detonation.

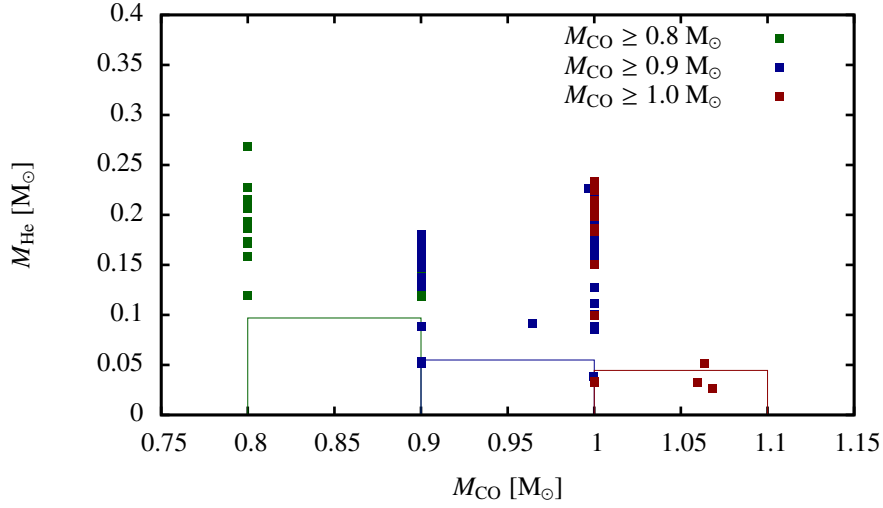


Figure 2.10.: Final He-Shell masses of detonating WDs with respect to their core mass. The colored outlines represent areas in which systems are considered to fulfill the conditions set in Table 2.1 for producing normal SN Ia-like spectra at detonation. Each outline is valid only for dots of the same color.

## 2. Close binary models for SNe Ia explosions

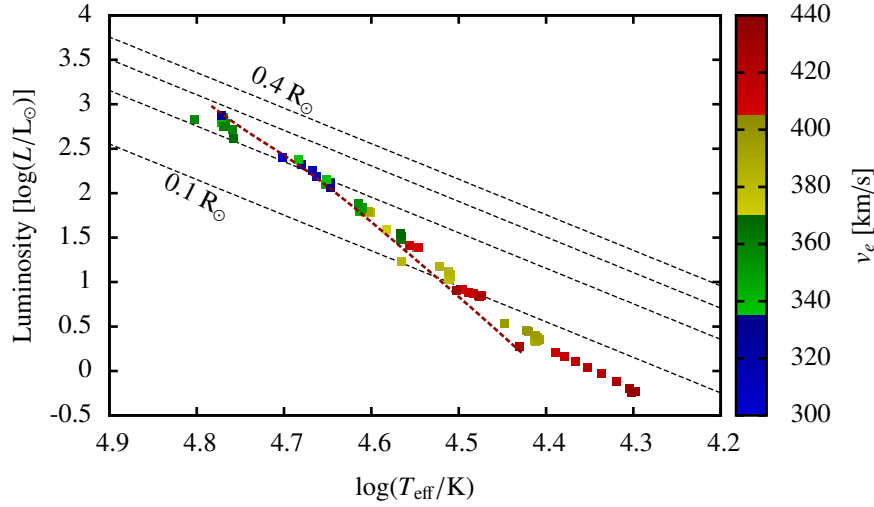


Figure 2.11.: Positions of the donor stars in the HR diagram at the point of detonation of the white dwarf. Color shading indicates the final orbital velocity of the donor. The dashed red line corresponds to the zero age main sequence for helium stars of masses between  $0.325 M_\odot$  and  $1.5 M_\odot$ .

be quantitatively compared with these previous results, but a qualitative comparison of the expected final orbital velocities can be used as a sanity check on both studies. While we can therefore neither confirm nor disprove the distributions calculated in Wang & Han (2009), we can at least confirm that in the relevant portion of the parameter space, the final orbital velocities of the donor star correspond closely to the values found in the present study. It should also be noted that the observed runaway helium star found by Geier et al. (2015) exhibits a galactic rest frame velocity higher than found in our sample. Since that particular runaway star has already left the galactic plane and has therefore lost a significant fraction of its initial velocity, its current state is not explained by these calculations.

Recently, progress on the question of the immediate pre-detonation state of SN Iax progenitors has been achieved with the observation of one such object by McCully et al. (2014), who have confirmed that the progenitor of SN 2012Z was a bright, blue source. The exact nature of this source is still being debated. Data seems to point to either a main sequence (hydrogen) star of  $M \sim 18.5 M_\odot$ , an early stage blue supergiant of  $M \sim 11.0 M_\odot$ , or a late stage blue supergiant of  $M \sim 7.5 M_\odot$ . However, a helium giant of  $M \sim 1.2 M_\odot$  cannot be excluded. Measuring the maximum luminosity at shock breakout, Yamanaka et al. (2015) determined the radius of the source to have been  $\sim 2.0 R_\odot$ . Assuming that the source is indeed a helium star, this radius measurement would indicate an extended envelope. While, at the time of writing, observation supports the notion that the above mentioned source was part of an interacting binary, robust observational confirmation of these data will require the SN itself to have faded. Discounting the possibility of the radius measurement being influenced by the existence of an accretion disc, it is likely that this particular progenitor is unlike the short-period WD+He star binaries studied here and that at least either the detonation mechanism or, if the progenitor is indeed a binary component, the mass-accretion or mass-transfer mechanism must be of a different nature. However, a recent effort Foley et al. (2015) has failed to identify the progenitor of the type Iax supernova SN 2014dt, but has excluded sources that are very similar to the progenitor of SN 2012Z. This indicates

that a variety of progenitor systems may be capable of producing SN Iax events, which, at present, do not seem to exclude WD+He star systems in general and double detonation scenarios in particular.

## 2.4. Conclusions

We conducted an extensive survey of the parameter space of very short-period He-star CO WD systems, varying initial donor mass, WD mass, and initial orbital period. Parameterizing detonation conditions and mass-accretion efficiency according to Woosley & Kasen (2011) and Kato & Hachisu (2004), we found that accumulated helium shell masses in the single degenerate double-detonation scenario are strongly biased toward values larger than  $\approx 0.1 M_{\odot}$ . Using the final helium shell mass as a yardstick as to the likelihood of resulting spectra resembling normal type SNe Ia, we infer that these spectra might be produced by about 10% of the systems in our sample that result in a detonation. With the rest of our sample we only expect peculiar SNe Ia-like events, which, according to Woosley & Kasen (2011), might include SNe Iax.

We conclude that the systems considered in this study are unlikely to account for more than a small fraction of the normal SN Ia rate. The obvious reason for this conclusion is that, if this were the main channel of SN Ia production, a much larger ratio than the reported value of 5-30% of SN Iax to normal SN Ia would be expected to be observed McCully et al. (2014).

We predict that the average WD in our sample will accumulate  $0.163 M_{\odot}$  of non-processed helium before detonating. The apparent absence of systems of this configuration in nature could point towards non-negligible contributions from physical processes not included in this study, such as the effects of rotation and/or magnetic fields, as well as mass-accretion dynamics (i.e., the existence of an accretion disk and non-uniform distribution of the accreted material). Quantitative issues might arise from the sparsity of previous model predictions concerning ignition conditions for a CO WD with respect to its mass, mass-transfer rate, and temperature, as well as the predicted mass retention efficiency. The possibility of helium accretors of the considered mass range being a significant contributor to supernova events exhibiting peculiar spectra merits further investigation, though the marked absence of observed events featuring amounts of helium as large as the ones predicted by this study casts doubt on the assumption of systems of the type considered here being a significant contributor to SNe Iax rates.

Furthermore, the question of how much variation in the spectrum could be expected for slight variations in the WD-mass and temperature would be a promising line of inquiry. Also, significant changes in the predicted outcomes of these systems would be expected depending on the state of the WD at the beginning of interaction with the He-rich companion due to the variation in the accreted helium mass required for detonation depending on the initial temperature of the accretor. In all likelihood, a more detailed understanding of the evolution of a degenerate component in a common-envelope system would be advantageous.



### 3. Helium ignition in rotating magnetized CO white dwarfs leading to fast and faint rather than classical Type Ia supernovae

P. Neunteufel, S.-C. Yoon & N. Langer (A&A 2017, 602, A55)

#### **Abstract:**

*Based mostly on stellar models that do not include rotation, CO white dwarfs that accrete helium at rates of about  $\sim 10^{-8} M_{\odot}/\text{yr}$  have been put forward as candidate progenitors for a number of transient astrophysical phenomena, including Type Ia supernovae and the peculiar and fainter Type Iax supernovae.*

*Here we study the impact of accretion-induced spin-up including the subsequent magnetic field generation, angular momentum transport, and viscous heating on the white dwarf evolution up to the point of helium ignition.*

*We resolve the structure of the helium accreting white dwarf models with a one-dimensional Lagrangian hydrodynamic code, modified to include rotational and magnetic effects, in 315 model sequences adopting different mass-transfer rates ( $10^{-8} - 10^{-7} M_{\odot}/\text{yr}$ ), and initial white dwarf masses ( $0.54 - 1.10 M_{\odot}$ ) and luminosities ( $0.01 - 1 L_{\odot}$ ).*

*We find magnetic angular momentum transport, which leads to quasi-solid-body rotation, profoundly impacts the evolution of the white dwarf models, and the helium ignition conditions. Our rotating lower mass ( $0.54$  and  $0.82 M_{\odot}$ ) models accrete up to 50% more mass up to ignition than the non-rotating case, while it is the opposite for our more massive models. Furthermore, we find that rotation leads to helium ignition densities that are up to ten times smaller, except for the lowest adopted initial white dwarf mass. Ignition densities on the order of  $10^6 \text{ g/cm}^3$  are only found for the lowest accretion rates and for large amounts of accreted helium ( $\gtrsim 0.4 M_{\odot}$ ). However, correspondingly massive donor stars would transfer mass at much higher rates. We therefore expect explosive He-shell burning to mostly occur as deflagrations and at  $\dot{M} > 2 \cdot 10^{-8} M_{\odot}/\text{yr}$ , regardless of white dwarf mass.*

*Our results imply that helium accretion onto CO white dwarfs at the considered rates is unlikely to lead to the explosion of the CO core or to classical Type Ia supernovae, but may instead produce events that belong to the recently identified classes of faint and fast hydrogen-free supernovae.*

#### 3.1. Introduction

For several decades, white dwarfs (WDs) have been considered a key component of the progenitors of a number of astrophysical transient phenomena. These include archetypical Type Ia supernovae (SNe Ia), Type Iax (SNe Iax; see Li et al. 2003; Foley et al. 2013), theoretically predicted subluminal SNe ".Ia" (Bildsten et al. 2007; Kilic et al. 2014), and other "peculiar" transients (Woosley &

### 3. Helium igniton in magnetized CO WDs

Kasen 2011). Owing to the key importance of SNe Ia in particular as a tool for high-redshift distance measurements (Perlmutter et al. 1999; Riess et al. 1998; Schmidt et al. 1998), observationally disentangling these kinds of transients and theoretically understanding the differences between their production mechanisms would have potentially far-reaching consequences.

Even in the light of numerous attempts, to date no direct progenitor of a SN Ia has been unambiguously identified, although a number of non-detections (see Kelly et al. 2014; Nelemans et al. 2008; Maoz & Mannucci 2008; Schaefer & Pagnotta 2012; Li et al. 2011) have considerably limited the available parameter space for candidate systems. Of these, Li et al. (2011), who attempted to identify the progenitor of the SN Ia 2011fe, is of particular interest with respect to the study of He-accreting models as it apparently excludes a large part of the available parameter space for He-donor stars but leaves open the possibility of a low-mass helium giant donor.

Interestingly the picture is somewhat clearer where SNe Iax are concerned. McCully et al. (2014) succeeded in identifying a possible progenitor of SN 2012Z as a luminous blue source, possibly a massive main sequence star or blue supergiant. However, a helium giant of  $\sim 2.0 M_{\odot}$  is not excluded. The ambiguity of the source is manifested in the failed attempt by Foley et al. (2015) to identify the progenitor of SN 2014dt, excluding some of the progenitor parameters found by McCully et al. (2014), thereby hinting at the existence of a variety of SN Iax progenitors.

These findings point to a possible connection between helium accreting WDs as progenitors of SNe Ia and/or Iax. Observed cases have been modeled with some success as deflagrations of near-Chandrasekhar-mass WDs (Magee et al. 2016; Foley et al. 2016; Kromer et al. 2015), while the observed properties of the companion stars imply high mass-transfer rates ( $\dot{M} \gtrsim 10^{-6} M_{\odot}/\text{yr}$ ). This leaves open the question whether systems with lower mass-accretion rates ( $\sim 10^{-8} M_{\odot}/\text{yr}$ ) and less-than near-Chandrasekhar-mass WDs could also be viable progenitors for any of these transients.

Recently, a possible connection between the theoretically predicted SNe Ia and AM Canum-Venaticorum systems (AM CVns) (Warner 1995; Nelemans 2005) was proposed (Shen et al. 2010; Bildsten et al. 2007; Shen & Bildsten 2009) and extensively studied (Shen & Moore 2014), suggesting a continuum of He-accretion-induced transients defined by the nature of the donor star, the system's orbital period and the associated mass-transfer rate.

The idea that the accumulation of material at rates of  $\sim 10^{-8} M_{\odot}/\text{yr}$  from a helium-rich companion on a sub-Chandrasekhar mass carbon-oxygen (CO) WD could lead to an explosive ignition was first seriously explored more than 30 years ago (Taam 1980a,b; Nomoto 1980, 1982b,a). While it was noted that some of these detonation left the CO core of the WD intact, thereby producing a faint supernova, there was a possibility that the detonation of the He-envelope lead to a secondary detonation of the CO core, resulting in the complete disruption of the star (double detonation mechanism). Later one- and multidimensional studies (Livne 1990; Livne & Glasner 1990, 1991; Livne & Arnett 1995; Benz 1997; Livne 1997; Fink et al. 2007, 2010; Sim et al. 2010; Kromer et al. 2010; Woosley & Kasen 2011) established He-accretion as a promising avenue in the search for the progenitors of explosive transients like SNe Ia. However, synthetic spectra (Woosley & Kasen 2011; Woosley & Weaver 1994; Woosley et al. 1986; Sim et al. 2010; Kromer et al. 2010) suggest that lower amounts of He generally lead to a better agreement with the spectra of regular SNe Ia. Studies trying to establish a link between naturally occurring binary systems and their ability to produce either SNe Iax or Ia using the double detonation mechanism were undertaken by Wang et al. (2013) and Neunteufel et al. (2016).

The state of the WD at ignition and the subsequent detonation or deflagration constitutes the crucial link between the progenitor and the resulting transient. The accretion behavior, including the amount

of mass that a WD is able to steadily accrete before He-ignition occurs, has previously been studied for the non-rotating case (Woosley & Kasen 2011, among others) and the rotating case (Yoon & Langer 2004b,a). These studies took into account the effects of a number of rotationally induced instabilities and the concurrent effects of angular momentum transport in differentially rotating stellar interiors. One of the most notable results of these studies was that, especially considering the effects of the dynamical shear instability, chemical mixing was strong and the amount of helium needed to induce ignition with an accretion rate of  $\sim 10^{-8} M_{\odot}/\text{yr}$  was very low when compared to the non-rotating case because of rotational energy dissipation. This indicates that angular momentum dissipation significantly impacts the parameter space for possible progenitor systems.

One mechanism for angular momentum transport, which was not taken into account in the above-mentioned studies of WD accretion, was proposed by Spruit (2002). This mechanism (referred to as the Tayler-Spruit mechanism or dynamo in the following) relies on the Tayler instability (Tayler 1973), and occurs in the radiative parts of differentially rotating stars. Small seed fields may be amplified to a predominantly toroidal magnetic field structure, with the associated magnetic torque leading to angular momentum transport which reduces the shear.

The effects of this mechanism on stellar evolution has been studied for massive stars by Maeder & Meynet (2003) and Heger et al. (2005). The case for low-mass stars was investigated by Maeder & Meynet (2004), and for the Sun by Eggenberger et al. (2005). Apart from having major implications for the evolution of non-degenerate stars, as discussed in these studies, it is concluded that the Tayler-Spruit mechanism tends to induce flat rotational profiles in the radiative zones of stars. It is therefore expected that the Tayler-Spruit mechanism could have a significant impact on the evolution of WDs, which - by their nature - are mostly non-convective. Angular momentum transport as provided by the Tayler-Spruit mechanism indeed appears to be required to understand the slow rotation of isolated neutron stars Heger et al. (2005) and white dwarfs (Suijs et al. 2008), and the spin-down of red giant cores as implied by asteroseismic observations (Mosser et al. 2012).

This present study attempts to further refine our understanding of binary systems in which an accreting WD ignites its He-shell. To do this, we investigate the response of rotating CO WD models to helium accretion, taking into account the effects of the Tayler-Spruit mechanism. Each model is calculated up to the point of ignition of the accumulated helium envelope. We then discuss the impact of variations of initial model parameters on the mass of the helium envelope and densities at ignition and the implications of our results for observations.

This paper is organized as follows. In Sect. 3.2 we describe the computational framework used, the mathematical description of the physics under consideration (Sect. 3.2.1), and the chosen initial models and input parameters (Sect. 3.2.2). In Sect. 3.3 we discuss the results obtained through our computations, first with an emphasis on the structural response of the WD to accretion (Sect. 3.3.1), then with regard to the observational implications of its state at the point of helium ignition (Sect. 3.3.3). We compare rotating models with and without including the Tayler-Spruit mechanism in Sect. 4, and discuss the fates of our simulated model WDs in Sect. 5. In Sect. 3.6 we discuss our findings, putting them into context with previously published works on the subject.

## 3.2. Numerical methods and physical assumptions

### 3.2.1. Numerical methods

The Binary Evolution Code (BEC) is a well-established computational framework capable of performing detailed one-dimensional numerical experiments of single or binary star systems (Langer et al. 2000; Yoon & Langer 2004b). The framework is capable of performing detailed hydrodynamical simulations of rotating and degenerate systems, including mass-accretion (Heger et al. 2000; Heger & Langer 2000).

#### Implementation of the Tayler-Spruit mechanism

Angular momentum transport within a stellar model is assumed to follow a diffusive process (as in Heger et al. 2000; Heger & Langer 2000; Endal & Sofia 1978; Yoon & Langer 2005), defined by a diffusion equation of the form

$$\left(\frac{\partial \omega}{\partial t}\right)_{M_r} = \frac{1}{i} \left(\frac{\partial}{\partial M_r}\right)_t \left[ (4\pi r^2 \rho)^2 \nu_{\text{turb}} \left(\frac{\partial \omega}{\partial M_r}\right)_t \right], \quad (3.1)$$

where  $\omega$  is the local angular velocity,  $t$  time,  $M_r$  the mass coordinate,  $i$  the local specific moment of inertia,  $r$  the radius,  $\rho$  the local density and  $\nu_{\text{turb}}$  the local shear viscosity as defined by the active diffusive processes.

It is possible to accurately compute models of diffusive processes in non-degenerate stars using an explicit initial value approach (see Heger et al. 2000). However, the sensitive dependence of some rotationally induced instabilities on the exact form of the angular velocity profile tends to lead to significant numerical errors in explicit schemes under certain circumstances. The pertinent problem here is encountered in cases of fast angular momentum redistribution occurring on a dynamical timescale, as encountered in studies of the dynamical shear instability. In order to deal with this problem, a non-linear solving routine was implemented by Yoon & Langer (2004b) in order to study the effects of dynamical shears. Further relevant mixing processes included in the framework are the secular shear instability, Goldreich-Schubert-Fricke instability and Eddington-Sweet circulation.

In addition to the dynamical shear instability, the Tayler-Spruit mechanism is capable of acting on dynamical timescales during the secular evolution of an accreting white dwarf. While an explicit treatment of the Tayler-Spruit mechanism, using the prescription by Spruit (2002), was successfully used to study angular momentum transport in massive stars (Heger et al. 2005), the above-mentioned problems regarding numerical stability preclude its use for the purposes of this study. Therefore, a new implicit numerical treatment is required, which was constructed on the basis of the implicit routines for the dynamical shear instability created by Yoon & Langer (2004b). We use essentially the same mathematical prescription as Yoon & Langer (2004b).

Spruit (2002) does not explicitly limit his derivations to non-degenerate matter, which is dealt with in this study through the use of appropriate material descriptions, as explained later in this section. However, the assumption of shellular rotation might not be entirely applicable to white dwarfs (as discussed by Heger et al. 2000; Yoon & Langer 2004b), although the angular momentum distribution of shellular rotation exhibits enough similarities to cylindrical rotation to serve as an adequate approximation.

It is assumed that the ordering of characteristic frequencies is such that

$$\omega_A \ll \omega \ll N, \quad (3.2)$$



### 3.2. Numerical methods and physical assumptions

where  $\omega_A$  is the well-known Alfvén frequency,  $\omega$  is the angular velocity and  $N$  is the Brunt-Väisälä frequency. The Brunt-Väisälä frequency can be decomposed into a chemical buoyancy frequency ( $N_\mu$ ) and a thermal buoyancy frequency ( $N_T$ ) such that

$$N^2 = N_\mu^2 + N_T^2 . \quad (3.3)$$

The prescription assumes a locally stably stratified stellar interior, which translates into the condition that  $N^2 > 0$ .

In order for the dynamo to work, the local angular velocity gradient has to be large enough to overcome the stabilizing effects of the buoyancy forces. This is accomplished by demanding that the dimensionless differential rotation rate  $q = |\frac{\partial \ln \omega}{\partial \ln r}|$  satisfies

$$q > q_{\min} \quad (3.4)$$

with

$$q_{\min} = q_0 + q_1 \quad (3.5)$$

the minimal rotation rate for dynamo action. The minimal rotation rates for the stabilizing effects of the chemical and thermal stratification, respectively  $q_0$  and  $q_1$ , can be written

$$q_0 = \left( \frac{N_\mu}{\omega} \right)^{\frac{7}{4}} \left( \frac{\eta}{r^2 N_\mu} \right)^{\frac{1}{4}} \quad (3.6)$$

and

$$q_1 = \left( \frac{N_T}{\omega} \right)^{\frac{7}{4}} \left( \frac{\eta}{r^2 N_T} \right)^{\frac{1}{4}} \left( \frac{\eta}{\kappa} \right)^{\frac{3}{4}} , \quad (3.7)$$

where  $\eta$  is the magnetic diffusivity and  $\kappa$  the thermal diffusivity.

We compute the magnetic diffusivity using the electrical conductivity according to Nandkumar & Pethick (1984), which has been found to adequately describe the conditions in the non-degenerate and the degenerate parts of the star. The thermal diffusivity is computed taking into account the conditions in degenerate matter (see Yoon & Langer 2004b).

The “effective viscosity”<sup>1</sup> for a predominantly chemically stable medium is given as

$$\nu_{e0} = r^2 \omega q^2 \left( \frac{\omega}{N_\mu} \right)^4 \quad (3.8)$$

and for a predominantly thermally stable medium as

$$\nu_{e1} = r^2 \omega \max \left[ \left( \frac{\omega}{N_T} \right)^{\frac{1}{2}} \left( \frac{\kappa}{r^2 N_T} \right)^{\frac{1}{2}} , q^2 \left( \frac{\omega}{N_T} \right)^4 \right] . \quad (3.9)$$

These expressions are then connected with a patching formula in the form

$$\nu = \frac{\nu_{e0} \nu_{e1}}{\nu_{e0} + \nu_{e1}} f(q) , \quad (3.10)$$

---

<sup>1</sup>According to Eq. 3.8 and Eq. 3.9, the magnitude of the turbulent viscosity may be independent of the shear, hence the term “effective viscosity”.

### 3. Helium igniton in magnetized CO WDs

where  $\nu$  is assumed to represent the effective viscosity for a thermally and chemically stable medium and  $f(q)$  is a term introduced to ensure that  $\nu$  vanishes smoothly as  $q$  approaches  $q_{\min}$ , and is defined as

$$f(q) = \begin{cases} 1 - \frac{q_{\min}}{q} & \text{if } q > q_{\min} \\ 0 & \text{if } q < q_{\min} \end{cases}. \quad (3.11)$$

We note that as  $N_T$  and  $N_\mu$  approach zero independently, indicating that the medium is becoming less stably stratified,  $\nu_{e0}$  and  $\nu_{e1}$  approach infinity. This means that as  $\nu_{e0}$  approaches infinity  $\nu_{e1}$  dominates Eq. 3.10 and vice versa. The thus computed effective viscosity is then summed with those resulting from all other active diffusive processes in  $\nu_{\text{turb}}$  (see Eq. (3.1)). Since the given Tayler-Spruit viscosity is singular in a number of variables, we introduce an artificial upper limit corresponding to the local maximum of the shear viscosity attainable through the dynamical shear instability. The condition reads thus

$$\nu_{\max} = \frac{h_p^2}{\tau_{\text{dyn}}}, \quad (3.12)$$

where  $h_p$  is the local pressure scale height and  $\tau_{\text{dyn}}$  the local dynamical timescale. Since the shortest timescale any diffusive process in a star can act on is the dynamical timescale and the dynamical shear instability acts on this timescale it is a justifiable lower limit for the operating timescale of the Tayler-Spruit mechanism.

The rate of energy dissipation is estimated following Kippenhahn & Thomas (1978) and Mochkovitch & Livio (1989) as

$$\epsilon_{\text{diss}} = \frac{1}{2} \nu_{\text{turb}} \sigma^2, \quad (3.13)$$

where  $\sigma = \frac{\partial \omega}{\omega \partial r}$  is the differential rotation rate (i.e.  $q = |r \cdot \sigma|$ ). The value of  $\nu_{\text{turb}}$  changes on short timescales. For the purposes of the non-linear diffusion solver,  $\epsilon_{\text{diss}}$  is calculated as the time average of the energy dissipation during each evolutionary time step of the entire stellar evolution code.

It should be mentioned at this point that tests on massive star models produced good agreement between the upgraded implicit diffusion solver and the explicit solver used by Heger et al. (2005).

#### Equation of momentum balance

For later reference, we note that BEC implements centrifugal effects via the description provided by Endal & Sofia (1978). The equation of momentum balance is given as

$$\left( \frac{\partial P}{\partial m_p} \right)_t = - \frac{Gr_p^4}{4\pi r_p^4} f_p - \frac{1}{4\pi r_p^2} \left( \frac{\partial^2 r_p}{\partial t^2} \right)_{m_p}, \quad (3.14)$$

where  $P$  is pressure,  $t$  is time,  $r_p$  is radius, and  $m_p$  is mass, the last two as contained within an equipotential surface. The effects of rotation are described by the quantity  $f_p$ , where

$$f_p = \frac{4\pi m_p^4}{Gm_p S_p} \langle g^{-1} \rangle^{-1}, \quad (3.15)$$

with  $S_p$  the area of the closed isobaric surface,  $g$  the absolute of the local effective gravitational acceleration and  $\langle g^{-1} \rangle$  the mean of its inverse. The correcting factor  $f_p$  is obtained iteratively and is consistent with the stellar structure equations (see Endal & Sofia 1976), but limited such that, locally,

Table 3.1.: Physical parameters of the initial white dwarf models:

Initial mass  $M_{\text{WD},i}$ , initial surface luminosity  $L_{s,i}$ , initial core temperature  $T_{c,i}$ , initial core density  $\rho_{c,i}$ , initial radius  $R_{\text{WD},i}$  and initial surface velocity  $v_{\text{rot},i}$

$M_{\text{WD},i}$ $M_{\odot}$	$\log(L_{s,i}/L_{\odot})$	$T_{c,i}$ $10^7 \text{ K}$	$\rho_{c,i}$ $10^6 \text{ g/cm}^3$	$R_{\text{WD},i}$ $R_{\odot}$	$v_{\text{rot},i}$ $\text{km/s}$
0.54	-0.006	0.621	3.33	0.0141	10.0
0.54	-0.998	0.427	3.52	0.0133	10.3
0.54	-2.003	0.176	3.65	0.0126	10.6
0.82	-0.004	0.660	11.4	0.0105	17.1
0.82	-1.024	0.417	11.8	0.0101	9.5
0.82	-1.998	0.168	12.1	0.0098	9.4
1.00	-0.001	0.783	31.7	0.0083	9.4
1.00	-1.000	0.414	32.8	0.0080	9.5
1.00	-1.995	0.155	33.6	0.0078	9.3
1.10	-0.011	0.858	65.5	0.0070	7.4
1.10	-1.017	0.317	68.5	0.0068	7.3

$f_p$  does not decrease if  $v/v_K > 0.6$ . This causes our methodology to generally underestimate effects relating to centrifugal forces wherever the local rotational velocity  $v$  approaches the Keplerian value  $v_K$ , which is defined as

$$v_K = \left( \frac{GM}{r} \right)^{1/2}, \quad (3.16)$$

where all variables are defined in the customary way.

### 3.2.2. Initial models and input parameters

In this study, we use CO WD models of masses  $0.54 M_{\odot}$ ,  $0.82 M_{\odot}$ ,  $1.0 M_{\odot}$  and  $1.1 M_{\odot}$ . These models were created by evolving a helium star of appropriate mass up to the end of the helium main sequence and then artificially removing most of the remaining helium envelope. This results in a WD of about 60% carbon and 40% oxygen (though retaining a small,  $< 0.01 M_{\odot}$ , helium layer for the  $0.82 M_{\odot}$  and  $1.0 M_{\odot}$  models), an effective temperature of about  $2 \cdot 10^5 \text{ K}$ , and a surface luminosity of  $\log(L/L_{\odot}) \approx 2.5$ . The models are then spun up to a surface velocity between 7 km/s and 20 km/s, which is in agreement with measurements of the rotational velocities of isolated white dwarfs (see Heber et al. 1997; Koester et al. 1998; Kawaler 2003; Suijs et al. 2008; Mosser et al. 2012), and then allowed to cool to surface luminosities of about  $\log(L/L_{\odot}) = 0, -1, -2$  (see Table 3.1). It is not immediately obvious whether these values are adequate. Since any He star+CO WD system will be a product of one common envelope event (or possibly two), the thermal history of the WD will be different from those usually obtained for isolated WDs (e.g., Renedo et al. 2010b). However, since the details of common envelope evolution are currently far from being completely understood (see Ivanova et al. 2013), the exact disposition of a WD at the onset of mass-accretion is subject to some uncertainty. Enlarging the parameter space to include the most likely initial luminosities is one way to address this problem. We note that the discrepancies in initial rotational velocities are expected to have negligible impact on the final result. Since the accreted material efficiently spins up the WD,

### 3. Helium igniton in magnetized CO WDs

surface velocities will reach values up to three magnitudes higher than the initial one long before any helium burning is expected to set in. For the purposes of this study, rotational velocities of the magnitude presented in Table 3.1 can be thought of as negligible. This is clarified in Sect. 3.3. In addition, non-rotating models are computed for comparison.

White dwarfs in binary systems are expected to accrete mass through a Keplerian accretion disk. The material falling onto the WD is therefore expected to move with a velocity close to the Keplerian value at the point of impact (Paczynski 1991; Popham & Narayan 1991), carrying a specific angular momentum of  $j_{\text{kepler}}$ . Within the context of the BEC framework, the amount of specific angular momentum ( $j_{\text{acc}}$ ) carried by accreted matter is manually controlled by the choice of  $f_{\text{acc}}$  in the expression  $j_{\text{acc}} = f_{\text{acc}} \cdot j_{\text{kepler}}$ . The choice of  $f_{\text{acc}} = 1.0$  is the most natural one. In order to investigate conditions deviating from this assumption, we also include systems calculated with  $f_{\text{acc}} = 0.6$  and  $f_{\text{acc}} = 0.3$ .

If the star is rotating critically, we avoid supercritical rotation by assuming that no further angular momentum is accumulated, the excess momentum being dissipated in the accretion disk. This is accomplished by setting  $f_{\text{acc}} = 0$  if further accretion would lead to supercritical rotation.

The accretion rates chosen in this study range between  $1 \cdot 10^{-8} \text{ M}_{\odot}/\text{yr}$  and  $1 \cdot 10^{-7} \text{ M}_{\odot}/\text{yr}$ , which are commensurate with average mass-transfer rates achievable in a short-period He star+CO WD system with the He star ( $M \leq 1.0 \text{ M}_{\odot}$ ) undergoing He main sequence evolution. Consequently, the accreting material is assumed to consist of helium with an admixture of hydrogen-burning products corresponding to solar metallicity. At accretion rates higher than  $1 \cdot 10^{-7} \text{ M}_{\odot}/\text{yr}$  the WD is expected to undergo a series of nova outbursts with individual ejecta masses that are comparatively low (Kato & Hachisu 2004; Piersanti et al. 2015). This mechanism is expected to have a profound impact on the outcome of the evolution of He star+CO WD systems (Neunteufel et al. 2016), but the nova cycle and the evolution of complete systems are both beyond the intended scope of this work. For studies of the regime of accretion rates  $\dot{M} \geq 3 \cdot 10^{-6} \text{ M}_{\odot}/\text{yr}$  the reader is referred to Yoon & Langer (2003) and more recently Brooks et al. (2016). In this regime, a period of steady burning and/or shell flashes potentially leads to a helium shell detonation, with the expectation of a detonation of the CO core of the WD.

#### 3.2.3. Ignition conditions

All models are computed up to the point of unstable He-ignition, which we define as the point where the helium burning timescale  $\tau_{\text{nuc,He}}$  approaches the dynamical timescale of the star (i.e.  $\tau_{\text{nuc,He}} \approx \tau_{\text{dyn}}$ ). Owing to our methodology, we are unable to follow the ignition through to the final outcome of the process (i.e. detonation or deflagration). It is therefore necessary to apply some quantitative criteria in order to distinguish one outcome from the other. Possible criteria to distinguish detonations from deflagrations have been previously proposed by Woosley & Weaver (1994) and Woosley & Kasen (2011). Both of these criteria use the density at the point of ignition as a measure to determine whether the ignition would subsequently develop into a (supersonic) detonation or a (subsonic) deflagration. The defining factor in both cases is whether the density at the point of ignition is sufficient to preclude the premature quenching of the thermonuclear runaway through thermally induced expansion. Woosley & Kasen (2011) introduce a critical density dependent on the ignition temperature. Woosley & Weaver (1994) set the critical density to a constant value of  $\rho_{\text{crit}} = 1 \cdot 10^6 \text{ g/cm}^3$  while Woosley & Kasen (2011) give

$$\rho_{6,\text{crit}} \gtrsim \left( \frac{0.0607}{T_8^2} \exp\left(\frac{20}{T_8}\right) \right)^{\frac{1}{2.3}}. \quad (3.17)$$

However, as stated by Woosley & Kasen (2011), the given function is an approximation which fails to properly identify detonating systems of the same study. The lowest predicted ignition density of all of the detonating systems in the above-mentioned study is  $\rho_{\text{ign}} \simeq 6.8 \cdot 10^5 \text{ g/cm}^3$  with most ignition densities exceeding  $\rho_{\text{crit}} = 1 \cdot 10^6 \text{ g/cm}^3$ . We therefore assume that the choice of a constant critical ignition density of  $\rho_{\text{crit}} = 1 \cdot 10^6 \text{ g/cm}^3$  as put forward by Woosley & Weaver (1994) is justified for the purposes of this study.

### 3.3. Results

In this section, we discuss the results obtained from our simulations. A selection of defining parameters of the systems under consideration (though limited to systems with  $f_{\text{acc}} = 1.0$  for the sake of brevity) at the point of He-ignition are presented in Table 3.3. For the sake of clarity, it should be mentioned that in the following section, “rotating” always refers to models in the context of this study, i.e. rotating models with an active Tayler-Spruit dynamo, dynamical shear instability, Eddington-Sweet circulation and secular shear instability and “non-rotating” refers to non-rotating models with no angular momentum diffusion. Rotating models as defined here are explicitly compared with non-magnetic rotating models (i.e. rotating models without an active Tayler-Spruit dynamo) in Sect. 3.4.

#### 3.3.1. Rotational profile

White dwarfs tend to be convectively stable throughout their interiors. Accordingly, the Tayler-Spruit mechanism will work on the entirety of their structures. When compared to dynamical shears, the strength of their associated shear viscosities is of the same magnitude for a given condition, but the critical rotational velocity gradient required to initiate the Tayler-Spruit mechanism (Eq. 3.5) is usually much smaller. Without angular momentum accretion, the dynamo will remain active until the velocity gradient is decreased to that of the threshold gradient.

Fig. 3.1A shows the radial velocity profile of model sequence Lm20510-5<sup>2</sup>. As can be seen, any residual differential rotation present at the beginning of mass-accretion (line i in Fig. 3.1A) is damped by the Tayler-Spruit mechanism until a situation close to solid-body rotation is attained (line m). A very small radial velocity gradient remains, but is barely noticeable in the plot. Line f in Fig. 3.1A shows the profile just after ( $\ll 1$  s) He-ignition. With the onset of rapid expansion, conservation of angular momentum in the expanding layers leads to the reemergence of an angular velocity gradient. The situation is similar for more massive WDs, as shown in Fig. 3.1B.

We note that there is no significant change in the rotational profile even as it passes areas with significant gradient in the chemical composition. Such a change might be expected due to the dependence of the effective viscosity on the chemical stratification (see Eq. 3.6).

Figure 3.2 shows the surface velocity of four representative model sequences at two different initial luminosities of  $\log L_{\text{init}}/L_{\odot} = 0$  and  $\log L_{\text{init}}/L_{\odot} = -2$  (L00510-5, Lm20510-5A and L01010-5, Lm21010-5B) in units of  $\omega_{\text{surf}}/\omega_{\text{crit}}$  ( $\omega_{\text{crit}}$  being the critical surface velocity) with respect to time. Less massive WDs spin up faster than more massive ones (See Fig. 3.2) due to their relatively smaller rotational inertia. The fact that the models with  $M_{\text{init}} = 0.54 M_{\odot}$  never quite reach  $\omega_{\text{crit}}$  is related to

<sup>2</sup>The model number is composed as follows: The first digit indicates the value of the initial luminosity, if preceded by the letter “m”, that value should be understood to be negative. The second and third digit is equal to ten times the value of the the initial mass rounded to the next  $0.1 M_{\odot}$ . The fourth and fifth digit are equal to the value of ten times the chosen value for  $f$ . The hyphenated number is equal to the value of the chosen mass-accretion rate divided by  $10^{-8}$ .

### 3. Helium ignition in magnetized CO WDs

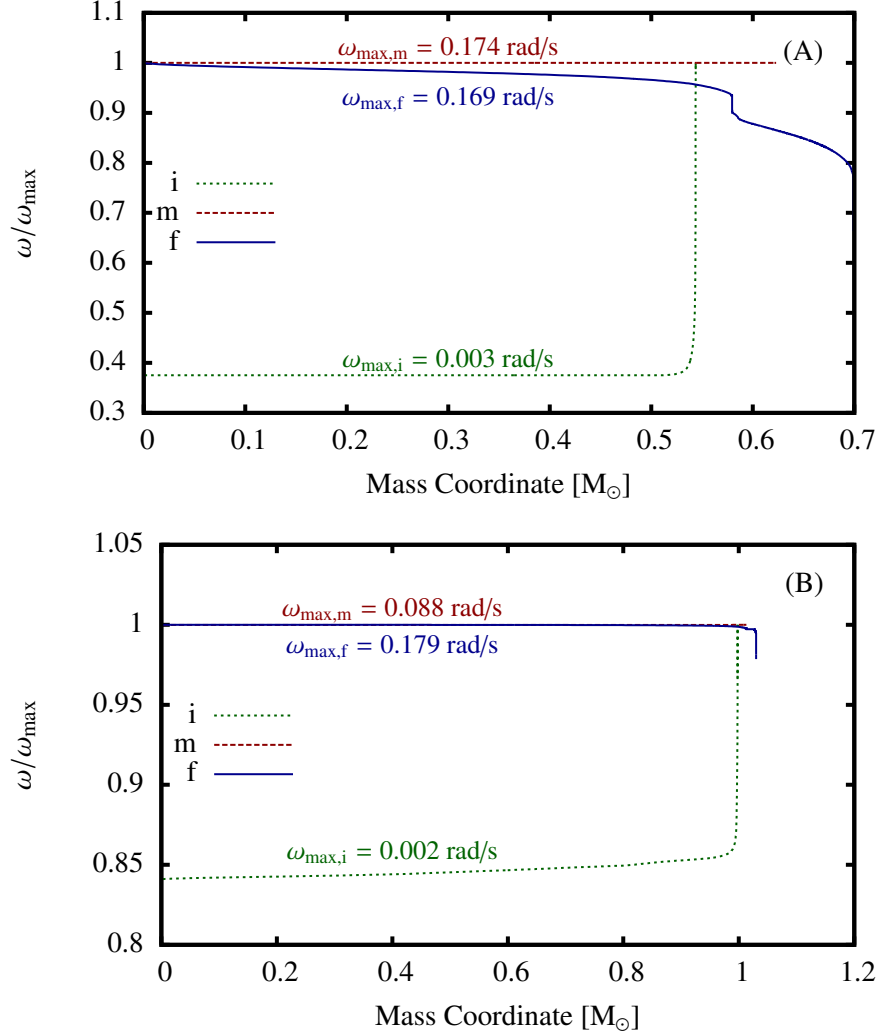


Figure 3.1.: Rotational velocity profile of model sequence Lm20510-5 ( $M_{\text{init}} = 0.54 M_{\odot}$ ) (A) and Lm21010-5 ( $M_{\text{init}} = 1.0 M_{\odot}$ ) (B) at three different times during its evolution ( $f_{\text{acc}} = 1.0$ ,  $\dot{M} = 5 \cdot 10^{-8} M_{\odot}/\text{yr}$  and  $\log(L_{\text{init}}/L_{\odot}) = -2$  in both cases). Line i corresponds to  $t = 0 \text{ yr}$ , the start of mass-accretion, m to the midpoint of the accretion phase and f to just after the point of He-ignition. In subfigure (A) this corresponds to m at  $t \sim 1.55 \text{ Myr}$  and f at  $t = 3.11 \text{ Myr}$ . In subfigure (B) the corresponding times are m at  $t \sim 0.3 \text{ Myr}$  and f at  $t = 0.64 \text{ Myr}$ . The y-axis is normalized to unity with the maximum value of each graph indicated in  $\omega_{\max}$ .

the treatment of supercritical accretion as explained in Sect. 3.2. The prescription calls for  $f_{\text{acc}} = 0$  if further accretion leads to supercritical rotation, which means that critical rotation itself can never actually be reached.

Figure 3.2 also shows that the fraction of the critical rotational velocity achievable by a WD strongly depends on the initial mass of each model. The reasons for this, while somewhat obvious, as well as the implications of this behavior are discussed in greater detail in Sect. 3.3.3. It should be noted, though, that none of our model sequences of  $M_{\text{init}} > 0.82 M_{\odot}$  reach critical rotation before He-ignition, which affects the mass-dependency of final He-shell masses, as is discussed in Sect. 3.3.3.

### 3.3.2. Chemical profile

Figure 3.3 shows the chemical development of two representative model sequences, Lm20510-5 and Lm21010-5. As can be seen, there is noticeable chemical mixing at the boundary layer of the less massive system (Fig. 3.3 A), while the more massive system (Fig. 3.3 B) shows barely any mixing at the boundary layer. Rotationally induced mixing has been found to be much more pronounced in non-magnetic rotating models (Yoon & Langer 2004a). With the Tayler-Spruit mechanism suppressing the overwhelming majority of any initially present angular velocity gradient, the only region where appreciable chemical mixing can plausibly take place is the outermost layer of the envelope where an angular velocity gradient is maintained by the continuous accumulation of rotating matter. With growing envelope mass, the area exhibiting the largest angular velocity gradient moves away from the initial surface mass coordinate. This means that with growing envelope mass, chemical mixing at the core-envelope interface gradually diminishes. The differences in the mixing behavior between the two presented model sequences are due to a difference in initial chemical profiles.

We therefore conclude that chemical mixing in these systems is fundamentally weak, but highly dependent on the initial chemical profile. The presence of a preexisting He-envelope considerably weakens the magnitude of expected chemical diffusion.

The expectation of an adequately well-defined interface between the original core and the accumulated material throughout the evolution of our WD models leads us to refer to this interface as the “core-envelope interface” from this point on.

### 3.3.3. Accretion behavior and ignition

Figures 3.4 and 3.5 show the evolution of representative model sequences in the  $\rho$ - $T$ -plane. The model sequence in Fig. 3.4A depicts model sequence Lm10510-5, which means that  $M_{\text{init}} = 0.54 M_{\odot}$ ,  $\log L_{\text{init}}/L_{\odot} = -1$  and  $f_{\text{acc}} = 1.0$ . Figure 3.4B is the same but non-rotating. The initial profile is as at the beginning of the mass-accretion phase, and the final profile is just before ( $\leq 1$  s) He-ignition as defined in Sect. 3.2. It should be noted, however, that the rotating model accumulated a significantly larger amount ( $0.05 M_{\odot}$ ) of helium at the point of detonation. This is a consequence of solid-body rotation. Helium ignition requires both sufficiently high temperatures and sufficiently high densities, the threshold temperature being a function of local density. In the rotating non-magnetic case, the WD would, at the point of He-ignition, show significant differential rotation, introducing a much larger amount of energy dissipation (Eq. 3.13) into the uppermost layers of the He-envelope, thereby providing the necessary temperature to facilitate He-ignition after a much smaller amount of helium has been accumulated (see Yoon & Langer 2004b). The Tayler-Spruit mechanism is active at much

### 3. Helium ignition in magnetized CO WDs

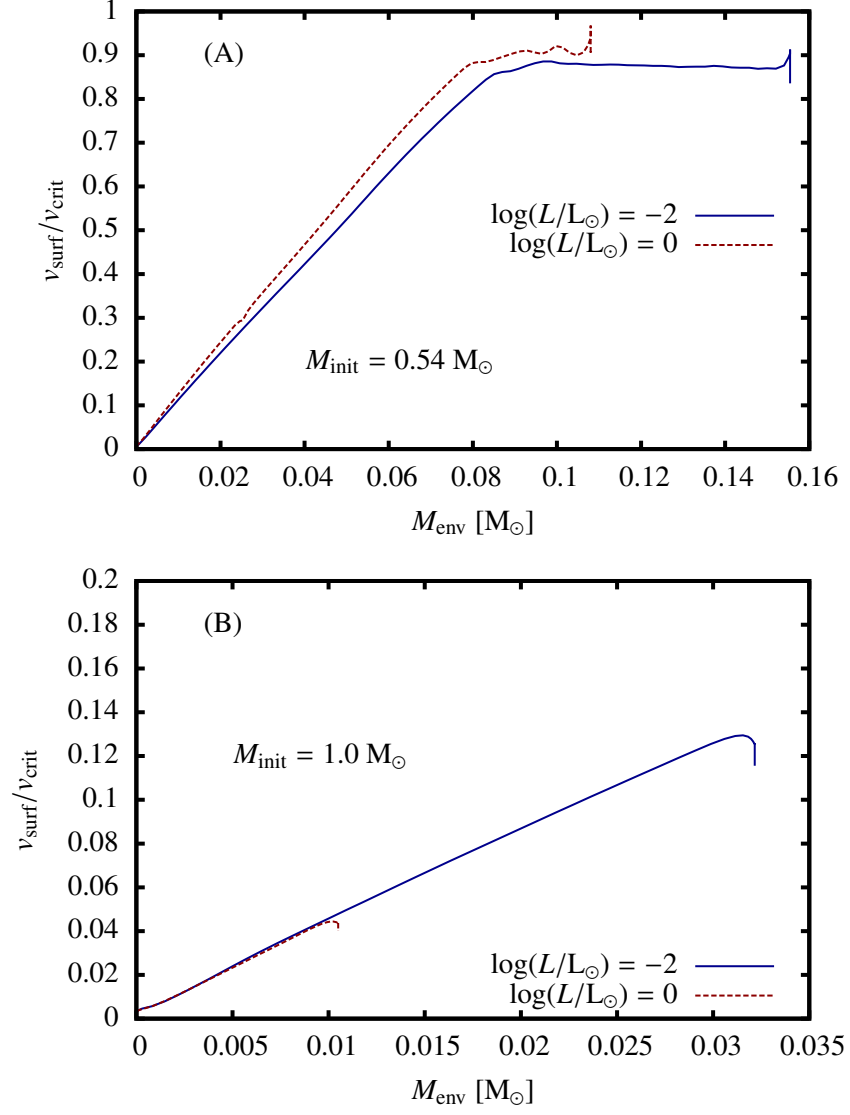


Figure 3.2.: Evolution of the surface velocities of model sequences L00510-5, Lm20510-5 (A) and L01010-5, Lm21010-5 (B). All model sequences are computed up to He-ignition. The y-axis is normalized to the critical rotational velocity.  $M_{\text{env}}$  is the mass of the helium envelope and corresponds to the amount of helium accreted. All models were computed with  $\dot{M} = 5 \cdot 10^{-8} M_{\odot}/\text{yr}$  and  $f_{\text{acc}} = 1.0$ .



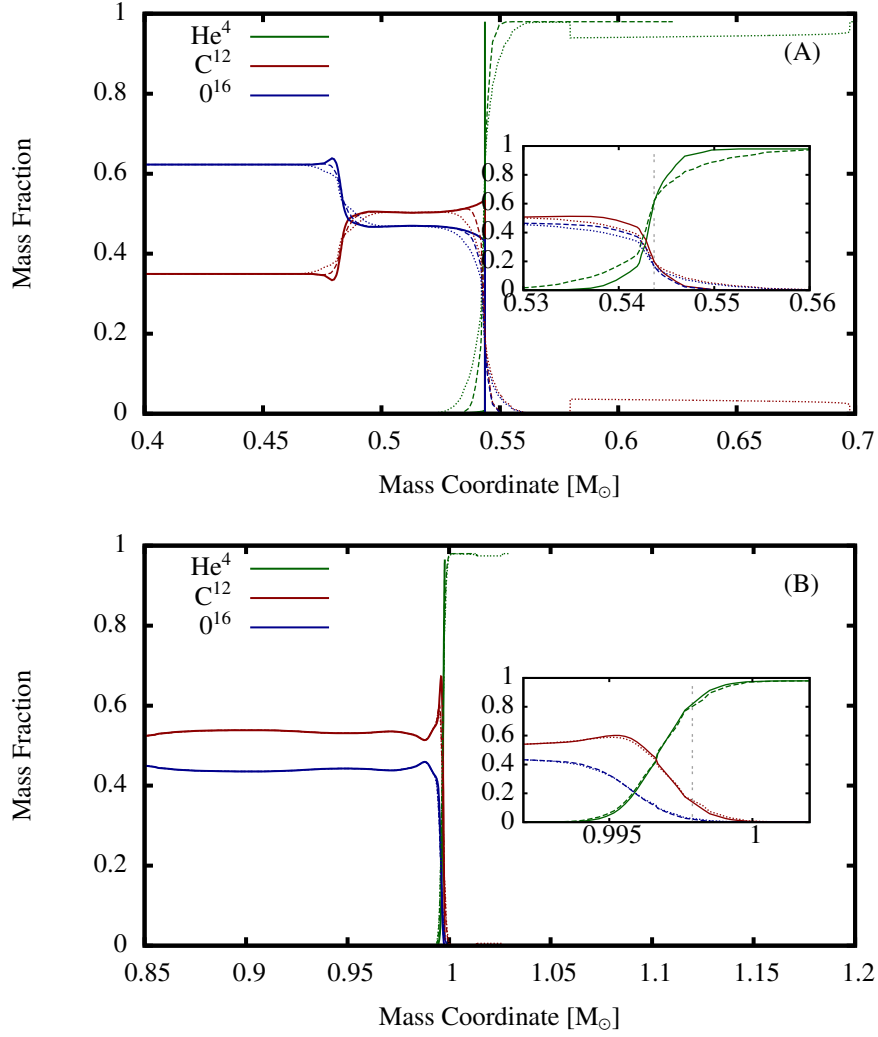


Figure 3.3.: Chemical profile of model sequence Lm20510-5 ( $M_{\text{init}} = 0.54 M_{\odot}$ ) (A) and Lm21010-5 ( $M_{\text{init}} = 1.0 M_{\odot}$ ) (B). The remaining initial parameters are the same for both model sequences:  $f_{\text{acc}} = 1.0$ ,  $\dot{M} = 5 \cdot 10^{-8} M_{\odot}/\text{yr}$  and  $\log(L_{\text{init}}/L_{\odot}) = -2$ . Included are the three most abundant isotopes  $\text{He}^4$ ,  $\text{C}^{12}$  and  $\text{O}^{16}$  in units of relative mass per shell over the shell's mass coordinate. Solid lines represent the profile at the time of the start of mass-accretion at  $t = 0$  yr, dashed lines at the midpoint of the accretion phase at  $t \sim 1.55$  Myr (A) and  $t \sim 0.3$  Myr (B), dotted lines just after the point of He-ignition at  $t = 3.11$  Myr (A) and  $t = 0.64$  Myr (B). The inset is a zoom of the area of the initial envelope-core interface (the interface is shown as a dashed gray line), where the initial profile has been omitted for the sake of clarity.

### 3. Helium ignition in magnetized CO WDs

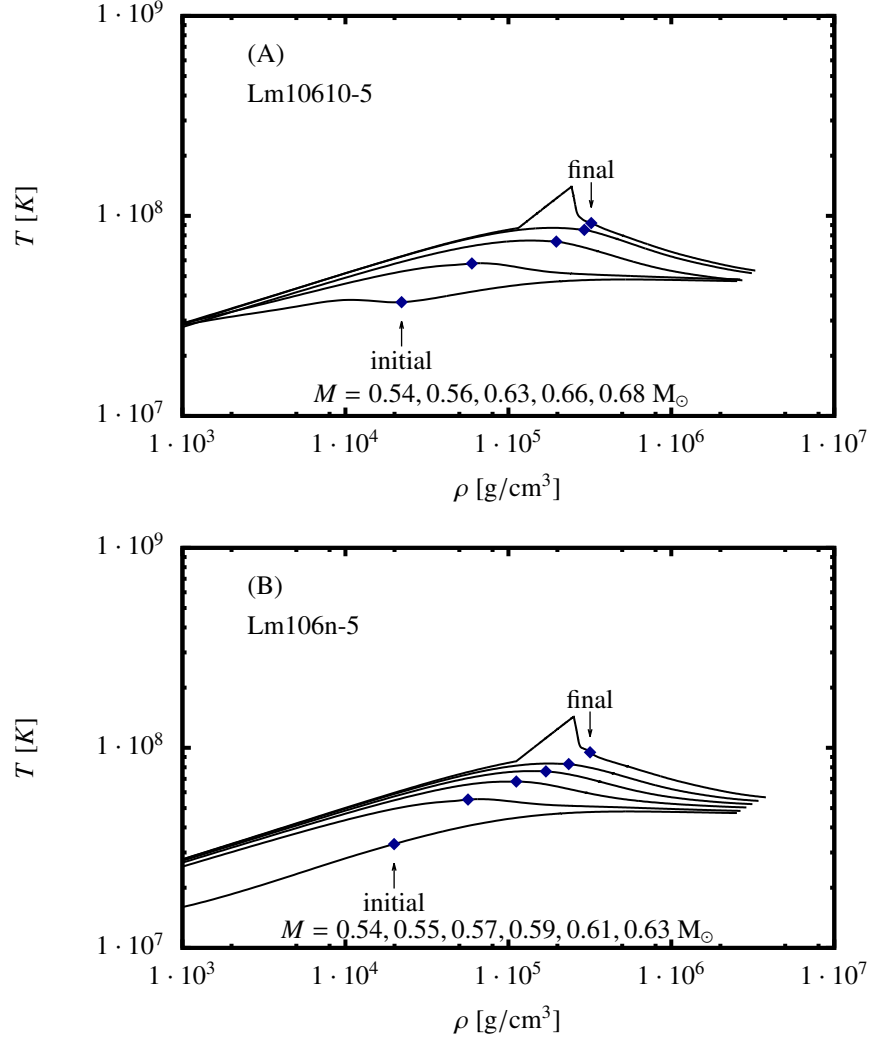


Figure 3.4.: Evolution of the temperature-density profile of a rotating (A) and non-rotating (B) WD with  $0.54 M_{\odot}$  accretion rate is  $5 \cdot 10^{-8} M_{\odot}/\text{yr}$ ,  $f_{\text{acc}} = 1.0$  and  $\log(L_{\text{init}}/L_{\odot}) = -1$ . Blue dots indicate the core-envelope interface. Initial (at the beginning of mass-accretion) and final (at the point of helium ignition) profiles are indicated. The given masses (left to right) correspond to the presented profiles (initial to final). We note that the profiles marked as "initial" are not the first models in their evolutionary sequence, having been evolved for about one kyr each.

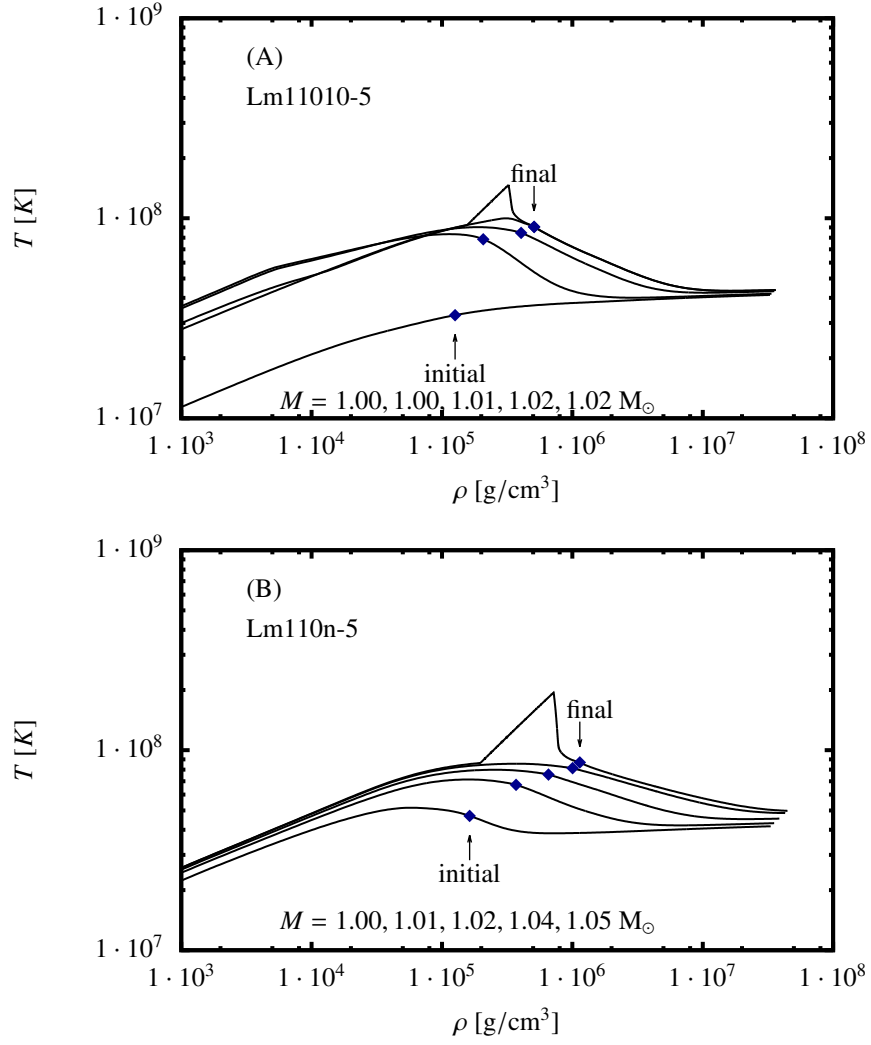


Figure 3.5.: Evolution of the temperature-density profile of a rotating (A) and non-rotating (B) WD with  $1.0 M_{\odot}$ . All other parameters and labels as in Fig. 3.4.

### 3. Helium igniton in magnetized CO WDs

smaller rotational velocity gradients than, for example, the dynamical shear instability under the conditions encountered in the present model sequences. This means that, as described in Sect. 3.3.1, a small rotational velocity gradient is induced which extends throughout the stellar envelope (i.e., a small, non-localized gradient). The energy dissipation caused by the Tayler-Spruit mechanism is correspondingly small (locally, practically  $\epsilon_{\text{diss}} \approx 0$ ). This means that a temperature increase resulting from energy dissipation due to the Tayler-Spruit mechanism will be smaller, but will affect a wider area when compared to that expected from, for example, the dynamical shear instability. Therefore, in order to increase the temperature of the stellar material at any given point sufficiently to induce He-ignition, a larger amount of angular momentum, and thus helium, has to be accumulated than in the rotating non-magnetic case. Furthermore, since the WD is rotating critically (see Fig. 3.2 A, this model sequence falls between the two depicted ones), the centrifugal force serves to decrease the local density of the stellar matter at any given coordinate compared to the non-rotating case, in turn increasing the temperature required for He-ignition. We therefore expect a significant increase in the required amount of material to be accreted before ignition. It should be noted at this point that the evolution of the rotational profile is the dominant factor in this prediction. This becomes evident when comparing the depicted model sequences with models computed with a variation of values of the  $f_{\text{acc}}$ -parameter. We find that when  $M_{\text{init}}$  is held constant at  $0.54 M_{\odot}$ , at high accretion rates, the final accumulated amount of helium decreases with increasing  $f_{\text{acc}}$  (see Fig. 3.7). Exceptions to this exist at low accretion rates. These exceptions are discussed in detail in Sect. 3.3.4.

Figure 3.5 is the same as Fig. 3.4, but the model sequence's initial mass is  $M_{\text{init}} = 1.00 M_{\odot}$ . Contrary to the less massive example, the effects of rotation lead to a decrease in the required mass to be accreted in order to initiate He-ignition. Partially this is a consequence of the physical differences in WDs of different mass at the onset of mass-accretion (see Table 3.1). Smaller size at a higher mass makes newly deposited material move at much higher angular velocity for a given value of  $f_{\text{acc}}$ . This leads to larger amounts of dissipational energy being introduced in the system. This combined with the compressional heating incurred by the accumulating material falling onto the WD with a significantly higher surface gravity than in less massive cases, leads to a much faster increase in temperature in the outer layers of the WD (compare Figs. 3.4A and 3.5A).

Rotational inertia of white dwarfs increases with increasing mass (see, e.g., Piersanti et al. 2003). The higher the rotational inertia of a solidly or quasi-solidly rotating object, the smaller the increase in rotational velocity incurred through accretion of a given amount of rotational momentum. This leads to He-ignition occurring before the WD has a chance to achieve critical or near-critical rotation (see Fig. 3.2), in turn leading to much diminished centrifugal effects compared to the case of lower masses.

In both of the cases presented above, it is useful to comment on the NCO reaction. The effects of the NCO reaction on accretion scenarios have been investigated before (e.g., Woosley & Weaver 1994; Hashimoto et al. 1986). The consensus is that the reaction is largely, but not completely (Hashimoto et al. 1986), independent of temperature, the dominant factors in a CO WD being a sufficiently high local abundance of nitrogen and a local density of more than  $10^6 \text{ g/cm}^3$ . In the present scenario, in the absence of strong chemical mixing (Sect. 3.3.2), the effect of increased energy generation due to the NCO reaction would be most important at the core-envelope interface. In both the rotating and non-rotating model sequences with  $M_{\text{init}} = 0.54 M_{\odot}$ , the interface never reaches densities high enough to facilitate the NCO reaction. In the heavier model sequences, only the non-rotating WD exhibits high enough densities at the interface, leading to an acceleration of the temperature increase due to the NCO reaction in the overlying layers and therefore earlier He-ignition than if the NCO reaction were

neglected. In our model sequences the NCO-reaction plays a limited role insofar as it provides some additional heat in models with low initial luminosities. It only leads to a slightly reduced final helium envelope mass and to the igniting layer being located somewhat lower in the star. The majority of the heat is still introduced through the accretion process itself. In models with higher initial luminosities, the role of the NCO-reaction is eclipsed by the residual heat of the WD.

The answer to the question whether rotating magnetic WDs accumulate more massive He-envelopes at He-ignition than non-rotating ones therefore depends strongly on whether the WD can achieve near-critical rotation before He-ignition, and therefore on the initial and on the efficiency of angular momentum accumulation.

Fig. 3.6 shows the time evolution of the location of the maximum temperature in the star ( $T_{\max}$ ) of several representative model sequences at different initial masses ( $0.54 M_{\odot}$ ,  $0.82 M_{\odot}$  and  $1.0 M_{\odot}$ ) with two initial luminosities of  $\log(L_{\text{init}}/L_{\odot}) = 0$  and  $\log(L_{\text{init}}/L_{\odot}) = -2$ , calculated with  $f_{\text{acc}} = 1.0$ .

Since the initial temperature of WDs of the same mass is, across the entire interior, significantly higher at higher initial luminosities, the tendency of  $M(T_{\max})$  to stay at lower values in models with higher initial luminosities is expected. If the core temperature is higher, a larger amount of thermal energy has to be introduced into the star in order to move  $M(T_{\max})$  towards the surface, albeit aided by extant heat in the core.

It is easily seen that the mass coordinate of He-ignition strongly depends on the initial luminosity of the WD. Higher initial luminosities cause the point of ignition to lie closer to the core-envelope interface (the presented model sequences at  $\log(L_{\text{init}}/L_{\odot}) = 0$  feature ignition coordinates not significantly above the core-envelope interface). As additional heat is introduced close to the WD's surface,  $M(T_{\max})$  moves towards the surface, but higher initial luminosities imply a higher core temperature, causing the  $M(T_{\max})$  to remain closer to the center of the WD. The visible downturn of  $M(T_{\max})$  in each of the depicted model sequences is the result of the burning point moving towards areas of higher density after ignition.

Woosley & Kasen (2011) investigated more closely two possible ways to induce SNe in sub-Chandrasekhar WDs via what has become known as the double-detonation scenario: in the first scenario, ignition of the He-envelope at the core-envelope interface induces a supersonic shock front that compresses the CO-core, inducing a secondary detonation at the center, resulting in the explosive destruction of the WD. In the second scenario, ignition occurs at some distance from the core-envelope interface inducing an inward and outward shock. The inward propagating shock then proceeds from the helium envelope into the CO core, resulting in a SN in what is known as the “edge-lit” scenario. In the light of this study, if an ignition is able to induce a detonation, the former case would be more likely in an initially hotter and more luminous WD, while the latter outcome would be more likely in an initially colder, lower luminosity WD.

### 3.3.4. Impact of parameter variations

In this section we describe the impact of variations of the most relevant input parameters on the entire set of simulated systems.

Fig. 3.7 shows the final masses of all computed model sequences with respect to the mass-accretion rate. We emphasize that the coordinate in the graphs does not correspond to the mass of the accumulated envelope but to the total mass of the star. The mass of the envelope can be obtained by subtracting the mass of the corresponding initial model (black lines) from the mass of the model sequence at He-ignition. We identify two distinct cases for accretion rates with  $\dot{M} \geq 3 \cdot 10^{-8} M_{\odot}/\text{yr}$

### 3. Helium ignition in magnetized CO WDs

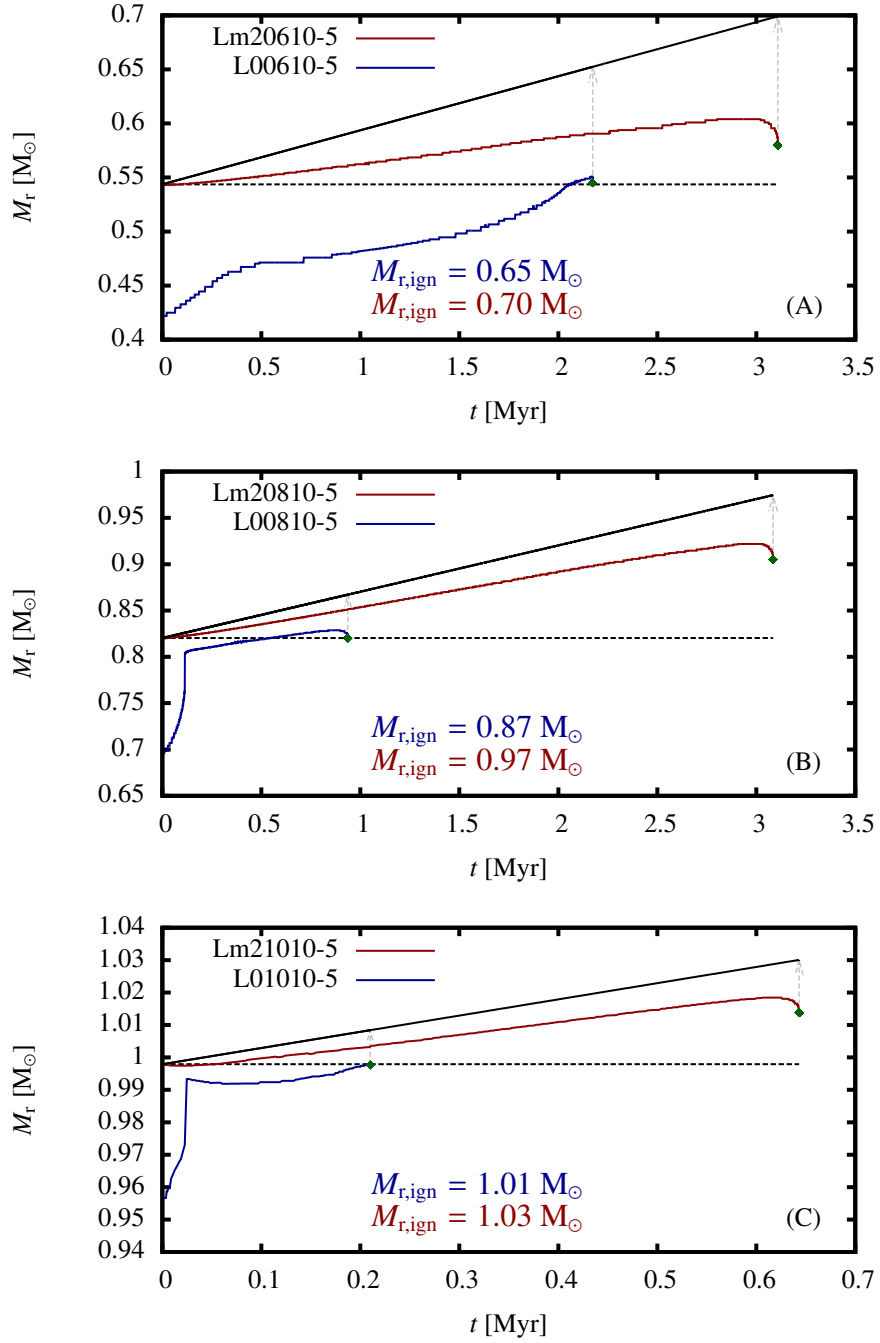


Figure 3.6.: Mass coordinates of the point of the temperature maximum ( $T_{\max}$ ) over time (solid colored lines) of several representative systems with initial masses of  $0.54 M_\odot$  (A),  $0.82 M_\odot$  (B) and  $1.0 M_\odot$  (C). The solid black line in each plot indicates the corresponding total mass of the WD ( $M_{WD}$ ), red lines correspond to an initial luminosity of  $\log(L_{\text{init}}/L_\odot) = 0$  and blue lines to  $\log(L_{\text{init}}/L_\odot) = -2$ . The dashed black line indicates the initial mass of the WD. The green dots indicate the He-ignition points. All depicted sequences were calculated with  $f_{\text{acc}} = 1.0$  and  $\dot{M} = 5 \cdot 10^{-8} M_\odot/\text{yr}$ . The gray arrows indicate the point of ignition in relation to  $M_{WD}$ .  $M_{r,ign}$  is the mass coordinate of the igniting shell.

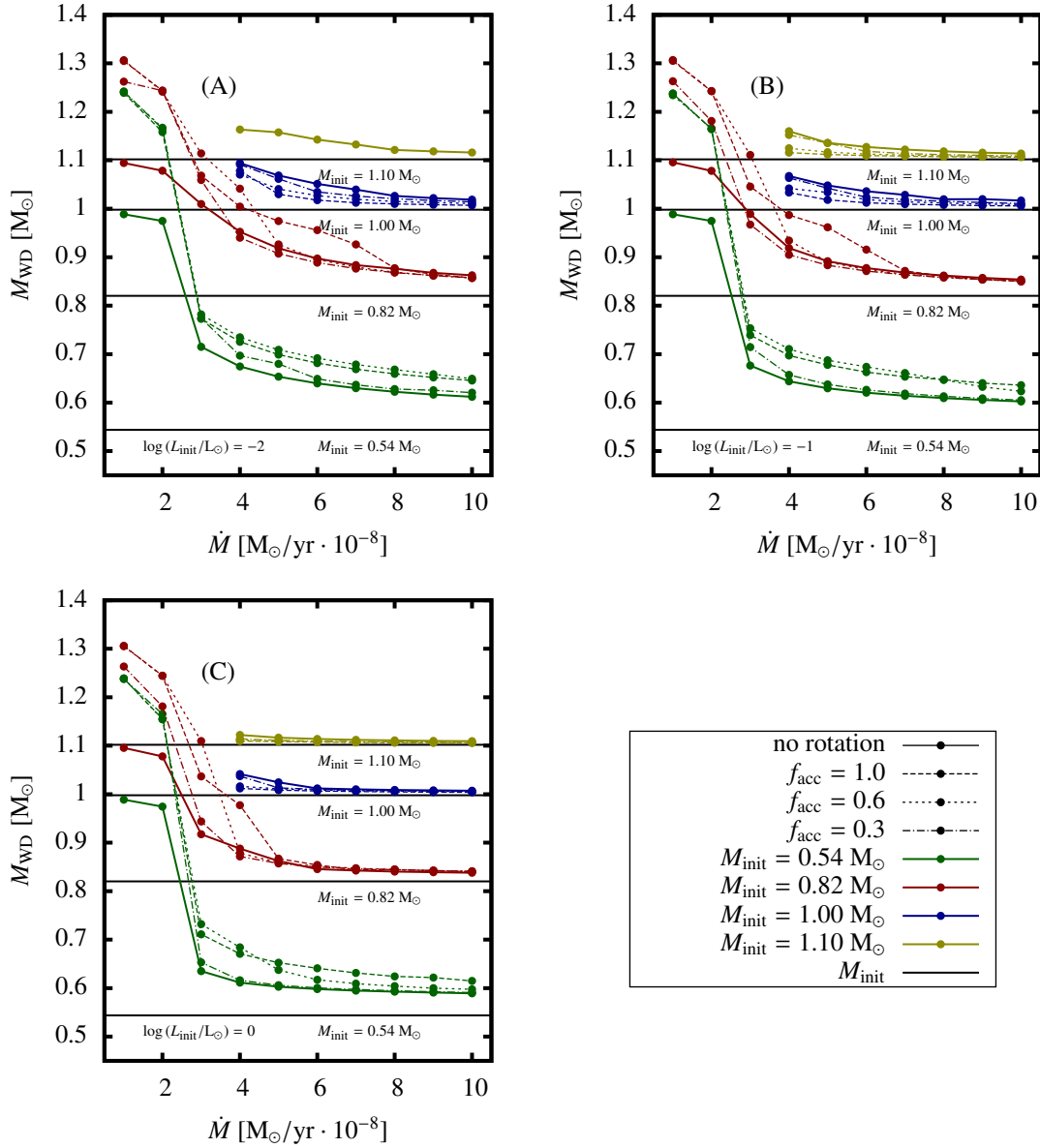


Figure 3.7.: Total masses ( $M$ ) of all computed model sequences of this study with respect to constant mass-accretion rate ( $\dot{M}$ ). The presented graphs differ in the chosen initial luminosity of the white dwarf model with  $\log(L_{\text{init}}/L_{\odot}) = -2$  in graph (A),  $\log(L_{\text{init}}/L_{\odot}) = -1$  in (B) and  $\log(L_{\text{init}}/L_{\odot}) = 0$  in (C). Black solid lines correspond to the initial mass of each model sequence with the initial mass being indicated. Colored lines indicate the final mass of each model sequence with green corresponding to  $M_{\text{init}} = 0.54 M_{\odot}$ , red to  $M_{\text{init}} = 0.82 M_{\odot}$ , blue to  $M_{\text{init}} = 1.00 M_{\odot}$  and yellow to  $M_{\text{init}} = 1.10 M_{\odot}$ . Line types indicate chosen rotational parameters. Solid colored lines for non-rotating models, dashed lines for  $f_{\text{acc}} = 1.0$ , dotted lines for  $f_{\text{acc}} = 0.6$  and dash-dotted lines for  $f_{\text{acc}} = 0.3$ . Dots indicate the masses of individual models.

### 3. Helium ignition in magnetized CO WDs

(effects at accretion rates lower than this, applicable to initial masses  $M \geq 0.82 M_{\odot}$  will be discussed separately), differentiated by their ignition mass when compared to the non-rotating case: The high initial mass case in which the WD ignites its helium envelope after accumulation of a smaller amount of helium than the non-rotating case and the low initial mass case in which the WD ignites its envelope with a larger amount of helium than in the non-rotating case. There is also the intermediate case where the behavior of the WD is principally governed by the accretion rate. Systems with accretion rates lower than  $\dot{M} < 3 \cdot 10^{-8} M_{\odot}/\text{yr}$  form a separate case, exhibiting vastly increased He-shell masses at detonation when compared to the non-rotating case as well as higher accretion rates. These systems will be collectively referred to as the low accretion rate case.

#### Low initial mass case

The behavior of the low initial mass case is illustrated by the model sequences with  $M_{\text{init}} = 0.54 M_{\odot}$ . The effects of close-to-critical rotation, discussed in Sect. 3.3.1 and Sect. 3.3.3, driving up ignition masses become obvious here. At all initial luminosities the model sequences with  $M_{\text{init}} = 0.54 M_{\odot}$  exhibit significantly higher envelope masses at He-ignition than in the non-rotating case (by up to  $\sim 0.14 M_{\odot}$ ). The observation that this behavior is related to the ability of the accumulated angular momentum to spin up the WD is strongly supported by the evident correlation between the increase of the required accretion and  $f_{\text{acc}}$ , since a variation in  $f_{\text{acc}}$  immediately and artificially impacts the amount of angular momentum imparted on the star for a given time period and therefore directly controls its spin-up timescale. The switch (with  $f_{\text{acc}} = 0.6$  showing higher ignition masses than  $f_{\text{acc}} = 1.0$ ) at  $\dot{M} \simeq 4 - 5 \cdot 10^{-8} M_{\odot}/\text{yr}$  in this behavior seen in Fig. 3.7 should be noted for further reference (see explanation in Sect. 3.3.4).

Systems with  $f_{\text{acc}} = 0.3$  generally do not spin up quickly enough for the WD to reach surface velocities close to  $v_{\text{crit}}$ , usually undergoing He-ignition at  $v_{\text{surf}} \sim 0.25 v_{\text{crit}}$ . As expected, these systems therefore most closely resemble non-rotating ones, with exceptions at the lowest considered mass-accretion rates if  $\log(L_{\text{init}}/L_{\odot}) \leq -1$ .

At  $\log(L_{\text{init}}/L_{\odot}) = -2$ , the initial temperatures are low enough, ensuring that the amount of required material is high enough to allow for a significant increase in rotational velocity, to ensure that the process described above is active over the entire range of considered mass-accretion rates.

We conclude that the rotating magnetic case leads to higher envelope masses in relatively low-mass CO WDs of about  $0.54 M_{\odot}$  compared to the non-rotating case.

#### High initial mass case

The behavior of the high initial mass case is illustrated by the model sequences with initial masses of  $M_{\text{init}} = 1.00 M_{\odot}$  and  $M_{\text{init}} = 1.10 M_{\odot}$ . Unlike the low initial mass case, WDs of this kind undergo He-ignition after a smaller amount of material has been accumulated than in the non-rotating case. As described in Sect. 3.3.1 and Sect. 3.3.3, the reason for this lies in the expectation, due to their higher rotational inertia, that higher mass WDs are spun up more slowly than lower mass objects. This means that higher mass WDs will not be spun up appreciably before He-ignition. The difference in ignition masses with respect to the value of  $f_{\text{acc}}$  in this case stems from the more efficient heating caused by rotational energy dissipation because of the larger rotational velocity gradient induced through accretion at larger values of  $f_{\text{acc}}$ . This is reflected in the ordering of the ignition masses with the divergence from the non-rotating case being smallest for  $f_{\text{acc}} = 0.3$  and largest for  $f_{\text{acc}} = 1.0$ .



It should be noted that the decrease in ignition masses in the high initial mass case in the rotating magnetic case mirrors the behavior of rotating non-magnetic ones (cf. Yoon & Langer 2004a). The non-rotating case and the rotating non-magnetic case can be thought of as upper and lower limits for the He-envelope mass at ignition for the high initial mass case ( $M \geq 1.0 M_{\odot}$ ).

### Intermediate case

The intermediate case is represented in this study by model sequences with  $M_{\text{init}} = 0.82 M_{\odot}$ . These systems exhibit the behavior of high initial mass case systems at high mass-transfer rates and low values of the  $f_{\text{acc}}$ -parameter and the behavior of low initial mass case systems at low mass-transfer rates and high values of the  $f_{\text{acc}}$ -parameter. Lower initial luminosity increases the propensity of the system to show an increased He-envelope mass at ignition when compared to the non-rotating case. The reason for this behavior again lies in the interplay between the spin-up of the WD and the heating effects of accretion: higher mass-accretion rates decrease the amount of helium needed to result in an ignition, allowing less time to spin up the WD. The intermediate case can therefore be viewed as a transitory case between the high and low initial mass cases. We again emphasize the expectation of the largest helium envelope masses to be reached to pass from model sequences with  $f_{\text{acc}} = 1.0$  to model sequences with  $f_{\text{acc}} = 0.6$  with decreasing  $\dot{M}$ .

### Low accretion rate case

As can be seen in Fig. 3.7, systems with  $\dot{M} < 3 \cdot 10^{-8} M_{\odot}/\text{yr}$  exhibit two features absent in the cases with  $\dot{M} \geq 3 \cdot 10^{-8} M_{\odot}/\text{yr}$ . First, the helium shell mass at detonation is much larger than in the corresponding non-rotating case and in the cases with higher mass-accretion rates. Second, the helium shell mass at detonation is practically independent of the initial luminosity of the WD.

Apart from the already discussed diminished effect of the NCO-reaction, both of these features are explained by the diminished effects of compressional heating at lower mass-accretion rates. The compressional heating timescale ( $\tau_c$ ) is proportional to the mass-accretion timescale ( $\tau_{\text{acc}}$ ), heating being further decreased by rotation (e.g., Piersanti et al. 2003). Therefore, if the initial temperature profile of the WD is higher than can be maintained through the given rate of mass-accretion, the WD will cool until an equilibrium between radiative cooling and compressional heating is achieved. If the WD's initial temperature profile is lower than the equilibrium profile, the WD will be heated. Fig. 3.8 shows that this leads to a period of low temperatures and flat temperature profiles in systems with mass-accretion rates  $\dot{M} < 3 \cdot 10^{-8} M_{\odot}/\text{yr}$ , while systems with higher mass-accretion rates maintain a temperature maximum in the upper parts of their envelope, which in turn aids ignition once an adequate amount of material has been accumulated. This accounts for the significantly increased envelope masses for  $\dot{M} < 3 \cdot 10^{-8} M_{\odot}/\text{yr}$ .

Independence from initial luminosity is explained by the same process. Fig. 3.9 shows the maximum envelope temperature of representative models with respect to mass-accretion rates and initial luminosity. As explained above, models with mass-accretion rates of  $\dot{M} < 3 \cdot 10^{-8} M_{\odot}/\text{yr}$  evolve towards a state of equilibrium, defined by an equilibrium temperature which depends on the mass-accretion rate. Once equilibrium is reached, further evolution becomes independent of initial parameters. Systems with  $\dot{M} \geq 3 \cdot 10^{-8} M_{\odot}/\text{yr}$  never reach this equilibrium, their evolution being influenced by their initial disposition up to the point of He-ignition.

As is shown in Sect. 3.3.5, systems conforming to the low accretion rate case are the most likely

### 3. Helium igniton in magnetized CO WDs

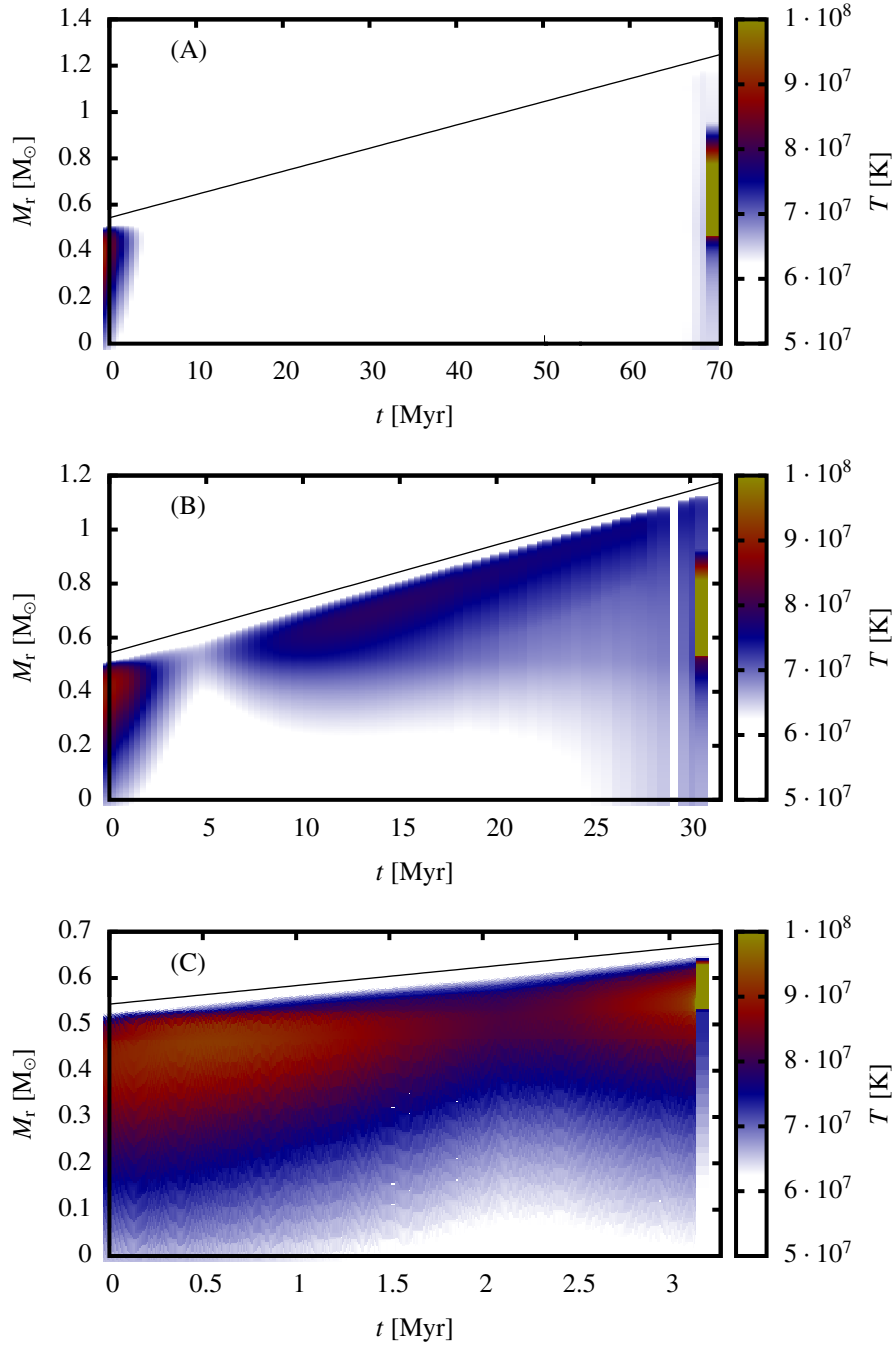


Figure 3.8.: Temperature profiles over time of individual representative model sequences.  $M_r$  is the mass coordinate,  $t$  the time since the start of the accretion phase. The color bar indicates temperature and the black line corresponds to the current total mass of the WD. All model sequences were computed with initial parameters of  $M_{\text{init}} = 0.54 M_\odot$ ,  $\log(L_{\text{init}}/L_\odot) = 0$  and  $f_{\text{acc}} = 1.0$ . Model sequence A (L00510-1) uses a mass-accretion rate of  $\dot{M} = 1 \cdot 10^{-8} M_\odot/\text{yr}$ , model B (L00510-2)  $\dot{M} = 2 \cdot 10^{-8} M_\odot/\text{yr}$  and model C (L00510-4)  $\dot{M} = 4 \cdot 10^{-8} M_\odot/\text{yr}$ . It should be noted that the temperature color scale was restricted to the indicated range. Temperatures higher and lower than the limits do occur. The gap visible in plot B is due to a subsequence of models computed with a larger time step than the rest of the sequence, resulting in a physically irrelevant discontinuity of the available data.

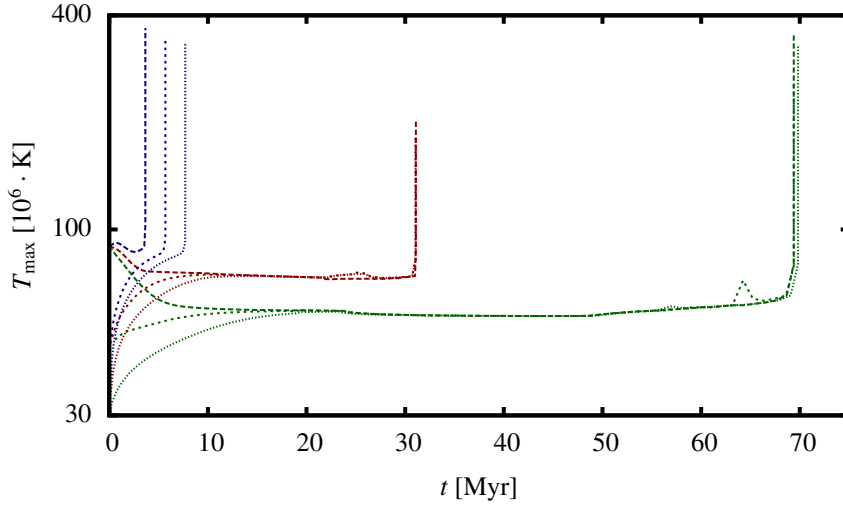


Figure 3.9.: Maximum temperature over time for a number of representative model sequences. All model depicted model sequences were calculated with  $M_{\text{init}} = 0.54 M_{\odot}$  and  $f_{\text{acc}} = 0.3$ . Blue lines indicate a mass-accretion rate of  $\dot{M} = 3 \cdot 10^{-8} M_{\odot}/\text{yr}$ , red lines  $\dot{M} = 2 \cdot 10^{-8} M_{\odot}/\text{yr}$  and green lines  $\dot{M} = 1 \cdot 10^{-8} M_{\odot}/\text{yr}$ . Solid lines indicate an initial luminosity of  $\log(L_{\text{init}}/L_{\odot}) = -2$ ,  $\log(L_{\text{init}}/L_{\odot}) = -1$  and dotted lines  $\log(L_{\text{init}}/L_{\odot}) = 0$ .

candidates for He-detonations (as opposed to deflagrations), but their high mass requirements make their natural occurrence highly unlikely. mass-transfer rates of  $\dot{M} < 3 \cdot 10^{-8} M_{\odot}/\text{yr}$  are expected to require a mass donor of  $M \leq 0.9 M_{\odot}$ . Such a low-mass donor does not have a mass budget large enough to provide the required amount of helium (see Neunteufel et al. 2016).

### $f_{\text{acc}}$ -dependence

As noted in the previous sections, in the low initial mass and intermediate cases, the ordering with respect to final He-envelope mass of models calculated with different values of the  $f_{\text{acc}}$ -parameter depends on the mass-accretion rate. In this section we will explain why this switch occurs and why it is related to the mass-accretion rate.

It is important to note that this behavior is unexpected insofar as the effects of rotation should be stronger for more rapid rotation (see Eq. 3.14). Since  $f_{\text{acc}}$  controls the amount of angular momentum accumulated per unit mass, a model calculated with a larger value of the  $f_{\text{acc}}$ -parameter should be rotating faster than in the case with a smaller  $f_{\text{acc}}$  after the same amount of material has been accreted. This criterion is satisfied in our models. Since the conditions for the onset of helium burning primarily depend on the local density and temperature, a fast, quasi-solidly, rotating star will have to accumulate a larger amount of helium than a slower rotating one in order to facilitate He-ignition. Therefore, naively, one would expect the ignition mass of a given WD to increase with the  $f_{\text{acc}}$ -parameter.

Fig. 3.10 shows the evolution of the density at the point of maximum temperature,  $\rho(T_{\text{max}})$ , with respect to the mass of the accumulated He-envelope,  $M_{\text{He}}$ . Color indicates the surface rotational velocity of the WD (owing to quasi-solid-body rotation, the angular velocity does not differ significantly at the surface or anywhere else in the star). Depicted are three model sequences, all with

### 3. Helium ignition in magnetized CO WDs

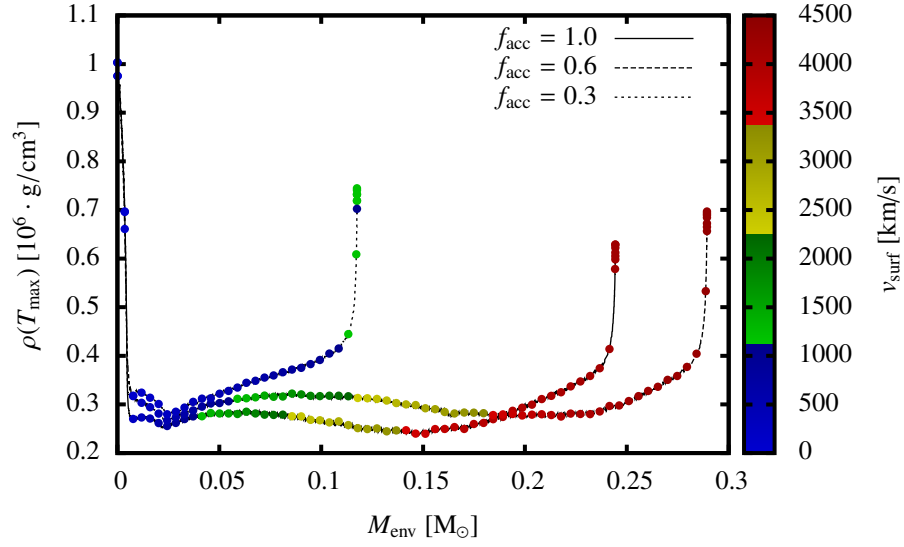


Figure 3.10.: Densities at the point of highest temperature ( $\rho(T_{\max})$ ) with respect to the total current mass of the accumulated He-envelope ( $M_{\text{He}}$ ). The colored dots indicate the current surface velocity of the model. Depicted are model sequences lm10810-3, lm10806-3 and lm10803-3. The model sequences differ in the chosen  $f_{\text{acc}}$ -parameter.

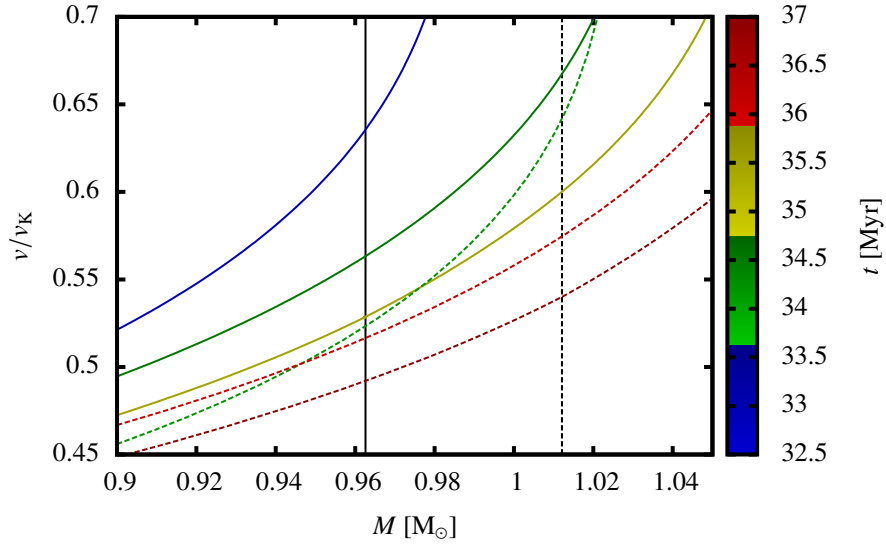


Figure 3.11.: Local rotational velocity ( $v$ ) divided by the local Keplerian velocity ( $v_K$ ) with respect to mass coordinate ( $M$ ). Depicted are model sequences lm10810-3 and lm10806-3. Solid lines represent the  $f_{\text{acc}} = 1.0$  case (lm10810-3), dotted lines the  $f_{\text{acc}} = 0.6$  case (lm10806-3). The color bar indicates the time-coordinate of the profile. The black lines indicate the mass coordinate of the point of ignition for the respective model. The solid black line is valid for  $f_{\text{acc}} = 1.0$  and the dotted line for  $f_{\text{acc}} = 0.6$ .

initial mass  $M_{\text{init}} = 0.82 M_{\odot}$ , initial luminosity  $\log(L_{\text{init}}/L_{\odot}) = -1$  and constant mass-accretion rate  $\dot{M} = 3 \cdot 10^{-8} M_{\odot}/\text{yr}$  for three different values of  $f_{\text{acc}}$ . The initial decrease in density is explained by the fact that, at the start of the accretion phase, the WDs have the highest temperature in the central region. With proceeding accretion of matter, thermal energy is introduced in the outermost layers of the WD while heat is radiated away from the center. This leads to a flattening of the temperature gradient with a peak somewhere in the upper envelope (cf. Fig. 3.4 and Fig. 3.5). Once high enough local temperature and density, are reached, the helium will ignite and a flame will propagate inwards, leading to the increase of  $\rho(T_{\text{max}})$  immediately before the end of the model sequence. Keeping in mind that Eq. 3.14 leads us to expect that slower rotational velocities lead to earlier ignition, the small helium shell mass of the  $f_{\text{acc}} = 0.3$  model sequence is easily explained by the observation that this model does not reach rotational velocities close to critical. Both the  $f_{\text{acc}} = 1.0$  and the  $f_{\text{acc}} = 0.6$  model sequences reach critical rotational velocities, the former sooner than the latter. After the initial decrease, the  $f_{\text{acc}} = 1.0$  model sequence exhibits lower values of  $\rho(T_{\text{max}})$  than the  $f_{\text{acc}} = 0.6$  model sequence. Owing to the relatively higher rotational velocity of the  $f_{\text{acc}} = 1.0$  model sequence, this is expected.

The subsequent unexpected increase in  $\rho(T_{\text{max}})$  in the  $f_{\text{acc}} = 1.0$  model sequence at an earlier time than in the  $f_{\text{acc}} = 0.6$ , leading to helium ignition, occurs because of a combination of the following factors: as the WD accumulates mass, the radial coordinate of any given mass coordinate decreases, increasing the local Keplerian velocity (Eq. 3.16). At the same time, as long as the WD has not reached critical rotation, accumulation of angular momentum through mass-accretion increases the local rotational velocity relative to the Keplerian velocity. As discussed in Sect. 3.2, once a model sequence reaches critical rotation,  $f_{\text{acc}}$  is assumed to be 0. This means that angular momentum is only accumulated at the rate allowed by the increase in mass of the WD instead of the rate dictated by the  $f_{\text{acc}}$ -parameter. This in turn means that, at lower mass coordinates, the local value of  $v/v_K$  decreases due to the increase in value of  $v_K$ . This behavior is evident in Fig. 3.11, which shows the evolution of the local value of  $v/v_K$  at the point of ignition with respect to the total mass of the WD for the same model sequences with different values chosen for the  $f_{\text{acc}}$ -parameter. The earlier ignition of the model sequence with  $f_{\text{acc}} = 1.0$  is therefore precipitated by the fact that it reaches critical rotation earlier than models with a smaller value of  $f_{\text{acc}}$ .

### 3.3.5. Ignition densities and detonations

Fig. 3.12 shows the density at the point of ignition at the time of ignition ( $\rho_{\text{ign}}$ ) in relation to the chosen mass-accretion rate ( $\dot{M}$ ). Most importantly, the expected ignition densities in rotating models are significantly lower than in the non-rotating case. There is a correlation of higher ignition densities with higher initial masses, lower mass-accretion rates and lower initial luminosities.

Apart from our baseline non-rotating models, only low accretion rate case systems reach high enough ignition densities for detonation. However, taking into account the fact that the conditions of the mass-accretion phase must be present in a physical CO-WD He-Star system in order to produce an observable event, the low accretion rate case presents us with two mutually exclusive conditions for detonation: 1. low accretion rates and 2. large amounts ( $\sim 0.45 M_{\odot}$ ) of transferred mass. As shown by Neunteufel et al. (2016), mass-transfer rates of  $\dot{M} \leq 3 \cdot 10^{-8} M_{\odot}/\text{yr}$  are only to be expected in close binary systems for He-donors of  $M \leq 0.9 M_{\odot}$ , varying with the evolution of the donor. Such a donor star would need to lose a majority of its mass in order to produce a detonation. The same criterion rules out the possibility that the required low mass-accretion rates could be provided through

### 3. Helium ignition in magnetized CO WDs

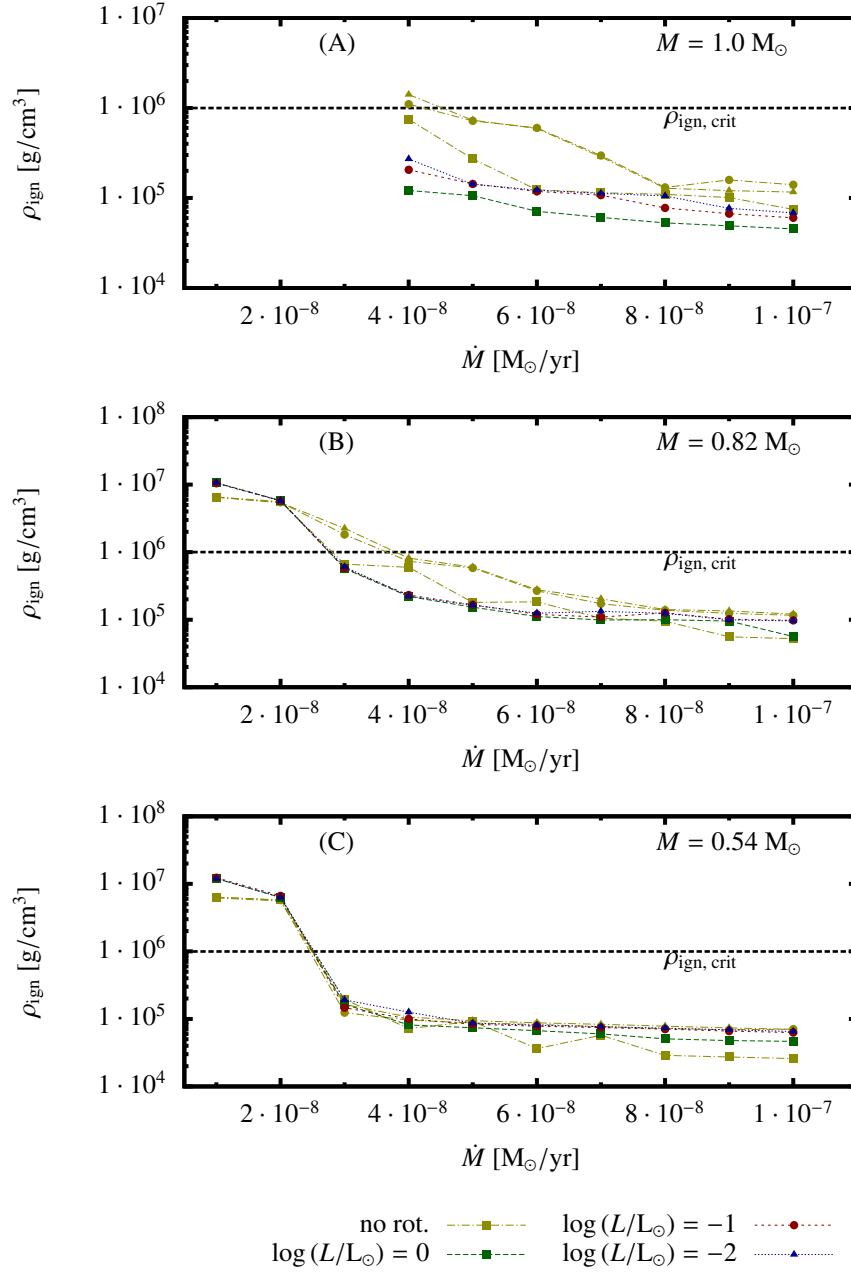


Figure 3.12.: Density at the point of ignition ( $\rho_{\text{ign}}$ ) plotted against mass-accretion rate. The black dotted line indicates the minimum density for a supersonic runaway according to Woosley & Weaver (1994). Only model sequences with  $f_{\text{acc}} = 1.0$  included.

wind accretion from a more massive donor. Previous studies (e.g., Theuns et al. 1996b) suggest that a companion star might be able to accrete a few percent ( $\sim 1 - 2\%$ ) of a primary's wind mass loss rate. A He-star exhibiting sufficiently high wind mass loss to lead to an accretion rate of  $\sim 1 \cdot 10^{-8} M_{\odot}/\text{yr}$  on an accompanying WD would be unlikely to be able to sustain it for long enough to allow for the accumulation of  $\sim 0.5 M_{\odot}$  of He.

We note that our non-rotating models, including the predictions of whether the WD is capable of producing a detonation, are in reasonably good agreement with previous results such as those obtained by Woosley & Kasen (2011), generally showing a discrepancy of less than 5% in final helium shell mass. Larger discrepancies of up to 30% in final helium shell mass in the comparable model sequences of initial masses around  $0.8 M_{\odot}$  at mass-accretion rates of  $2 - 3 \cdot 10^{-8} M_{\odot}/\text{yr}$  can be attributed to the presence of more massive He-layer in our  $0.82 M_{\odot}$ -model. Comparisons with comparable models obtained by Piersanti et al. (2014) yield a discrepancy of 5 – 20%, which can be attributed to the higher initial luminosities used in that source. We also note that the chosen methodology does not take into account changes in the mass-accretion rate, which would occur in any natural interacting binary. We nevertheless conclude that, while it may be theoretically possible to induce a He-detonation on a rotating WD with an active Tayler-Spruit dynamo, the conditions necessary to do so are unlikely to exist in a naturally occurring binary system. Any naturally occurring accretor will far more likely undergo a helium deflagration rather than a detonation. However, we stress again the limitations of using the prescription introduced in Woosley & Weaver (1994) and point to Woosley & Kasen (2011) where detonations have been found to occur at lower (but not much lower) ignition densities than the  $\rho_{\text{crit}} = 10^6 \text{ g/cm}^3$  used here. More detailed calculations using a more specialized simulation framework would have to be used in order to resolve this problem.

As far as resulting transients are concerned, we find it unlikely that any of the rotating models under consideration here might be able to produce classical Type Ia SNe. Returning to Woosley & Kasen (2011) for reference (although only non-rotating WDs are discussed, and so this comparison must be considered approximate), Type Ia-like spectra and light curves depend on low He-shell masses  $\lesssim 0.05 M_{\odot}$  at ignition and on the ignition turning into a supersonic shock. As discussed above, comparable He-shell masses only occur in our model sequences with  $M_{\text{init}} \geq 1.0 M_{\odot}$  and  $\dot{M} \geq 5 \cdot 10^{-8} M_{\odot}/\text{yr}$ , which are incapable of producing a detonation when rotation is included. On the other hand, the only systems in our sample which are able to produce a detonation are systems with  $M_{\text{init}} \leq 0.82 M_{\odot}$  at mass-accretion rates  $\dot{M} \leq 3 \cdot 10^{-8} M_{\odot}/\text{yr}$ . But the He-shell masses at detonation of these systems, which - as explained above - we do not expect to occur naturally, are large enough to render a SN Ia-like spectrum very unlikely.

We emphasize at this point that our parameter space excludes accretion rates of  $\dot{M} < 4 \cdot 10^{-8} M_{\odot}/\text{yr}$  for WDs with  $M_{\text{init}} \geq 1.0 M_{\odot}$ . Although we cannot specifically exclude ignitions developing into detonations in this part of the parameter space, the resulting He-shell masses would nevertheless suggest resulting spectra unlike those of classical SNe Ia.

However, the comparatively high ignition masses and ignition densities just below  $10^6 \text{ g/cm}^3$ , in systems with accretion rates of  $\dot{M} \simeq 2 - 3 \cdot 10^{-8} M_{\odot}/\text{yr}$ , could correspond acceptably well with the properties of the fast, faint calcium-rich SNe, as discussed by Waldman et al. (2011).

### 3.4. Comparison with the non-magnetic rotating case

As mentioned before, the impact of rotation with non-magnetic angular momentum diffusion and energy dissipation, the non-magnetic rotating case, has been studied by Yoon & Langer (2004a); it differs from the systems in this study, the magnetic rotating case, in its neglect of the Tayler-Spruit mechanism.

Table 3.2.: Comparison between model sequences obtained by Yoon & Langer (2004a) (A) and this study (B):

Initial mass  $M_{\text{WD},i}$ , mass-accretion rate  $\dot{M}$ ,  $f_{\text{acc}}$ -parameter, helium shell mass at ignition  $M_{\text{He},f}$  and whether the system is expected to detonate.

All systems were calculated with an initial luminosity of  $\log L_{\text{init}}/L_{\odot} = -2$ .

Study	$M_{\text{WD},i}$ $M_{\odot}$	$\dot{M}$ [ $10^{-8} \cdot M_{\odot}/\text{yr}$ ]	$f_{\text{acc}}$	$M_{\text{He},f}$ $M_{\odot}$	Det?
A	0.60	2	1.0	0.08	No
A	0.60	3	1.0	0.06	No
A	0.80	2	1.0	0.02	No
A	0.80	3	1.0	0.02	No
A	0.60	2	0.6	0.15	No
A	0.60	3	0.6	0.11	No
A	0.80	2	0.6	0.07	No
A	0.80	3	0.6	0.05	No
B	0.54	2	1.0	0.61	Yes
B	0.54	3	1.0	0.23	No
B	0.82	2	1.0	0.42	Yes
B	0.82	3	1.0	0.25	No
B	0.54	2	0.6	0.62	Yes
B	0.54	3	0.6	0.24	No
B	0.82	2	0.6	0.42	No
B	0.82	3	0.6	0.32	No

Table 3.2 allows a comparison between systems the taken from Yoon & Langer (2004a) and this study. While there are some differences in the initial mass of the model sequences, these are sufficiently small to make this comparison meaningful.

Comparing models with  $f_{\text{acc}} = 1.0$ , it is evident that the amount of helium required to induce ignition is significantly smaller in the rotating non-magnetic case than in the rotating magnetic case. The impact of the inclusion of the Tayler-Spruit mechanism is drastic; the state of initially very similar systems is very different at the point of helium ignition. For example, in the rotating non-magnetic case sufficiently high ignition densities are precluded by a strong localized input of thermal energy through energy dissipation near the core-shell interface (see Sect. 3.3.3); instead, given a sufficiently large mass budget, a rotating, magnetic system would actually result in a helium detonation.

Another important difference is that in the rotating, non-magnetic case, the amount of accreted helium until ignition is smaller when compared to the non-rotating case, while it is larger in the rotating, magnetic case.



However, in both the rotating, non-magnetic case and the rotating, magnetic case, we expect He-detonations to be an unlikely outcome of the WD's evolution. In the rotating, non-magnetic case this is a consequence of the already mentioned localized input of thermal energy through viscous dissipation. In the rotating, magnetic case, the reason lies in the flatter density stratification brought about by quasi-solid-body rotation in cases with  $\dot{M} \geq 3 \cdot 10^{-8} M_{\odot}/\text{yr}$  and the expected insufficient mass budget of prospective mass donors in cases with  $\dot{M} \leq 3 \cdot 10^{-8} M_{\odot}/\text{yr}$ . Owing to the significant differences in the He-shell mass at ignition, the transients resulting from helium ignition in rotating non-magnetic and rotating magnetic systems would differ significantly from each other.

### 3.5. Evolutionary fates

As described in Sect. 3.3.5, our magnetic, rotating WDs are not promising progenitor models for classical Type Ia supernovae or for other potential transients requiring the ignition of the underlying CO core. The question naturally arises: What do they result in?

To discuss this question, we may divide the parameter space of our models into three parts: the low accretion rate regime, i.e.,  $\dot{M} \leq 2 \cdot 10^{-8} M_{\odot}/\text{yr}$ ; the high accretion rate regime, i.e.,  $\dot{M} \geq 4 \cdot 10^{-8} M_{\odot}/\text{yr}$ ; and the transition regime between the two.

In the low accretion rate regime, ignition densities would be sufficiently high to produce detonations. However, as argued above, since a high mass of helium needs to be accreted for the ignition to occur, this may not happen in nature. Instead, the accretion may stop before the helium can ignite (Neunteufel et al. 2016), leading to a close binary consisting of a CO white dwarf covered by a degenerate helium envelope and a He white dwarf with some amount of CO in its core. Gravitational wave radiation may lead to a merger of such binaries, which could either produce a cataclysmic event (e.g., van Kerkwijk et al. 2010; Dan et al. 2014) or an R CrB star (e.g., Staff et al. 2012; Menon et al. 2013).

In the high accretion rate regime, our rotating models accrete only  $0.01\text{--}0.2 M_{\odot}$  until helium ignites (Fig. 7), which occurs at densities below  $\sim 3 \cdot 10^5 \text{ g/cm}^3$  (Fig. 12) and renders helium detonations unlikely. Such events might be comparable to the faint He-flashes discussed by Bildsten et al. (2007) in the context of AM CVn systems.

In the transition regime, however, we find some rotating models that only ignite helium after accreting slightly more than  $0.2 M_{\odot}$ , at a density above  $\sim 5 \cdot 10^5 \text{ g/cm}^3$  (e.g., Models Lm20810-3, Lm10810-3, L00810-3). When our density criterion for He detonation is applied to these models, a helium shell deflagration is predicted to occur. While our density criterion is uncertain (Sect. 2.3), we cannot exclude that a detonation would occur in this case. However, the ignition conditions in these models are similar to those investigated by Waldman et al. (2011), who argue that even if a helium detonation does occur, the CO core might remain unaffected in this situation.

It was shown by Waldman et al. (2011) that the helium shell explosion with parameters corresponding to our transition regime models, even if it occurs as a detonation, leads to an incomplete burning of the accumulated helium and a rich production of intermediate mass elements (see also Hashimoto et al. 1983). Waldman et al. (2011) suggest that the resulting explosions may correspond to the observationally identified class of Ca-rich supernovae, which are a fast and faint subtype of Type Ib supernovae (Perets et al. 2010), although arguments favoring a core-collapse origin have been put forward as well (Kawabata et al. 2010).

Overall, it appears unlikely in the light of our models that helium accreting white dwarfs provide

### 3. Helium igniton in magnetized CO WDs

the conditions for classical Type Ia supernovae. Instead, they may be good progenitors for fast and faint hydrogen-free transient events, with helium novae occurring for the lowest accumulated helium masses ( $\leq 0.01 M_{\odot}$ ) at the faint end, up to subluminoous Type I supernovae like the Ca-rich supernovae at the bright end.

It has been shown observationally by Perets et al. (2011) that Ca-rich supernovae tend to be offset from their host galaxies by a considerable distance and located in regions where low-mass progenitors in old stellar populations would be expected. The corresponding progenitor age is subject to an ongoing debate. Yuan et al. (2013) argue for delay times of 10 Gyr or more, while Suh et al. (2011) give characteristic ages as low as 300 Myr. Calculating delay times for the systems under consideration here is beyond the scope of this paper; however Wang et al. (2013) used similar masses in their study, but neglected rotation. According to their estimates, a delay time for sub-Chandrasekhar mass detonations in He+WD systems close to 1 Gyr is most probable. Questions concerning the delay times of these transients are equally applicable to white dwarf as to core-collapse progenitors (Yuan et al. 2013; Zapartas et al. 2017) and will have to be addressed in future research.

## 3.6. Conclusions

We have carried out detailed simulations of CO-WDs accreting helium-rich matter at constant accretion rates of  $10^{-8} - 10^{-7} M_{\odot}/\text{yr}$ , allowing for the accumulation of angular momentum and rotational energy dissipation and considering the effects of the Tayler-Spruit mechanism, dynamical shear instability, secular shear instability and the Goldreich-Schubert-Fricke instability up to the point of He-ignition.

We find that inclusion of the Tayler-Spruit mechanism profoundly impacts the expected rotational profile of the WD, inducing quasi-solid-body rotation on the object. We also find that, due to the apparent rotational profile, the role of the NCO-effect in facilitating ignition of the helium envelope is diminished compared to the non-rotating case. Our calculations show a stark difference in the relation of the amount of helium accreted at the point of ignition between rotating and non-rotating model sequences. The magnitude of the difference depends on the initial mass of the WD. Low-mass WDs generally accrete up to  $0.1 M_{\odot}$  more ( $0.3 M_{\odot}$  in total) at accretion rates of  $\dot{M} \geq 3 \cdot 10^{-8} M_{\odot}/\text{yr}$  and up to  $0.2 M_{\odot}$  more ( $0.7 M_{\odot}$  in total) at accretion rates of  $\dot{M} < 3 \cdot 10^{-8} M_{\odot}/\text{yr}$ . High-mass WDs accrete on the order of  $0.01 M_{\odot}$  less than in the non-rotating case.

Rotating magnetic systems are also found to exhibit significantly increased ignition masses when compared to previous non-magnetic rotating models (Yoon & Langer 2004a).

We find that rotating magnetic WDs, accreting helium at rates  $\dot{M} \geq 3 \cdot 10^{-8} M_{\odot}/\text{yr}$ , will not reach ignition densities above  $10^6 \text{ g/cm}^3$ , which indicates that helium ignitions in these systems are unlikely to develop into a detonation. Only systems with  $\dot{M} \leq 2 \cdot 10^{-8} M_{\odot}/\text{yr}$  exhibit ignition densities larger than  $10^6 \text{ g/cm}^3$ . However, naturally occurring systems of this type are unlikely to eventually produce a He-detonation since the expected large amount ( $\gtrsim 0.5 M_{\odot}$ ) of helium required to induce helium ignition would call for a suitably massive donor star. Such a donor would in turn be unable to provide sufficiently low mass-transfer rates (Neunteufel et al. 2016).

This means that identifying any of these models as the progenitors of classical SNe Ia via the double detonation mechanism is not seen as viable. However, the obtained ignition masses and densities for rotating magnetic WDs with accretion rates of  $\dot{M} \simeq 3 \cdot 10^{-8} M_{\odot}/\text{yr}$  resemble the conditions which appear promising for reproducing the faint and fast Ca-rich supernovae. More research, especially

concerning explosion physics, is needed in order to strengthen this indication.

In any case, the stark difference between the expected states of the accreting WD at the time of ignition between the rotating magnetic case, as discussed in this study, the rotating non-magnetic case (e.g., Yoon & Langer 2004a) and the non-rotating case (e.g., Woosley & Kasen 2011) are a clear indication that rotation and magnetic effects should not be neglected in the future study of accretion scenarios in the lead-up to explosive stellar transients.

Table 3.3.: This table lists the most important parameters of simulated systems with  $f = 1.0$  (see Sect. 3.2.2) at the point of He-ignition. The leftmost column lists the model number.  $L_{\text{init}}$  is the luminosity at the start of mass-accretion,  $\dot{M}$  the accretion rate,  $M_{\text{init}}$  the initial mass of the model,  $t$  the time since the start of mass-accretion,  $M_{\text{He,f}}$  the mass of the accumulated He-envelope at the time of ignition,  $T_{4,\text{f}}$  the effective temperature at the time of ignition in units of  $10^4$  K,  $L_{\text{f}}$  the luminosity at ignition,  $\rho_{6,\text{c}}$  the core density at the time of ignition in units of  $[10^6 \text{ g/cm}^3]$ ,  $T_{8,\text{ign}}$  the temperature the the point of ignition in units of  $[10^8 \text{ K}]$ ,  $\rho_{6,\text{ign}}$  the density at the point of ignition in units of  $[10^6 \text{ g/cm}^3]$  and  $M_{\text{r,ign}}$  the location of the point of ignition expressed in terms of the mass coordinate. The model number is composed as follows: The first digit indicates the value of the initial luminosity, if preceded by the letter "m", that value should be understood to be negative. The second and third digit is equal to ten times value of the the initial mass rounded to the next  $0.1 M_{\odot}$ . The fourth and fifth digit are equal to the value of ten times the chosen value for  $f$ . The hyphenated number is equal to the value of the chosen mass-accretion rate divided by  $10^{-8}$ .

#	$L_{\text{init}}$ [log( $L/L_{\odot}$ )]	$\dot{M}/10^8$ [ $M_{\odot}/\text{yr}$ ]	$M_{\text{init}}$ [ $M_{\odot}$ ]	$t$ [Myr]	$M_{\text{He,f}}$ [ $M_{\odot}$ ]	$T_{4,\text{f}}$	$L_{\text{f}}$ [log( $L/L_{\odot}$ )]	$\rho_{6,\text{c}}$	$T_{8,\text{ign}}$	$\rho_{6,\text{ign}}$	$M_{\text{r,ign}}$ [ $M_{\odot}$ ]
Lm20510-1	-2	1	0.54	69.55	0.70	13.27	1.45	39.49	1.94	11.98	0.50
Lm20510-2	-2	2	0.54	30.72	0.61	8.33	0.71	25.84	2.08	6.32	0.56
Lm20510-3	-2	3	0.54	7.64	0.229	4.99	0.37	4.36	3.42	0.19	0.62
Lm20510-4	-2	4	0.54	4.54	0.182	4.62	0.35	3.67	3.33	0.13	0.59
Lm20510-5	-2	5	0.54	3.11	0.155	4.08	0.23	3.35	3.41	0.09	0.58
Lm20510-6	-2	6	0.54	2.30	0.138	4.53	0.41	3.23	3.17	0.08	0.57
Lm20510-7	-2	7	0.54	1.79	0.125	4.91	0.54	3.14	3.02	0.08	0.57
Lm20510-8	-2	8	0.54	1.45	0.116	5.24	0.66	3.07	2.92	0.07	0.57
Lm20510-9	-2	9	0.54	1.20	0.108	5.47	0.74	3.02	2.85	0.07	0.56
Lm20510-10	-2	10	0.54	1.02	0.102	5.64	0.80	2.97	2.82	0.07	0.56
Lm10510-1	-1	1	0.54	69.40	0.69	16.50	1.83	44.29	0.82	1.23	0.51
Lm10510-2	-1	2	0.54	31.03	0.62	7.81	0.59	26.83	1.87	6.63	0.56
Lm10510-3	-1	3	0.54	6.52	0.196	4.31	0.22	3.65	3.62	0.15	0.58
Lm10510-4	-1	4	0.54	3.84	0.154	4.03	0.20	3.14	3.42	0.10	0.56
Lm10510-5	-1	5	0.54	2.68	0.134	3.99	0.22	2.97	3.30	0.08	0.56
Lm10510-6	-1	6	0.54	1.99	0.119	4.46	0.41	2.89	3.08	0.08	0.55
Lm10510-7	-1	7	0.54	1.57	0.110	4.83	0.55	2.84	2.97	0.07	0.55
Lm10510-8	-1	8	0.54	1.30	0.104	5.07	0.64	2.80	2.91	0.07	0.55

*Continued on next page*

Table 3.3 – *Continued from previous page*

#	$L_{\text{init}}$	$\dot{M}$	$M_{\text{init}}$	$t$	$M_{\text{He,f}}$	$T_{4,\text{f}}$	$L_{\text{f}}$	$\rho_{6,\text{c}}$	$T_{8,\text{ign}}$	$\rho_{6,\text{ign}}$	$M_{\text{r,ign}}$
Lm10510-9	-1	9	0.54	1.07	0.097	5.36	0.74	2.76	2.84	0.07	0.55
Lm10510-10	-1	10	0.54	0.92	0.092	5.50	0.79	2.73	2.81	0.06	0.55
L00510-1	0	1	0.54	69.50	0.69	12.69	1.37	39.27	1.88	11.98	0.49
L00510-2	0	2	0.54	30.58	0.61	8.85	0.82	25.55	1.74	6.31	0.56
L00510-3	0	3	0.54	5.58	0.167	4.78	0.36	3.34	3.01	0.17	0.56
L00510-4	0	4	0.54	3.18	0.127	3.66	0.08	2.82	3.22	0.08	0.55
L00510-5	0	5	0.54	2.17	0.109	4.24	0.33	2.69	2.95	0.07	0.55
L00510-6	0	6	0.54	1.62	0.097	4.60	0.47	2.61	2.80	0.07	0.54
L00510-7	0	7	0.54	1.25	0.088	4.91	0.59	2.55	2.68	0.06	0.54
L00510-8	0	8	0.54	1.01	0.081	4.83	0.59	2.50	2.70	0.05	0.54
L00510-9	0	9	0.54	0.87	0.078	4.98	0.67	2.49	2.72	0.05	0.54
L00510-10	0	10	0.54	0.71	0.071	5.39	0.78	2.46	2.60	0.05	0.54
Lm20810-1	-2	1	0.82	48.46	0.48	7.98	0.43	66.99	2.01	10.61	0.78
Lm20810-2	-2	2	0.82	21.17	0.42	8.36	0.59	46.57	2.15	5.77	0.83
Lm20810-3	-2	3	0.82	8.27	0.248	8.29	0.77	19.28	1.75	0.60	0.97
Lm20810-4	-2	4	0.82	4.60	0.184	6.95	0.64	14.30	4.11	0.22	0.92
Lm20810-5	-2	5	0.82	3.09	0.154	6.92	0.68	12.90	3.86	0.16	0.90
Lm20810-6	-2	6	0.82	2.26	0.136	6.71	0.68	12.11	3.97	0.12	0.89
Lm20810-7	-2	7	0.82	1.51	0.105	7.75	0.88	11.72	3.38	0.13	0.87
Lm20810-8	-2	8	0.82	0.71	0.057	8.74	0.98	12.98	3.45	0.12	0.84
Lm20810-9	-2	9	0.82	0.49	0.044	8.78	0.99	13.03	3.76	0.10	0.84
Lm20810-10	-2	10	0.82	0.37	0.037	9.40	1.08	13.03	3.61	0.10	0.83
Lm10810-1	-1	1	0.82	48.49	0.48	7.61	0.35	67.15	2.01	10.47	0.78
Lm10810-2	-1	2	0.82	21.12	0.42	8.33	0.59	46.33	2.14	5.75	0.83
Lm10810-3	-1	3	0.82	7.51	0.225	8.20	0.78	17.25	1.71	0.58	0.94
Lm10810-4	-1	4	0.82	4.17	0.167	6.94	0.65	13.10	3.91	0.23	0.90
Lm10810-5	-1	5	0.82	2.83	0.142	6.79	0.67	11.97	3.92	0.17	0.89
Lm10810-6	-1	6	0.82	1.59	0.095	6.44	0.62	11.44	4.24	0.12	0.86
Lm10810-7	-1	7	0.82	0.74	0.051	7.53	0.77	12.51	4.32	0.11	0.83

*Continued on next page*

Table 3.3 – *Continued from previous page*

#	$L_{\text{init}}$	$\dot{M}$	$M_{\text{init}}$	$t$	$M_{\text{He,f}}$	$T_{4,\text{f}}$	$L_{\text{f}}$	$\rho_{6,\text{c}}$	$T_{8,\text{ign}}$	$\rho_{6,\text{ign}}$	$M_{\text{r,ign}}$
Lm10810-8	-1	8	0.82	0.51	0.041	9.20	1.03	12.72	3.69	0.13	0.83
Lm10810-9	-1	9	0.82	0.38	0.034	8.87	1.00	12.61	3.84	0.10	0.83
Lm10810-10	-1	10	0.82	0.30	0.030	9.40	1.09	12.58	3.67	0.10	0.82
L00810-1	0	1	0.82	48.57	0.49	8.43	0.53	67.09	2.01	10.61	0.78
L00810-2	0	2	0.82	21.21	0.42	8.36	0.59	46.48	2.13	5.83	0.83
L00810-3	0	3	0.82	7.21	0.216	8.15	0.78	16.52	1.70	0.57	0.93
L00810-4	0	4	0.82	3.93	0.157	6.76	0.62	12.46	4.06	0.22	0.89
L00810-5	0	5	0.82	0.94	0.047	7.46	0.70	12.27	4.23	0.15	0.82
L00810-6	0	6	0.82	0.56	0.034	7.48	0.72	12.16	4.27	0.11	0.82
L00810-7	0	7	0.82	0.34	0.024	8.79	0.97	12.17	3.77	0.10	0.82
L00810-8	0	8	0.82	0.30	0.024	8.83	0.98	12.10	3.75	0.10	0.82
L00810-9	0	9	0.82	0.24	0.022	9.38	1.08	12.06	3.59	0.10	0.82
L00810-10	0	10	0.82	0.20	0.020	7.63	0.85	11.84	4.45	0.06	0.82
Lm21010-4	-2	4	1.00	2.01	0.080	10.29	0.95	40.94	4.68	0.27	1.05
Lm21010-5	-2	5	1.00	0.64	0.032	9.52	0.83	38.03	4.96	0.14	1.01
Lm21010-6	-2	6	1.00	0.33	0.020	11.12	1.10	36.58	4.43	0.12	1.00
Lm21010-7	-2	7	1.00	0.21	0.015	11.41	1.14	35.86	4.13	0.11	1.00
Lm21010-8	-2	8	1.00	0.15	0.012	11.65	1.17	35.50	3.89	0.11	1.00
Lm21010-9	-2	9	1.00	0.12	0.010	10.92	1.10	35.14	4.48	0.08	1.00
Lm21010-10	-2	10	1.00	0.09	0.009	11.13	1.14	34.97	4.46	0.07	1.00
Lm11010-4	-1	4	1.00	0.89	0.035	9.42	0.80	37.40	5.17	0.21	1.01
Lm11010-5	-1	5	1.00	0.41	0.020	10.91	1.07	35.68	4.74	0.14	1.00
Lm11010-6	-1	6	1.00	0.24	0.015	10.48	1.00	34.93	4.41	0.12	1.00
Lm11010-7	-1	7	1.00	0.17	0.012	11.15	1.10	34.58	4.00	0.11	1.00
Lm11010-8	-1	8	1.00	0.12	0.010	10.60	1.06	34.24	4.49	0.08	1.00
Lm11010-9	-1	9	1.00	0.10	0.009	10.76	1.09	34.06	4.51	0.07	1.00
Lm11010-10	-1	10	1.00	0.08	0.008	11.27	1.18	33.94	4.50	0.06	1.00
L01010-4	0	4	1.00	0.35	0.014	9.56	0.86	33.79	4.53	0.12	1.00
L01010-5	0	5	1.00	0.21	0.010	10.31	0.97	33.32	3.91	0.11	1.00

*Continued on next page*

Table 3.3 – *Continued from previous page*

#	$L_{\text{init}}$	$\dot{M}$	$M_{\text{init}}$	$t$	$M_{\text{He,f}}$	$T_{4,\text{f}}$	$L_{\text{f}}$	$\rho_{6,\text{c}}$	$T_{8,\text{ign}}$	$\rho_{6,\text{ign}}$	$M_{\text{r,ign}}$
L01010-6	0	6	1.00	0.15	0.009	9.85	0.95	32.95	4.47	0.07	1.00
L01010-7	0	7	1.00	0.11	0.008	10.85	1.13	32.77	4.48	0.06	1.00
L01010-8	0	8	1.00	0.09	0.007	11.94	1.31	32.63	4.52	0.05	1.00
L01010-9	0	9	1.00	0.07	0.006	12.84	1.44	32.54	4.50	0.05	1.00
L01010-10	0	10	1.00	0.06	0.006	13.43	1.52	32.51	4.47	0.05	1.00
Lm11110-4	-1	4	1.10	0.35	0.014	11.20	0.95	73.91	5.45	0.15	1.11
Lm11110-5	-1	5	1.10	0.20	0.010	11.72	1.01	72.65	4.60	0.14	1.10
Lm11110-6	-1	6	1.10	0.13	0.008	16.78	1.76	71.27	5.99	0.07	1.10
Lm11110-7	-1	7	1.10	0.10	0.007	19.61	2.05	70.91	6.00	0.06	1.10
Lm11110-8	-1	8	1.10	0.07	0.006	24.90	2.51	70.41	6.00	0.05	1.10
Lm11110-9	-1	9	1.10	0.06	0.005	28.76	2.79	70.18	6.00	0.04	1.10
Lm11110-10	-1	10	1.10	0.05	0.005	32.16	3.01	70.00	6.00	0.04	1.10
L01110-4	0	4	1.10	0.20	0.008	10.67	0.87	68.70	4.64	0.12	1.10
L01110-5	0	5	1.10	0.13	0.006	19.38	2.05	67.72	6.00	0.06	1.10
L01110-6	0	6	1.10	0.09	0.006	23.09	2.38	67.38	6.00	0.05	1.10
L01110-7	0	7	1.10	0.07	0.005	27.35	2.71	67.12	6.00	0.04	1.10
L01110-8	0	8	1.10	0.06	0.004	32.29	3.04	66.90	6.00	0.03	1.10
L01110-9	0	9	1.10	0.05	0.004	36.19	3.28	66.73	6.00	0.03	1.10
L01110-10	0	10	1.10	0.04	0.004	39.39	3.47	66.59	6.00	0.02	1.10





## 4. Ignition in white dwarf models undergoing time-varying helium accretion.

### **Abstract:**

*Binary systems composed of a carbon-oxygen white dwarf and a helium star are considered promising candidate progenitors for a number of explosive transients, which include classical type Ia, type Iax and carbon-enhanced type Ib, the theoretically predicted .Ia, helium novae and AM Canum-Venaticorum systems.*

*Mass transfer in binary systems generally varies with time. This fact has been neglected in most studies of helium ignition on white dwarfs in the past. This study attempts to resolve the relationship between models with constant accretion and models undergoing time-variable accretion and describe the outcomes of systems undergoing time-variable accretion.*

*We use a well established Lagrangian 1-D hydrodynamical stellar evolution code, fully considering the effects of rotation as well as magnetic instabilities, to simulate the evolution of a single WD model undergoing time variable mass-accretion. The investigated models include a number of synthetic benchmark prescriptions (20 model sequences) as well as prescriptions mimicking a realistic system with physical time-variability (14 model sequences).*

*It is shown that time variability reduces the parameter space for the induction of helium detonation on WDs when compared to constant accretion, thereby decreasing the probability for the production of helium supernovae but increasing the probability for massive helium novae. It is further shown that time variability introduces a degeneracy into the available parameter space of the mass of accreted helium required to induce detonation, complicating cursory identifications of expected outcomes using mass-transfer rates.*

### 4.1. Introduction

The study of binary star systems containing at least one white dwarf (WD) has long been considered promising approach to identifying a number of astrophysical transient phenomena. Undoubtedly the most observationally important of these phenomena are supernovae of the Ia type (SNe Ia), due to their use as "standard candles" in cosmological distance measurements (Perlmutter et al. 1999; Riess et al. 1998; Schmidt et al. 1998), and classical novae (Gallagher & Starrfield 1978). While SNe Ia and classical novae provided the impetus for the attempt to link explosive transients to binaries, a number of additional classes and subclasses of transients have been either theoretically proposed or observationally confirmed. Among these are SNe Iax (Li et al. 2003; Foley et al. 2013), the (theoretical) subluminal type ".Ia" (Bildsten et al. 2007; Kilic et al. 2014), AM Canum-Venaticorum (AM CVn) systems (Warner 1995; Nelemans 2005) and other "peculiar" transients (Woosley & Kasen 2011). Somewhat recently, a connection between interacting WDs and observationally identified fast-faint Ca-enhanced SNe Ib (Perets et al. 2010) was proposed by Waldman et al. (2011). Given the importance of these transients, of classical SNe Ia in particular, the comparative lack of understanding

#### 4. Effects of variable mass-transfer rates

concerning the progenitors, and their evolution, of most of these transients, and their relation to each other, needs to be addressed.

While those of the mentioned transients which can be grouped as cataclysmic variables (namely: classical novae and AM CVns) are adequately well understood observationally, the others still lack definitive observational evidence:

Despite decades of intensive observational search, SNe Ia still need to be connected to a prototype progenitor, although a number of nondetections (see Kelly et al. 2014; Nelemans et al. 2008; Maoz & Mannucci 2008; Schaefer & Pagnotta 2012; Li et al. 2011) have considerably limited the available parameter space for candidate systems.

While McCully et al. (2014) succeeded in identifying a possible progenitor of SN 2012Z as a luminous blue source, possibly a massive main sequence star, blue supergiant or a helium giant of  $\sim 2.0 M_{\odot}$ , a nondetection by Foley et al. (2015) of the progenitor SN 2014dt excluded some of the former study's progenitor parameters. Therefore, in spite of the arguably better observational groundwork, the identity of the prototype progenitor of SNe Iax is only marginally better known than that of SNe Ia. Furthermore Foley et al. (2015) provide a case for the assumption that SNe Iax are possibly products of several profoundly dissimilar progenitor systems.

In any case, these findings provide evidence that SNe Ia as well as Iax might occur in binary systems consisting of a WD and a nondegenerate companion of some description. This scenario, as first proposed for SNe Ia (Whelan & Iben 1973), has become known as the "single degenerate" (SD-scenario) scenario. This is in contrast to the "double degenerate" (DD-scenario) scenario, which assumes, again specifically in the context of SNe Ia, a system consisting of two WDs merging to produce a SN Ia (Iben & Tutukov 1984; Webbink 1984). In the context of cataclysmic variables, the SD-scenario is usually linked to classical novae and the DD-scenario to AM CVn systems, although a role as the possible progenitor of R Coronae Borealis stars has also been proposed (Webbink 1984; van Kerkwijk et al. 2010).

An interesting aspect of the observational evidence of SNe Ia and Iax progenitors is that He-stars are not excluded as mass donors (although Li et al. (2011) failing to identify the progenitor of the SN Ia 2011fe excludes a large part of the available parameter space for He-donor stars, leaving only a small margin for low-mass helium giant donors). Further, observed SNe Iax have been modeled with some success as deflagrations of near-Chandrasekhar-mass WDs (Magee et al. 2016; Foley et al. 2016; Kromer et al. 2015).

Recently, a number of groups (Shen et al. 2010; Bildsten et al. 2007; Shen & Bildsten 2009) proposed a possible connection between the theoretically predicted SNe Ia and AM CVn systems. Further studies (Shen & Moore 2014) seem to suggest a continuum of He-accretion-induced transients defined by the nature of the donor star, the system's orbital period and the associated mass-transfer rate.

In the 1980s, the possibility of mass-accretion precipitating an ignition and subsequent detonation of the accumulated He-shell on a sub-Chandrasekhar mass WD was first seriously explored (Taam 1980a,b; Nomoto 1980, 1982b,a). The required mass-accretion rates would have to be low enough ( $\sim 10^{-8} M_{\odot}/\text{yr}$ ) to preclude premature ignition of the accumulated material, resulting in a cataclysmic variable star. While some of these detonations were predicted to leave the CO core of the WD intact, producing a faint supernova, a clear possibility for the developing shock in the He-envelope to induce a subsequent detonation of the core became apparent, which resulted in the complete disruption of the star. This mechanism became known as the double detonation mechanism (also called, confusingly, DD-mechanism). Later one- and multidimensional studies (Livne 1990; Livne & Glasner 1990, 1991;

Livne & Arnett 1995; Benz 1997; Livne 1997; Fink et al. 2007, 2010; Sim et al. 2010; Kromer et al. 2010; Woosley & Kasen 2011) established He-accretion as a promising avenue in the search for the progenitors of explosive transients like SNe Ia. However, synthetic spectra (Woosley & Kasen 2011; Woosley & Weaver 1994; Woosley et al. 1986; Sim et al. 2010; Kromer et al. 2010) suggest that lower amounts of He generally lead to a better agreement with the spectra of regular SNe Ia.

Further refinement in the understanding of the ignition conditions in accreting WDs was obtained through the inclusion of the effects of rotation and rotational instabilities (Yoon & Langer 2004b,a) and magnetic effects (Neunteufel et al. 2017), showing that these effects cannot be neglected in the study of accretion-induced explosive transients. All these studies showed an enhanced probability for He-accretion to result in deflagratory events instead of detonations while Neunteufel et al. (2017) showed a possible connection between He-accretion and fast, faint Ca-enhanced SNe Ib.

However, many of the aforementioned studies assume a constant accretion rate onto a single model WD. This assumption, while facilitating the creation of physically plausible ignition conditions, is at odds with the physical variability of the mass-transfer rate in a naturally occurring He-Star WD binary system. This variability, driven, interdependently, by the evolution of the donor star, its reaction to mass loss, the accretor's reaction to mass gain and the evolution of the orbital parameters has been shown to have a potentially profound effect on the attainable ignition conditions of the WD (Neunteufel et al. 2016; Wang et al. 2013). The uncertainty whether evolutionary models obtained under the assumption of constant accretion rates can be transposed onto non-constant naturally variable mass-transfer rates leaves a gap in the theoretical understanding of the viability of a naturally occurring binary system as any of the theoretically computed transient progenitors.

In this study we investigate the evolution of fully resolved CO-WDs accreting helium with non-constant accretion rates, including the effects of rotational as well as magnetic instabilities. This paper is organized as follows: In Sec. 4.2 we discuss the utilized computational framework, physical assumptions and describe the nature of our chosen initial stellar models. In Sec. 3.3 we discuss our findings, summarizing the effects of rotation and magnetic effects and predicted outcomes of representative systems, also commenting on the expected observational properties of prospective progenitor systems. In Sec. 3.4 we comment on the applicability of constant accretion rate-models to naturally occurring progenitor systems. In Sec. 3.6 we summarize our findings, putting them into context with preexisting research and observations.

## 4.2. Methods and physical assumptions

### 4.2.1. Numerical methods

The Binary Evolution Code (BEC) is a well established computational framework capable of performing detailed one-dimensional numerical experiments of single or binary star systems (Langer et al. 2000; Yoon & Langer 2004b). The framework is capable of performing detailed hydrodynamical simulations of rotating and degenerate systems, including mass-accretion (Heger et al. 2000; Heger & Langer 2000).

For the purposes of this study, the BEC has been modified to allow for the inclusion time-dependent accretion rates in single star models. These rates may be chosen arbitrarily or resemble rates expected in a naturally occurring binary system. The advantage of this approach over the simulation of fully resolved binary systems is that it allows disentangling the effects of time variable accretion on the accretor from possible uncertainties and effects of mass loss in the donor star.

#### 4. Effects of variable mass-transfer rates

We make use of the full treatment of rotational instabilities currently available in BEC, namely the Solberg-Hoiland instability, the secular shear instability, dynamical shear instability and Eddington-Sweet circulation, we further include magnetic effect in the form of the Tayler-Spruit instability (Spruit 2002; Neunteufel et al. 2017). In WD models, rotational instabilities that induce fast angular momentum redistribution, like the dynamical shear instability necessitate an implicit numerical solver, which was implemented into BEC by Yoon & Langer (2004b) in order to investigate the behaviour of accreting, rotating WDs. The same is true for the treatment of the Tayler-Spruit instability, as implemented by Neunteufel et al. (2017) in an attempt to study accreting, rotating, “magnetic” WDs.

Note that, unless explicitly stated otherwise, the nomenclature in this paper will be the following: “magnetic” refers to models in which the Tayler-Spruit effect is active. Unlike the conventional definition of a “magnetic WD”, these models feature an initially weak radial magnetic field and can conventionally be thought of as non-magnetic. The majority of the magnetic field active in these models is azimuthally oriented and originates in the Tayler-Spruit dynamo. Models with included effects of rotation, such as the dynamical shear instability, and the Tayler-Spruit dynamo will be referred to as “rotating”. Models with included effects of rotation but without the effects of the Tayler-Spruit dynamo are referred to as “rotating, non-magnetic”. Models without rotation are referred to as “non-rotating”.

We investigate the reaction of accreting white dwarf models with respect to three different time-variability scenarios: *linear*, i.e. a linear increase of the mass-transfer rate with respect to time, described by  $1.0 M_{\odot} = \int_0^{t_{\text{rise}}} \dot{M} dt$ . *Step*, i.e. an immediate increase of the mass-transfer rate from a low value to a higher one (low and high values as defined below) and *realistic*.

The realistic scenario consists of two separate simulation runs, a mass-loss simulation and an accretion simulation. In the mass loss simulation, a fully resolved donor star is placed in a system with an appropriate orbital separation and a point mass of the same mass as the intended white dwarf model. The system is then simulated and the encountered mass-transfer rates are recorded.

The step scenario uses a mass-transfer function that can mathematically be described as

$$\dot{M}(t) = \dot{M}_{\text{low}} + \Theta(t_0 - t) \cdot \dot{M}_{\text{high}}, \quad (4.1)$$

where  $\dot{M}_{\text{low}}$  is a constant accretion rate commensurate with those identified as belonging to the *low-accretion-rate case* and  $\dot{M}_{\text{high}}$  as belonging to the *high-accretion-rate case* by Neunteufel et al. (2017).

If the WD would require a higher mass budget than what can be provided by the donor star in order to achieve helium ignition (which, from a programming standpoint would be realized by the model overrunning the end of the mass-accretion scheme provided by the input file), the mass-accretion rate is fixed to the last provided mass-accretion rate.

In close binary systems, angular momentum loss due to gravitational radiation (GWR) has a significant impact on the evolution of the system. BEC incorporates this following the canonical description (see, for example Landau & Livshitz 1975).

BEC calculates the mass-transfer rate by implicitly solving

$$R_L - R + H_P \ln \left( \frac{\dot{M}}{\dot{M}_0} \right) = 0 \quad (4.2)$$

according to the prescription by Ritter (1988) and Kolb & Ritter (1990). Here,  $H_P$  is the photospheric pressure scale height,  $R$  the stellar radius as defined by the lower edge of the photosphere,  $R_L$  the

Table 4.1.: Physical parameters of our initial white dwarf models: Initial mass  $M_{\text{WD},i}$ , initial surface luminosity  $L_{\text{s},i}$ , initial central temperature  $T_{\text{c},i}$ , initial central density  $\rho_{\text{c},i}$ , initial radius  $R_{\text{WD},i}$  and initial surface velocity  $v_{\text{rot},i}$

$M_{\text{WD},i}$ $M_{\odot}$	$\log(L_{\text{s},i}/L_{\odot})$	$T_{\text{c},i}$ $10^7 \text{ K}$	$\rho_{\text{c},i}$ $10^6 \text{ g/cm}^3$	$R_{\text{WD},i}$ $R_{\odot}$	$v_{\text{rot},i}$ $\text{km/s}$
0.54	-0.998	0.427	3.52	0.0133	10.3
0.82	-1.024	0.417	11.8	0.0101	9.5
1.00	-1.000	0.414	32.8	0.0080	9.5
1.10	-1.017	0.317	68.5	0.0068	7.3

Roche lobe radius.  $R_{\text{L}}$  is calculated following the widely used prescription by Eggleton (1983). Further,

$$\dot{M}_0 = \frac{1}{\sqrt{e}} \rho v_s Q, \quad (4.3)$$

where  $v_s$  is the speed of sound in a plasma as defined by  $v_s^2 = \mathfrak{R}T/\mu$  with  $\mathfrak{R}$  being the ideal gas constant,  $T$  the plasma temperature,  $\mu$  the mean molecular weight, and  $Q$  is the effective stream cross section calculated as prescribed by Meyer & Meyer-Hofmeister (1983).

Prior to impacting the accretor, the material transferred from the donor is expected to form a Keplerian accretion disc (Paczynski 1991; Popham & Narayan 1991), carrying with it a specific angular momentum as defined by  $j_{\text{kepler}} = \sqrt{rGM/\delta m^2}$ , where  $r$  is the distance from the center of force (the radius of the star, in this case) and  $\delta m$  the mass of the accreted material. Within the context of the BEC framework, the amount of specific angular momentum ( $j_{\text{acc}}$ ) carried by accreted matter is manually controlled by the choice of  $f_{\text{acc}}$  in the expression  $j_{\text{acc}} = f_{\text{acc}} \cdot j_{\text{kepler}}$ . Neunteufel et al. (2017) showed that the choice of  $f_{\text{acc}}$  has a significant impact on the outcome of the accreting WD's evolution if constant accretion is assumed. However, in the absence of observational evidence to the contrary, the most natural choice of  $f_{\text{acc}} = 1.0$  is the value adopted for the purposes of this study.

Super-critical rotation of the accretor is avoided by demanding that  $f_{\text{acc}} = 0$  if further accretion would lead to super-critical rotation, the excess angular momentum is assumed to be dissipated in the accretion disc.

#### 4.2.2. Input models

We investigate binary systems consisting of one CO WD and one non-degenerate He-star as a mass donor. Initially the donor is assumed to be at the beginning of its He-main-sequence (Helium "zero-age-main-sequence" - "HeZAMS").

#### WD models

Tab. 4.1 summarizes relevant parameters of the utilized WD models. CO WD-He star binaries are deemed to result from initial hydrogen MS systems which then undergo at least one common-envelope (CE) phase. The selection of the correct initial state of the binary components is thus a non-trivial problem. The state of our model systems is designed to most closely resemble the state of the system at the end of the ultimate CE phase (which formed the He-star). CE phases are not well understood

#### 4. Effects of variable mass-transfer rates

Table 4.2.: Physical parameters of initial donor models. Initial mass  $M_{D,i}$ , initial surface luminosity  $L_{s,i}$ , initial effective temperature  $T_{\text{eff}}$ , initial radius  $R_{D,i}$ , central temperature  $T_c$  and central density  $\rho_c$ .

$M_{D,i}$ $M_\odot$	$\log(L_{s,i}/L_\odot)$	$T_{\text{eff}}$ K	$R_{D,i}$ $R_\odot$	$T_c$ $10^8 \text{K}$	$\rho_c$ $10^6 \text{ g/cm}^3$
0.60	1.571	39749	0.1304	1.224	0.0146
0.80	2.047	45728	0.1681	1.313	0.0092
1.00	2.390	50927	0.2012	1.350	0.0064

(see Ivanova et al. 2013), but it stands to reason that the thermal history of a WD at the end of a CE phase will differ significantly from that of an isolated WD (e.g. Renedo et al. 2010b). CE phases tend to be relatively short and, assuming that the accretor reached its WD state before the start of the CE phase, any accretional heating during the CE phase will mostly have heated up the WDs outermost layers. This heat is expected to be radiated away after a relatively short time once the CE phase ends. We therefore assume that, unless the WD was at a very high temperature prior to the start of the CE phase, it will not have been heated up to a large degree. We therefore opt to assume an initial luminosity of  $\log(L_{s,i}/L_\odot) = -1$ . Accretion during the CE phase is assumed to be isotropic, therefore the spin angular velocity of the WD is assumed to be largely unchanged from its pre-CE evolution. The chosen surface velocities ( $v_{\text{surf}}$ ) are commensurate with measurements of isolated WDs (see Heber et al. 1997; Koester et al. 1998; Kawaler 2003; Suijs et al. 2008; Mosser et al. 2012). In any case, the exact values of  $v_{\text{surf}}$  are not expected to have a significant impact on the state of the WD at the end of a mass-transfer phase, as angular momentum accumulation during an interactive binary phase (as opposed to our assumption concerning the CE phase) has been shown (Neunteufel et al. 2017) to efficiently spin up the WD to significantly higher rotational velocities. Thus, for the purposes of this study, the utilized initial WD models can be thought of as non-rotating.

The accretor models were created by evolving a stellar model of appropriate mass and solar metallicity from the HeZAMS to the point of core helium exhaustion and then artificially removing the non-degenerate envelope. This results in a WD of about 70% carbon and 30% oxygen (though a non-vanishing amount of  $< 0.01 M_\odot$  of surface helium is retained in the cases of the  $0.82 M_\odot$  and  $1.0 M_\odot$  models), an effective temperature of about  $2 \cdot 10^5 \text{ K}$  and a surface luminosity of  $\log(L/L_\odot) \approx 2.5$ . The models are then spun up to the given surface velocities and allowed to cool to surface a luminosity of about  $\log(L/L_\odot) = -1$  (see Table 4.1).

#### Donor star models

Tab. 4.2 summarizes relevant initial parameters of the utilized He-star models in the realistic scenario. The chosen donor masses exhibit a number of characteristics desirable for the purposes of this study. The nuclear timescales of helium stars of  $M = 0.6..1.0 M_\odot$  are of  $\tau_{\text{nuc}} \approx 10^9..10^7 \text{ yr}$ , which limits the mass-transfer rates during case BA<sup>1</sup> mass-transfer to low enough values to allow helium ignition to result in a detonation (see Woosley & Kasen 2011; Woosley & Weaver 1994; Neunteufel et al.

<sup>1</sup>In the context of hydrogen stars, case A mass-transfer describes mass-transfer starting before core hydrogen is exhausted and case B after core hydrogen is exhausted. Accordingly, case BA denotes a mass-transfer phase before the end of core helium burning and case BB after.

2016, 2017). Stars of this mass range also provide a large enough mass-budget to allow for the accumulation of a substantial helium envelope, again facilitating detonation instead of deflagration (Neunteufel et al. 2017).

It should be noted that He-star models of this mass exhibit a tendency to thermal pulses towards the end of their main sequence lifetime, which has potentially far-reaching consequences for their host system’s ability to produce certain classes of explosive transients. The reader is referred to Eggleton (2011) and Neunteufel et al. (2016) for a more detailed discussion of the impact of donor star behavior on transient progenitors.

The initial donor star models were created by evolving a hydrogen star of solar metallicity and appropriate mass to the point of core hydrogen exhaustion and then artificially removing the envelope. The star was then evolved further for the length of a few times the thermal timescale ( $\tau_{KH}$ ) until thermal equilibrium was attained.

### 4.3. Results

This section discusses the obtained results. Note that in the following, the term “actual mass-accretion rate” refers to  $\dot{M}(t)$  while the term “average mass-accretion rate” refers to the time averaged mass-accretion rate (i.e.  $\langle \dot{M}(t) \rangle$ ). Furthermore, “constant accretion” refers to systems with  $\dot{M} = \text{constant}$ . Particular emphasis in this section is placed on the comparability of time-variable accretion and constant accretion, the main comparative parameter being the amount of helium accreted at the point of helium ignition (the “final helium shell mass”).

#### 4.3.1. Linear scenario systems

Previous studies have shown that, without exception, the amount of helium required to induce an ignition as well as the ignition density in accreting WDs of the same initial mass decreases with an increasing constant mass-transfer rate (Woosley & Kasen 2011; Neunteufel et al. 2017). Neunteufel et al. (2017) showed that, in rotating WDs, a significant increase of the expected mass of the accumulated helium shell at ignition is expected when moving from a constant accretion rate of  $\sim 3 \cdot 10^{-8} \text{ M}_{\odot}/\text{yr}$  to one of  $\sim 1 \cdot 10^{-8} \text{ M}_{\odot}/\text{yr}$ . This increase is due to compressional heating ceasing to be efficient enough to sustain the fossil heat contained in the WD at the beginning of the accreting evolution. The resulting shortfall in temperature leaves the density of the accreted medium at the base of the helium envelope as the dominant factor in the initiation of helium ignition. The NCO-process in a minor capacity.

We simulated a number of single WD models with linearly increasing mass-transfer rates chosen such that accretion of a He-shell of  $1.0 \text{ M}_{\odot}$  will result in a time-averaged mass-transfer rate of between  $1 \cdot 10^{-8} \text{ M}_{\odot}/\text{yr}$  and  $1 \cdot 10^{-7} \text{ M}_{\odot}/\text{yr}$ . Table 4.3 provides a number of significant parameters of the simulated linear-scenario model sequences, while the mass-transfer history of a representative system (10817<sup>2</sup>) is shown in Fig. 4.2 (A).

The model sequences were chosen in such a way as to facilitate comparison with either  $\langle \dot{M}(t) \rangle$  or  $\dot{M}(t)$  at the point of helium ignition of the linear system, i.e.  $2 \cdot 10^{-8} \text{ M}_{\odot}/\text{yr}$  for the time averaged mass-

<sup>2</sup>The model designation for linear systems is composed as follows: the letter “l” designates the system as of the linear variety, the second and third digit are the initial mass of the WD rounded to the next  $0.1 \text{ M}_{\odot}$  times ten, the third digit is equal to the coefficient of the exponential describing the rise-time and the fourth is equal to the exponent of the rise time.

#### 4. Effects of variable mass-transfer rates

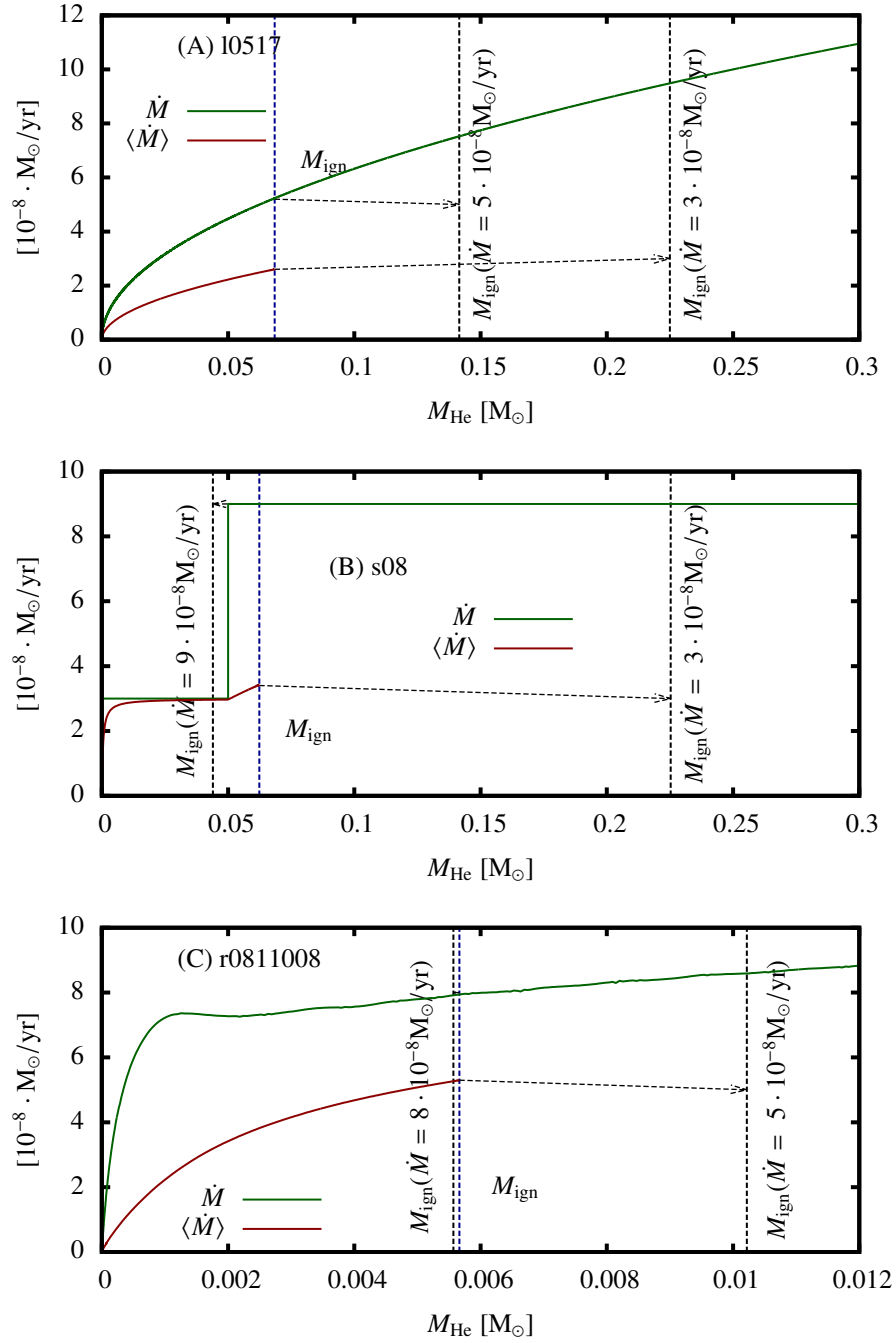


Figure 4.1.: Evolution of the mass-accretion rate of representative systems of each of the accretion scenarios. (A) represents the linear scenario, (B) the step scenario and (C) the realistic scenario. As before  $\dot{M}$  is the mass-transfer rate (including how it would have developed after helium ignition) and  $\langle \dot{M} \rangle$  is the time-averaged mass-transfer rate. Model sequence serial numbers are as indicated. The blue dashed line indicates the point of helium ignition in the model. The black dashed lines indicate the point of helium ignition in systems with constant mass-transfer rates (as presented in Neunteufel et al. 2017) comparable to the final mass-transfer rate and time averaged mass-transfer rate of this model. The grey arrow point from the point of helium ignition to the point where, at comparable mass-transfer rates, helium ignition would happen in a constant accretion rate scenario.



Table 4.3.: Physical parameters at helium ignition of the set of linear scenario systems.  $M_{\text{WD}}$  is the mass of the WD at the start of the accretion phase,  $t_{\text{rise}}$  is the rise-time (as defined by  $1.0 M_{\odot} = \int_0^{t_{\text{rise}}} \dot{M} dt$ ) the of the mass-transfer rate,  $\dot{M}_{\text{f}}$  is the mass-transfer rate at the point of helium ignition,  $\langle \dot{M}_{\text{f}} \rangle$  is the time-averaged mass-accretion rate at the point of helium ignition,  $t_{\text{ign}}$  is the age of the model at the time of helium ignition,  $M_{\text{He}}$  is the mass of the accumulated helium envelope,  $T_{\text{max}}$  is the maximum temperature in the model,  $\rho(T_{\text{max}})$  is the density at the point of  $T_{\text{max}}$  and  $M_r(T_{\text{max}})$  is the mass-coordinate of  $T_{\text{max}}$ .

#	$M_{\text{WD}}$ [ $M_{\odot}$ ]	$t_{\text{rise}}$	$\dot{M}_{\text{f}}$ [ $10^{-8} M_{\odot}/\text{yr}$ ]	$\langle \dot{M}_{\text{f}} \rangle$ [ $10^{-8} M_{\odot}/\text{yr}$ ]	$t_{\text{ign}}$ [Myr]	$M_{\text{He}}$ [ $M_{\odot}$ ]	$T_{\text{max}}$ [ $10^8 \text{K}$ ]	$\rho(T_{\text{max}})$ [ $10^3 \text{g}/\text{cm}^6$ ]	$M_r(T_{\text{max}})$ [ $M_{\odot}$ ]
10516	0.54	$1 \cdot 10^6$	40.94	19.47	21.41	0.040	3.15	0.0047	0.5441
10556	0.54	$5 \cdot 10^6$	12.48	6.20	22.76	0.097	2.85	0.0672	0.5511
10517	0.54	$1 \cdot 10^7$	7.27	3.63	24.84	0.132	3.08	0.0880	0.5634
10557	0.54	$5 \cdot 10^7$	2.61	1.30	53.78	0.424	1.68	0.5655	0.8256
10816	0.82	$1 \cdot 10^6$	25.58	10.18	49.71	0.013	3.88	0.0024	0.8187
10856	0.82	$5 \cdot 10^6$	7.63	3.70	50.54	0.035	4.08	0.1074	0.8251
10817	0.82	$1 \cdot 10^7$	5.26	2.60	52.22	0.068	2.03	0.3202	0.8435
10857	0.82	$5 \cdot 10^7$	2.47	1.24	80.50	0.382	2.18	4.1081	0.8345
11016	1.00	$1 \cdot 10^6$	19.70	5.59	41.87	0.006	4.38	0.0022	0.9975
11056	1.00	$5 \cdot 10^6$	5.76	2.69	42.50	0.019	5.12	0.1445	0.9995
11017	1.00	$1 \cdot 10^7$	3.69	1.80	43.62	0.033	4.83	0.2402	1.0070
11057	1.00	$5 \cdot 10^7$	1.03	0.51	54.59	0.065	0.65	0.2539	1.0537
11016	1.10	$1 \cdot 10^6$	13.92	5.33	53.16	0.004	6.00	0.0256	1.1021
11056	1.10	$5 \cdot 10^6$	4.10	1.98	53.60	0.010	4.69	0.1529	1.1037
11017	1.10	$1 \cdot 10^7$	3.05	1.51	54.62	0.023	5.08	0.2890	1.1101
11057	1.10	$5 \cdot 10^7$	2.05	1.03	78.77	0.264	2.10	6.0859	1.1159

#### 4. Effects of variable mass-transfer rates

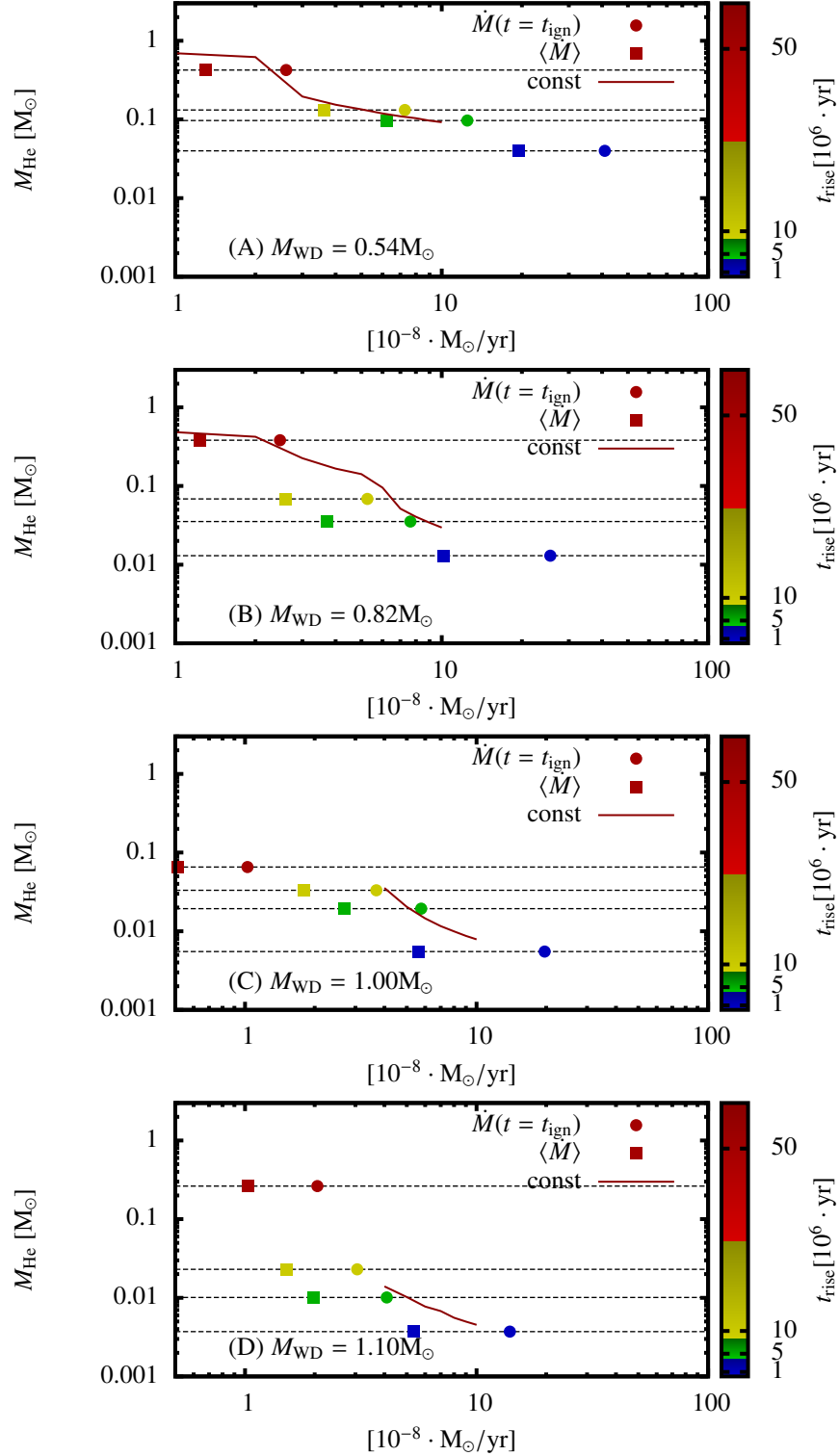


Figure 4.2.: Relation between mass-transfer rate and helium shell mass at ignition for the linear mass accretion scenario as compared with the constant accretion scenario (red lines). The y-axis indicates the amount of helium accreted at the point of helium ignition. The x-axis indicates mass-transfer rate. The color indicates the adopted rise-time in the linear scenario. Squares represent  $\langle \dot{M}(t) \rangle$ , dots represent  $\dot{M}$ . Each pair of squared and dots connected by a dashed line belongs to one model sequence calculated with the same rise-time.

accretion rate at helium ignition and  $5 \cdot 10^{-8} M_{\odot}/\text{yr}$  for the actual mass-accretion rate. As can be seen, the final helium shell mass in the linear accretion scenario is smaller than in the constant accretion rate scenario using both  $\langle \dot{M}(t) \rangle$  and  $\dot{M}(t)$  as a criterion. The reason for this can be seen in Fig. 4.3 (A), which shows the evolution of the point of maximum temperature for model 10817. The initially lower accretion rates allow the interior of the WD to cool, which, in the constant scenario, is inhibited by immediately higher temperatures at the surface, created by viscous heating, while a substantive helium layer is built up. As the mass-transfer rate increases, viscous heating increases proportionally. Helium ignition itself is driven by the local temperature as much as the local density of the medium, with less dense helium requiring higher temperatures in order to ignite and vice versa. In the constant scenario, helium ignition at mass-accretion rates higher than  $3 \cdot 10^{-8} M_{\odot}/\text{yr}$  is driven by temperature, while in the linearly increasing scenario, the deciding factor is density, with helium ignition occurring at a lower temperature but higher local density than in the constant accretion scenario.

This effect depends on the cooling timescale of the WD. Specifically, it is necessary for the cooling timescale to be shorter than the compressional heating timescale (which is proportional to the accretion timescale, see Nomoto & Sugimoto 1977) early in the accretion phase. The amount of the helium layer that can be built up before ignition then increases with the length of time where compressional heating remains insufficient to balance radiative cooling. If this condition is met (as expected, e.g. in less massive WDs - compare Fig. 4.2 A - or model sequences with large values of  $t_{\text{rise}}$ ), a WD in the linear scenario will accrete more than the same WD in the constant scenario. This is true even if  $\langle \dot{M}(t) \rangle$  or  $\dot{M}(t)$  are comparable to the accretion rate in the constant scenario. Figure 4.2 shows the mass of the helium envelope at ignition with respect to mass-transfer rate for all model sequences calculated in the linear scenario. From this (and the data given in Tab. 4.3) it is evident that, according to expectations, the helium shell mass at ignition qualitatively follows the same pattern as in the constant scenario. Namely, the higher the mass-transfer rate at the point of ignition, the smaller the mass of the helium shell. This is true for  $\langle \dot{M}(t) \rangle$  as well as  $\dot{M}(t)$  one.

At this point it is opportune to comment on the expected explosion characteristics of these hypothetical models. Woosley & Weaver (1994) studied the ability of a localized ignition in quiescent helium-rich stellar matter to induce a sustained supersonic burn, i.e. a detonation front. It was found that a local density of  $\sim 10^6 \text{ g/cm}^3$  was sufficient to inhibit a premature quenching of the supersonic flame. It was found that lower densities would lead to a subsonic burn, i.e. a deflagration. Woosley & Kasen (2011) subsequently argued that a detonation in the accumulated helium envelope of a CO WD would invariably lead to a detonation of the core, inducing a supernova (as opposed to a strong helium nova, as would be expected in a deflagration). In this light, detonations are more probable the longer the rise-time of the mass-accretion rate in a model sequence in the linear scenario. Further, models with lower initial mass tend to exhibit lower ignition densities.

Model sequences with either  $M_{\text{WD}} \geq 0.82 M_{\odot}$  or  $t_{\text{rise}} \leq 1 \cdot 10^7 \text{ yr}$  underestimate the final helium shell mass if  $\dot{M}(t)$  is used as a criterion and overestimate it if  $\langle \dot{M}(t) \rangle$  is used. In model sequences with  $M_{\text{WD}} = 0.54 M_{\odot}$  the discrepancy between  $\dot{M}(t)$  and the constant scenario and  $\langle \dot{M}(t) \rangle$  and the constant scenario is about equal ( $\sim 0.3 M_{\odot}$  in both cases). In all other cases  $\dot{M}(t)$  is approximated better, with a maximum discrepancy of  $\sim 0.1 M_{\odot}$ , than  $\langle \dot{M}(t) \rangle$ , which exhibits discrepancies of up to  $\sim 0.3 M_{\odot}$ . For this scenario, constant accretion seems to approximate the  $\dot{M}(t)$  better than  $\langle \dot{M}(t) \rangle$ .

#### 4. Effects of variable mass-transfer rates

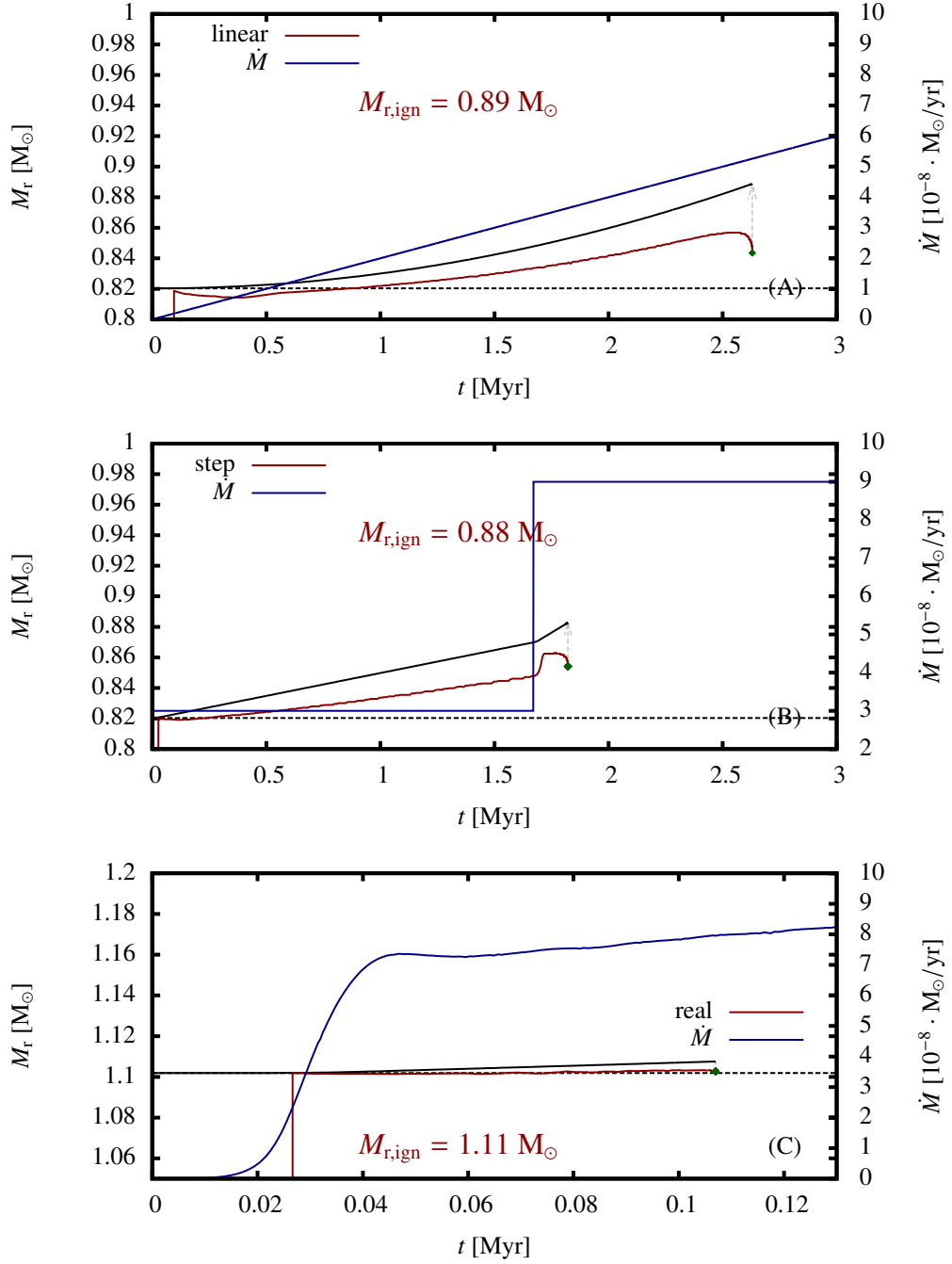


Figure 4.3.: Evolution of the point of maximum temperature (red line) during the mass-accretion phase in mass coordinates. The black line indicates the surface of the star in mass coordinates. The green dot indicated the point of helium ignition. The blue line is the current mass-transfer rate (mapped to the right y-axis).

Table 4.4.: Physical parameters at helium ignition of the set of step scenario systems.  $M_{\text{WD}}$  is the mass of the WD at the start of the accretion phase,  $\langle \dot{M}_f \rangle$  is the time-averaged mass-accretion rate at the point of helium ignition,  $t_{\text{ign}}$  is the age of the model at the time of helium ignition,  $M_{\text{He}}$  is the mass of the accumulated helium envelope,  $T_{\text{max}}$  is the maximum temperature in the model,  $\rho(T_{\text{max}})$  is the density at the point of  $T_{\text{max}}$  and  $M_r(T_{\text{max}})$  is the mass-coordinate of  $T_{\text{max}}$ .

#	$M_{\text{WD}}$ [ $M_{\odot}$ ]	$\langle \dot{M}_f \rangle$ [ $M_{\odot}/\text{yr}$ ]	$t_{\text{ign}}$ [Myr]	$M_{\text{He}}$ [ $M_{\odot}$ ]	$T_{\text{max}}$ [ $10^8 \text{ K}$ ]	$\rho(T_{\text{max}})$ [ $10^3 \text{ g/cm}^6$ ]	$M_r(T_{\text{max}})$ [ $M_{\odot}$ ]
s05	0.54	3.72	24.99	0.141	3.06	0.0777	0.5864
s08	0.82	3.42	51.41	0.062	3.62	0.1160	0.8540
s10	1.00	3.10	42.15	0.012	4.71	0.0031	1.0027

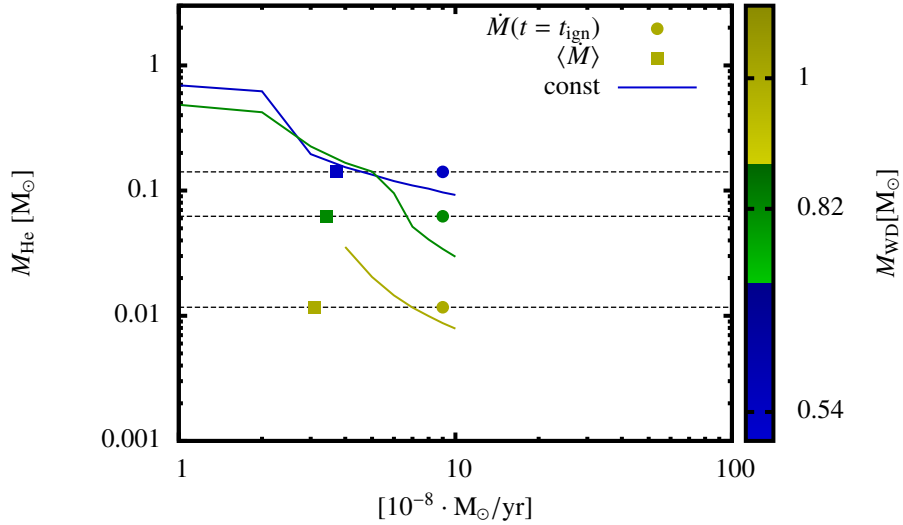


Figure 4.4.: Mass transfer rates in individual systems of the step scenario with respect to helium shell mass at ignition. Here color indicates the mass of the WD. Solid lines correspond to dots of the same color and indicate the amount of helium accumulated at corresponding mass-transfer rates in the constant accretion rate scenario, as presented by Neunteufel et al. (2017). Nomenclature is otherwise the same as in Fig. 4.2.

### 4.3.2. Step scenario systems

One of the mass-transfer modes discussed by Neunteufel et al. (2016) is the *biphasic* model. In these systems, which usually include a donor star of  $0.6 M_{\odot} < M_d < 0.9 M_{\odot}$  and feature short ( $< 0.07$  d) initial periods, a somewhat extended period of mass-transfer during the donor's helium main sequence proceeds at nuclear-timescale mass-transfer rates (case BA mass-transfer) of about  $\dot{M} \sim 3 \cdot 10^{-8} M_{\odot}/\text{yr}$ . After the initial nuclear-timescale mass-transfer phase, the donor contracts, ending mass-transfer, and exhausts its core helium supply. In the ensuing expansion the donor refills its Roche-lobe, initiating a phase of thermal-timescale mass-transfer (case BB mass-transfer).

The step scenario attempts to resolve whether, in this context, the time averaged mass-transfer rate in conjunction with results of constant accretion rate simulations is a good estimate of the expected final helium shell mass. The mass-transfer scheme of one representative system (s08<sup>3</sup>) is depicted in Fig. 4.1 (B). The model starts accreting at a constant mass-accretion rate, falling into the range of the low mass-accretion rate case as defined by Neunteufel et al. (2017), of  $\dot{M} \sim 3 \cdot 10^{-8} M_{\odot}/\text{yr}$ , and is allowed to accrete a certain amount helium. The amount of helium allowed to accumulate is less than required for detonation in the constant mass-accretion scenario ( $0.1 M_{\odot}$  for the  $M_{\text{WD}} = 0.54 M_{\odot}$ -sequence,  $0.05 M_{\odot}$  for the  $M_{\text{WD}} = 0.82 M_{\odot}$ -sequence and  $0.01 M_{\odot}$  for the  $M_{\text{WD}} = 1.00 M_{\odot}$ -sequence). The mass-accretion rate is subsequently increased to a value commensurate with the high accretion rate case as defined in Neunteufel et al. (2017). Figure 4.4 shows the final helium shell mass with respect to both  $\langle \dot{M}(t) \rangle$  and  $\dot{M}(t)$ .

In the step scenario, as in the linear scenario,  $\langle \dot{M}(t) \rangle$  overestimates the final helium shell mass by up to  $\sim 0.1 M_{\odot}$  at initial WD masses of  $M_{\text{WD}} = 0.54 M_{\odot}$  (see also Fig. 4.1 (B)), while  $\dot{M}(t)$  underestimates it by  $\sim 0.05 M_{\odot}$ . Figure 4.3 (B) shows the evolution of  $T_{\text{max}}$  of s08. As can be seen, the start of mass-accretion immediately heats up the surface of the WD, moving  $T_{\text{max}}$  from the center of the WD to the core-envelope interface and then into the helium envelope. Once the mass-accretion rate is increased,  $T_{\text{max}}$ , driven by the increase in compressional and viscous heating, moves further towards the surface of the envelope toward lower densities and remains there as an equilibrium between radiative cooling and heating effects is reached.  $T_{\text{max}}$  then moves rapidly inward through the helium envelope as a flame develops with the onset of helium ignition. This behavior is in concordance with the decrease of the compressional heating timescale (which, as mentioned, is proportional to the mass-accretion timescale) after the increase in the mass-transfer rate and thus entirely expected.

Figure 4.4 backs this up as the actual mass-transfer rate provides a - still too low, but - better estimate of the constant mass-transfer rate scenario. It does, however, pose a number of interesting questions regarding the evolution of accreting binaries, especially in the biphasic case alluded to in Neunteufel et al. (2016). Primarily this indicates that a substantial helium shell accumulated during a slow mass-transfer phase can be ignited after a comparatively short time when the mass-transfer rate suddenly increases. This may not only happen in instances of biphasic mass-transfer, but also if the donor experiences core helium exhaust during the mass-transfer phase, thereby proceeding to thermal timescale mass-transfer.

The onset of mass-transfer, as well as the length of the slow case BA mass-transfer phase heavily depends on the initial period of the system. This means that a final helium shell mass far lower than the one expected for low constant accretion rates but higher than for high constant accretion is the likeliest outcome for these biphasic systems.

<sup>3</sup>the model designation for step systems is composed as follows: "s" indicates the scenario, the appended number is equal to the initial mass of the WD rounded to the next  $0.1 M_{\odot}$  times ten

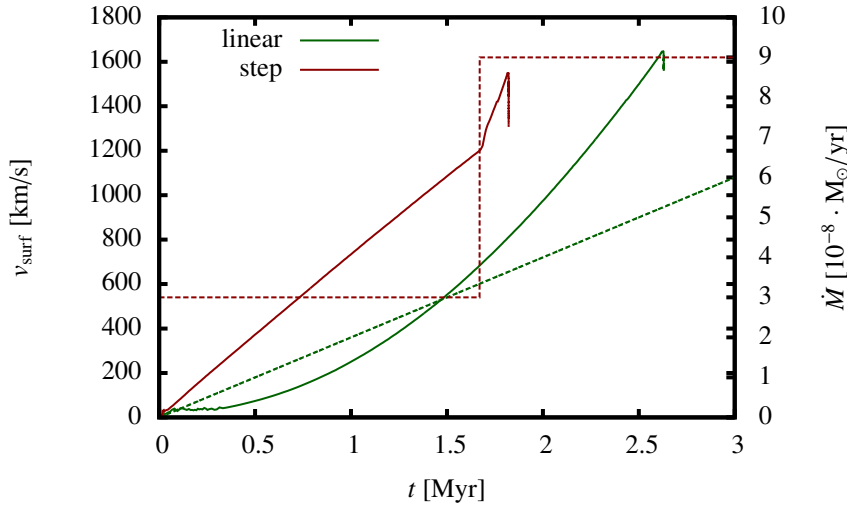


Figure 4.5.: Evolution of the surface rotational velocity of one linear system and one step system. The dotted line indicate the current mass-accretion rate, mapped to the right hand y-axis.

Another scenario, explicitly excluded for constant mass-transfer rates, is the induction of massive helium deflagration as a result of wind accretion. Neunteufel et al. (2017) explicitly excluded the possibility that wind accretion could lead to massive helium flashes or detonations owing to the insufficient main-sequence lifetime of helium stars massive enough to facilitate sufficiently high mass-accretion rates on a wind-accreting WD. In this scenario, a comparatively short ( $\sim 1$  Myr) could deposit a helium shell of a few percent of a solar mass onto the WD which would then be ignited by the donor undergoing RLOF.

At the same time the ignition densities are expected to be low (see Tab. 4.4), making a massive helium nova, more massive than would be expected in an assumed constant accretion scenario, the most likely outcome of such a system. Importantly, the ignition densities in this case are lower than would be expected for a constantly accreting WD with the same final helium shell mass. This result is significant since it indicates that previous studies have systematically underestimated the (already dominant) rate of occurrence of massive helium deflagrations as well as underestimated the mass of the deflagrating helium shell. These results also make the case that the initial orbital separation of He-accreting binary systems as well as the evolutionary behavior of the donor star (as argued by Neunteufel et al. (2016)) needs to be taken into account in predictions of the state of an accreting WD at the point of helium ignition.

#### 4.3.3. Rotation

The rotational development of an accreting WD with magnetic fields was extensively discussed by Neunteufel et al. (2017), but at this point a few comments with respect to variable mass-accretion rates are appropriate. Figure 4.5 shows the development of the surface velocity of model sequences l0817 (linear scenario) and s08 (step scenario). As was shown by Neunteufel et al. (2017), accreting white dwarfs subject to the Tayler-Spruit instability exhibit quasi-solid body rotation. Spin-up due to constant accretion is therefore expected to proceed approximately linearly proportional to the mass-

#### 4. Effects of variable mass-transfer rates

accretion rate. This was found to be realized in constantly accretion systems (by Neunteufel et al. 2017) as well as during the distinct phases of the step scenario systems. In the linear scenario, the surface velocity increases faster than linearly. It has been shown that increasing rotational velocities significantly increase the mass of the helium envelope necessary to induce helium ignition owing to the shallower density gradient induced by centrifugal forces. While step scenario models always ignite before a massive helium envelope is built up, linear scenario models, especially those featuring long rise-times (see Tab. 4.3) may acquire significant helium envelopes prior to helium ignition.

##### 4.3.4. Realistic scenario systems

The mass-accretion schemes used in realistic scenario model sequences are taken from separate runs that include a He-main sequence star and a point mass, used as a stand-in for the resolved WD model used in the accretion calculation. The resulting mass-transfer scheme is deemed to resemble that of a naturally occurring system of the given parameters.

For this scenario, we have calculated a representative sample of systems, containing several WD masses, donor star masses and initial orbital periods. The initial periods were chosen such that for each pair of WD and donor star masses one system would undergo case BA mass-transfer (realized with  $P = 0.04$  d) and the other case BB ( $P = 0.08$  d).

The evolution of the mass-transfer rate of one representative realistic scenario system is shown in Fig. 4.1 (C). As can be seen, as in the linear and step scenarios,  $\langle \dot{M}(t) \rangle$  greatly overestimates the mass of the helium shell. Brooks et al. (2015), whose resolved non-rotating binary systems resemble the slow (mass-transfer-wise) end ( $P_{\text{init}} = 0.04$  d) of the systems considered here support this conclusion. Similarly does Brooks et al. (2016), who considered He-shell flashes in fast accreting, non-rotating binary systems.

Table 4.5 gives the defining parameters of the simulated systems. Unlike with model sequences of the step or linear scenarios, where the mass-transfer rate monotonically increases, realistic systems undergoing case BA mass-transfer tend to experience an initial maximum in their mass-transfer rate (caused by the donor star’s envelope structure reconfiguring to take the mass loss into account) before decreasing to rates more aligned with the low mass-transfer rate case as defined by Neunteufel et al. (2017). The maximum of the mass-transfer rate is likewise recorded in Tab. 4.5. r050604N<sup>4</sup> and r080604N are deemed unphysical. The helium shell mass required in order to induce a helium ignition exceeds the available mass budget of the donor star in these systems (the donor becoming a WD). This was seen to be the major constraining factor by Neunteufel et al. (2017) for the production of helium detonations in He-star+WD systems.

A number of systems, however, namely r081004, r110604 and r110804 do accumulate a comparatively massive helium envelope and exhibit ignition densities in excess of  $\rho_{\text{crit}} = 10^6$  g/cm<sup>3</sup>, conforming to the low mass-accretion rate case as defined by Neunteufel et al. (2017). Ignition in these WDs would likely result in a supersonic runaway, and thus a supernova. According to Woosley & Kasen (2011), a detonation in the helium envelope of a sub-Chandrasekhar mass WD can lead to the destruction of the CO core in two ways. Either the detonation occurs at some distance from the core-envelope interface, leading to an inward-propagating shock front which ignites the CO core at

---

<sup>4</sup>the model designation for rotating systems is composed as follows: the letter designates the scenario, the first and second digit are the mass of the WD rounded to the nearest 0.1  $M_{\odot}$  times ten, the third and fourth digits are the same for the mass of the donor, the last two digits are the initial rotational period in days times 100 and the optional letter “N” signifies that the system is deemed unphysical



the interface, or a detonation at the interface compresses the core, leading to a secondary ignition at the center of the core. The result in both cases is, depending on the mass of the helium envelope, a spectrally peculiar SN Ia. The ignitions observed in the three model sequences mentioned above occur almost directly at the interface and would therefore fall into the core-compression category. In the remaining systems, ignition of the helium envelope is precipitated by high mass-accretion rates, exhibiting ignition points close to the surface of the envelope and correspondingly leading to low helium shell masses at ignition (see Fig 4.3 (C)). These systems conform to the high mass-accretion rate case as defined by Neunteufel et al. (2017), their outcomes representing He-novae of different strengths.

Notable is the absence of systems with  $M_{\text{He}} \approx 0.2 M_{\odot}$  and ignition densities of slightly less than  $\rho_{\text{crit}}$ , which were identified as promising candidate progenitors of fast, faint Ca-enhanced SNe (Waldman et al. 2011) by Neunteufel et al. (2017). This may be due to an insufficiently large sample size.

Figure 4.6 shows the final mass of the helium shell of the realistic scenario systems with respect to the calculated mass-transfer rates with the red lines, as before, indicating the the results for constant accretion systems. Notably, systems with  $P_{\text{init}} = 0.08$  d (leading, as mentioned, to case BA mass-transfer), irrespective of the mass of the accretor, seem to be very well described by the maximum mass-transfer rate with  $\langle \dot{M}(t) \rangle$  again overestimating the mass of the expected helium envelope by a considerable margin. Due to lack of data for constant accretion for the higher mass systems, the accuracy for low mass-accretion regimes cannot be commented on. For systems with  $M_{\text{WD}} = 0.54 M_{\odot}$  and  $M_{\text{WD}} = 0.82 M_{\odot}$ ,  $\dot{M}(t)$  seems to be the best fit.

## 4.4. Conclusions

We calculated a number of CO WD model sequences with time-varying mass-transfer rates, adhering to prescribed mass-transfer schemes. Our model sequences are resolved, including numerical treatment of rotation, angular momentum transfer through the dynamical shear instability, secular shear instability, Solberg-Hoyland instability and the Tayler-Spruit instability.

Our models confirm previous results in that lower mass-transfer rates, actual, time averaged and maximal, of time variable mass-transfer histories are correlated with higher helium shell masses at ignition. Higher helium shell masses, in turn, are correlated with higher ignition densities. Helium detonations, as opposed to deflagrations, are therefore more likely if the system undergoes case BA mass-transfer, which implies nuclear-timescale mass-transfer, than case BB mass-transfer, which implies thermal-timescale mass-transfer, and vice versa. This also reinforces the previously held conceit that faint, fast Ca-rich SNe (Waldman et al. 2011), should a connection to helium accretion in He-star CO binaries be established, require initial case BA mass-transfer. Helium deflagrations of  $M_{\text{He}} < 0.05 M_{\odot}$  are the most probable outcome of any of these systems.

We further confirm that very low mass-transfer rates  $\dot{M} \leq 2 \cdot 10^{-8} M_{\odot}/\text{yr}$  will not lead to helium ignition in low-mass WDs ( $M \leq 0.82 M_{\odot}$ ) but to the creation of a detached double WD system with two CO WDs, the more massive of which will feature a massive, inert helium envelope and rapid rotation. These systems may either merge in time due to angular momentum loss by gravitational radiation and produce cataclysmic event (e.g., van Kerkwijk et al. 2010; Dan et al. 2014) or an R CrB star (e.g., Staff et al. 2012; Menon et al. 2013). Since, as shown by Neunteufel et al. (2017), ignition of objects undergoing slow mass-transfer is inhibited by the shallow density gradient prescribed by their high rotational velocity, helium ignition could also be triggered by an increase of the density of

#### 4. Effects of variable mass-transfer rates

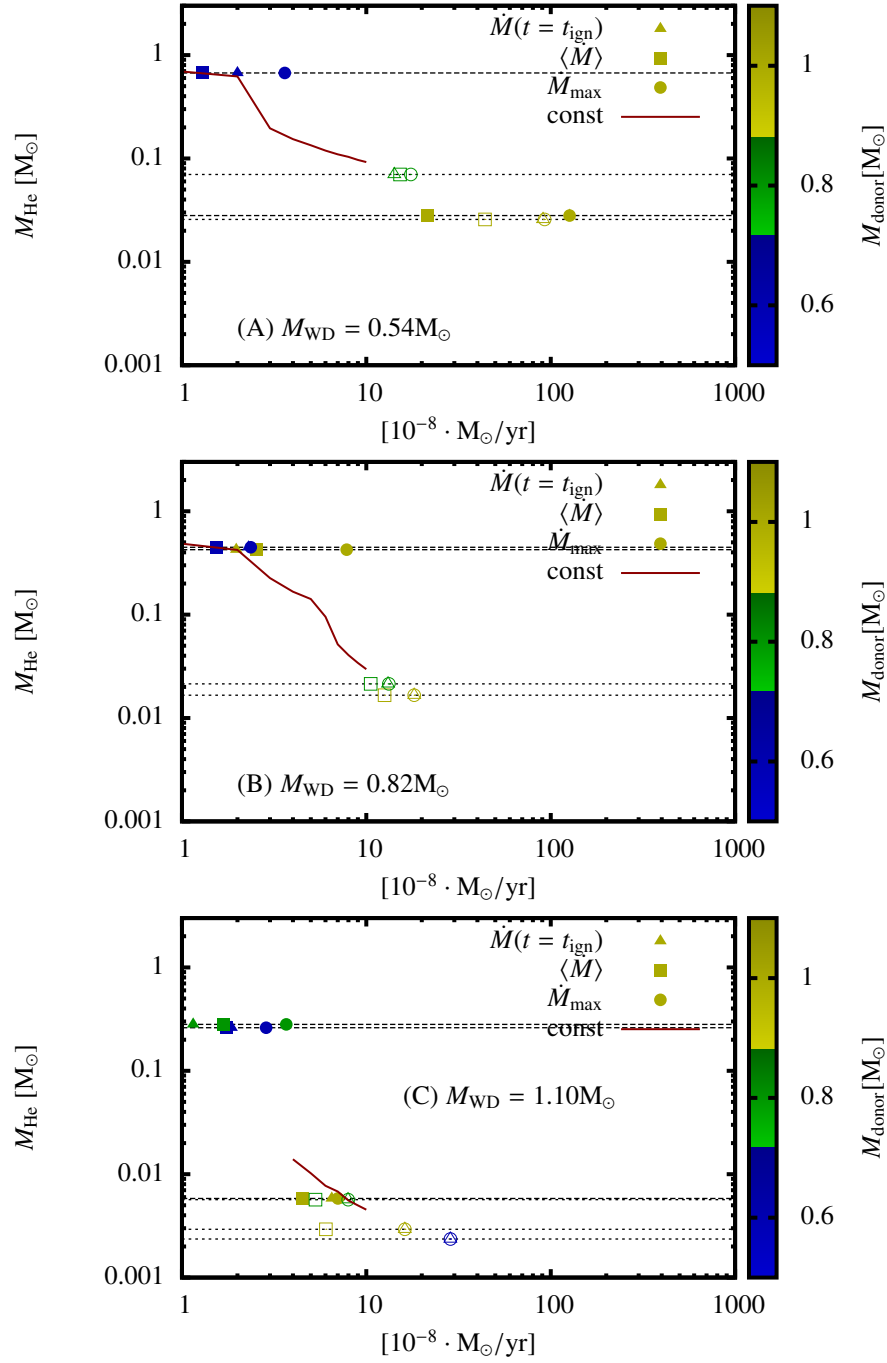


Figure 4.6.: Comparison of the attained mass-transfer rates in individual systems of the realistic scenario with respect to helium shell mass at ignition. Here color indicates the mass of the donor star. Filled dots and dashed grey lines indicate that the model sequence was computed with an initial period of 0.04 d, blank dots and dotted lines indicate an initial period of 0.08 d. Nomenclature otherwise like in Fig. 4.2

the accreted material at the core-envelope interface if the WD is spun down by tidal interaction with the - now degenerate - companion. This possibility, however, would have to be investigated in greater detail.

Independent of the chosen mass-transfer scheme, our calculations show that the assumption of constant mass-transfer rates does not adequately describe the mass of the helium shell at the point of helium ignition. This should be understood as a word of caution in that progenitor candidate models obtained under this assumption can, if they occur in nature, only be the possible endpoint of a variable mass-transfer history. Further we note that the helium shell mass at the point of helium ignition resulting from a WD undergoing variable mass-transfer cannot be adequately modeled by using the time averaged mass-transfer rate ( $\langle \dot{M}(t) \rangle$ ) in conjunction with the results of constant mass-transfer models as a criterion. Application of this criterion consistently overestimates the mass-transfer rate. This problem is most pronounced in systems with consistently high mass-transfer rates (such as systems with case BB mass-transfer), whose behavior is better predicted by using  $\dot{M}(t)$  instead of  $\langle \dot{M}(t) \rangle$ . In systems with consistently low mass-transfer rates, such as biphasic systems,  $\dot{M}(t)$  consistently underestimates the mass of the accumulated helium, the realistic value lying between those given by using the time-averaged mass-transfer rate as a criterion and using  $\dot{M}(t)$  as a criterion.

Comparison of our step scenario models with the realistic scenario models reveals that a change of the accretion regime, slow to fast, as is expected either in systems undergoing biphasic mass-transfer (see Neunteufel et al. 2016) or if the donor star reaches the end of its core helium burning phase during mass-transfer, introduces an additional degree of freedom into the relation between mass-transfer rate and final helium shell mass and the relation between final helium shell mass and ignition density. Especially the realization that, depending on the behavior of the donor star, a high final helium shell mass does not necessarily imply a high ignition density should be taken into account in the modeling of the explosion physics of these objects as well as in population synthesis calculations.

Previous attempts at predicting the resulting rate of helium detonations (Woosley & Kasen 2011; Wang et al. 2013; Neunteufel et al. 2016) would have to be revised towards lower occurrence rates, irrespective of the type of expected transient. On the other hand, it also follows that there should be a continuum of helium shell masses able to undergo a deflagration of the accumulated helium. Systems like this are expected to exhibit helium shell masses between those given as the low-mass-accretion-rate case and those given as the high-mass-accretion-rate case by Neunteufel et al. (2017), albeit with comparatively low ignition densities. These systems would increase the parameter space where massive helium novae would be expected. Unfortunately the literature on explosion calculations in helium envelopes of sub-Chandrasekhar mass CO WD's is sparse. Further work on the subject would be necessary in order to link these progenitor candidates to existing transient observations.

Table 4.5.: Physical parameters at helium ignition for the set of realistic scenario systems.  $M_{\text{WD}}$  is the mass of the WD at the start of the accretion phase,  $M_{\text{d}}$  the mass of the donor,  $\dot{M}_{\text{f}}$  is the mass-transfer rate at the point of helium ignition,  $\langle \dot{M}_{\text{f}} \rangle$  is the time-averaged mass-accretion rate at the point of helium ignition,  $\dot{M}_{\text{max}}$  the maximum accretion rate reached during the accretion phase,  $t_{\text{ign}}$  is the age of the model at the time of helium ignition,  $M_{\text{He}}$  is the mass of the accumulated helium envelope,  $T_{\text{max}}$  is the maximum temperature in the model,  $\rho(T_{\text{max}})$  is the density at the point of  $T_{\text{max}}$ ,  $M_r(T_{\text{max}})$  is the mass-coordinate of  $T_{\text{max}}$  and  $v_{\text{f,surf}}$  is the surface velocity of the WD at the point of ignition. Systems having the letter “N” appended to their designation exceed their plausible mass budget and are deemed to be unphysical.

#	$M_{\text{WD}}$ [ $M_{\odot}$ ]	$M_{\text{d}}$ [ $M_{\odot}$ ]	$P$ [d]	$\dot{M}_{\text{f}}$ [ $M_{\odot}/\text{yr}$ ]	$\langle \dot{M}_{\text{f}} \rangle$ [ $M_{\odot}/\text{yr}$ ]	$\dot{M}_{\text{max}}$ [ $M_{\odot}/\text{yr}$ ]	$t_{\text{ign}}$ [Myr]	$M_{\text{He}}$ [ $M_{\odot}$ ]	$T_{\text{max}}$ [ $10^8 \text{K}$ ]	$\rho(T_{\text{max}})$ [ $10^6 \text{g/cm}^3$ ]	$M_r(T_{\text{max}})$ [ $M_{\odot}$ ]	$v_{\text{f,surf}}$ [ $10^3 \text{km/s}$ ]
r050604N	0.54	0.60	0.04	2.00	1.30	3.61	72.93	0.672	2.00	10.1477	0.5042	4.426
r050808	0.54	0.80	0.08	14.17	15.22	17.42	21.67	0.070	3.06	0.0309	0.5445	1.723
r051004	0.54	1.00	0.04	126.63	21.43	126.64	21.34	0.028	2.85	0.0026	0.5447	1.033
r051008	0.54	1.00	0.08	90.85	44.02	92.75	21.26	0.026	2.87	0.0029	0.5439	1.080
r080604N	0.82	0.60	0.04	2.29	1.55	2.36	78.53	0.448	1.85	6.9956	0.8281	4.762
r080808	0.82	0.80	0.08	13.11	10.56	13.25	49.79	0.021	3.55	0.0806	0.8208	0.537
r081004	0.82	1.00	0.04	1.97	2.54	7.83	66.34	0.425	2.14	5.8265	0.8283	4.602
r081008	0.82	1.00	0.08	18.18	12.56	18.18	49.72	0.017	2.49	0.0931	0.8207	0.466
r110604	1.10	0.60	0.04	1.86	1.74	2.86	68.10	0.261	2.20	5.7602	1.1142	5.510
r110608	1.10	0.60	0.08	28.52	0.01	28.61	85.88	0.002	4.41	0.0019	1.1019	0.021
r110804	1.10	0.80	0.04	1.15	1.68	3.68	69.76	0.281	1.90	7.0294	1.1138	5.728
r110808	1.10	0.80	0.08	7.96	5.30	7.96	53.20	0.006	6.00	0.0492	1.1026	0.184
r111004	1.10	1.00	0.04	6.50	4.49	7.01	53.22	0.006	6.00	0.0534	1.1025	0.193
r111008	1.10	1.00	0.08	16.16	6.03	16.16	53.14	0.003	4.64	0.0021	1.1019	0.029

## 5. Conclusions

The relationship between He-star + CO WD binaries and explosive transients has been studied from a variety of angles in this thesis:

### 5.1. SNe Ia from He accreting WDs

The lack of hydrogen makes the helium accretion an attractive proposition for the progenitors of canonical SNe Ia and light curve models suggest that helium accreting CO WDs undergoing double detonation at sub-Chandrasekhar masses could conceivably produce these events. These SNe Ia-like light curves require a comparatively low-mass ( $\lesssim 0.05M_{\odot}$ ) helium layer to undergo a strong enough ignition to produce a supersonic burn. In chapter 2 it was shown that under the conditions of realistic mass-transfer and donor star evolution (neglecting rotational effects), about 10 % of systems with final helium shell masses could be expected to feature Ia-like spectra. SN Ia-like spectra are correlated with WD masses of  $\gtrsim 0.8M_{\odot}$  and at least some of them are expected to experience at least one helium ignition prior to exploding in an SN Ia-like event. Peculiar spectra (possibly SN Iax-like) are expected to dominate the double-detonation-induced supernova-rate. Taking into account rotational and magnetic effects (ch. 3), the parameter space for explosions in general is diminished, with rotational effects acting to decrease the ignition density to below the critical density of  $\rho_{\text{crit}} = 10^6 \text{ g/cm}^3$  for WDs accumulating less than  $\sim 0.1M_{\odot}$  of helium before ignition. Using the mass of the helium shell as a yardstick, these systems are not expected to feature SN Ia-like spectra. However, as seen in Ch. 4, models assuming constant accretion rates tend to overestimate the amount of helium accumulated at ignition and underestimate the ignition density. This means that, while the possibility for SN Ia-like spectra is diminished for sub-Chandrasekhar WDs, depending on the mass retention efficiency of these non-detonating ignitions (which would more likely take the guise of massive helium novae), a initially sufficiently massive WD could increase in mass until Chandrasekhar-mass detonations become a possibility.

### 5.2. Ignition conditions

The question of which kind of explosive transient is produced by a helium ignition on a sub-Chandrasekhar-mass WD intimately depends on the conditions at the point of ignition. The conditions in turn are influenced by how the WD reacts to the accreted material. Chapter 3 investigates the accretion of helium onto WDs of adequate mass ( $\sim 0.5 - 1.1 M_{\odot}$ ) to expect sub-Chandrasekhar-mass ignition considering the influence of rotation and magnetic instabilities. Inclusion of the Tayler-Spruit instability results in quasi-solid body rotation of the WD, as opposed to strong differential rotation if only dynamic effects are considered. The mass-requirements for helium ignition are shifted towards higher masses, consequent to the less-localized effect of viscous heating and the shallower density structure imposed by quasi-solid body rotation. The ignition density is shifted towards lower densities, making

## 5. Conclusions

detonations less likely and increasing the expected rate of massive helium novae with helium shell masses of  $\sim 0.01 - 0.1 M_{\odot}$ . Helium ignitions seem to be excluded for lower mass ( $\leq 0.82 M_{\odot}$ ) WDs undergoing accretion with rates of  $\leq 2 \cdot 10^{-8} M_{\odot}/\text{yr}$ , because prospective donor stars capable of providing these low mass-transfer rates (which requires a helium star of  $M \leq 0.7 M_{\odot}$ ) would be unable to provide a sufficient mass budget. These binaries are expected to merge at some point during their evolution and could conceivably produce a supernova along the lines of the double-degenerate scenario (e.g., van Kerkwijk et al. 2010; Dan et al. 2014) or, possibly, an R CrB star (e.g., Staff et al. 2012; Menon et al. 2013). Systems undergoing massive helium nova events can continue to accrete matter, possibly repeating the helium ignition. Since these objects would carry over a significant amount of heat and angular momentum from their previous accretion phase, subsequent ignitions would, in all likelihood, require comparable amounts of helium (depending on the accretion rate). If a significant amount of mass is retained in these deflagrations, the CO WD could still detonate when approaching the Chandrasekhar mass.

Mass transfer rates of  $\sim 3 - 5 \cdot 10^{-8} M_{\odot}/\text{yr}$  produce final helium shell masses of  $0.1 - 0.2 M_{\odot}$  and ignition densities of  $\sim 7 \cdot 10^5 \text{ g/cm}^3$ , which would be commensurate with accretion induced models (Waldman et al. 2011) of fast, faint Ca-enhanced SNe Ib.

Taking into account variable mass-transfer rates, as studied in Ch. 4, the picture changes somewhat. The intensity of mass-accretion is the dominant factor in determining the mass of the helium shell at ignition. This fact puts increased emphasis on the initial orbital separation of the system and the evolutionary behavior of the donor star, which together control the development of the mass-transfer rate with time. A rapid increase in the mass-transfer rate (most likely when the donor star reaches the end of core helium burning) can induce an ignition in a comparatively massive helium envelope which the star accumulated during the slow phase. These donor-induced ignitions feature very low ignition densities, increasing the likelihood of massive helium novae and introducing a degeneracy into the He-shell-ignition-density-parameter-space. This implies that future progenitor calculations are advised to take the time variability of the mass-transfer rate into account.

### 5.3. Outlook

The findings of this thesis run counter to the idea that SNe Ia could be produced by sub-Chandrasekhar-mass He-accreting WDs, closing this scenario even as a side-channel. The search for the elusive progenitor of these transients will have to be conducted by other means.

Ignition densities, especially in rotating systems, mostly seem to contradict a relation to SNe Iax, although dedicated explosion simulations and light curve modeling using more specialized computing framework could conceivably reveal connections to observed transients. Especially the possibility of a connection with the Ca-enhanced SNe Ib should be investigated using explosion simulations and light curve modeling.

The high-mass helium deflagrations (massive helium novae) found in many of the computed model sequences do not seem to have any readily available, frequently observed, counterpart, although one could speculate about a connection to the theoretically predicted SNe .Ia. Explosion calculations and light curve modeling for progenitors of this type would be needed in order to establish connections with other models.

The increase of the ignition mass of low-mass  $\leq 0.05 M_{\odot}$  helium ignitions, mostly found at high mass-accretion rates could have some bearing on the theoretical modeling of AV CVn systems.

Rotation and magnetic effects were shown to have a profound effect on the development of the unstable helium ignition. Future simulations of this kind would be well advised to take this into consideration.

Time variability of the mass-transfer rate introduces a degeneracy into the ignition parameter space. Future calculations of this kind should, wherever possible, include the development of the donor star and the change in orbital separation.

As these systems are invariably the result of common-envelope evolution, further refinement of the understanding of this phase of stellar evolution, especially with regards to the resulting orbital separation and luminosity of the accretor, will allow more accurate predictions in future studies.

Although He-star + CO WD binaries seem to be excluded as progenitors of SNe Ia, this interesting type of system with its potential connections to other important and, as of yet, mysterious transient phenomena, is an encouraging object of further theoretical study.





## A. Model parameters for chapter 2

Table A.1.: Most relevant model parameters of the model sequences produced in chapter 2.  $M_{\text{donor}}$  is the mass of the donor,  $M_{\text{WD}}$  the mass of the WD,  $P_{\text{init}}$  the initial period in days,  $M_{\text{f,donor}}$  The final mass of the donor,  $M_{\text{f,WD}}$  the final mass of the WD,  $M_{\text{He}}$  the final mass of the he-shell, # defl the number of massive deflagration  $M_{\text{defl}}$  is the mass lost in massive deflagrations and  $M_{\text{nova}}$  the mass lost in low mass novae (empty rows indicate that the non-logarithmic value of the parameter is zero). “Fate” indicates the final outcome of the system with “det” standing for a detonation, “n” for the donor becoming a red giant, terminating calculations, “me” a possible merger and “f” for a failed run.

#	$M_{\text{donor}}$ [ $M_{\odot}$ ]	$M_{\text{WD}}$ [ $M_{\odot}$ ]	$P_{\text{init}}$ [d]	$M_{\text{f,donor}}$ [ $M_{\odot}$ ]	$M_{\text{f,WD}}$ [ $M_{\odot}$ ]	$M_{\text{He}}$ [ $M_{\odot}$ ]	# defl	$M_{\text{defl}}$ log $M/M_{\odot}$	$M_{\text{nova}}$ log $M/M_{\odot}$	fate
05080025	0.5	0.8	0.025	0.329	0.971	0.171	0		-4.886	det
05080030	0.5	0.8	0.030	0.327	0.973	0.173	0		-3.979	det
05080035	0.5	0.8	0.035	0.321	0.979	0.179	0		-4.585	det
05080040	0.5	0.8	0.040	0.306	0.994	0.194	0		-4.119	det
05080045	0.5	0.8	0.045	0.290	1.010	0.210	0		-4.187	det
05080050	0.5	0.8	0.050	0.273	1.027	0.227	0		-3.648	det
05080055	0.5	0.8	0.055	0.278	1.022	0.222	0		-3.650	det?
05080060	0.5	0.8	0.060	0.268	1.032	0.236	0		-4.252	f
05080065	0.5	0.8	0.065	0.242	1.058	0.258	0			det?
05080070	0.5	0.8	0.070	0.293	1.007	0.207	0		-8.523	det
05080075	0.5	0.8	0.075	0.394	0.800	0.000	2	-1.282	-1.268	n
05080080	0.5	0.8	0.080	0.500	0.800	0.000	0		-5.939	n
05080085	0.5	0.8	0.085	0.500	0.800	0.000	0		-6.578	n
05080090	0.5	0.8	0.090	0.500	0.800	0.000	0			n
05080095	0.5	0.8	0.095	0.500	0.800	0.000	0		-5.361	n

*Continued on next page*

Table A.1 – *Continued from previous page*

#	$M_{\text{donor}}$	$M_{\text{WD}}$	$P_{\text{init}}$	$M_{\text{f,donor}}$	$M_{\text{f,WD}}$	$M_{\text{He}}$	# defl	$M_{\text{defl}}$	$M_{\text{nova}}$	fate
05080100	0.5	0.8	0.100	0.500	0.800	0.000	0		-7.377	n
05080105	0.5	0.8	0.105	0.500	0.800	0.000	0		-7.398	n
05080110	0.5	0.8	0.110	0.500	0.800	0.000	0		-7.377	n
05080115	0.5	0.8	0.115	0.500	0.800	0.000	0			n
05080120	0.5	0.8	0.120	0.500	0.800	0.000	0			n
06080030	0.6	0.8	0.030	0.414	0.986	0.186	0		-4.367	det
06080035	0.6	0.8	0.035	0.394	1.006	0.206	0		-4.658	det
06080040	0.6	0.8	0.040	0.372	1.028	0.228	0		-4.215	det
06080045	0.6	0.8	0.045	0.351	1.049	0.249	0		-5.523	det
06080050	0.6	0.8	0.050	0.332	1.068	0.268	0		-7.553	det
06080055	0.6	0.8	0.055	0.463	0.937	0.273	0			det
06080060	0.6	0.8	0.060	0.378	0.808	0.000	7	-1.407	-0.758	n
06080065	0.6	0.8	0.065	0.550	0.800	0.000	1	-1.298	-5.488	n
06080070	0.6	0.8	0.070	0.585	0.800	0.000	1	-1.834	-5.656	n
06080075	0.6	0.8	0.075	0.600	0.800	0.000	0	-3.618	-6.033	n
06080080	0.6	0.8	0.080	0.600	0.800	0.000	0		-7.699	n
06080085	0.6	0.8	0.085	0.600	0.800	0.000	0		-7.854	n
06080090	0.6	0.8	0.090	0.600	0.800	0.000	0		-8.046	n
06080095	0.6	0.8	0.095	0.600	0.800	0.000	0		-8.222	n
06080100	0.6	0.8	0.100	0.600	0.800	0.000	0			n
06080105	0.6	0.8	0.105	0.600	0.800	0.000	0		-7.959	n
06080110	0.6	0.8	0.110	0.600	0.800	0.000	0		-8.000	n
06080115	0.6	0.8	0.115	0.600	0.800	0.000	0		-8.222	n
06080120	0.6	0.8	0.120	0.600	0.800	0.000	0			n
07080030	0.7	0.8	0.030	0.528	0.972	0.172	0			det
07080035	0.7	0.8	0.035	0.514	0.986	0.186	0			det
07080040	0.7	0.8	0.040	0.480	1.020	0.220	0		-5.000	det
07080045	0.7	0.8	0.045	0.448	1.052	0.252	0		-5.999	det
07080050	0.7	0.8	0.050	0.433	1.067	0.267	0		-7.066	det

*Continued on next page*

Table A.1 – *Continued from previous page*

#	$M_{\text{donor}}$	$M_{\text{WD}}$	$P_{\text{init}}$	$M_{\text{f,donor}}$	$M_{\text{f,WD}}$	$M_{\text{He}}$	# defl	$M_{\text{defl}}$	$M_{\text{nova}}$	fate
07080055	0.7	0.8	0.055	0.546	0.800	0.000	1	-0.989	-1.286	n
07080060	0.7	0.8	0.060	0.594	0.800	0.000	1	-0.974	-5.625	n
07080065	0.7	0.8	0.065	0.618	0.800	0.000	1	-1.084	-6.133	n
07080070	0.7	0.8	0.070	0.633	0.800	0.000	1	-1.177	-6.274	n
07080075	0.7	0.8	0.075	0.644	0.856	0.056	0			n
07080080	0.7	0.8	0.080	0.645	0.806	0.000	1	-1.307	-6.609	n
07080085	0.7	0.8	0.085	0.653	0.804	0.000	1	-1.368	-6.475	n
07080090	0.7	0.8	0.090	0.659	0.804	0.000	1	-1.425	-7.149	n
07080095	0.7	0.8	0.095	0.667	0.800	0.000	1	-1.481		n
07080100	0.7	0.8	0.100	0.671	0.800	0.000	1	-1.536	-6.393	n
07080105	0.7	0.8	0.105	0.674	0.800	0.000	1	-1.590	-6.943	n
07080110	0.7	0.8	0.110	0.677	0.800	0.000	1	-1.646		n
07080115	0.7	0.8	0.115	0.680	0.800	0.000	1	-1.702		n
07080120	0.7	0.8	0.120	0.684	0.800	0.000	1	-1.801	-7.046	n
08080030	0.8	0.8	0.030	0.642	0.958	0.158	0		-4.469	det
08080035	0.8	0.8	0.035	0.636	0.964	0.164	0		-15.955	det
08080040	0.8	0.8	0.040	0.629	0.971	0.171	0		-15.955	det
08080045	0.8	0.8	0.045	0.572	1.028	0.228	0			det
08080050	0.8	0.8	0.050	0.566	0.800	0.000	2	-0.823	-1.077	n
08080055	0.8	0.8	0.055	0.628	0.915	0.115	2	-2.332	-1.281	det
08080060	0.8	0.8	0.060	0.681	0.919	0.119	0		-15.955	det
08080065	0.8	0.8	0.065	0.648	0.805	0.000	2	-1.205	-1.073	n
08080070	0.8	0.8	0.070	0.666	0.800	0.000	2	-1.730	-0.936	n
08080075	0.8	0.8	0.075	0.674	0.800	0.000	2	-2.244	-0.920	n
08080080	0.8	0.8	0.080	0.680	0.800	0.000	1	-2.359	-0.937	n
08080085	0.8	0.8	0.085	0.686	0.800	0.000	1	-2.448	-0.957	n
08080090	0.8	0.8	0.090	0.691	0.800	0.000	1	-2.528	-0.975	n
08080095	0.8	0.8	0.095	0.696	0.800	0.000	1	-2.546	-0.993	n
08080100	0.8	0.8	0.100	0.700	0.800	0.000	1	-2.597	-1.009	n

*Continued on next page*

Table A.1 – *Continued from previous page*

#	$M_{\text{donor}}$	$M_{\text{WD}}$	$P_{\text{init}}$	$M_{\text{f,donor}}$	$M_{\text{f,WD}}$	$M_{\text{He}}$	# defl	$M_{\text{defl}}$	$M_{\text{nova}}$	fate
08080105	0.8	0.8	0.105	0.703	0.800	0.000	1	-2.638	-1.024	n
08080110	0.8	0.8	0.110	0.706	0.802	0.002	0	-3.622	-1.038	n
08080115	0.8	0.8	0.115	0.709	0.800	0.000	1	-2.693	-1.051	n
08080120	0.8	0.8	0.120	0.712	0.802	0.002	0	-3.682	-1.063	n
09080035	0.9	0.8	0.035	0.683	0.951	0.151	17	-1.248	-2.055	det
09080040	0.9	0.8	0.040	0.632	1.016	0.216	15	-1.318	-2.365	det
09080045	0.9	0.8	0.045	0.735	0.965	0.165	0		-6.000	det
09080050	0.9	0.8	0.050	0.604	0.909	0.000	1	-1.011	-1.050	n
09080055	0.9	0.8	0.055	0.640	0.800	0.000	1	-1.798	-0.613	n
09080060	0.9	0.8	0.060	0.660	0.800	0.000	2	-2.060	-0.637	n
09080065	0.9	0.8	0.065	0.676	0.800	0.000	2	-2.222	-0.661	n
09080070	0.9	0.8	0.070	0.686	0.800	0.000	1	-2.445	-0.677	n
09080075	0.9	0.8	0.075	0.695	0.800	0.000	1	-2.568	-0.693	n
09080080	0.9	0.8	0.080	0.702	0.800	0.000	1	-2.639	-0.708	n
09080085	0.9	0.8	0.085	0.708	0.802	0.002	0	-3.499	-0.721	n
09080090	0.9	0.8	0.090	0.713	0.800	0.000	1	-2.759	-0.733	n
09080095	0.9	0.8	0.095	0.718	0.801	0.001	0	-3.595	-0.743	n
09080100	0.9	0.8	0.100	0.722	0.801	0.001	0	-3.640	-0.753	n
09080105	0.9	0.8	0.105	0.725	0.801	0.001	0	-3.703	-0.761	n
09080110	0.9	0.8	0.110	0.729	0.801	0.001	0	-3.733	-0.769	n
09080115	0.9	0.8	0.115	0.728	0.865	0.000	1	-2.914	-0.976	n
09080120	0.9	0.8	0.120	0.730	0.881	0.000	1	-2.923	-1.059	n
10080035	1.0	0.8	0.035	0.662	0.981	0.181	17	-1.246	-0.997	det
10080040	1.0	0.8	0.040	0.526	0.853	0.000	18	-0.529	-0.903	n
10080045	1.0	0.8	0.045	0.597	0.830	0.000	18	-0.660	-0.812	n
10080050	1.0	0.8	0.050	0.659	1.038	0.038	0	-2.708	-0.995	det
10080055	1.0	0.8	0.055	0.644	0.934	0.000	1	-1.951	-0.677	n
10080060	1.0	0.8	0.060	0.676	0.800	0.000	1	-2.336	-0.496	n
10080065	1.0	0.8	0.065	0.690	0.800	0.000	1	-2.542	-0.512	n

*Continued on next page*

Table A.1 – *Continued from previous page*

#	$M_{\text{donor}}$	$M_{\text{WD}}$	$P_{\text{init}}$	$M_{\text{f,donor}}$	$M_{\text{f,WD}}$	$M_{\text{He}}$	# defl	$M_{\text{defl}}$	$M_{\text{nova}}$	fate
10080070	1.0	0.8	0.070	0.702	0.800	0.000	1	-2.637	-0.529	n
10080075	1.0	0.8	0.075	0.712	0.801	0.001	0	-3.382	-0.543	n
10080080	1.0	0.8	0.080	0.714	0.930	0.001	0	-2.957	-0.808	n
10080085	1.0	0.8	0.085	0.718	0.974	0.001	0	-3.040	-0.971	n
10080090	1.0	0.8	0.090	0.723	1.000	0.001	0	-3.116	-1.118	n
10080095	1.0	0.8	0.095	0.727	1.016	0.000	0	-3.087	-1.253	n
10080100	1.0	0.8	0.100	0.732	1.022	0.000	0	-3.156	-1.337	n
10080105	1.0	0.8	0.105	0.735	1.028	0.000	0	-3.149	-1.440	n
10080110	1.0	0.8	0.110	0.739	1.030	0.000	0	-3.203	-1.515	n
10080115	1.0	0.8	0.115	0.741	1.031	0.001	0	-3.939	-1.563	n
10080120	1.0	0.8	0.120	0.744	1.031	0.001	0	-3.975	-1.612	n
05090025	0.5	0.9	0.025	0.353	1.047	0.147	0		-3.879	det
05090030	0.5	0.9	0.030	0.349	1.051	0.151	0		-4.921	det
05090035	0.5	0.9	0.035	0.346	1.054	0.154	0		-3.889	det
05090040	0.5	0.9	0.040	0.341	1.059	0.159	0		-4.886	det
05090045	0.5	0.9	0.045	0.336	1.064	0.164	0		-4.268	det
05090050	0.5	0.9	0.050	0.332	1.068	0.168	0		-3.372	det
05090055	0.5	0.9	0.055	0.327	1.073	0.173	0		-4.721	det
05090060	0.5	0.9	0.060	0.322	1.078	0.178	0		-5.155	det
05090065	0.5	0.9	0.065	0.320	1.080	0.180	0		-7.699	det
05090070	0.5	0.9	0.070	0.323	1.077	0.177	0		-5.945	det
05090075	0.5	0.9	0.075	0.375	0.972	0.000	0	-2.621	-1.296	n
05090080	0.5	0.9	0.080	0.500	0.900	0.000	0	-6.000	-4.350	n
05090085	0.5	0.9	0.085	0.500	0.900	0.000	0		-5.598	n
05090090	0.5	0.9	0.090	0.500	0.900	0.000	0			n
05090095	0.5	0.9	0.095	0.500	0.900	0.000	0			n
05090100	0.5	0.9	0.100	0.500	0.900	0.000	0			n
05090105	0.5	0.9	0.105	0.500	0.900	0.000	0		-7.398	n
05090110	0.5	0.9	0.110	0.500	0.900	0.000	0		-7.456	n

*Continued on next page*

Table A.1 – *Continued from previous page*

#	$M_{\text{donor}}$	$M_{\text{WD}}$	$P_{\text{init}}$	$M_{\text{f,donor}}$	$M_{\text{f,WD}}$	$M_{\text{He}}$	# defl	$M_{\text{defl}}$	$M_{\text{nova}}$	fate
05090115	0.5	0.9	0.115	0.500	0.900	0.000	0		-7.310	n
05090120	0.5	0.9	0.120	0.500	0.900	0.000	0			n
06090030	0.6	0.9	0.030	0.445	1.055	0.155	0		-3.746	det
06090035	0.6	0.9	0.035	0.440	1.060	0.160	0		-5.398	det
06090040	0.6	0.9	0.040	0.435	1.065	0.165	0		-3.790	det
06090045	0.6	0.9	0.045	0.429	1.071	0.171	0		-5.222	det
06090050	0.6	0.9	0.050	0.424	1.076	0.176	0		-5.999	det
06090055	0.6	0.9	0.055	0.420	1.080	0.180	0		-7.569	det
06090060	0.6	0.9	0.060	0.425	1.075	0.175	0		-7.328	det
06090065	0.6	0.9	0.065	0.520	0.900	0.000	2	-1.123	-2.301	n
06090070	0.6	0.9	0.070	0.574	0.926	0.026	0			n
06090075	0.6	0.9	0.075	0.596	0.900	0.000	1	-2.413	-5.956	n
06090080	0.6	0.9	0.080	0.600	0.900	0.000	0		-7.553	n
06090085	0.6	0.9	0.085	0.600	0.900	0.000	0			n
06090090	0.6	0.9	0.090	0.600	0.900	0.000	0			n
06090095	0.6	0.9	0.095	0.600	0.900	0.000	0			n
06090100	0.6	0.9	0.100	0.600	0.900	0.000	0			n
06090105	0.6	0.9	0.105	0.600	0.900	0.000	0			n
06090110	0.6	0.9	0.110	0.600	0.900	0.000	0	-6.000		n
06090115	0.6	0.9	0.115	0.600	0.900	0.000	0		-8.046	n
06090120	0.6	0.9	0.120	0.600	0.900	0.000	0			n
07090030	0.7	0.9	0.030	0.552	1.048	0.148	0		-5.397	det
07090035	0.7	0.9	0.035	0.545	1.055	0.155	0		-5.046	det
07090040	0.7	0.9	0.040	0.539	1.061	0.161	0		-4.495	det
07090045	0.7	0.9	0.045	0.532	1.068	0.168	0		-4.721	det
07090050	0.7	0.9	0.050	0.524	1.076	0.176	0			det
07090055	0.7	0.9	0.055	0.509	0.940	0.000	2	-1.149	-1.097	n
07090060	0.7	0.9	0.060	0.585	0.900	0.000	1	-0.938	-6.038	n
07090065	0.7	0.9	0.065	0.612	0.900	0.000	1	-1.054	-5.832	n

*Continued on next page*

Table A.1 – *Continued from previous page*

#	$M_{\text{donor}}$	$M_{\text{WD}}$	$P_{\text{init}}$	$M_{\text{f,donor}}$	$M_{\text{f,WD}}$	$M_{\text{He}}$	# defl	$M_{\text{defl}}$	$M_{\text{nova}}$	fate
07090070	0.7	0.9	0.070	0.630	0.970	0.070	0			n
07090075	0.7	0.9	0.075	0.641	0.959	0.059	0			n
07090080	0.7	0.9	0.080	0.645	0.905	0.000	1	-1.307	-6.728	n
07090085	0.7	0.9	0.085	0.657	0.900	0.000	1	-1.371		n
07090090	0.7	0.9	0.090	0.663	0.900	0.000	1	-1.431	-6.379	n
07090095	0.7	0.9	0.095	0.668	0.900	0.000	1	-1.489		n
07090100	0.7	0.9	0.100	0.671	0.900	0.000	1	-1.541	-6.317	n
07090105	0.7	0.9	0.105	0.673	0.900	0.000	1	-1.576	-6.480	n
07090110	0.7	0.9	0.110	0.677	0.900	0.000	1	-1.631	-7.143	n
07090115	0.7	0.9	0.115	0.679	0.900	0.000	1	-1.685	-6.932	n
07090120	0.7	0.9	0.120	0.683	0.917	0.017	0		-15.955	n
08090030	0.8	0.9	0.030	0.672	1.028	0.128	0		-5.222	det
08090035	0.8	0.9	0.035	0.662	1.038	0.138	0		-5.698	det
08090040	0.8	0.9	0.040	0.653	1.047	0.147	0		-5.700	det
08090045	0.8	0.9	0.045	0.642	1.058	0.158	0		-5.523	det
08090050	0.8	0.9	0.050	0.609	0.915	0.000	1	-0.978	-1.154	n
08090055	0.8	0.9	0.055	0.604	0.900	0.000	1	-0.901	-1.151	n
08090060	0.8	0.9	0.060	0.681	1.019	0.119	0		-8.699	det
08090065	0.8	0.9	0.065	0.711	0.989	0.089	0		-15.955	det
08090070	0.8	0.9	0.070	0.665	0.900	0.000	2	-1.503	-0.987	n
08090075	0.8	0.9	0.075	0.674	0.900	0.000	2	-1.945	-0.942	n
08090080	0.8	0.9	0.080	0.682	0.900	0.000	1	-2.352	-0.945	n
08090085	0.8	0.9	0.085	0.688	0.900	0.000	1	-2.433	-0.966	n
08090090	0.8	0.9	0.090	0.693	0.900	0.000	1	-2.501	-0.985	n
08090095	0.8	0.9	0.095	0.698	0.900	0.000	1	-2.539	-1.003	n
08090100	0.8	0.9	0.100	0.702	0.900	0.000	0	-2.587	-1.019	n
08090105	0.8	0.9	0.105	0.705	0.901	0.001	0	-2.841	-1.034	n
08090110	0.8	0.9	0.110	0.708	0.901	0.001	0	-2.826	-1.048	n
08090115	0.8	0.9	0.115	0.711	0.900	0.000	0	-2.676	-1.061	n

*Continued on next page*

Table A.1 – *Continued from previous page*

#	$M_{\text{donor}}$	$M_{\text{WD}}$	$P_{\text{init}}$	$M_{\text{f,donor}}$	$M_{\text{f,WD}}$	$M_{\text{He}}$	# defl	$M_{\text{defl}}$	$M_{\text{nova}}$	fate
08090120	0.8	0.9	0.120	0.712	0.902	0.002	0	-3.635	-1.066	n
09090035	0.9	0.9	0.035	0.779	1.021	0.121	0		-5.097	det
09090040	0.9	0.9	0.040	0.776	1.024	0.124	0		-8.398	det
09090045	0.9	0.9	0.045	0.767	1.033	0.133	0		-9.000	det
09090050	0.9	0.9	0.050	0.615	1.056	0.092	1	-1.369	-1.064	det
09090055	0.9	0.9	0.055	0.642	0.910	0.010	0	-2.236	-0.617	n
09090060	0.9	0.9	0.060	0.663	0.900	0.000	2	-2.070	-0.640	n
09090065	0.9	0.9	0.065	0.678	0.900	0.000	2	-1.733	-0.691	n
09090070	0.9	0.9	0.070	0.690	0.900	0.000	2	-2.402	-0.685	n
09090075	0.9	0.9	0.075	0.698	0.900	0.000	0	-2.571	-0.702	n
09090080	0.9	0.9	0.080	0.706	0.900	0.000	0	-2.644	-0.717	n
09090085	0.9	0.9	0.085	0.712	0.901	0.001	0	-2.912	-0.730	n
09090090	0.9	0.9	0.090	0.715	0.901	0.001	0	-3.502	-0.738	n
09090095	0.9	0.9	0.095	0.720	0.901	0.001	0	-3.572	-0.748	n
09090100	0.9	0.9	0.100	0.724	0.901	0.001	0	-3.616	-0.758	n
09090105	0.9	0.9	0.105	0.727	0.901	0.001	0	-3.650	-0.766	n
09090110	0.9	0.9	0.110	0.730	0.900	0.000	1	-2.915	-0.774	n
09090115	0.9	0.9	0.115	0.733	0.901	0.001	0	-3.721	-0.781	n
09090120	0.9	0.9	0.120	0.736	0.901	0.001	0	-3.762	-0.788	n
10090035	1.0	0.9	0.035	0.839	0.952	0.052	16	-1.279	-1.245	det
10090040	1.0	0.9	0.040	0.856	0.953	0.053	16	-1.326	-1.362	det
10090045	1.0	0.9	0.045	0.607	0.922	0.000	16	-0.598	-0.923	n
10090050	1.0	0.9	0.050	0.678	1.095	0.027	1	-1.395	-1.060	det
10090055	1.0	0.9	0.055	0.649	1.042	0.000	1	-1.987	-0.702	n
10090060	1.0	0.9	0.060	0.682	0.900	0.000	1	-2.403	-0.502	n
10090065	1.0	0.9	0.065	0.696	0.900	0.000	1	-2.537	-0.521	n
10090070	1.0	0.9	0.070	0.708	0.901	0.001	0	-2.847	-0.538	n
10090075	1.0	0.9	0.075	0.717	0.900	0.000	0	-2.741	-0.551	n
10090080	1.0	0.9	0.080	0.724	0.901	0.001	0	-3.472	-0.561	n

*Continued on next page*



Table A.1 – *Continued from previous page*

#	$M_{\text{donor}}$	$M_{\text{WD}}$	$P_{\text{init}}$	$M_{\text{f, donor}}$	$M_{\text{f, WD}}$	$M_{\text{He}}$	# defl	$M_{\text{defl}}$	$M_{\text{nova}}$	fate
10090085	1.0	0.9	0.085	0.722	1.080	0.001	0	-3.051	-1.012	n
10090090	1.0	0.9	0.090	0.727	1.098	0.000	0	-3.053	-1.132	n
10090095	1.0	0.9	0.095	0.752	1.100	0.000	0	-3.721	-1.320	n
10090100	1.0	0.9	0.100	0.764	1.100	0.000	0	-3.775	-1.446	n
10090105	1.0	0.9	0.105	0.767	1.100	0.000	0	-3.821	-1.480	n
10090110	1.0	0.9	0.110	0.769	1.100	0.000	0	-3.883	-1.509	n
10090115	1.0	0.9	0.115	0.771	1.100	0.000	0	-3.924	-1.535	n
10090120	1.0	0.9	0.120	0.772	1.100	0.000	0	-3.936	-1.558	n
05100025	0.5	1.0	0.025	0.344	1.156	0.156	0		-4.319	det
05100030	0.5	1.0	0.030	0.338	1.162	0.162	0		-4.260	det
05100035	0.5	1.0	0.035	0.331	1.169	0.169	0		-3.947	det
05100040	0.5	1.0	0.040	0.322	1.178	0.178	0		-4.921	det
05100045	0.5	1.0	0.045	0.312	1.188	0.188	0		-3.772	det
05100050	0.5	1.0	0.050	0.301	1.199	0.199	0		-4.796	det
05100055	0.5	1.0	0.055	0.290	1.210	0.210	0		-4.662	det
05100060	0.5	1.0	0.060	0.280	1.220	0.220	0		-4.444	det
05100065	0.5	1.0	0.065	0.276	1.224	0.227	0		-5.046	det
05100070	0.5	1.0	0.070	0.274	1.226	0.226	0			det
05100075	0.5	1.0	0.075	0.314	1.186	0.186	0		-5.046	det
05100080	0.5	1.0	0.080	0.398	1.018	0.000	2	-1.260	-1.528	n
05100085	0.5	1.0	0.085	0.500	1.000	0.000	0		-5.982	n
05100090	0.5	1.0	0.090	0.500	1.000	0.000	0		-6.416	n
05100095	0.5	1.0	0.095	0.500	1.000	0.000	0			n
05100100	0.5	1.0	0.100	0.500	1.000	0.000	0			n
05100105	0.5	1.0	0.105	0.500	1.000	0.000	0			n
05100110	0.5	1.0	0.110	0.500	1.000	0.000	0		-7.721	n
05100115	0.5	1.0	0.115	0.500	1.000	0.000	0			n
05100120	0.5	1.0	0.120	0.500	1.000	0.000	0		-6.967	n
06100030	0.6	1.0	0.030	0.422	1.178	0.178	0			det

*Continued on next page*

Table A.1 – *Continued from previous page*

#	$M_{\text{donor}}$	$M_{\text{WD}}$	$P_{\text{init}}$	$M_{\text{f,donor}}$	$M_{\text{f,WD}}$	$M_{\text{He}}$	# defl	$M_{\text{defl}}$	$M_{\text{nova}}$	fate
06100035	0.6	1.0	0.035	0.411	1.189	0.189	0		-5.046	det
06100040	0.6	1.0	0.040	0.400	1.200	0.200	0		-3.785	det
06100045	0.6	1.0	0.045	0.387	1.213	0.213	0		-5.097	det
06100050	0.6	1.0	0.050	0.376	1.224	0.224	0		-5.999	det
06100055	0.6	1.0	0.055	0.367	1.233	0.233	0		-5.222	det
06100060	0.6	1.0	0.060	0.368	1.232	0.232	0		-6.226	det
06100065	0.6	1.0	0.065	0.404	1.048	0.000	4	-1.122	-1.141	n
06100070	0.6	1.0	0.070	0.560	1.040	0.040	0			n
06100075	0.6	1.0	0.075	0.591	1.000	0.000	1	-2.024	-6.511	n
06100080	0.6	1.0	0.080	0.600	1.000	0.000	0		-6.425	n
06100085	0.6	1.0	0.085	0.600	1.000	0.000	0			n
06100090	0.6	1.0	0.090	0.600	1.000	0.000	0			n
06100095	0.6	1.0	0.095	0.600	1.000	0.000	0		-8.000	n
06100100	0.6	1.0	0.100	0.600	1.000	0.000	0		-8.301	n
06100105	0.6	1.0	0.105	0.600	1.000	0.000	0			n
06100110	0.6	1.0	0.110	0.600	1.000	0.000	0			n
06100115	0.6	1.0	0.115	0.600	1.000	0.000	0			n
06100120	0.6	1.0	0.120	0.600	1.000	0.000	0			n
07100030	0.7	1.0	0.030	0.531	1.169	0.169	0		-9.000	det
07100035	0.7	1.0	0.035	0.516	1.184	0.184	0		-4.769	det
07100040	0.7	1.0	0.040	0.501	1.199	0.199	0			det
07100045	0.7	1.0	0.045	0.485	1.215	0.215	0			det
07100050	0.7	1.0	0.050	0.472	1.228	0.228	0			det
07100055	0.7	1.0	0.055	0.411	1.090	0.000	3	-0.912	-1.114	n
07100060	0.7	1.0	0.060	0.572	1.000	0.000	1	-0.894		n
07100065	0.7	1.0	0.065	0.606	1.000	0.000	1	-1.028		n
07100070	0.7	1.0	0.070	0.627	1.000	0.000	1	-1.135	-6.721	n
07100075	0.7	1.0	0.075	0.640	1.000	0.000	1	-1.220		n
07100080	0.7	1.0	0.080	0.649	1.051	0.051	0			n

*Continued on next page*

Table A.1 – *Continued from previous page*

#	$M_{\text{donor}}$	$M_{\text{WD}}$	$P_{\text{init}}$	$M_{\text{f, donor}}$	$M_{\text{f, WD}}$	$M_{\text{He}}$	# defl	$M_{\text{defl}}$	$M_{\text{nova}}$	fate
07100085	0.7	1.0	0.085	0.656	1.000	0.000	1	-1.361		n
07100090	0.7	1.0	0.090	0.663	1.000	0.000	1	-1.427		n
07100095	0.7	1.0	0.095	0.667	1.000	0.000	1	-1.486	-6.788	n
07100100	0.7	1.0	0.100	0.671	1.000	0.000	1	-1.545		n
07100105	0.7	1.0	0.105	0.675	1.000	0.000	1	-1.603	-7.398	n
07100110	0.7	1.0	0.110	0.678	1.000	0.000	1	-1.662	-6.690	n
07100115	0.7	1.0	0.115	0.681	1.000	0.000	1	-1.721	-7.432	n
07100120	0.7	1.0	0.120	0.684	1.000	0.000	1	-1.783	-6.588	n
08100030	0.8	1.0	0.030	0.672	1.128	0.128	0		-8.523	det
08100035	0.8	1.0	0.035	0.649	1.151	0.151	0		-3.726	det
08100040	0.8	1.0	0.040	0.626	1.174	0.174	0		-4.432	det
08100045	0.8	1.0	0.045	0.599	1.201	0.201	0			det
08100050	0.8	1.0	0.050	0.533	1.066	0.000	2	-0.776	-1.469	n
08100055	0.8	1.0	0.055	0.387	1.098	0.000	4	-0.917	-1.025	n
08100060	0.8	1.0	0.060	0.700	1.100	0.100	0			det
08100065	0.8	1.0	0.065	0.715	1.085	0.085	0			det
08100070	0.8	1.0	0.070	0.661	1.003	0.000	2	-1.319	-1.057	n
08100075	0.8	1.0	0.075	0.674	1.000	0.000	2	-1.752	-0.966	n
08100080	0.8	1.0	0.080	0.682	1.000	0.000	2	-2.294	-0.948	n
08100085	0.8	1.0	0.085	0.688	1.000	0.000	1	-2.417	-0.968	n
08100090	0.8	1.0	0.090	0.694	1.000	0.000	1	-2.491	-0.987	n
08100095	0.8	1.0	0.095	0.697	1.022	0.000	0	-2.540	-1.106	n
08100100	0.8	1.0	0.100	0.700	1.031	0.000	1	-2.574	-1.178	n
08100105	0.8	1.0	0.105	0.704	1.035	0.000	1	-2.608	-1.228	n
08100110	0.8	1.0	0.110	0.707	1.038	0.001	0	-2.875	-1.267	n
08100115	0.8	1.0	0.115	0.709	1.040	0.001	0	-2.865	-1.310	n
08100120	0.8	1.0	0.120	0.712	1.041	0.001	0	-2.875	-1.336	n
09100035	0.9	1.0	0.035	0.799	1.101	0.101	0		-8.699	det
09100040	0.9	1.0	0.040	0.788	1.112	0.112	0		-8.398	det

*Continued on next page*

Table A.1 – *Continued from previous page*

#	$M_{\text{donor}}$	$M_{\text{WD}}$	$P_{\text{init}}$	$M_{\text{f,donor}}$	$M_{\text{f,WD}}$	$M_{\text{He}}$	# defl	$M_{\text{defl}}$	$M_{\text{nova}}$	fate
09100045	0.9	1.0	0.045	0.740	1.160	0.160	0			det
09100050	0.9	1.0	0.050	0.650	1.116	0.052	1	-1.167	-1.182	det
09100055	0.9	1.0	0.055	0.694	1.092	0.032	2	-1.562	-1.063	det
09100060	0.9	1.0	0.060	0.664	1.000	0.000	2	-2.061	-0.643	n
09100065	0.9	1.0	0.065	0.680	1.000	0.000	2	-1.410	-0.741	n
09100070	0.9	1.0	0.070	0.687	1.061	0.000	2	-2.030	-0.845	n
09100075	0.9	1.0	0.075	0.695	1.088	0.000	1	-2.493	-0.942	n
09100080	0.9	1.0	0.080	0.714	1.100	0.000	0	-3.321	-1.070	n
09100085	0.9	1.0	0.085	0.737	1.100	0.000	0	-3.382	-1.204	n
09100090	0.9	1.0	0.090	0.744	1.100	0.000	0	-3.472	-1.254	n
09100095	0.9	1.0	0.095	0.749	1.100	0.000	0	-3.553	-1.294	n
09100100	0.9	1.0	0.100	0.753	1.100	0.000	0	-3.613	-1.329	n
09100105	0.9	1.0	0.105	0.756	1.100	0.000	0	-3.648	-1.360	n
09100110	0.9	1.0	0.110	0.759	1.100	0.000	0	-3.678	-1.387	n
09100115	0.9	1.0	0.115	0.761	1.100	0.000	0	-3.730	-1.412	n
09100120	0.9	1.0	0.120	0.763	1.100	0.000	0	-3.757	-1.435	n
10100035	1.0	1.0	0.035	0.892	1.033	0.033	14	-1.290	-1.627	det
10100040	1.0	1.0	0.040	0.911	1.033	0.033	14	-1.345	-1.964	det
10100045	1.0	1.0	0.045	0.912	1.088	0.088	0		-8.301	det
10100050	1.0	1.0	0.050	0.812	1.100	0.000	1	-1.180	-1.659	me
10100055	1.0	1.0	0.055	0.876	1.100	0.000	0	-4.071	-1.616	me
10100060	1.0	1.0	0.060	0.721	1.100	0.000	0	-3.502	-0.748	me
10100065	1.0	1.0	0.065	0.792	1.100	0.000	0	-3.203	-0.968	me
10100070	1.0	1.0	0.070	0.824	1.100	0.000	0	-3.168	-1.122	me
10100075	1.0	1.0	0.075	0.850	1.100	0.000	0	-3.256	-1.304	me
10100080	1.0	1.0	0.080	0.861	1.100	0.000	0	-3.390	-1.412	me
10100085	1.0	1.0	0.085	0.868	1.100	0.000	0	-3.511	-1.497	me
10100090	1.0	1.0	0.090	0.873	1.100	0.000	0	-3.631	-1.566	me
10100095	1.0	1.0	0.095	0.876	1.100	0.000	0	-3.719	-1.624	me

*Continued on next page*

Table A.1 – *Continued from previous page*

#	$M_{\text{donor}}$	$M_{\text{WD}}$	$P_{\text{init}}$	$M_{\text{f,donor}}$	$M_{\text{f,WD}}$	$M_{\text{He}}$	# defl	$M_{\text{defl}}$	$M_{\text{nova}}$	fate
10100100	1.0	1.0	0.100	0.879	1.100	0.000	0	-3.752	-1.675	me
10100105	1.0	1.0	0.105	0.881	1.100	0.000	0	-3.824	-1.721	me
10100110	1.0	1.0	0.110	0.883	1.100	0.000	0	-3.857	-1.764	me
10100115	1.0	1.0	0.115	0.884	1.100	0.000	0	-3.900	-1.804	me
10100120	1.0	1.0	0.120	0.886	1.100	0.000	0	-3.924	-1.842	me



## B. Additional data for chapter 3

Table B.1.: Model sequences omitted from Tab. 3.3 for  $f_{\text{acc}} = 0.6$ . Nomenclature is same as in Tab. 3.3.

#	$L_{\text{init}}$ [log( $L/L_{\odot}$ )]	$\dot{M}/10^8$ [ $M_{\odot}/\text{yr}$ ]	$M_{\text{init}}$ [ $M_{\odot}$ ]	$t$ [Myr]	$M_{\text{He,f}}$ [ $M_{\odot}$ ]	$T_{4,\text{f}}$	$L_{\text{f}}$ [log( $L/L_{\odot}$ )]	$\rho_{6,\text{c}}$	$T_{8,\text{ign}}$	$\rho_{6,\text{ign}}$	$M_{\text{r,ign}}$ [ $M_{\odot}$ ]
Lm20506-1	-2	1	0.54	182.00	0.70	18.21	2.02	40.20	1.92	11.89	0.51
Lm20506-2	-2	2	0.54	143.45	0.62	7.91	0.61	27.17	1.92	6.74	0.56
Lm20506-3	-2	3	0.54	120.21	0.24	4.92	0.35	4.51	3.56	0.19	0.63
Lm20506-4	-2	4	0.54	117.05	0.19	4.37	0.27	3.78	3.50	0.12	0.60
Lm20506-5	-2	5	0.54	115.58	0.17	4.27	0.29	3.50	3.40	0.09	0.59
Lm20506-6	-2	6	0.54	114.73	0.15	4.57	0.42	3.35	3.24	0.08	0.58
Lm20506-7	-2	7	0.54	114.20	0.13	4.87	0.53	3.25	3.10	0.08	0.58
Lm20506-8	-2	8	0.54	113.83	0.12	5.17	0.64	3.16	3.00	0.08	0.57
Lm20506-9	-2	9	0.54	113.55	0.11	5.41	0.72	3.08	2.92	0.07	0.57
Lm20506-10	-2	10	0.54	113.33	0.11	5.56	0.77	3.02	2.88	0.07	0.56
Lm10506-1	-1	1	0.54	90.25	0.69	8.53	0.67	38.41	1.97	11.12	0.51
Lm10506-2	-1	2	0.54	52.31	0.62	7.94	0.62	26.93	1.94	6.66	0.56
Lm10506-3	-1	3	0.54	28.20	0.21	5.16	0.45	4.00	3.29	0.19	0.59
Lm10506-4	-1	4	0.54	25.38	0.17	4.97	0.47	3.39	3.18	0.14	0.57
Lm10506-5	-1	5	0.54	24.08	0.14	4.17	0.27	3.09	3.31	0.09	0.56
Lm10506-6	-1	6	0.54	23.37	0.13	4.61	0.44	2.99	3.14	0.09	0.56
Lm10506-7	-1	7	0.54	22.88	0.12	4.64	0.48	2.89	3.09	0.08	0.55
Lm10506-8	-1	8	0.54	22.50	0.10	4.89	0.56	2.82	2.96	0.07	0.55
Lm10506-9	-1	9	0.54	22.19	0.09	5.36	0.69	2.81	2.85	0.07	0.55
Lm10506-10	-1	10	0.54	22.00	0.08	5.69	0.78	2.81	2.79	0.07	0.55

*Continued on next page*

Table B.1 – *Continued from previous page*

#	$L_{\text{init}}$	$\dot{M}$	$M_{\text{init}}$	$t$	$M_{\text{He,f}}$	$T_{4,\text{f}}$	$L_{\text{f}}$	$\rho_{6,\text{c}}$	$T_{8,\text{ign}}$	$\rho_{6,\text{ign}}$	$M_{\text{r,ign}}$
L00506-1	0	1	0.54	82.19	0.70	42.14	3.89	43.48	3.13	0.00	1.24
L00506-2	0	2	0.54	43.22	0.61	9.02	0.86	25.37	1.75	6.26	0.56
L00506-3	0	3	0.54	18.96	0.19	5.40	0.51	3.73	2.83	0.22	0.57
L00506-4	0	4	0.54	16.19	0.14	3.60	0.05	2.94	3.41	0.09	0.55
L00506-5	0	5	0.54	14.55	0.09	4.33	0.32	2.74	2.90	0.07	0.54
L00506-6	0	6	0.54	13.90	0.07	4.88	0.50	2.70	2.74	0.06	0.54
L00506-7	0	7	0.54	13.61	0.07	4.79	0.49	2.65	2.79	0.05	0.54
L00506-8	0	8	0.54	13.43	0.06	1.27	-1.01	2.48	3.39	0.01	0.54
L00506-9	0	9	0.54	13.30	0.06	5.89	0.79	2.64	2.53	0.05	0.54
L00506-10	0	10	0.54	13.22	0.05	1.48	-1.05	2.48	3.29	0.01	0.54
Lm20806-1	-2	1	0.82	215.46	0.49	7.34	0.28	67.51	2.00	10.63	0.78
Lm20806-2	-2	2	0.82	187.91	0.42	8.70	0.66	46.93	0.75	0.60	1.19
Lm20806-3	-2	3	0.82	176.64	0.29	8.69	0.82	23.45	1.82	0.65	1.02
Lm20806-4	-2	4	0.82	172.37	0.22	7.29	0.67	17.12	3.98	0.24	0.97
Lm20806-5	-2	5	0.82	168.97	0.11	7.54	0.69	15.99	4.59	0.16	0.88
Lm20806-6	-2	6	0.82	168.10	0.08	7.58	0.71	15.11	4.57	0.13	0.86
Lm20806-7	-2	7	0.82	167.69	0.06	8.01	0.80	14.58	4.30	0.11	0.85
Lm20806-8	-2	8	0.82	167.45	0.05	8.46	0.89	14.22	4.08	0.11	0.84
Lm20806-9	-2	9	0.82	167.31	0.04	9.08	1.00	13.96	3.83	0.10	0.84
Lm20806-10	-2	10	0.82	167.21	0.04	9.48	1.07	13.75	3.69	0.10	0.83
Lm10806-1	-1	1	0.82	98.22	0.49	7.35	0.28	67.51	2.02	10.60	0.78
Lm10806-2	-1	2	0.82	70.71	0.42	8.35	0.59	46.19	2.15	5.72	0.83
Lm10806-3	-1	3	0.82	59.28	0.29	8.59	0.80	23.03	1.81	0.64	1.01
Lm10806-4	-1	4	0.82	52.44	0.11	7.88	0.72	15.95	4.25	0.27	0.87
Lm10806-5	-1	5	0.82	50.99	0.07	7.67	0.70	14.49	4.61	0.17	0.84
Lm10806-6	-1	6	0.82	50.48	0.05	8.57	0.86	14.08	3.83	0.18	0.83
Lm10806-7	-1	7	0.82	50.22	0.04	7.91	0.79	13.53	4.39	0.12	0.83
Lm10806-8	-1	8	0.82	50.06	0.04	8.36	0.88	13.31	4.16	0.11	0.83
Lm10806-9	-1	9	0.82	49.96	0.03	8.83	0.97	13.16	3.95	0.10	0.83

*Continued on next page*



Table B.1 – *Continued from previous page*

#	$L_{\text{init}}$	$\dot{M}$	$M_{\text{init}}$	$t$	$M_{\text{He,f}}$	$T_{4,\text{f}}$	$L_{\text{f}}$	$\rho_{6,\text{c}}$	$T_{8,\text{ign}}$	$\rho_{6,\text{ign}}$	$M_{\text{r,ign}}$
Lm10806-10	-1	10	0.82	49.89	0.03	9.28	1.05	13.04	3.77	0.10	0.82
L00806-1	0	1	0.82	86.95	0.49	7.50	0.32	67.33	1.91	10.71	0.78
L00806-2	0	2	0.82	59.63	0.42	8.44	0.61	47.01	1.37	5.97	0.83
L00806-3	0	3	0.82	48.08	0.29	8.51	0.78	22.95	1.82	0.65	1.01
L00806-4	0	4	0.82	39.89	0.06	7.87	0.70	13.95	3.98	0.25	0.82
L00806-5	0	5	0.82	39.20	0.04	7.50	0.67	12.96	4.36	0.14	0.82
L00806-6	0	6	0.82	38.95	0.03	7.46	0.70	12.59	4.34	0.11	0.82
L00806-7	0	7	0.82	38.82	0.03	8.04	0.82	12.45	4.07	0.10	0.82
L00806-8	0	8	0.82	38.73	0.02	8.63	0.93	12.37	3.83	0.10	0.82
L00806-9	0	9	0.82	38.68	0.02	9.03	1.01	12.30	3.67	0.10	0.82
L00806-10	0	10	0.82	38.63	0.02	9.39	1.07	12.23	3.58	0.09	0.82
Lm21006-4	-2	4	1.00	179.08	0.07	9.85	0.80	46.30	4.55	0.32	1.04
Lm21006-5	-2	5	1.00	178.13	0.04	10.49	0.94	41.31	4.26	0.21	1.02
Lm21006-6	-2	6	1.00	177.76	0.03	10.80	1.04	38.68	4.89	0.14	1.01
Lm21006-7	-2	7	1.00	177.58	0.02	10.55	1.00	37.40	4.56	0.12	1.01
Lm21006-8	-2	8	1.00	177.49	0.02	10.98	1.07	36.61	4.25	0.12	1.00
Lm21006-9	-2	9	1.00	177.44	0.01	11.33	1.12	36.18	4.04	0.11	1.00
Lm21006-10	-2	10	1.00	177.40	0.01	11.57	1.16	35.86	4.03	0.10	1.00
Lm11006-4	-1	4	1.00	42.88	0.04	10.97	1.01	40.46	4.61	0.31	1.02
Lm11006-5	-1	5	1.00	42.49	0.04	12.76	1.22	39.55	1.73	0.58	1.00
Lm11006-6	-1	6	1.00	42.12	0.02	10.47	0.98	36.28	4.47	0.16	1.00
Lm11006-7	-1	7	1.00	42.01	0.02	10.52	1.01	35.50	4.51	0.13	1.00
Lm11006-8	-1	8	1.00	41.95	0.01	10.86	1.06	35.08	4.28	0.11	1.00
Lm11006-9	-1	9	1.00	41.91	0.01	11.26	1.12	34.80	3.99	0.11	1.00
Lm11006-10	-1	10	1.00	41.88	0.01	11.67	1.17	34.60	3.85	0.10	1.00
L01006-4	0	4	1.00	26.09	0.02	9.36	0.79	34.79	4.53	0.17	1.00
L01006-5	0	5	1.00	25.89	0.01	9.38	0.82	33.83	4.45	0.12	1.00
L01006-6	0	6	1.00	25.81	0.01	10.16	0.94	33.47	3.96	0.11	1.00
L01006-7	0	7	1.00	25.76	0.01	9.80	0.93	33.11	4.50	0.08	1.00

*Continued on next page*

Table B.1 – *Continued from previous page*

#	$L_{\text{init}}$	$\dot{M}$	$M_{\text{init}}$	$t$	$M_{\text{He,f}}$	$T_{4,\text{f}}$	$L_{\text{f}}$	$\rho_{6,\text{c}}$	$T_{8,\text{ign}}$	$\rho_{6,\text{ign}}$	$M_{\text{r,ign}}$
L01006-8	0	8	1.00	25.74	0.01	9.87	0.95	32.94	4.46	0.07	1.00
L01006-9	0	9	1.00	25.72	0.01	10.20	1.01	32.92	4.44	0.06	1.00
L01006-10	0	10	1.00	25.70	0.01	12.91	1.47	32.67	4.74	0.05	1.00
Lm11106-4	-1	4	1.10	53.66	0.02	12.26	1.09	78.66	6.00	0.20	1.11
Lm11106-5	-1	5	1.10	53.39	0.02	10.63	0.85	75.05	5.41	0.16	1.11
Lm11106-6	-1	6	1.10	53.28	0.01	11.04	0.92	73.30	4.98	0.14	1.10
Lm11106-7	-1	7	1.10	53.22	0.01	11.84	1.02	72.42	4.36	0.13	1.10
Lm11106-8	-1	8	1.10	53.18	0.01	18.51	1.94	71.24	6.00	0.07	1.10
Lm11106-9	-1	9	1.10	53.16	0.01	21.67	2.24	70.89	6.00	0.06	1.10
Lm11106-10	-1	10	1.10	53.15	0.01	24.93	2.51	70.58	6.00	0.05	1.10
L01106-4	0	4	1.10	25.93	0.01	9.71	0.72	69.64	5.43	0.13	1.10
L01106-5	0	5	1.10	25.83	0.01	10.62	0.86	68.80	4.61	0.12	1.10
L01106-6	0	6	1.10	25.79	0.01	11.11	0.94	68.21	4.47	0.11	1.10
L01106-7	0	7	1.10	25.76	0.01	23.27	2.40	67.45	6.00	0.05	1.10
L01106-8	0	8	1.10	25.74	0.01	26.29	2.63	67.23	6.00	0.04	1.10
L01106-9	0	9	1.10	25.73	0.00	29.77	2.88	67.05	6.00	0.04	1.10
L01106-10	0	10	1.10	25.72	0.00	33.53	3.12	66.89	6.00	0.03	1.10

Table B.2.: Model sequences omitted from Tab. 3.3 for  $f_{\text{acc}} = 0.3$ . Nomenclature is same as in Tab. 3.3.

#	$L_{\text{init}}$ [log( $L/L_{\odot}$ )]	$\dot{M}/10^8$ [ $M_{\odot}/\text{yr}$ ]	$M_{\text{init}}$ [ $M_{\odot}$ ]	$t$ [Myr]	$M_{\text{He,f}}$ [ $M_{\odot}$ ]	$T_{4,\text{f}}$	$L_{\text{f}}$ [log( $L/L_{\odot}$ )]	$\rho_{6,\text{c}}$	$T_{8,\text{ign}}$	$\rho_{6,\text{ign}}$	$M_{\text{r,ign}}$ [ $M_{\odot}$ ]
Lm20503-1	-2	1	0.54	182.10	0.70	30.18	4.49	55.55	3.18	0.00	1.24
Lm20503-2	-2	2	0.54	143.33	0.62	7.85	0.60	26.87	1.93	6.64	0.56
Lm20503-3	-2	3	0.54	119.87	0.23	5.66	0.46	5.56	3.69	0.23	0.64
Lm20503-4	-2	4	0.54	116.03	0.15	4.84	0.32	4.10	3.81	0.12	0.59
Lm20503-5	-2	5	0.54	115.00	0.14	5.60	0.56	3.76	3.77	0.15	0.55
Lm20503-6	-2	6	0.54	113.96	0.11	5.18	0.47	3.58	3.38	0.09	0.57
Lm20503-7	-2	7	0.54	113.53	0.09	5.67	0.61	3.47	3.20	0.08	0.56

*Continued on next page*

Table B.2 – *Continued from previous page*

#	$L_{\text{init}}$	$\dot{M}$	$M_{\text{init}}$	$t$	$M_{\text{He,f}}$	$T_{4,\text{f}}$	$L_{\text{f}}$	$\rho_{6,\text{c}}$	$T_{8,\text{ign}}$	$\rho_{6,\text{ign}}$	$M_{\text{r,ign}}$
Lm20503-8	-2	8	0.54	113.25	0.08	6.10	0.73	3.40	3.08	0.08	0.56
Lm20503-9	-2	9	0.54	113.18	0.08	6.19	0.78	3.30	3.18	0.08	0.55
Lm20503-10	-2	10	0.54	113.04	0.08	6.58	0.88	3.28	3.06	0.08	0.55
Lm10503-1	-1	1	0.54	90.59	0.69	41.84	3.83	44.29	3.20	0.00	1.24
Lm10503-2	-1	2	0.54	52.26	0.62	7.91	0.61	26.76	1.97	6.60	0.56
Lm10503-3	-1	3	0.54	26.90	0.17	5.15	0.36	4.31	3.85	0.18	0.58
Lm10503-4	-1	4	0.54	24.04	0.11	4.46	0.21	3.44	3.63	0.10	0.55
Lm10503-5	-1	5	0.54	23.08	0.09	4.70	0.32	3.25	3.42	0.09	0.55
Lm10503-6	-1	6	0.54	22.58	0.08	5.21	0.49	3.18	3.22	0.08	0.55
Lm10503-7	-1	7	0.54	22.28	0.08	5.66	0.62	3.13	3.07	0.08	0.55
Lm10503-8	-1	8	0.54	22.07	0.07	5.98	0.72	3.08	3.00	0.07	0.54
Lm10503-9	-1	9	0.54	21.93	0.07	6.28	0.80	3.04	2.94	0.07	0.54
Lm10503-10	-1	10	0.54	21.82	0.06	6.69	0.91	3.03	2.85	0.07	0.54
L00503-1	0	1	0.54	82.07	0.69	34.31	3.45	44.50	3.36	0.01	1.24
L00503-2	0	2	0.54	43.76	0.62	8.33	0.71	26.88	2.03	6.64	0.56
L00503-3	0	3	0.54	16.33	0.11	3.80	-0.03	3.31	3.72	0.09	0.55
L00503-4	0	4	0.54	14.49	0.07	4.85	0.35	3.03	3.01	0.08	0.54
L00503-5	0	5	0.54	13.92	0.06	5.42	0.53	2.93	2.82	0.07	0.54
L00503-6	0	6	0.54	13.63	0.06	1.26	-1.24	2.56	3.55	0.01	0.54
L00503-7	0	7	0.54	13.44	0.05	3.81	0.13	2.71	3.21	0.03	0.54
L00503-8	0	8	0.54	13.31	0.05	3.94	0.20	2.68	3.17	0.03	0.54
L00503-9	0	9	0.54	13.22	0.05	1.45	-1.14	2.54	3.43	0.01	0.54
L00503-10	0	10	0.54	13.15	0.05	1.40	-1.16	2.52	3.40	0.01	0.54
Lm20803-1	-2	1	0.82	211.03	0.44	7.41	0.24	78.72	1.98	11.98	0.78
Lm20803-2	-2	2	0.82	188.01	0.42	8.35	0.59	46.56	2.15	5.78	0.83
Lm20803-3	-2	3	0.82	174.81	0.24	9.39	0.77	34.16	2.27	2.69	0.85
Lm20803-4	-2	4	0.82	169.84	0.12	9.58	0.87	20.87	1.71	0.51	0.89
Lm20803-5	-2	5	0.82	168.59	0.09	7.99	0.70	17.43	4.59	0.18	0.87
Lm20803-6	-2	6	0.82	167.98	0.07	7.77	0.71	16.01	4.63	0.13	0.86

*Continued on next page*

Table B.2 – *Continued from previous page*

#	$L_{\text{init}}$	$\dot{M}$	$M_{\text{init}}$	$t$	$M_{\text{He,f}}$	$T_{4,\text{f}}$	$L_{\text{f}}$	$\rho_{6,\text{c}}$	$T_{8,\text{ign}}$	$\rho_{6,\text{ign}}$	$M_{\text{r,ign}}$
Lm20803-7	-2	7	0.82	167.65	0.06	8.10	0.79	15.22	4.37	0.12	0.85
Lm20803-8	-2	8	0.82	167.44	0.05	8.50	0.87	14.72	4.13	0.11	0.84
Lm20803-9	-2	9	0.82	167.31	0.04	9.00	0.97	14.37	3.88	0.11	0.84
Lm20803-10	-2	10	0.82	167.22	0.04	9.35	1.03	14.11	3.73	0.10	0.83
Lm10803-1	-1	1	0.82	93.87	0.44	7.63	0.29	78.83	1.97	12.11	0.78
Lm10803-2	-1	2	0.82	67.62	0.36	8.56	0.55	56.11	2.12	6.55	0.83
Lm10803-3	-1	3	0.82	54.49	0.15	8.93	0.74	23.18	2.01	0.76	0.89
Lm10803-4	-1	4	0.82	51.70	0.08	9.42	0.87	17.50	1.72	0.51	0.85
Lm10803-5	-1	5	0.82	50.85	0.06	7.83	0.70	15.16	4.58	0.18	0.84
Lm10803-6	-1	6	0.82	50.44	0.05	7.57	0.69	14.31	4.69	0.13	0.83
Lm10803-7	-1	7	0.82	50.21	0.04	7.84	0.76	13.88	4.47	0.12	0.83
Lm10803-8	-1	8	0.82	50.06	0.04	8.34	0.86	13.62	4.17	0.11	0.83
Lm10803-9	-1	9	0.82	49.96	0.03	8.71	0.93	13.42	4.00	0.11	0.83
Lm10803-10	-1	10	0.82	49.89	0.03	9.14	1.01	13.27	3.82	0.10	0.83
L00803-1	0	1	0.82	82.75	0.44	7.38	0.23	78.84	1.97	11.96	0.78
L00803-2	0	2	0.82	56.48	0.36	8.57	0.55	56.06	2.12	6.53	0.83
L00803-3	0	3	0.82	42.55	0.12	8.86	0.74	20.85	1.92	0.71	0.87
L00803-4	0	4	0.82	39.71	0.05	7.27	0.58	14.00	4.81	0.19	0.82
L00803-5	0	5	0.82	39.17	0.04	7.12	0.60	13.09	4.59	0.13	0.82
L00803-6	0	6	0.82	38.92	0.03	7.55	0.71	12.72	4.24	0.11	0.82
L00803-7	0	7	0.82	38.80	0.03	7.96	0.80	12.55	4.04	0.10	0.82
L00803-8	0	8	0.82	38.73	0.02	8.33	0.87	12.48	3.91	0.10	0.82
L00803-9	0	9	0.82	38.68	0.02	8.82	0.96	12.40	3.72	0.10	0.82
L00803-10	0	10	0.82	38.64	0.02	9.20	1.03	12.34	3.60	0.10	0.82
Lm21003-4	-2	4	1.00	179.61	0.09	11.50	0.96	57.65	2.09	1.23	1.03
Lm21003-5	-2	5	1.00	178.55	0.06	11.99	1.07	48.77	1.88	0.68	1.03
Lm21003-6	-2	6	1.00	177.89	0.04	9.59	0.83	40.96	5.35	0.15	1.02
Lm21003-7	-2	7	1.00	177.68	0.03	10.17	0.93	39.16	4.84	0.13	1.01
Lm21003-8	-2	8	1.00	177.56	0.02	10.43	0.98	37.96	4.61	0.12	1.01

*Continued on next page*

Table B.2 – *Continued from previous page*

#	$L_{\text{init}}$	$\dot{M}$	$M_{\text{init}}$	$t$	$M_{\text{He,f}}$	$T_{4,\text{f}}$	$L_{\text{f}}$	$\rho_{6,\text{c}}$	$T_{8,\text{ign}}$	$\rho_{6,\text{ign}}$	$M_{\text{r,ign}}$
Lm21003-9	-2	9	1.00	177.49	0.02	10.82	1.04	37.21	4.37	0.12	1.01
Lm21003-10	-2	10	1.00	177.44	0.02	11.28	1.11	36.65	4.13	0.11	1.00
Lm11003-4	-1	4	1.00	43.41	0.07	11.65	1.02	48.01	2.18	0.91	1.02
Lm11003-5	-1	5	1.00	42.67	0.04	11.87	1.08	42.54	1.87	0.67	1.01
Lm11003-6	-1	6	1.00	42.21	0.03	10.13	0.91	37.62	4.66	0.18	1.01
Lm11003-7	-1	7	1.00	42.07	0.02	10.25	0.94	36.58	4.51	0.15	1.00
Lm11003-8	-1	8	1.00	41.99	0.02	10.39	0.98	35.88	4.48	0.13	1.00
Lm11003-9	-1	9	1.00	41.94	0.01	10.81	1.05	35.44	4.28	0.12	1.00
Lm11003-10	-1	10	1.00	41.91	0.01	11.17	1.10	35.08	4.13	0.11	1.00
L01003-4	0	4	1.00	26.61	0.04	11.60	1.05	40.47	1.89	0.68	1.00
L01003-5	0	5	1.00	25.93	0.02	8.87	0.73	34.21	4.80	0.12	1.00
L01003-6	0	6	1.00	25.83	0.01	9.68	0.87	33.74	4.21	0.11	1.00
L01003-7	0	7	1.00	25.78	0.01	10.30	0.97	33.46	3.92	0.11	1.00
L01003-8	0	8	1.00	25.75	0.01	9.72	0.91	33.17	4.50	0.08	1.00
L01003-9	0	9	1.00	25.73	0.01	9.95	0.96	33.03	4.47	0.07	1.00
L01003-10	0	10	1.00	25.71	0.01	10.09	1.00	32.91	4.50	0.06	1.00
Lm11103-4	-1	4	1.10	54.35	0.05	12.71	1.02	98.27	2.11	1.24	1.12
Lm11103-5	-1	5	1.10	53.76	0.03	13.87	1.20	87.04	1.97	0.74	1.11
Lm11103-6	-1	6	1.10	53.36	0.02	10.46	0.82	76.10	5.59	0.16	1.11
Lm11103-7	-1	7	1.10	53.26	0.01	11.03	0.92	73.99	5.14	0.14	1.11
Lm11103-8	-1	8	1.10	53.21	0.01	12.21	1.06	72.93	4.09	0.15	1.10
Lm11103-9	-1	9	1.10	53.18	0.01	12.01	1.06	72.26	4.52	0.12	1.10
Lm11103-10	-1	10	1.10	53.16	0.01	18.75	1.96	71.37	6.00	0.06	1.10
L01103-4	0	4	1.10	25.99	0.01	9.49	0.67	70.86	5.67	0.17	1.10
L01103-5	0	5	1.10	25.86	0.01	10.18	0.79	69.38	4.96	0.13	1.10
L01103-6	0	6	1.10	25.80	0.01	10.89	0.90	68.70	4.51	0.12	1.10
L01103-7	0	7	1.10	25.77	0.01	11.42	0.98	68.40	4.29	0.12	1.10
L01103-8	0	8	1.10	25.75	0.01	21.36	2.23	67.66	6.00	0.06	1.10
L01103-9	0	9	1.10	25.74	0.01	24.26	2.48	67.43	6.00	0.05	1.10

*Continued on next page*

Table B.2 – *Continued from previous page*

#	$L_{\text{init}}$	$\dot{M}$	$M_{\text{init}}$	$t$	$M_{\text{He,f}}$	$T_{4,\text{f}}$	$L_{\text{f}}$	$\rho_{6,\text{c}}$	$T_{8,\text{ign}}$	$\rho_{6,\text{ign}}$	$M_{\text{r,ign}}$
L01103-10	0	10	1.10	25.73	0.01	26.07	2.62	67.30	6.00	0.04	1.10

Table B.3.: Model sequences omitted from Tab. 3.3 for  $f_{\text{acc}} = 0.3$ . Nomenclature is same as in Tab. 3.3.

#	$L_{\text{init}}$ [log( $L/L_{\odot}$ )]	$\dot{M}/10^8$ [ $M_{\odot}/\text{yr}$ ]	$M_{\text{init}}$ [ $M_{\odot}$ ]	$t$ [Myr]	$M_{\text{He,f}}$ [ $M_{\odot}$ ]	$T_{4,\text{f}}$	$L_{\text{f}}$ [log( $L/L_{\odot}$ )]	$\rho_{6,\text{c}}$	$T_{8,\text{ign}}$	$\rho_{6,\text{ign}}$	$M_{\text{r,ign}}$ [ $M_{\odot}$ ]
Lm205n-1	-2	1	0.54	156.21	0.45	6.97	0.23	27.20	1.96	6.22	0.54
Lm205n-2	-2	2	0.54	133.26	0.43	8.18	0.54	24.85	1.96	5.58	0.54
Lm205n-3	-2	3	0.54	117.42	0.17	5.07	0.25	5.08	4.41	0.16	0.60
Lm205n-4	-2	4	0.54	114.98	0.13	4.55	0.18	4.15	4.01	0.11	0.58
Lm205n-5	-2	5	0.54	113.90	0.11	4.96	0.34	3.86	3.65	0.09	0.57
Lm205n-6	-2	6	0.54	113.31	0.10	5.45	0.50	3.69	3.40	0.09	0.56
Lm205n-7	-2	7	0.54	112.94	0.09	5.91	0.64	3.57	3.22	0.08	0.56
Lm205n-8	-2	8	0.54	112.69	0.08	6.27	0.75	3.48	3.11	0.08	0.56
Lm205n-9	-2	9	0.54	112.52	0.07	6.54	0.82	3.41	3.04	0.07	0.56
Lm205n-10	-2	10	0.54	112.39	0.07	6.82	0.90	3.35	2.98	0.07	0.55
Lm105n-1	-1	1	0.54	65.66	0.45	7.02	0.24	27.50	1.66	6.35	0.54
Lm105n-2	-1	2	0.54	42.70	0.43	8.28	0.56	25.25	1.56	5.75	0.54
Lm105n-3	-1	3	0.54	25.58	0.13	4.20	0.03	3.98	4.21	0.12	0.56
Lm105n-4	-1	4	0.54	23.66	0.10	4.33	0.14	3.47	3.72	0.10	0.55
Lm105n-5	-1	5	0.54	22.87	0.09	4.85	0.34	3.32	3.44	0.09	0.55
Lm105n-6	-1	6	0.54	22.43	0.08	5.41	0.52	3.25	3.21	0.08	0.55
Lm105n-7	-1	7	0.54	22.16	0.07	5.83	0.64	3.20	3.08	0.08	0.55
Lm105n-8	-1	8	0.54	21.97	0.07	6.16	0.74	3.15	2.99	0.07	0.55
Lm105n-9	-1	9	0.54	21.84	0.06	6.47	0.83	3.11	2.93	0.07	0.55
Lm105n-10	-1	10	0.54	21.74	0.06	7.02	0.95	3.09	2.80	0.07	0.54
L005n-1	0	1	0.54	57.17	0.45	7.01	0.24	27.47	1.68	6.34	0.54
L005n-2	0	2	0.54	34.21	0.43	8.29	0.56	25.33	1.47	5.78	0.54
L005n-3	0	3	0.54	15.71	0.09	6.45	0.62	3.69	2.40	0.19	0.54

*Continued on next page*

Table B.3 – *Continued from previous page*

#	$L_{\text{init}}$	$\dot{M}$	$M_{\text{init}}$	$t$	$M_{\text{He,f}}$	$T_{4,\text{f}}$	$L_{\text{f}}$	$\rho_{6,\text{c}}$	$T_{8,\text{ign}}$	$\rho_{6,\text{ign}}$	$M_{\text{r,ign}}$
L005n-4	0	4	0.54	14.36	0.07	4.87	0.34	3.07	3.05	0.07	0.54
L005n-5	0	5	0.54	13.85	0.06	6.79	0.81	3.06	2.36	0.09	0.54
L005n-6	0	6	0.54	13.58	0.05	3.78	0.08	2.78	3.26	0.04	0.54
L005n-7	0	7	0.54	13.40	0.05	6.37	0.80	2.87	2.62	0.06	0.54
L005n-8	0	8	0.54	13.28	0.05	4.02	0.22	2.71	3.18	0.03	0.54
L005n-9	0	9	0.54	13.19	0.05	4.16	0.29	2.69	3.15	0.03	0.54
L005n-10	0	10	0.54	13.12	0.05	4.26	0.34	2.67	3.13	0.03	0.54
Lm208n-1	-2	1	0.82	196.50	0.27	7.68	0.23	60.20	1.66	6.50	0.82
Lm208n-2	-2	2	0.82	181.99	0.26	9.00	0.55	52.92	2.20	5.39	0.82
Lm208n-3	-2	3	0.82	175.38	0.19	9.63	0.77	33.44	2.19	2.25	0.85
Lm208n-4	-2	4	0.82	172.37	0.13	9.95	0.90	23.91	2.11	0.82	0.88
Lm208n-5	-2	5	0.82	171.02	0.10	10.40	1.02	19.91	1.75	0.60	0.86
Lm208n-6	-2	6	0.82	170.35	0.08	9.29	0.93	17.19	4.30	0.28	0.85
Lm208n-7	-2	7	0.82	169.97	0.06	9.00	0.92	15.91	4.55	0.20	0.84
Lm208n-8	-2	8	0.82	169.76	0.06	8.75	0.91	15.30	4.93	0.14	0.84
Lm208n-9	-2	9	0.82	169.59	0.05	8.70	0.92	14.62	4.63	0.13	0.83
Lm208n-10	-2	10	0.82	169.49	0.04	8.81	0.95	14.29	4.53	0.12	0.83
Lm108n-1	-1	1	0.82	77.76	0.28	7.84	0.27	60.60	1.76	6.54	0.82
Lm108n-2	-1	2	0.82	63.11	0.26	9.02	0.55	53.05	1.87	5.46	0.82
Lm108n-3	-1	3	0.82	55.82	0.17	9.47	0.77	29.37	2.19	1.83	0.85
Lm108n-4	-1	4	0.82	52.65	0.10	9.77	0.91	19.51	1.96	0.73	0.84
Lm108n-5	-1	5	0.82	51.62	0.07	10.21	1.02	16.86	1.73	0.58	0.83
Lm108n-6	-1	6	0.82	51.15	0.06	9.05	0.91	15.02	4.30	0.27	0.82
Lm108n-7	-1	7	0.82	50.88	0.05	8.36	0.84	14.12	4.92	0.17	0.82
Lm108n-8	-1	8	0.82	50.71	0.04	8.19	0.84	13.69	4.88	0.14	0.82
Lm108n-9	-1	9	0.82	50.61	0.04	8.41	0.89	13.46	4.64	0.12	0.82
Lm108n-10	-1	10	0.82	50.53	0.03	8.72	0.95	13.32	4.41	0.12	0.82
L008n-1	0	1	0.82	67.22	0.28	7.84	0.27	60.59	1.73	6.55	0.82
L008n-2	0	2	0.82	52.58	0.26	9.09	0.56	53.32	1.66	5.60	0.82

*Continued on next page*

Table B.3 – *Continued from previous page*

#	$L_{\text{init}}$	$\dot{M}$	$M_{\text{init}}$	$t$	$M_{\text{He,f}}$	$T_{4,\text{f}}$	$L_{\text{f}}$	$\rho_{6,\text{c}}$	$T_{8,\text{ign}}$	$\rho_{6,\text{ign}}$	$M_{\text{r,ign}}$
L008n-3	0	3	0.82	42.93	0.10	8.88	0.74	19.38	1.85	0.67	0.85
L008n-4	0	4	0.82	41.38	0.07	9.69	0.93	16.35	1.74	0.60	0.82
L008n-5	0	5	0.82	40.53	0.04	8.06	0.76	13.58	4.32	0.18	0.82
L008n-6	0	6	0.82	40.11	0.03	9.56	1.00	12.81	2.47	0.18	0.82
L008n-7	0	7	0.82	40.01	0.02	8.20	0.83	12.39	3.76	0.11	0.82
L008n-8	0	8	0.82	39.94	0.02	8.62	0.92	12.29	3.61	0.09	0.82
L008n-9	0	9	0.82	39.90	0.02	6.90	0.67	12.02	4.50	0.06	0.82
L008n-10	0	10	0.82	39.87	0.02	7.06	0.71	11.96	4.47	0.05	0.82
Lm210n-4	-2	4	1.00	183.84	0.10	11.33	0.92	61.95	2.14	1.41	1.03
Lm210n-5	-2	5	1.00	182.84	0.07	11.81	1.02	52.31	1.97	0.73	1.04
Lm210n-6	-2	6	1.00	182.32	0.05	12.23	1.11	46.71	1.76	0.59	1.02
Lm210n-7	-2	7	1.00	182.02	0.04	11.27	1.04	42.73	4.73	0.29	1.02
Lm210n-8	-2	8	1.00	181.79	0.03	10.15	0.93	39.44	4.80	0.13	1.01
Lm210n-9	-2	9	1.00	181.70	0.02	10.60	1.00	38.46	4.54	0.12	1.01
Lm210n-10	-2	10	1.00	181.64	0.02	11.00	1.07	37.77	4.33	0.12	1.01
Lm110n-4	-1	4	1.00	43.47	0.07	11.09	0.92	50.54	2.13	1.10	1.01
Lm110n-5	-1	5	1.00	42.74	0.05	11.61	1.03	44.63	1.94	0.72	1.01
Lm110n-6	-1	6	1.00	42.37	0.04	12.04	1.11	41.39	1.77	0.60	1.01
Lm110n-7	-1	7	1.00	42.17	0.03	11.15	1.04	38.84	4.63	0.30	1.00
Lm110n-8	-1	8	1.00	42.01	0.02	10.02	0.92	36.80	4.85	0.13	1.00
Lm110n-9	-1	9	1.00	41.98	0.02	10.46	1.00	36.56	5.38	0.16	1.00
Lm110n-10	-1	10	1.00	41.93	0.02	10.67	1.04	36.09	5.10	0.14	1.00
L010n-4	0	4	1.00	26.72	0.04	10.96	0.94	41.93	1.99	0.75	1.00
L010n-5	0	5	1.00	26.16	0.03	10.22	0.91	36.86	4.72	0.27	1.00
L010n-6	0	6	1.00	25.87	0.01	9.32	0.81	34.11	4.58	0.12	1.00
L010n-7	0	7	1.00	25.80	0.01	9.91	0.91	33.77	4.23	0.11	1.00
L010n-8	0	8	1.00	25.77	0.01	10.49	1.00	33.55	3.94	0.11	1.00
L010n-9	0	9	1.00	25.74	0.01	10.85	1.06	33.37	3.85	0.10	1.00
L010n-10	0	10	1.00	25.72	0.01	10.13	0.99	33.13	4.49	0.07	1.00

*Continued on next page*



Table B.3 – *Continued from previous page*

#	$L_{\text{init}}$	$\dot{M}$	$M_{\text{init}}$	$t$	$M_{\text{He,f}}$	$T_{4,\text{f}}$	$L_{\text{f}}$	$\rho_{6,\text{c}}$	$T_{8,\text{ign}}$	$\rho_{6,\text{ign}}$	$M_{\text{r,ign}}$
Lm211n-4	-2	4	1.10	152.21	0.06	11.69	0.84	111.42	2.05	0.78	1.14
Lm211n-5	-2	5	1.10	151.79	0.06	12.72	1.00	106.32	2.12	0.87	1.14
Lm211n-6	-2	6	1.10	151.36	0.04	13.17	1.09	94.42	1.87	0.67	1.13
Lm211n-7	-2	7	1.10	151.11	0.03	13.51	1.15	87.27	1.77	0.57	1.12
Lm211n-8	-2	8	1.10	150.92	0.02	13.53	1.16	80.24	0.95	0.27	1.12
Lm211n-9	-2	9	1.10	150.86	0.02	11.73	1.01	77.91	4.90	0.14	1.11
Lm211n-10	-2	10	1.10	150.82	0.01	12.12	1.07	76.52	4.69	0.13	1.11
Lm111n-4	-1	4	1.10	51.81	0.06	11.98	0.89	106.19	2.04	1.65	1.11
Lm111n-5	-1	5	1.10	51.04	0.03	12.08	0.95	88.00	1.78	0.56	1.12
Lm111n-6	-1	6	1.10	50.79	0.03	10.49	0.81	81.35	5.99	0.19	1.12
Lm111n-7	-1	7	1.10	50.65	0.02	13.03	1.10	79.17	1.59	0.37	1.11
Lm111n-8	-1	8	1.10	50.57	0.02	11.24	0.94	76.30	5.18	0.15	1.11
Lm111n-9	-1	9	1.10	50.51	0.01	11.59	1.00	74.94	4.96	0.14	1.11
Lm111n-10	-1	10	1.10	50.48	0.01	11.99	1.06	73.97	4.76	0.13	1.11
L011n-4	0	4	1.10	26.20	0.02	11.74	0.92	76.40	1.79	0.62	1.10
L011n-5	0	5	1.10	25.99	0.01	9.81	0.72	72.06	5.99	0.19	1.10
L011n-6	0	6	1.10	25.89	0.01	10.23	0.80	70.73	5.49	0.16	1.10
L011n-7	0	7	1.10	25.84	0.01	10.70	0.88	69.96	5.13	0.15	1.10
L011n-8	0	8	1.10	25.80	0.01	11.21	0.95	69.45	4.79	0.14	1.10
L011n-9	0	9	1.10	25.78	0.01	11.56	1.01	69.05	4.72	0.13	1.10
L011n-10	0	10	1.10	25.77	0.01	12.10	1.08	68.78	4.37	0.13	1.10



# Acknowledgements

Modern science is a collaborative effort, and even though each individual researcher may work on their own part of a project, the people around them shape and inform their creation of new knowledge.

My utmost gratitude belongs in equal parts to Sung-Chul and Norbert. Norbert, whose patient advice and unparalleled scientific experience was always freely given, set an example for any aspiring scientist to follow. Sung-Chul not only provided the impetus for this thesis but also support in its realization with his extensive technical expertise and profound knowledge of the field. Without the support of these two, this thesis would doubtlessly never have come into existence.

I further wish to thank Thomas for his support and willingness to engage in useful discussions about mass-transfer in compact binaries. Further thanks belongs to Zhengwei, who provided interesting and relevant insights into the structure of Iax progenitors. Phillip Podsiadlowski is entitled to my thanks for providing the impetus to consider Ca-enhanced SNe Ib.

I extend my gratitude to Frank, who was kind enough to give me the opportunity to gain some teaching experience.

I am grateful to Rob Izzard for providing valuable insights into problems of population synthesis and Elisabeth Kramer's competent handling of administrative matters (especially when communication proved difficult during my stay in Korea) was much appreciated.

I also wish to thank Matthias for providing an enjoyable atmosphere in the office and for countless reminders of correct code syntax (repaid in kind). I also thank Abel for always providing a dash of humor to the work environment.

But of course the entirety of the stellar astrophysics group, whether they're still around or have moved on to new challenges at the time of the submission of this thesis, are to be thanked for providing a friendly and sophisticated environment where theses like this can be created by aspiring researchers.

I would also like to thank the Korea Astronomy and Space Science Institute (Project No. 3348-20160002) and the Deutsche Forschungsgemeinschaft (Grant No. Yo 194/1-1) who kindly provided funding for these projects.

My work on these projects had its ups and its regrettable downs, but, hearkening back to the quote at the beginning of this treatise, it was an exercise in character building as much as one of scientific endeavor. It was a humbling experience, not only with regards to the awesomeness of the subject matter but also on an interpersonal level. Above all, not least thanks to everyone mentioned above, it will be a time to fondly remember, like one remembers the arch of the Milky Way in a dark and cloudless night.



# Bibliography

- Abbott, B. P., Abbott, R., Abbott, T. D., et al. 2016, *Physical Review Letters*, 116, 241103
- Antonucci, R. 1993, *ARA&A*, 31, 473
- Anzer, U., Boerner, G., & Monaghan, J. J. 1987, *A&A*, 176, 235
- Bedin, L. R., King, I. R., Anderson, J., et al. 2008, *ApJ*, 678, 1279
- Benetti, S., Cappellaro, E., Mazzali, P. A., et al. 2005, *ApJ*, 623, 1011
- Benz, W. 1997, in *NATO Advanced Science Institutes (ASI) Series C*, Vol. 486, NATO Advanced Science Institutes (ASI) Series C, ed. P. Ruiz-Lapuente, R. Canal, & J. Isern, 457
- Bergeron, P., Saffer, R. A., & Liebert, J. 1992, *ApJ*, 394, 228
- Bernasconi, P. A. & Maeder, A. 1996, *A&A*, 307, 829
- Bildsten, L., Shen, K. J., Weinberg, N. N., & Nelemans, G. 2007, *ApJ*, 662, L95
- Braun, A. 1998, PhD Thesis
- Brooks, J., Bildsten, L., Marchant, P., & Paxton, B. 2015, *ApJ*, 807, 74
- Brooks, J., Bildsten, L., Schwab, J., & Paxton, B. 2016, *The Astrophysical Journal*, 821, 28
- Burrows, A., Hubbard, W. B., Lunine, J. I., & Liebert, J. 2001, *Reviews of Modern Physics*, 73, 719
- Burrows, A. & Liebert, J. 1993, *Reviews of Modern Physics*, 65, 301
- Carr, B. J., Bond, J. R., & Arnett, W. D. 1984, *ApJ*, 277, 445
- Carroll, B. W. & Ostlie, D. A. 2007, *An Introduction to Modern Astrophysics* (Addison-Wesley)
- Carroll, S. M. 2004, *Spacetime and geometry. An introduction to general relativity* (Addison Wesley)
- Chandrasekhar, S. 1931a, *MNRAS*, 91, 456
- Chandrasekhar, S. 1931b, *ApJ*, 74, 81
- Clark, P. C., Glover, S. C. O., Smith, R. J., et al. 2011, *Science*, 331, 1040
- Colless, M., Dalton, G., Maddox, S., et al. 2001, *MNRAS*, 328, 1039
- Dan, M., Rosswog, S., Brüggen, M., & Podsiadlowski, P. 2014, *MNRAS*, 438, 14
- de Val-Borro, M., Karovska, M., & Sasselov, D. 2009, *ApJ*, 700, 1148

## *BIBLIOGRAPHY*

- Demorest, P. B., Pennucci, T., Ransom, S. M., Roberts, M. S. E., & Hessels, J. W. T. 2010, *Nature*, 467, 1081
- Eggenberger, P., Maeder, A., & Meynet, G. 2005, *A&A*, 440, L9
- Eggleton, P. 2011, *Evolutionary Processes in Binary and Multiple Stars* (Cambridge Univ. Press)
- Eggleton, P. P. 1983, *ApJ*, 268, 368
- Endal, A. S. & Sofia, S. 1976, *ApJ*, 210, 184
- Endal, A. S. & Sofia, S. 1978, *ApJ*, 220, 279
- ESA, ed. 1997, *ESA Special Publication*, Vol. 1200, *The HIPPARCOS and TYCHO catalogues. Astrometric and photometric star catalogues derived from the ESA HIPPARCOS Space Astrometry Mission*
- Fink, M., Hillebrandt, W., & Röpke, F. K. 2007, *A&A*, 476, 1133
- Fink, M., Röpke, F. K., Hillebrandt, W., et al. 2010, *A&A*, 514, A53
- Foley, R. J., Challis, P. J., Chornock, R., et al. 2013, *ApJ*, 767, 57
- Foley, R. J., Jha, S. W., Pan, Y.-C., et al. 2016, *MNRAS*, 461, 433
- Foley, R. J., Van Dyk, S. D., Jha, S. W., et al. 2015, *ApJ*, 798, L37
- Fricke, K. 1969, *Astrophys. Lett.*, 3, 219
- Gallagher, J. S. & Starrfield, S. 1978, *ARA&A*, 16, 171
- Gamow, G. 1938, *Physical Review*, 53, 595
- Geier, S., Fürst, F., Ziegerer, E., et al. 2015, *Science*, 347, 1126
- Gilfanov, M. & Bogdán, Á. 2010, *Nature*, 463, 924
- Gliese, W. & Jahreiß, H. 1991, *Preliminary Version of the Third Catalogue of Nearby Stars*, Tech. rep., ARI
- Gold, T. 1968, *Nature*, 218, 731
- Goldreich, P. & Schubert, G. 1968, *ApJ*, 154, 1005
- González-Gaitán, S., Hsiao, E. Y., Pignata, G., et al. 2014, *ApJ*, 795, 142
- Hachinger, S., Mazzali, P. A., Taubenberger, S., et al. 2012, *MNRAS*, 422, 70
- Hachisu, I., Kato, M., Saio, H., & Nomoto, K. 2012, *ApJ*, 744, 69
- Hamuy, M., Phillips, M. M., Suntzeff, N. B., et al. 2003, *Nature*, 424, 651
- Hashimoto, M.-A., Hanawa, T., & Sugimoto, D. 1983, *PASJ*, 35, 1

- Hashimoto, M.-A., Nomoto, K.-I., Arai, K., & Kaminisi, K. 1986, *ApJ*, 307, 687
- Hawking, S. W. 1974, *Nature*, 248, 30
- Heber, U., Napiwotzki, R., & Reid, I. N. 1997, *A&A*, 323, 819
- Heger, A. & Langer, N. 2000, *ApJ*, 544, 1016
- Heger, A., Langer, N., & Woosley, S. E. 2000, *ApJ*, 528, 368
- Heger, A., Woosley, S. E., & Spruit, H. C. 2005, *The Astrophysical Journal*, 626, 350
- Hillebrandt, W. & Niemeyer, J. C. 2000, *ARA&A*, 38, 191
- Iben, Jr., I. & Tutukov, A. V. 1984, *ApJS*, 54, 335
- Iben, Jr., I. & Tutukov, A. V. 1985, *ApJS*, 58, 661
- Iben, Jr., I. & Tutukov, A. V. 1989, *ApJ*, 342, 430
- Iben, Jr., I. & Tutukov, A. V. 1991, *ApJ*, 370, 615
- Ivanova, N., Justham, S., Chen, X., et al. 2013, *A&A Rev.*, 21, 59
- Ivanova, N. & Taam, R. E. 2004, *ApJ*, 601, 1058
- Janka, H.-T., Langanke, K., Marek, A., Martínez-Pinedo, G., & Müller, B. 2007, *Phys. Rep.*, 442, 38
- Kalogera, V. & Baym, G. 1996, *ApJ*, 470, L61
- Kato, M. & Hachisu, I. 2004, *The Astrophysical Journal Letters*, 613, L129
- Kawabata, K. S., Maeda, K., Nomoto, K., et al. 2010, *Nature*, 465, 326
- Kawaler, S. D. 2003, *ArXiv Astrophysics e-prints*
- Kelly, P. L., Fox, O. D., Filippenko, A. V., et al. 2014, *ApJ*, 790, 3
- Kilic, M., Hermes, J. J., Gianninas, A., et al. 2014, *MNRAS*, 438, L26
- Kippenhahn, R. & Thomas, H.-C. 1978, *A&A*, 63, 265
- Kippenhahn, R. & Weigert, A. 1990, *Stellar Structure and Evolution* (Springer-Verlag Berlin Heidelberg New York), 192
- Koester, D., Dreizler, S., Weidemann, V., & Allard, N. F. 1998, *A&A*, 338, 612
- Kolb, U. & Ritter, H. 1990, *A&A*, 236, 385
- Kromer, M., Ohlmann, S. T., Pakmor, R., et al. 2015, *MNRAS*, 450, 3045
- Kromer, M., Sim, S. A., Fink, M., et al. 2010, *ApJ*, 719, 1067
- Kroupa, P. 2002, *Science*, 295, 82

## *BIBLIOGRAPHY*

- Landau, L. & Livshitz, E. 1975, *The Classical Theory of Fields, Course of theoretical physics* (Butterworth Heinemann)
- Langer, N. 1991, *A&A*, 252, 669
- Langer, N. 1998, *A&A*, 329, 551
- Langer, N., Deutschmann, A., Wellstein, S., & Höflich, P. 2000, *A&A*, 362, 1046
- Larson, R. B. 1969, *MNRAS*, 145, 271
- Li, W., Bloom, J. S., Podsiadlowski, P., et al. 2011, *Nature*, 480, 348
- Li, W., Filippenko, A. V., Chornock, R., et al. 2003, *PASP*, 115, 453
- Liddle, A. 2003, *An Introduction to Modern Cosmology, Second Edition* (Wiley-VCH)
- Liebert, J. 1980, *ARA&A*, 18, 363
- Liu, Z.-W., Moriya, T. J., Stancliffe, R. J., & Wang, B. 2015a, *A&A*, 574, A12
- Liu, Z.-W., Stancliffe, R. J., Abate, C., & Wang, B. 2015b, *ApJ*, 808, 138
- Livio, M. & Warner, B. 1984, *The Observatory*, 104, 152
- Livne, E. 1990, *ApJ*, 354, L53
- Livne, E. 1997, in *NATO Advanced Science Institutes (ASI) Series C, Vol. 486, NATO Advanced Science Institutes (ASI) Series C*, ed. P. Ruiz-Lapuente, R. Canal, & J. Isern, 425
- Livne, E. & Arnett, D. 1995, *ApJ*, 452, 62
- Livne, E. & Glasner, A. S. 1990, *ApJ*, 361, 244
- Livne, E. & Glasner, A. S. 1991, *ApJ*, 370, 272
- Luhman, K. L. 2012, *ARA&A*, 50, 65
- Maeder, A. 2009, *Physics, Formation and Evolution of Rotating Stars* (Springer Berlin Heidelberg)
- Maeder, A. & Meynet, G. 2003, *A&A*, 411, 543
- Maeder, A. & Meynet, G. 2004, *A&A*, 422, 225
- Magee, M. R., Kotak, R., Sim, S. A., et al. 2016, *A&A*, 589, A89
- Maoz, D. & Mannucci, F. 2008, *MNRAS*, 388, 421
- Maoz, D. & Mannucci, F. 2012, *PASA*, 29, 447
- McCully, C., Jha, S. W., Foley, R. J., et al. 2014, *Nature*, 512, 54
- Menon, A., Herwig, F., Denissenkov, P. A., et al. 2013, *ApJ*, 772, 59



- Meyer, F. & Meyer-Hofmeister, E. 1983, *A&A*, 128, 420
- Misner, C. W., Thorne, K. S., & Wheeler, J. A. 1973, *Gravitation* (W.H. Freeman and Co.)
- Mochkovitch, R. & Livio, M. 1989, *A&A*, 209, 111
- Mosser, B., Goupil, M. J., Belkacem, K., et al. 2012, *A&A*, 548, A10
- Mulligan, B. W. & Wheeler, J. C. 2015, *ArXiv e-prints*
- Nakamura, F. & Umemura, M. 1999, *ApJ*, 515, 239
- Nandkumar, R. & Pethick, C. J. 1984, *MNRAS*, 209, 511
- Nelemans, G. 2005, in *Astronomical Society of the Pacific Conference Series*, Vol. 330, *The Astrophysics of Cataclysmic Variables and Related Objects*, ed. J.-M. Hameury & J.-P. Lasota, 27
- Nelemans, G., Voss, R., Roelofs, G., & Bassa, C. 2008, *MNRAS*, 388, 487
- Neunteufel, P., Yoon, S.-C., & Langer, N. 2016, *A&A*, 589, A43
- Neunteufel, P., Yoon, S.-C., & Langer, N. 2017, *A&A*, 602, A55
- Nomoto, K. 1980, in *Texas Workshop on Type I Supernovae*, ed. J. C. Wheeler, 164–181
- Nomoto, K. 1982a, *ApJ*, 257, 780
- Nomoto, K. 1982b, *ApJ*, 253, 798
- Nomoto, K., Saio, H., Kato, M., & Hachisu, I. 2007, *ApJ*, 663, 1269
- Nomoto, K. & Sugimoto, D. 1977, *PASJ*, 29, 765
- Novikov, I. D., Polnarev, A. G., Starobinskii, A. A., & Zeldovich, I. B. 1979, *A&A*, 80, 104
- Oppenheimer, J. R. & Volkoff, G. M. 1939, *Physical Review*, 55, 374
- Paczynski, B. 1991, *ApJ*, 370, 597
- Perets, H. B., Gal-yam, A., Crockett, R. M., et al. 2011, *ApJ*, 728, L36
- Perets, H. B., Gal-Yam, A., Mazzali, P. A., et al. 2010, *Nature*, 465, 322
- Perlmutter, S., Aldering, G., Goldhaber, G., et al. 1999, *ApJ*, 517, 565
- Persson, S. E., Madore, B. F., Krzemiński, W., et al. 2004, *AJ*, 128, 2239
- Piersanti, L., Gagliardi, S., Iben, Jr., I., & Tornambé, A. 2003, *ApJ*, 583, 885
- Piersanti, L., Tornambé, A., & Yungelson, L. R. 2014, *MNRAS*, 445, 3239
- Piersanti, L., Yungelson, L. R., & Tornambé, A. 2015, *MNRAS*, 452, 2897
- Popham, R. & Narayan, R. 1991, *ApJ*, 370, 604

## *BIBLIOGRAPHY*

- Rana, N. C. 1987, *A&A*, 184, 104
- Renado, I., Althaus, L. G., Miller Bertolami, M. M., et al. 2010a, *ApJ*, 717, 183
- Renado, I., Althaus, L. G., Miller Bertolami, M. M., et al. 2010b, *ApJ*, 717, 183
- Riess, A. G., Filippenko, A. V., Challis, P., et al. 1998, *AJ*, 116, 1009
- Ritter, H. 1988, *A&A*, 202, 93
- Ruiter, A. J., Belczynski, K., Sim, S. A., et al. 2011, *MNRAS*, 417, 408
- Ruiter, A. J., Belczynski, K., Sim, S. A., Seitenzahl, I. R., & Kwiatkowski, D. 2014, *MNRAS*, 440, L101
- Russell, H. N. 1914a, *Nature*, 93, 227
- Russell, H. N. 1914b, *Nature*, 93, 252
- Salpeter, E. E. 1952, *Physical Review*, 88, 547
- Salpeter, E. E. 1955, *ApJ*, 121, 161
- Schaefer, B. E. & Pagnotta, A. 2012, *Nature*, 481, 164
- Schaerer, D. 2002, *A&A*, 382, 28
- Schmidt, B. P., Suntzeff, N. B., Phillips, M. M., et al. 1998, *ApJ*, 507, 46
- Schulze, H.-J., Polls, A., Ramos, A., & Vidaña, I. 2006, *Phys. Rev. C*, 73, 058801
- Shen, K. J. & Bildsten, L. 2009, *ApJ*, 699, 1365
- Shen, K. J., Kasen, D., Weinberg, N. N., Bildsten, L., & Scannapieco, E. 2010, *ApJ*, 715, 767
- Shen, K. J. & Moore, K. 2014, *ApJ*, 797, 46
- Sim, S. A., Röpke, F. K., Hillebrandt, W., et al. 2010, *ApJ*, 714, L52
- Sion, E. M. 1999, *PASP*, 111, 532
- Sion, E. M. & Godon, P. 2012, *Mem. Soc. Astron. Italiana*, 83, 539
- Spruit, H. C. 2002, *A&A*, 381, 923
- Staff, J. E., Menon, A., Herwig, F., et al. 2012, *ApJ*, 757, 76
- Stebbins, J. 1908, *ApJ*, 27
- Suh, H., Yoon, S.-c., Jeong, H., & Yi, S. K. 2011, *ApJ*, 730, 110
- Suijs, M. P. L., Langer, N., Poelarends, A.-J., et al. 2008, *A&A*, 481, L87
- Taam, R. E. 1980a, *ApJ*, 237, 142

- Taam, R. E. 1980b, *ApJ*, 242, 749
- Tayler, R. J. 1973, *MNRAS*, 161, 365
- Theuns, T., Boffin, H. M. J., & Jorissen, A. 1996a, *MNRAS*, 280, 1264
- Theuns, T., Boffin, H. M. J., & Jorissen, A. 1996b, *MNRAS*, 280, 1264
- Theuns, T. & Jorissen, A. 1993, *MNRAS*, 265, 946
- Thorne, K. S. & Żytkow, A. N. 1975, *ApJ*, 199, L19
- Thorne, K. S. & Żytkow, A. N. 1977, *ApJ*, 212, 832
- van Kerkwijk, M. H., Chang, P., & Justham, S. 2010, *ApJ*, 722, L157
- Waldman, R., Sauer, D., Livne, E., et al. 2011, *The Astrophysical Journal*, 738, 21
- Wang, B. & Han, Z. 2009, *A&A*, 508, L27
- Wang, B., Justham, S., & Han, Z. 2013, *A&A*, 559, A94
- Warner, B. 1995, *Ap&SS*, 225, 249
- Webbink, R. F. 1984, *ApJ*, 277, 355
- Whelan, J. & Iben, Jr., I. 1973, *ApJ*, 186, 1007
- Woosley, S. & Janka, T. 2005, *Nature Physics*, 1, 147
- Woosley, S. E. & Kasen, D. 2011, *ApJ*, 734, 38
- Woosley, S. E., Langer, N., & Weaver, T. A. 1993, *ApJ*, 411, 823
- Woosley, S. E., Taam, R. E., & Weaver, T. A. 1986, *ApJ*, 301, 601
- Woosley, S. E. & Weaver, T. A. 1994, *ApJ*, 423, 371
- Yamanaka, M., Maeda, K., Kawabata, K. S., et al. 2015, *ApJ*, 806, 191
- Yoon, S.-C. & Langer, N. 2003, *A&A*, 412, L53
- Yoon, S.-C. & Langer, N. 2004a, *A&A*, 419, 645
- Yoon, S.-C. & Langer, N. 2004b, *A&A*, 419, 623
- Yoon, S.-C. & Langer, N. 2005, *A&A*, 435, 967
- Yoon, S.-C., Woosley, S. E., & Langer, N. 2010, *ApJ*, 725, 940
- Yoshida, N., Bromm, V., & Hernquist, L. 2004, *ApJ*, 605, 579
- Yuan, F., Kobayashi, C., Schmidt, B. P., et al. 2013, *MNRAS*, 432, 1680

## *BIBLIOGRAPHY*

Zahn, J.-P. 1974, in IAU Symposium, Vol. 59, Stellar Instability and Evolution, ed. P. Ledoux, A. Noels, & A. W. Rodgers, 185–194

Zahn, J.-P. 1992, *A&A*, 265, 115

Zapartas, E., de Mink, S. E., Izzard, R. G., et al. 2017, ArXiv e-prints

Zdunik, J. L. & Haensel, P. 2013, *A&A*, 551, A61

# CURRICULUM VITAE

## PERSONAL DETAILS

Name:	Patrick Neunteufel
Date of Birth:	09/20/1986
Email:	neunteufel@astro.uni-bonn

---

## EDUCATION

2006-2012:	Diploma in Physics, Karlsruher Institut für Technologie (KIT), Karlsruhe, Germany
2013-2017:	PhD in Stellar Physics, Rheinische Friedrich-Wilhelms-Universität, Bonn, Germany.

---

## PROFESSIONAL EXPERIENCE

2009-2012:	Teaching assistant (consecutive) for experimental physics and theoretical physics (KIT)
2010:	Student research assistant at the Institute for Experimental Nuclear Physics - KATRIN (KIT)
2013-2017:	Teaching assistant for theoretical physics (AlfA)
2016-2017:	Visiting scholar at the College of Physics and Astronomy (Seoul National University)

---

## LANGUAGES

German:	Native speaker
English:	Fluent

## PEER-REVIEWED PUBLICATIONS

- Smida et al.,  
**First Experimental Characterization of Microwave Emission from Cosmic Ray Air Shower**  
Physical Review Letters, Volume 113, Issue 22, id.221101 (co-author)
- Stasielak et al.,  
**Feasibility of radar detection of extensive air shower**  
Astroparticle Physics, Volume 73, p. 14-27 (co-author)
- Neunteufel et al.,  
**Models for the evolution of close binaries with He-star and white dwarf components towards Type Ia supernova explosions**  
Astronomy & Astrophysics, Volume 589, A43 (corresponding author)
- Neunteufel et al.,  
**Helium ignition in rotating magnetized CO white dwarfs leading to fast and faint rather than classical type Ia supernova**  
Astronomy & Astrophysics, Volume 602, A55 (corresponding author)

## NON-PEER-REVIEWED PUBLICATIONS

- Stasielak et al.,  
**Radar reflection off extensive air showers,**  
arXiv:1210.1427v1, 2012 (co-author)
- Smida et al.,  
**Observation of Polarised Microwave Emission from Cosmic Ray Air Showers,**  
arXiv:1306.6738, 2013 (co-author)